Seismic Performance of Reinforced Earth Walls.

A thesis

submitted in partial fulfilment

of the requirements for the Degree

of

Doctor of Philosophy

in the

University of Canterbury

by

G. J. Fairless

University of Canterbury

1989

ABSTRACT

Previous seismic testing of reinforced earth walls, and present design methods, are outlined.

Six one metre tall model reinforced earth walls were tested under normal gravity on a shaking table. Accelerations, displacements and reinforcing strip forces were measured. A series of simple sinusoidal single-pulse wave forms, and the El Centro 1940 north-south recorded earthquake motion were used as input to the shaking table.

Permanent outward displacement of a block consisting of the facing, part of the reinforced block, and a wedge of retained soil behind the reinforced block occurred when a limiting or yield acceleration was exceeded. The wall facing remained essentially vertical. The critical (minimum) yield acceleration was found to occur when and after the failure surface outcropped at the fill surface. This critical yield acceleration was calculable using a limiting equilibrium formulation, within the variability of the observed results. A sensitivity analysis of the formulation is presented.

The apparent soil friction angle is found to reduce during repeated seismic shaking, while the apparent soil-strip friction coefficient is found to increase, probably to a limiting value. In design, the peak value of the friction coefficient found from direct shear tests between the soil and reinforcing can be used. To calculate design strip forces, an upper bound seismic earth pressure coefficient based on the Mononobe-Okabe dynamic earth pressure coefficient K_{AE} is proposed.

Measured displacements are plotted on charts for three sliding block displacement prediction methods. One approach, using random vibration and probability theory, is more rational and complete than the others, and provides an estimate of the probability of exceedence of the calculated displacement. The method is quite complicated, however, and for everyday design a simple upper bound on a chart derived from an equivalent pulse technique is recommended.

ACKNOWLEDGEMENTS

I wish to express my gratitude to my supervisor, Prof. David Elms, for assistance, guidance, and encouragement during the course of this work. My often woolly thinking was quickly banished by our discussions. My passage through some aspects of the University and course regulations was also eased by his efforts on my behalf.

Dr R O Davis was always approachable and ready to offer help and encouragement during the course of the work, for which I am grateful. Rob cheerfully stood in for my supervisor in his absence.

Mr W K Kennedy of the Dept of Electrical and Electronic Engineering is thanked for his assistance with Fourier transform theory, and seemingly endless patience with the minutiae of calculating power spectra.

Dr J B Berrill is thanked for assistance at different times, and for nearly always being able to specify a suitable reference.

Without the help of the technical staff the testing would not have been possible. Mr J van Dyk helped greatly, with both ideas and construction expertise, in the setting up of much of the testing equipment. Mr G E Hill operated the shaking table and data logging equipment, as well as offering advice on testing in general and on the use of the equipment. Mr P F Coursey assisted with modifications and fabrication of additional equipment before and during the second series of tests, as well as operating the shaking table. Others helped in many ways also, and to all of them, I am very grateful for their assistance. Working in the dusty environment of sand raining was not pleasant.

Many times, informal discussions with my fellow graduate students have helped formulate an idea or a line of inquiry. It has been a pleasure to have met and worked (and sometimes relaxed) with them, and for their presence I am grateful.

I am grateful for the encouragement and support of my parents, sometimes from overseas, during my return to university. Their initial reticence over my continuing with graduate study seemed to be quickly forgotten.

The financial assistance of my employer, the Ministry of Works and Development (latterly the Works and Development Services Corporation) is gratefully acknowledged. The testing was made possible by grants from the NZ National Roads Board and the Reinforced Earth Company (NZ) Ltd.

CONTENTS -

Chapter		Page
ABSTRACT		i
CONTENTS.		v
LIST OF FIGURES.		xi
LIST OF TABLES.		xxxi
NOTATION		xli
1.	INTRODUCTION TO REINFORCED EARTH	1
1.1.	About Reinforced Earth.	1
1.2.	Seismic performance of RE.	3
1.3.	Structure of the thesis.	4
2.	PREVIOUS DYNAMIC TESTING	7
2.1.	Introduction.	7
2.2.	UCLA testing.	7
2.3.	Ohio State University.	19
2.4.	Japanese National Railways.	20
2.5.	University of Canterbury.	24
3.	DESIGN METHODS	29
3.1.	Introduction.	29
3.2.	Static design method.	30
3.3.	Richardson and Lee (1975)	32
3.4.	Richardson (1978).	33
3.5.	Prendergast and Ramsay (1980)	38
3.6.	Seed and Mitchell.	39
3.7.	Bracegirdle (1979,1980).	43
3.8.	About the present study.	44

4. THE LIMITING DISPLACEMENT APPROACH 47
4.1. Introduction. 47
4.2. Failure surface contained. 49
4.3. Failure surface not contained. 51
4.4. Extension to two-step block structure. 53
4.5. Modifications to the formulation. 57
4.6. Calculation of displacement. 58
4.6.1. Equivalent pulse technique (Sarma, 1979). 59
4.6.2. Standardized displacements by double integration (Newmark, 1965). 62
4.6.3. Random vibration theory (Lin and Whitman, 1986). . . . 65
4.7. Requirements to verify the system. 71

5. DESCRIPTION OF TESTING 75
5.1. Introduction. 75
5.2. Dynamic modelling and similitude. 76
5.2.1. Introduction. 76
5.2.2. Similitude theory and discussion relative to dynamic testing of model RE walls. 79
5.2.2.1. Similitude theory.. 79
5.2.2.2. Modelling of reinforced earth.. 81
5.2.2.2.1. Small-strain elastic response, and the natural frequencies of vibration. 82
5.2.2.2.2. Formation of the failure surface. 84
5.2.2.2.3. Post-failure displacement.. 86
5.2.2.2.4. Analysis comments.. 86
5.2.2.2.5. About the present study.. 88
5.2.3. Hornbeck's study. 89
5.3. Testing procedures and methods. 91
5.3.1. The containing box. 91
5.3.2. The sand. 93
5.3.3. Sand raining. 93
5.3.4. Density determinations. 96
5.3.5. Facing panels. 97
5.3.6. Reinforcing strips. 99
5.3.6.1. Introduction.. 99
5.3.6.2. Surface preparation of reinforcing strips. 100

5.3.6.3. Instrumentation of reinforcing strips. 100
5.3.6.4. Attachment of strips to the wall facing. 101
5.3.6.5. Strip attachment.. 103
5.3.7. Displacement measurements. 104
5.3.8. Wall construction. 104
5.3.9. Acceleration measurement. 105
5.3.10. Shake table inputs. 106
5.3.11. Data logging. 109
5.3.12. Failure surface measurements. 111
5.3.13. Test configurations. 113
5.4. Testing for shear strength parameters. 113
5.4.1. Pullout tests for soil/strip coefficient of friction. . 114
5.4.2. Sliding shear tests. 118
5.4.3. Angle of internal friction of the sand. 119

6. RESULTS AND ANALYSIS 123
6.1. Introduction. 123
6.2. Data treatment methods. 124
6.2.1. Computing methods and problems. 124
6.2.2. Wild point removal. 125
6.2.3. Dimensional scaling. 128
6.2.4. Scanning slew removal. 129
6.2.5. Smoothing the data. 129
6.2.6. Data file format. 131
6.2.7. Aliasing. 131
6.2.8. Graphing systems. 132
6.3. Observed k_h and α in the limiting equilibrium formulation. . 133
6.3.1. Observed yield accelerations, k_h. 133
6.3.2. Observed failure geometry. 134
6.3.3. Comparison of observed k_h and α, with limiting equilibrium formulation predictions. 140
6.4. Observed strip forces. 143
6.4.1. Time histories of strip forces. 144
6.4.2. Strip force distributions. 155
6.4.2.1. Construction forces. 155
6.4.2.2. Dynamically induced forces.. 156
6.4.2.3. Force distributions adjacent to the wall face. . . 167

6.4.2.4. Forces observed at the failure surfaces. 171
6.5. Observed forces in the limiting equilibrium formulation. . 177
6.5.1. Calculated k_h using observed failure surface angle α and observed forces. 178
6.5.2. Mobilised f* using observed α, observed k_h, and observed forces. 179
6.5.3. Mobilised ϕ using observed forces, k_h and α. 180
6.6. Mobilised f* from strip pullout force formulations. 182
6.6.1. Mobilised friction coefficient f* from forces at the failure surface, using the R formulation (Eq. 4.6). 183
6.6.2. Mobilised friction coefficient f*: strip by strip using Eq. 5.3. 184
6.7. Strip-soil friction in reinforced earth. 190
6.7.1. Introduction. 190
6.7.2. Previous research. 191
6.7.3. Values for use in design. 197
6.7.4. Comparison of observed f* and present current specifications. 199
6.7.4.1. Introduction.. 199
6.7.4.2. Comparison of observed f* values and f* test values 199
6.7.4.3. Conclusion.. 206
6.8. Mobilised ϕ using the limiting equilibrium formulation and f* 207
6.9. Dimensionless tension T*, a pseudo-earth pressure coefficient 209
6.10. Displacements. 216
6.10.1. Measured displacements and accelerations. 216
6.10.2. Sarma's equivalent pulse method of displacement calculation. 231
6.10.3. Lin and Whitman's method using random vibration theory. 232
6.10.4. Standardized displacements using the Newmark / Franklin and Chang chart. 239
6.10.5. Conclusions on displacement prediction. 241
6.11. A sensitivity analysis of the limiting equilibrium formulation.. 242
6.11.1. Sensitivity of parameters as it affects model walls. . 243
6.11.2. Sensitivity of parameters as it affects a full scale wall.. 246
6.11.3. Conclusions on sensitivity to parameters. 250

7. CONCLUSIONS 251
7.1. Conclusions of the study. 251
7.2. Some closing remarks, and further work required. 259

REFERENCES. 263

APPENDIX A. ADDITIONAL DETAILS ON EXPERIMENTAL WORK 275
A.1. Sidewall friction in the containing box. 275
A.2. Sand placement. 277
A.3. Shaking table. 281
A.4. Data Logging. 281
A.5. Reinforcing strip instrumentation. 283
A.5.1. Strain gauge attachment and wiring. 283
A.6. Calibration. 285
A.7. Test Excitations. 285

APPENDIX B. DESIGN OF TEST WALLS. 289

APPENDIX C. TABULATED DATA FROM CHAPTER 6. 293

APPENDIX D. ON CALCULATING SPECTRAL DENSITY FUNCTIONS 305
D.1. Introduction. 305
D.2. Computation procedures. 305
D.3. Leakage. 307
D.4. Verification of the program. 310

x

LIST OF FIGURES.

Figure number		Page
1.1	Cross section of a typical RE wall.	2
2.1.	Envelope of maximum seismic earth pressures (Richardson and Lee 1975)	9
2.2.	Resonance response of model RE wall (Richardson et al, 1977). .	10
2.3.	Dynamic modulus and damping from shaking table tests (Richardson and Lee 1975).	10
2.4.	Measured and calculated first and second mode natural frequencies for different height of R/E walls (Richardson et al 1977).	12
2.5(a)	Field measured dynamic properties of backfill soil at UCLA test wall compared with published data (Richardson et al 1977)	14
2.5(b)	Shear moduli of sands at different relative densities (Seed and Idriss, 1970)	14
2.6.	Magnification factors for acceleration pulses (Rea and Wolfe, 1980).	17
2.7.	Effect of acceleration intensity on permanent displacements (Rea and Wolfe, 1980).	18
2.8.	Effect of factor of safety on yield accelerations (Rea and Wolfe, 1980).	18
2.9.	JNR model RE embankment cross-sections (Cormack et al 1980). .	21
2.10.	Results of JNR vibration test, configuration shown (Cormack et al 1980).	22
2.11.	Wall 2 after failure (Nagel, 1985).	25
2.12.	Wall 6 after failure (Nagel, 1985).	25
2.13.	Typical acceleration and displacement time histories, late in test (Nagel 1985).	26
2.14.	Typical acceleration time history after full failure surface formation (Nagel 1985).	27
3.1.	Static design parameters (Boyd, 1985).	31
3.2.	Reinforced Earth Company Design method (Nagel 1985).	32
3.3.	Estimating peak dynamic strains (Richardson, 1978).	33
3.4.	Estimating the level of damping (Richardson, 1978).	33

3.5. Design response spectra synthesis (Richardson, 1978). 34
3.6. Natural frequency reduction factor (Richardson, 1978). 35
3.7. Stiffness vs Dynamic Earth Pressure (Richardson 1978). 35
3.8. Earthquake earth pressure (MWD, 1980). 38
3.9. Seismic active zone definition (MWD, 1980). 39
3.10. Active zone from Japanese work (TAI, 1985). 41
3.11. Static, dynamic, and inertia earth pressures (TAI, 1985). . . 41
4.1. Limiting equilibrium, failure surface contained. 49
4.2. Limiting equilibrium, failure not contained. 51
4.3. Cases for two-step reinforced block. 53
4.4. Case 4 for two step structure. 54
4.5. Loads on a slice consisting of the top half of a wall. 55
4.6. Rigid block on a sloping surface (Sarma 1975). 59
4.7. Rectangular, triangular, and half sine pulses (Sarma 1975). . . 60
4.8. Variation of dimensionless displacement with k_h/K_m (Sarma 1975). 61
4.9. Newmark's chart after Franklin and Chang (1977). 63
4.10. Permanent displacement caused by one cycle of excitation (Lin and Whitman, 1986). 69
4.11. Plot of function $g(k_h/\sigma)$ (Lin and Whitman 1986). 71
4.12. Comparison of predicted and calculated permanent displacements at k_h/A_{max} = 0.1 level (after Lin and Whitman, 1986). . . 71
4.13. Comparison of predicted and calculated permanent displacements at k_h/A_{max} = 0.5 level (after Lin and Whitman, 1986). . . 71
5.1. Typical curves from a drained triaxial test on a dense sand (from Atkinson and Bransby, 1978) 84
5.2. Failure of dense sands in drained triaxial tests (after Atkinson and Bransby, 1978) 85
5.3. The steel frame of the test box on the shake table, prior to lining with plywood. 91
5.4. Grading curve of Mt Somers sand. 93
5.5. Scanning electron microscope photograph of Mt Somers sand. . . 94
5.6. Sand raining during filling for test 1. 94
5.7. Cardboard cover in place to protect the toe area from sand placement before the completion of construction. 95
5.8. Cross section of facing panels. 98

5.9. Panel end sealing in place, tests 2 to 6. Usually only three small pieces of tape were used. 98
5.10. End sealing details, tests 2 to 6. Visible are the end of the facing panel, the knit fabric (dark colour), the synthetic flap at the end, and the PVC parcel tape along one edge of the panel. 98
5.11. Leakage crater in test 1. A similar crater formed at the other end of the wall. 99
5.12. Strain gauge wiring laid out on the sand surface. 101
5.13. Strip attachment cloth loop. Also shown is the strain gauge closest to the facing panel. 102
5.14. Strip attachment detail: a) plan view, b) elevation. 102
5.15. Strip attachment detail at wall outside facing. 103
5.16. Test 2 near end of test, showing displacement transducers and exit of wiring loom. 104
5.17. A wall ready for the fitting of a new panel, showing the wedge of sand removed for the sealing flap. 106
5.18. a) Acceleration, and b) displacement traces of FARLS2. The displacement zero is mid-travel of the table top, its normal resting place. 107
5.19. Acceleration, displacement, and velocity traces of EQCV1D. . . 108
5.20. Power spectral density function of El Centro 1940 NS, at natural time scale. 109
5.21. Power spectral density function of Test 5 run 6: El Centro 1940 NS at time scale factor 10. 110
5.22. Power spectral density function of test 6 run 2: El Centro 1940 NS, at time scale factor 3. 110
5.23. Dark sand in place to enable mapping of the failure surface during dismantling. The Proctor mould for density determination is also seen in place. 111
5.24. Perspex box used for logging the failure surface. Discontinuities in the dark sand show the position of the failure surface. 112
5.25. Strips from test 6. Bends were logged to help determine the failure surface position. 112
5.26. The pullout wall, showing PVC sleeves fitted. 114
5.27. The pulling device. 115

5.28. Steel surcharge in place during pullout test. 116
5.29. Surcharge-test wall strip spacings. 116
5.30. f* vs depth from pullout tests. 116
5.31. f* vs resistant length of strip remaining in pullout tests. . 117
5.32. Vacuum triaxial test results. 121
5.33. Angle of internal friction vs. normal stress for Mt Somers sand. 121
6.1. Test 1 run 9 input acceleration: with wild points (top), and after running through the Tukey53H procedure, *eps* = 9. 128
6.2. Failure surface outcrops, plan views, test 1 to 6. The arrows point outwards, toward the walls. 135
6.3. Failure geometry, test 1. Wall final position not measured. . 136
6.4. Failure geometry, test 2. 136
6.5. Failure geometry, test 3. 136
6.6. Failure geometry, test 4. 136
6.7. Failure geometry, test 5. 137
6.8. Failure geometry, test 6. 137
6.9. Surface outcrops of graben-like structures seen late in test 3 138
6.10. End view of the bottom panel after test 6. On the right is the nylon sealing flap attached to the panel. 139
6.11. Yield acceleration k_h vs failure surface angle α. 140
6.12. Acceleration traces for test 2 run 1. 146
6.13. Displacement traces for test 2 run 1. 146
6.14. Forces, strip 1 (bottom of wall), test 2 run 1. 146
6.15. Forces, strip 2, test 2 run 1. 146
6.16. Forces, strip 3, test 2 run 1. 147
6.17. Forces, strip 4, test 2 run 1. 147
6.18. Forces, strip 5, test 2 run 1. 147
6.19. Forces, strip 6, test 2 run 1. 147
6.20. Forces, strip 7, test 2 run 1. 148
6.21. Forces, strip 8, test 2 run 1. 148
6.22. Forces, strip 9, test 2 run 1. 148
6.23. Forces, strip 10, test 2 run 1. 148
6.24. Acceleration traces for test 5 run 4. 149
6.25. Displacement traces for test 5 run 4. 149
6.26. Forces, strip 1 (bottom of wall), test 5 run 4. 150

6.27. Forces, strip 2, test 5 run 4. 150
6.28. Forces, strip 3, test 5 run 4. 151
6.29. Forces, strip 4, test 5 run 4. 151
6.30. Forces, strip 5, test 5 run 4. 152
6.31. Forces, strip 6, test 5 run 4. 152
6.32. Forces, strip 7, test 5 run 4. 153
6.33. Forces, strip 9, test 5 run 4. 153
6.34. Forces, strip 10, test 5 run 4. 154
6.35. Forces, strip 9, test 6 run 2. 154
6.36. Construction forces in the reinforcing strips. 157
6.37. Construction forces in the reinforcing strips, with position in the strip normalised against strip length. 158
6.38. Forces in the reinforcing strips for several runs in test 1. . 159
6.39. Forces in the reinforcing strips for several runs in test 2. . 160
6.40. Forces in the reinforcing strips for several runs in test 3. . 161
6.41. Forces in the reinforcing strips for several runs in test 4. . 162
6.42. Forces in the reinforcing strips for several runs in test 5. . 163
6.43. Forces in the reinforcing strips for several runs in test 6. . 164
6.44. Maximum forces adjacent to the wall facing, test 1. 168
6.45. Maximum forces adjacent to the wall facing, test 2. 168
6.46. Maximum forces adjacent to the wall facing, test 3. 169
6.47. Maximum forces adjacent to the wall facing, test 4. 169
6.48. Maximum forces adjacent to the wall facing, test 5. 170
6.49. Maximum forces adjacent to the wall facing, test 6. 170
6.50. Distribution of residual (end of run) forces at the wall facing, test 1. 171
6.51. Distribution of residual (end of run) forces at the wall facing, test 2. 172
6.52. Distribution of residual (end of run) forces at the wall facing, test 3. 172
6.53. Distribution of residual (end of run) forces at the wall facing, test 4. 173
6.54. Distribution of residual (end of run) forces at the wall facing, test 5. 173
6.55. Distribution of residual (end of run) forces at the wall facing, test 6. 174

6.56. Mobilised friction coefficient f* at the failure surface, test 1. Failure was at run 28. 184
6.57. Mobilised friction coefficient f* at the failure surface, test 2. Failure was at run 13. 184
6.58. Mobilised friction coefficient f* at the failure surface, test 3. Failure was in run 11. 184
6.59. Mobilised friction coefficient f* at the failure surface, test 4. Failure was in run 17. 184
6.60. Mobilised friction coefficient f* at the failure surface, test 5. Failure was in run 6. 185
6.61. Mobilised friction coefficient f* at the failure surface, test 6. Failure was in run 3. 185
6.62. Mobilised friction coefficient f* for maximum forces at the facing, test 1. 185
6.63. Mobilised friction coefficient f* for maximum forces at the facing, test 2. 185
6.64. Mobilised friction coefficient f* for maximum forces at the facing, test 3. 185
6.65. Mobilised friction coefficient f* for maximum forces at the facing, test 4. 185
6.66. Mobilised friction coefficient f* for maximum forces at the facing, test 5. 186
6.67. Mobilised friction coefficient f* for maximum forces at the facing, test 6. 186
6.68. Mobilised friction coefficient f* from maximum forces, test 1. 189
6.69. Mobilised friction coefficient f* for maximum forces, test 2. . 189
6.70. Mobilised friction coefficient f* for maximum forces, test 3. . 189
6.71. Mobilised friction coefficient f* for maximum forces, test 4. . 189
6.72. Mobilised friction coefficient f* for maximum forces, test 5. . 189
6.73. Mobilised friction coefficient f* for maximum forces, test 6. . 189
6.74. Observed f* values at the failure surface, at 'failure'. . . . 200
6.75. Observed f* values at the facing, at 'failure'. 200
6.76. Observed f* values at the maximum force position, at 'failure'. 201
6.77. Observed maximum f* values at the failure surface. 202
6.78. Observed maximum f* values at the facing. 202

6.79. Observed maximum f* values at the position of the maximum forces. 203
6.80. Observed maximum f* values at the failure surface, adjusted for increased shear surface area. 204
6.81. Maximum observed f* values at the facing, adjusted for increased shear surface area. 204
6.82. Maximum observed f* values at the position of the maximum forces, adjusted for increased shear surface area. 205
6.83. Mobilised dimensionless tension T* for maximum forces at the facing, test 1. 209
6.84. Mobilised dimensionless tension T* for maximum forces at the facing, test 2. 209
6.85. Mobilised dimensionless tension T* for maximum forces at the facing, test 3. 210
6.86. Mobilised dimensionless tension T* for maximum forces at the facing, test 4. 210
6.87. Mobilised dimensionless tension T* for maximum forces at the facing, test 5. 210
6.88. Mobilised dimensionless tension T* for maximum forces at the facing, test 6. 210
6.89. Mobilised dimensionless tension T* for maximum forces, test 1. 210
6.90. Mobilised dimensionless tension T* for maximum forces, test 2. 210
6.91. Mobilised dimensionless tension T* for maximum forces, test 3. 211
6.92. Mobilised dimensionless tension T* for maximum forces, test 4. 211
6.93. Mobilised dimensionless tension T* for maximum forces, test 5. 211
6.94. Mobilised dimensionless tension T* for maximum forces, test 6. 211
6.95. Dimensionless tension at the facing for dynamic forces, test 1. 212
6.96. Dimensionless tension at the facing for dynamic forces, test 2. 212

6.97. Dimensionless tension at the facing for dynamic forces, test 3. 212
6.98. Dimensionless tension at the facing for dynamic forces, test 4. 212
6.99. Dimensionless tension at the facing for dynamic forces, test 5. 212
6.100. Dimensionless tension at the facing for dynamic forces, test 6. 212
6.101. Dimensionless tension at the maximum force for dynamic forces, test 1. 213
6.102. Dimensionless tension at the maximum forces for dynamic forces, test 2. 213
6.103. Dimensionless tension at the maximum forces for dynamic forces, test 3. 213
6.104. Dimensionless tension at the maximum forces for dynamic forces, test 4. 213
6.105. Dimensionless tension at the maximum forces for dynamic forces, test 5. 213
6.106. Dimensionless tension at the maximum forces for dynamic forces, test 6. 213
6.107. Accelerations and displacements, test 1 run 28. 219
6.108. Accelerations and displacements, test 2 run 1. 219
6.109. Accelerations and displacements, test 3 run 8. 220
6.110. Accelerations and displacements, test 3 run 20. 220
6.111. Accelerations and displacements, test 4 run 8. 221
6.112. Accelerations and displacements, test 4 run 17. 221
6.113. Accelerations and displacements, test 5 run 2. 222
6.114. Accelerations and displacements, test 5 run 4. 223
6.115. Accelerations and displacements, test 5 run 6. 224
6.116. Accelerations and displacements, test 6 run 1. 225
6.117. Accelerations and displacements, test 6 run 2. 226
6.118. Accelerations and displacements, test 6 run 3. 227
6.119. Accelerations and displacements, test 6 run 4. 228
6.120. Sarma's chart of dimensionless displacement vs k_h/k_m, with test data plotted. 231
6.121. Observed displacements vs. displacements predicted using the Lin and Whitman (1986) method. 234

6.122. Observed and calculated displacements plotted on Lin and Whitman's (1986) chart of normalized conditional expected displacement vs. normalized yield acceleration. 235
6.123. Normalized conditional probability of exceedence of a permanent displacement for sliding blocks. 235
6.124. Displacements calculated using the Kanai-Tajimi spectral density function in the Lin and Whitman (1986) method. 238
6.125. Observed displacements plotted on the Newmark / Franklin and Chang chart. 240
6.126. Effect of ϕ on k_h and α. 243
6.127. Effect of f^* on k_h and α. 243
6.128. Effect of ϕ on the failure surface angle α. 244
6.129. Effect of the friction coefficient f^* on α. 244
6.130. Effect of ratio of strip lengths in two-step block. 244
6.131. Effect of ratio of strip lengths in two-step structure when shorter strips are closer together. 244
6.132. Effect of the failure surface outcrop position at the facing. . 245
6.133. The effect of the soil friction angle on the predicted yield acceleration and failure surface angle. A line for n=1.96 is also shown. 246
6.134. Effect of soil-strip friction coefficient on the predicted yield acceleration and failure surface angle. 247
6.135. Effect of soil-strip friction coefficient f^* on yield acceleration k_h. 247
6.136. Effect of friction coefficient f^* on failure surface angle α. . 247
6.137. Effect of strip length on k_h and α. 248
6.138. Height at which the failure surface meets the facing vs. yield acceleration for two values of ϕ. 248
6.139. Effect of the position of a step in strip length on the yield acceleration. 249
A.1. Strip calibrations, first set. 285
A.2. Strip calibrations, second set. 285
D.1. Operations in the computation of the discrete Fourier transform of a bandlimited function, truncated at an integral multiple of the period. 307

D.2. Operations in the computation of the discrete Fourier transform of a bandlimited function, *not* truncated at an integral multiple of the period. 309

D.3. Expanded central portions of spectra of a) truncation at integer multiple of period and b) truncation interval not a multiple of period. 309

LIST OF TABLES.

Table number — Page

2.1. Predicted and observed yield accelerations and failure surface angles after Nagel (1985). 28
5.1. Scaling relationships, gravity neglected. 81
5.2. Density determinations for sand fill. 97
5.3. Test configurations. Top is the top half of the wall (5 strips), bottom is the bottom half of the wall (5 strips). N is the number of strips per metre length of wall. 113
5.4. f* determined from direct shear tests. 118
5.5. Results of tests for determination of angle of internal friction of Mt Somers sand. max means maximum, res means residual. 120
6.1. Number of wild points removed from each channel of test 5 run 8 data, for *eps* = 9 and 35. There were 1604 points in the data file. 127
6.2. Yield accelerations for selected test runs. Italic run numbers are those at which the failure surface became fully developed 134
6.3. Calculated and observed yield accelerations k_h and failure surface angles α, for $\phi = 45°$ and $f^* = 0.85$. 141
6.4. Calculated and observed yield accelerations k_h and failure surface angles α, for $\phi = 40°$ and $f^* = 0.85$. 141
6.5. Calculated and observed yield accelerations k_h and failure surface angles α, for $\phi = 38°$ and $f^* = 1.40$. 142
6.6. Observed forces at failure surface, and the geometry used, test 1. 174
6.7. Observed forces at failure surface, and the geometry used, test 2. 175
6.8. Observed forces at failure surface, and the geometry used, test 3. 175
6.9. Observed forces at failure surface, and the geometry used, test 4. 176

6.10. Observed forces at failure surface, and the geometry used, test 5. 176
6.11. Observed forces at failure surface, and the geometry used, test 6. 176
6.12. Yield accelerations calculated using observed forces and failure surface geometry, for ϕ=40°. 178
6.13. Calculated f* and total force R, for ϕ=40°, using observed k_h and α. Observed forces are shown for comparison. 179
6.14. Mobilised ϕ calculated using observed forces, k_h and α in the limiting equilibrium formulation. Run numbers in italics are those in which 'failure' occurred. 181
6.15. f* calculated using the R formulation of Eq. 4.6; for tests 4 and 5 it summed over the top and bottom steps of the structure separately. 183
6.16. Mobilised ϕ calculated using observed f*, and observed k_h and α in the limiting equilibrium formulation. Run numbers in italics denote 'failure'. 207
6.17. Mean permanent displacements for several runs in each test. Italic run numbers are where the failure surface became fully formed. The potentiometers were removed after test 6 run 4. . 216
6.18. Displacements D and dimensionless displacement ratios at wall failure. 230
6.19. Displacements observed and calculated using the Lin and Whitman (1986) method. 233
A.1. Effect of side friction for H/W=2.0, μ=0.1, K=0.37. (Bransby and Smith, 1975) 276
A.2. Gauge positions, test 1. Strips 750mm long. 284
A.3. Gauge positions, test 2. Strips 1000mm long. 284
A.4. Gauge positions, test 3. Strips 750mm long. 284
A.5. Gauge positions, tests 4 and 5. Strips 1 to 5, 500mm long, strips 6 to 10 900mm long. 284
A.6. Gauge positions, test 6. Strips 750mm long. 284
A.7 (first part). Test excitations. The failure surface outcropped at the fill surface in T1R28, T2R13. 286
A.7 (continued). Test excitations. The failure surface outcropped at the fill surface in T3R12, T4R17, T5R6, and T6R3. 287

B.1. Calculations of strip length. The seismic calculations are for load case static + seismic. 290
C.1. Observed forces T and mobilised friction coefficient f* at the failure surface, test 1. Forces are in Newtons. 293
C.2. Observed forces T and mobilised friction coefficient f* at the failure surface, test 2. Forces are in Newtons. 293
C.3. Observed forces T and mobilised friction coefficient f* at the failure surface, test 3. Forces are in Newtons. 294
C.4. Observed forces T and mobilised friction coefficient f* at failure surface, test 4. 294
C.5. Observed forces T and mobilised friction coefficient f* at failure surface, test 5. Forces are in Newtons. 294
C.6. Observed forces T and mobilised friction coefficient f* at failure surface, test 6. 295
C.7. Observed forces T and mobilised friction coefficient f* at the facing, test 1. Forces are in Newtons. 295
C.8. Observed forces T (N) and mobilised friction coefficient f* at the facing, test 2. 295
C.9. Observed forces T and mobilised friction coefficient f* at the facing, test 3. Forces are in Newtons. 296
C.10. Observed forces T and mobilised friction coefficient f* at the facing, test 4. Forces are in Newtons. 296
C.11. Observed forces T and mobilised friction coefficient f* at the facing, test 5. Forces are in Newtons. 296
C.12. Observed forces T and mobilised friction coefficient f* at the facing, test 6. Forces are in Newtons. 297
C.13. Maximum observed forces T and mobilised friction coefficient f*, test 1. L is the length in cm. to the free end of the strip from the position of the maximum force. 297
C.14. Maximum observed forces T (in N) and mobilised friction coefficient f*, test 2. L is the length in cm. to the free end of the strip, from the position of the maximum force. . . 297
C.15. Maximum observed forces T (in N) and mobilised friction coefficient f*, test 3. L is the length in cm. to the free end of the strip, from the position of the maximum force. . . 298

C.16. Maximum observed forces T (in N) and mobilised friction coefficient f*, test 4. L is the length in cm. to the strip free end, from the position of the maximum force. 298
C.17. Maximum observed forces T (in N) and mobilised friction coefficient f*, test 5. L is the length in cm. to the strip free end, from the position of the maximum force. 298
C.18. Maximum observed forces T (N) and mobilised friction coefficient f*, test 6. L is the length in cm. to the strip free end, from the position of the maximum force. 299
C.19. Observed forces T (in N) and mobilised dimensionless tension T* at the facing, test 1. g = 16196 N/m^3, S_h = 0.25. . . . 299
C.20. Observed forces T (in N) and mobilised dimensionless tension T* at the facing, test 2. g = 16108 N/m^3, S_h = 0.33. . . . 299
C.21. Observed forces T (in N) and mobilised dimensionless tension T* at the facing, test 3. g = 15529 N/m^3, S_h = 0.33. . . . 300
C.22. Observed forces T (in N) and mobilised dimensionless tension T* at the facing, test 4. g = 15843 N/m^3, S_h = 0.16 (strips 1 to 5), and 0.25 (strips 6 to 10). 300
C.23. Observed forces T and mobilised dimensionless tension T* at the facing, test 5. g = 15647 N/m^3, S_h = 0.16 (strips 1 to 5), and 0.25 (strips 6 to 10). 300
C.24. Observed forces T (in N) and mobilised dimensionless tension T* at the facing, test 6. g = 15912 N/m^3, S_h = 0.25. . . . 301
C.25. Observed maximum forces T (in N) and mobilised dimensionless tension T* at location of the max. forces, test 1. g = 16196 N/m^3, S_h = 0.25. 301
C.26. Observed maximum forces T (in N) and mobilised dimensionless tension T* at the location of the maximum forces, test 2. g = 16108 N/m^3, S_h = 0.33. 301
C.27. Observed maximum forces T (in N) and mobilised dimensionless tension T* at the location of the maximum, test 3. g = 15529 N/m^3, S_h = 0.33. 302
C.28. Observed maximum forces T and mobilised dimensionless tension T* at the maximum force, test 4. g = 15843 N/m^3, S_h = 0.16 (strips 1 to 5), and 0.25 (6 to 10). 302

C.29. Observed maximum forces T and mobilised dimensionless tension T* at the maximum forces, test 5. g = 15647 N/m³, S_h = 0.16 (strips 1 to 5), and 0.25 (6 to 10). 302

C.30. Observed maximum forces T (in N) and mobilised dimensionless tension T* at the location of the maximum forces, test 6. g = 15912 N/m³, S_h = 0.25. 303

D.1. Earthquake properties calculated by Vanmarke and Lai (1980) and using a PSD estimation program from Press et al (1986). . 311

NOTATION

a	peak ground acceleration
a	base area of a sliding block on a slope (Sarma's analysis)
A, B	Skempton's pore pressure parameters
A, V	earthquake peak acceleration and velocity
A_b	acceleration of a sliding block relative to the surface on which it is sitting
A_{max}	maximum acceleration of an earthquake
A_{des}	Richardson and Lee's design acceleration
b	width of reinforcing strip
B_2-2e	width over which the Meyerhoff bearing pressure is applied
CU	coefficient of uniformity of soil, $=D_{60}/D_{10}$
D	depth of the change in strip length in a two-stepped block structure
D	downslope driving force of a sliding block
D	displacement predicted by the Lin and Whitman (1985) method
d_i	height above wall base to the i-th strip
d_i	displacement caused by cycle i during earthquake shaking
D_r	relative density
D_0	displacement tested for probability of exceedence in the Lin and Whitman (1985) displacement prediction method
D_{10}	seive size through which 10% of the sand passes
D_{60}	seive size through which 60% of the sand passes
E	Young's modulus
E(d)	expected displacement
E_d	internal dynamic force, Seed and Mitchell analysis (1980)
eps	test criterion for "Tukey53H" wild point removal procedure
E_{AE}	dynamic active earth force from Coulomb wedge behind a wall
E_i	inertia force from the mass of the wall itself
F	a characteristic force
FCF_ε	frequency correction factor for strain
F_i	minimum yield strength (force) in reinforcing strip in i-th layer
f_n	n-th mode fundamental frequency

FS factor of safety

F_y force in a strip at depth y below the top of the wall

f_0^* value, used in design, of friction coefficient at the fill surface

f_1, f_2 strained fundamental frequencies, first and second modes

f_1, f_2 undamped low strain first and second mode fundamental frequencies

f^* apparent soil-reinforcing strip friction coefficient

g acceleration due to gravity

G shear modulus

$G(\omega)$ spectral density function

g_{model}, $g_{prototype}$ model and prototype gravity accelerations

$G_x(\omega)$ Kanai-Tajimi spectral density function

G_0 constant (scale factor) in Kanai-Tajimi spectral density function

h distance from failure surface to wall top at facing

H thickness of layer of soil

H clear height of wall

H_w height of active wedge of soil retained behind wall

i strip level number, i=1 at the lowest layer of strips in the wall; i = p at the lowest level of strips intercepted by the failure surface, and m is the total number of layers of strips in the structure.

i backfill slope in the Mononobe-Okabe equations

I Richardson's (1978) normalized wall stiffness

I the moment of inertia of a strip cross section about the longitudinal axis of bending

I' Richardson's design wall stiffness

I_{ref} Richardson's reference wall stiffness

I_0 Arias intensity

k equivalent spring stiffness, beam-on-elastic-foundation calculation

K ground acceleration coefficient (fraction of g)

K_a active earth pressure coefficient

K_{AE} Mononobe-Okabe seismic earth pressure coefficient

K_E modelling law for Young's modulus

K_F modelling law for forces

k_h yield acceleration of sliding block

K_L modelling law for length

K_m Sarma's design maximum acceleration acting on the active (sliding) block

K_M modelling law for moments

K_u modelling law for displacements

k_v vertical acceleration coefficient; assumed to be zero

K_0 'at rest' earth pressure coefficient

K_2 Seed and Idriss (1970) shear modulus coefficient for sands

K_ν modelling law for Poisson's ratio

K_σ modelling law for stress

L distance of wall from the toe of embankment (JNR tests)

L reinforcing strip length

L a representative length in modelling theory

L_1, L_2 length of strips in bottom and top steps of two-stepped block structure

M a representative moment in modelling theory

M earthquake magnitude

M mass of the sliding block in limiting equilibrium formulation

M number of strips in design wall

M_{eff} Richardson's effective mass of wall

MF magnification factor

M_2 mass of the top step in a two-stepped block structure

n n-th mode of vibration (Seed and Idriss 1970)

n length (geometric) scale factor: prototype length / model length

n number of strips per lineal metre of wall in a layer of strips

N number of strips in a tributary width

N normal force on failure surface

n_1, n_2 number of strips per lineal metre of wall in a layer of strips in the bottom and top steps of a two-stepped block structure

N_1, N_2 normal forces on the bottom and top parts of the failure surface in a two-stepped block structure

p vertical force on trapped wedge behind bottom step of two-stepped block structure

p probability of exceedence of peak acceleration A_{max}

p' mean effective normal stress

P_{AE} Mononobe-Okabe dynamic active earth pressure force

ΔP_{AE} dynamic earth pressure force on the top step in a two-stepped block structure

P_{AE1}, P_{AE2} Mononobe-Okabe dynamic earth pressure forces on the two wedges in the case 4 analysis of a two-stepped block structure

p_2 Meyerhoff bearing pressure

q layer number of the highest layer of strips intersected by the failure surface (layer 1 at the base)

q' effective deviatoric stress, $q' = \sigma'_1 - \sigma'_3$ when $\sigma'_2 = \sigma'_3$

r peak factor = A_{max}/σ_x

$r_{s,p}$ peak factor in calculation of PSD from response spectrum, = A_{max}/σ_x

R force resisting sliding of a block on a slope (Sarma's derivation)

R resistant force in the reinforcing strips at the failure surface

R_s relative stiffness factor in beam-on-elastic-foundation theory

R_1, R_2 sum of strip forces at the failure surface in the bottom and top steps in the case 4 analysis of a two-stepped block structure

S horizontal spacing of strips in Richardson's reference wall

S, S_0 strong motion duration

Sa_1, Sa_2 spectral acceleration for periods corresponding to the first and second modes of the wall

S_h horizontal strip spacing

S_j horizontal spacing of strips in j-th layer in design wall

S_v vertical strip spacing

S_v damped velocity response spectrum

T fundamental period of a layer of soil

T duration of pulse in Sarma's analysis; predominant period of earthquake shaking

T tension force in a strip

t, t_{model}, $t_{prototype}$ time, model and prototype time

T_i tension force in the i-th strip

T^* dimensionless tension, a pseudo-earth pressure coefficient

T_0 predominant period, corresponding to predominant frequency Ω

T_1, T_2 periods corresponding to the first and second modes of vibration of the wall

u a displacement

u_f pore pressure at limiting equilibrium of a sliding block on a slope

Δu change in pore pressure

u_s standardized permanent seismic displacement

V_{max} maximum ground velocity in an earthquake

V_s shear wave velocity in soil

W weight of wall in Seed and Mitchell's analysis

W weight of a sliding block

x displacement (eq. 2.7)

x_m displacement downslope of a sliding block (Sarma's equations)

$x_{prototype}$, x_{model} prototype and model displacements

y depth from wall top to item of interest, such as a reinforcing strip

y_i depth y of the i-th layer of strips

α failure surface angle ie. the angle the failure surface makes with the horizontal;

α $\sin^{-1}(k_h/K_m)$ in Sarma's analysis.

β angle the rear of the trapped wedge behind the bottom step of a two-stepped block structure makes with the horizontal

β Sarma's slope angle (to the horizontal) for the slope on which a sliding block moves

β slope of the rear of a retaining wall, in the Mononobe-Okabe equations; positive when heel of wall is further into fill than top rear of wall

δ wall-soil friction angle

δ a measure of frequency bandwidth

Δh depth of slice of wall in Seed and Mitchell analysis

ε strain

ε_a axial strain

ε_{LEVSFC} strain derived from finite element computer program LEVSFC.

ε_v volumetric strain

γ unit weight of the soil

Γ_1, Γ_2 modal participation factors

λ fraction of critical damping

λ ratio of position of peak to pulse length for a triangular pulse (Sarma's analysis)

λ_g ground damping for use in Kanai-Tajimi spectral density function

λ_i i-th moment of the spectral density function

ν Poisson's ratio

ν_r^+ upcrossing rate for earthquake acceleration magnitude passing the peak level r

ω circular frequency

ω_g ground predominant frequency for use in Kanai-Tajimi spectral density function

Ω predominant or central frequency of earthquake record

π_c soil cohesion dimensionless ratio

π_g gravity dimensionless ratio

π_i inertia dimensionless ratio

π_2 a dimensionless ratio derived from the product of two other dimensionless ratios

π_ϕ soil friction dimensionless ratio

ρ soil density

ϕ soil angle of internal friction

Ψ soil-strip friction angle for smooth strips

σ stress

σ'_1, σ'_2, σ'_3 effective principal stresses

σ_a the "σ-spectrum" derived part way through the derivation of a PSD from a velocity response spectrum

σ_H horizontal stress

σ_m mean normal stress

σ_x root-mean-square acceleration

$\Delta\sigma_1$, $\Delta\sigma_2$, $\Delta\sigma_3$ changes in the principal stresses

θ $\tan^{-1} k_h/(1-k_v)$

CHAPTER 1

INTRODUCTION TO REINFORCED EARTH

1.1. About Reinforced Earth.

Reinforced earth (RE) is a composite material in which the strength of an engineering fill is augmented by the addition of inextensible reinforcing elements. These elements usually take the form of galvanised steel strips. The composite material gains its strength from the mobilisation of frictional forces between the reinforcing strips and the soil, resulting in an apparent cohesion in the material. Free-draining cohesionless soils are required for the fill, and a facing is used to prevent frittering of the fill by the action of water, wind, etc. When a facing is used the reinforced fill is referred to as a reinforced earth wall.

RE was developed by a French engineer, Henri Vidal (Vidal, 1966, 1969a, 1969b, 1970). Patents are held by Vidal, in many countries, covering the technique, and in some countries the term "Reinforced Earth" is a trademark (Ingold, 1982). Other composite soil techniques (for example, the York method - Jones, 1978; and TRRL anchored earth - Murray and Irwin, 1981) have been developed, and in this thesis, the term reinforced earth is meant to include such systems that use relatively inextensible reinforcements (as opposed to those that use extensible reinforcing, such as some geotextiles).

A typical RE wall is shown in cross section in Fig. 1.1. It can be seen that the facing is made up of concrete cruciform-shaped panels, usually of gross dimensions 1715 wide x 1705 tall x 180mm thick. They contain only minimal reinforcing, because they are not structural. Attachment between panels consists of only steel locating dowels, so the facing is articulated and flexible. Early RE walls used semi-cylindrical steel facing panel

sections, with the reinforcing strips attached at the horizontal joins between the sections (Vidal, 1970). These steel facings have been superseded by the concrete panels, which can be cast with a wide variety of architectural finishes.

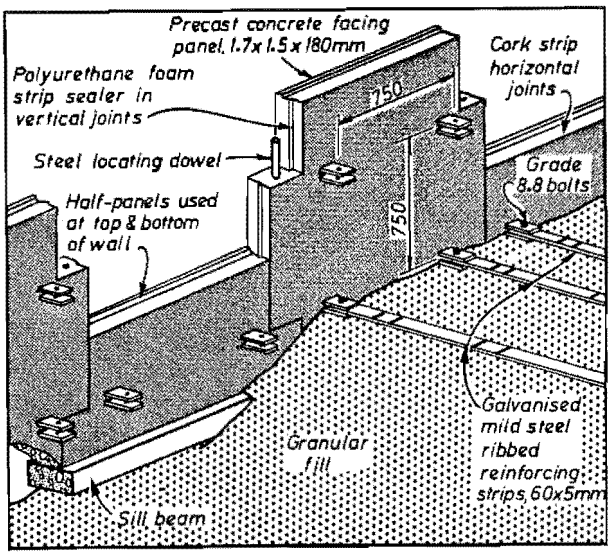

Fig. 1.1 Cross section of a typical RE wall.

One of the most important characteristics of RE is its flexibility. For this reason it is ideal for structures such as retaining walls on soft foundations. While they are flexible, however, RE walls act as coherent gravity structures, as evidenced by some spectacular slope failures where RE walls have been born along on the slide debris with comparatively little damage (McKittrick, 1978).

A strong advantage of RE over gravity retaining walls is that of cost. Ingold (1982) reports savings over the cost of conventional structures may be in the range of 20-65%, with the largest savings being made where a conventional structure would require piled foundations ie. in poor foundation conditions. In Australia, Ingold says the overall average saving in walls and abutments was 32%, over a wide range of soil types.

RE has been used in many traditional retaining wall situations, as well as in some less usual circumstances. Bridge abutments, retaining walls for road embankments on slopes, walls for railway embankments, containment dykes at petro-chemical tank farms, and approaches to rock crusher tip faces are some of the more usual uses. The facing of a small dam, and sloped walls of a coal slot storage facility, are examples of less usual situations (Vidal, 1978). Jones (1985) gives many more examples, as well as an outline of the historical uses of reinforced soil. Different facing panels may be used sometimes, such as in the sloping walls mentioned above, and in a tiered wall built at Vail Pass, Colorado (Vidal, 1978).

An important consideration in the design of RE walls is that of the durability of the strips. Much work has been done to verify the long term durability of the strips, being as they are steel buried in soil. Presently they are galvanised, and there is a sacrificial metal thickness allowed for in the design of RE structures. In harsh environments, such as marine situations, additional special measures must be taken to ensure the durability of the reinforcing. There are several papers in the proceedings of the Paris, Pittsburgh, and TRRL Edinburgh symposiums that concern themselves with reinforcement durability. It is, however, beyond the scope of this report.

1.2. Seismic performance of RE.

The present design methods for RE in seismic zones do not take advantage of the inherent flexibility of such structures. They seem to be based on an attempt to limit the seismic response of RE walls to purely elastic vibration about the base, and may thus be described as working stress methods. Such methods are often quite conservative and do not gain from the ductility of the structure. The RE design methods are derived from testing of mostly small models, plus one 6m. tall wall using explosives to provide the excitation. No information is available from these methods about the "ductility" of the structure, ie. how it will perform when the design earthquake is exceeded. Neither is there any information about the likely deformation levels when excitation is less than the design earthquake, or on the serviceability of the structure after a moderate or severe earthquake.

In fact, the exact performance of a RE wall in an earthquake is still uncertain. Models may or may not properly represent the failure mechanism during an earthquake. The full scale wall tested used blast excitations, where the excitation pulses were of very short predominant period and may not well represent true seismic excitations. There have been no reports of a RE wall being subjected to even a moderate earthquake.

The limiting equilibrium approach proposed by Bracegirdle (1979) seems to answer most of the criticisms mentioned above about the present design methods. The concept is simple and lends itself to application to the many geometries used for the RE wall reinforced block. In association with a

displacement prediction method, it can give an idea of "ductility" and of allowances necessary for seismically induced displacements. Accordingly the limiting equilibrium approach was adopted for study in this project.

This approach assumes that a block consisting of a part of the RE wall, and perhaps a wedge of retained soil behind the wall, will slide outwards during seismic shaking. A planar failure surface is assumed, which may or may not be entirely contained within the reinforced block. A limiting acceleration, or more precisely a yield acceleration, is derived, which is the excitation level above which the failure block will slide outwards. The restraining forces against sliding are soil friction, and forces in the reinforcing strips that pass through the failure surface. These forces are mobilised by friction between the strips and soil as the strips pull out of the resistant zone behind the sliding block. Breakage of the strips is avoided completely, as it usually leads to catastrophic collapse of the wall.

To date there is a paucity of information about what happens to the reinforcing strip forces during seismic excitation. Forces have been measured near the facing of some model test walls, and also in the 6m tall wall tested with explosives. To properly test the limiting equilibrium approach it was necessary to have some measurement of the forces at the failure surface. Thus a testing program was initiated where the strip forces could be measured throughout the height of a model wall, and at several positions on the instrumented strips, during seismic shaking. Measured forces would allow a study of the soil-strip friction mobilised during shaking, as well as the earth pressure on the facing. The testing would also provide a check on the failure mechanism at a larger scale than had been previously used. For excitation, a computer-driven shaking table would be used: this would allow the use of simple sinusoidal wave forms, as well as recorded earthquake motions, to excite the models. Measurement of displacements of the model walls would allow comparison with some displacement prediction systems.

1.3. Structure of the thesis.

Chapter 2 describes previous testing of seismic performance of RE walls. The chapter is subdivided according to the sites of the testing: University

of California, Los Angeles (UCLA); Ohio State University; the Japanese National Railways; and the University of Canterbury. As a result of the UCLA testing, design methods were proposed, which are outlined and discussed in Chapter 3, together with static and other seismic design methods. Chapter 4 provides the theory for the limiting equilibrium approach, and includes three displacement prediction systems to be tested. The limiting equilibrium formulation is applied there to a rectangular reinforced block, and to a structure with a two-step block (ie. strips are of two lengths, being shorter in the bottom half of the structure).

Chapter 5 describes the testing set-up. First, though, there is discussion of the theory and limitations of similitude and model testing, together with a critique of the only attempt, seen in the literature, at a similitude study on RE walls. Appendix A contains some additional details about the testing, including discussion of the edge effects arising from testing inside a box. The excitations to which each test wall were subject are also tabulated in Appendix A. At the end of Chapter 5 the results of tests to establish the shear strength parameters - the soil angle of internal friction and the soil-strip friction coefficient - are given.

Chapter 6 discusses the test results. First there are some comments on data treatment methods used, then the observed yield accelerations and failure geometries are presented and tested in the limiting equilibrium formulation. Agreement is reasonable, within the range of variability of the observed results. Next, the observed strip forces are shown: first some typical time histories of strip forces are discussed, then strip force distributions are given, strip by strip for each test and for construction forces. Reinforcing strip force distributions are shown at the wall face for maximum forces and for residual (end of run) forces, and then some observed forces are given for those strips crossing the failure surfaces.

The observed forces are then used in the limiting equilibrium formulation. First, with the failure surface angle to the horizontal, to calculate the yield acceleration. Then observed forces are compared against calculated forces, using observed yield acceleration and failure surface angle. Finally, the apparent mobilised soil friction angle is calculated using the observed forces, yield acceleration and failure surface angle.

Data is then presented, and discussed, for the mobilised soil-reinforcing friction coefficient, using observed forces. The soil-strip friction data is discussed with respect to the value to be used in seismic design of RE walls. Included is a summary of the factors that have been found to affect the value of the friction coefficient.

In order to calculate forces, we need an estimate for the seismic earth pressure coefficient. Dimensionless tension, a pseudo-earth pressure coefficient, is calculated for the observed forces at the facing, and also at the positions of the maximum forces observed. Construction forces are subtracted from the total measured forces to derive the forces due to seismic excitation of the test walls, and the values of dimensionless tension derived from those forces are compared to the usual active, at-rest, and Mononobe-Okabe dynamic earth pressure coefficients.

Next, in Chapter 6, there is analysis of the displacements. They are plotted on charts from the three displacement prediction systems outlined in Chapter 4, and a recommendation made as to which seems the best to use. The chapter concludes with a sensitivity analysis of the limiting equilibrium formulation, as it affects both the model walls tested and full size walls.

In Chapter 7 the conclusions of the project are aggregated, and recommendations made for further study.

Appendix B gives the design of a typical test wall, based on the MWD (1980) method. In Appendix C data for the friction coefficient and dimensionless tension plots in Chapter 6 is tabulated, and in Appendix D there is discussion of the calculation of the power spectral density (PSD) function required in one of the displacement prediction methods. This is presented because of the difficulty experienced in matching previously published results from PSD calculations.

CHAPTER 2

PREVIOUS DYNAMIC TESTING

2.1. Introduction.

Previous dynamic testing has been reported from four main organisations: the University of California at Los Angeles (UCLA), Ohio State University, Japanese National Railways, and the University of Canterbury. Most testing has been on model scale reinforced walls, although a series of forced vibration tests on full scale walls were reported by UCLA and JNR. Below is an outline of each series of tests.

2.2. UCLA testing.

Richardson and Lee (1975) report a series of tests on model walls. Initially, they simulated a horizontal force component in the fill using tilt-up tests on model walls ranging in height from 280 to 410mm. Aluminium foil was used for the reinforcement with dry sand backfill. Wall horizontal displacement and reinforcing tie force measurements were made during tilting, until failure. Failure modes were not stated, but failure always by strip breakage is implied. Such failures are sudden and catastrophic, and so do not demonstrate ductility. They are avoided in design.

Broken ties were consistently found in the top third of the walls, in contrast to the static case where maximum forces are found near the base. Measured failure surface locations were a little flatter than predicted by the Mononobe-Okabe (M-O) theory (summarised by Seed and Whitman (1970)), and also than observed in shaking table tests. This was most pronounced at large k_h (horizontal force coefficient $k_h \approx \tan \alpha$, where α is the tilt angle measured from horizontal). The pseudo-static earth pressure coefficient K_{AE}

calculated was compared with the M-O value: it increased with k_h but less quickly than the M-O value.

Richardson and Lee concluded from this work that compared to static conditions, seismic effects caused a flatter failure plane, larger lateral earth force, and a distribution of total lateral earth pressure on the facing panels that does not increase linearly below the surface.

They then described a series of shaking table tests on model walls, 300mm high by 760mm wide, subject to (mostly) 11.6Hz sinusoidal vibrations. Acceleration levels used were 0.05g to about 0.5g. Input and response accelerations, relative displacements at several places on the wall, and reinforcing strip forces at the wall were measured, and recorded on a strip chart recorder. Semi-cylindrical aluminium facings 25mm high (concave towards the fill, in the same fashion as the steel panels used at the time in full scale walls), and aluminium foil strips were used for one series of tests: their low tensile failure strength caused failure of the walls by strip breakage. Mylar magnetic recording tape was used for reinforcing in the second series of tests, to produce failure by strip pullout. The facing for these tests was 38mm high flat aluminium sheet.

The characteristic deformation pattern for strip breakage failure was: the wall rotated out about the toe (rate of rotation proportional to the base acceleration) to about 13mm outward movement at the top. Movement of the top almost stopped at that point and rapid bulging at the base occurred, followed by quick and complete collapse. Strip breakage generally occurred in the second and third ties from the bottom, near the wall facing, immediately before collapse. They were able to monitor to some degree the stress transfer to other ties just after strip breakage and prior to collapse. (They had trouble with the tie force transducers in this part of the testing.) In strip pullout failure, there was some initial movement at the wall top, then the whole wall moved out uniformly, with the bottom facing panel rotating to lie flat. The rate of movement (whether against time or per pulse is not clear) was proportional to the input acceleration, and decreased with longer reinforcing ties. Supporting blocks were used to prevent complete collapse in most (tie breaking) tests, to preserve small-strain conditions after tie breakage. The authors concluded that the ductile behaviour of the pullout

failure was desirable and suggested a lower factor of safety in design for pullout than for breakage. There was no detailed study of rate or amount of wall movements.

Tie forces were found to be scattered erratically, tie to tie and test to test. When shaking stopped, forces remained at about the mean force immediately before stopping. The mean forces increased with increasing acceleration level. By converting forces at the face to an effective K_{AE} it was found that the dynamic earth pressure coefficient was about twice the M-O value. Fig. 2.1 shows the seismic earth pressure envelope they suggested.

For these single frequency tests, magnification of the input accelerations was greatest at the wall face, and decreased toward the rear of the containing box. The amount of magnification varied with the input acceleration, indicating non-linear backfill behaviour.

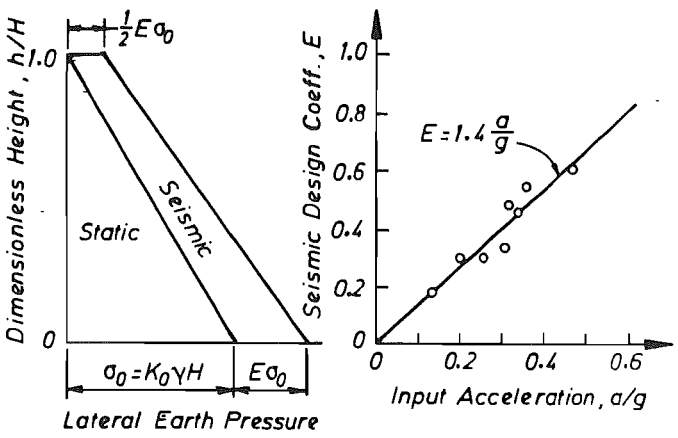

Fig. 2.1. Envelope of maximum seismic earth pressures (Richardson and Lee 1975)

A 380mm high wall was built and subjected to a variety of base accelerations and frequencies. Richardson and Lee observed that the wall always behaved as a damped single mode elastic oscillator, with a well defined frequency distribution curve. The data was reproducible, even after intervening tests at different conditions. Different response curves were obtained for different input accelerations: increasing dynamic strain was accompanied by decreasing shear modulus and increasing damping (see Figs. 2.2 and 2.3).

To show how the damping varied with acceleration, they used

$$\lambda \approx \frac{1}{2MF} \qquad \text{.....(2.1)}$$

where λ is the critical damping ratio, and MF is the magnification factor defined as the ratio of surface to base acceleration at resonance. Using

one-dimensional wave propagation theory, (Idriss and Seed, 1968), the shear modulus, G, may be estimated from

$$G = \frac{16H^2\rho}{T^2} \qquad \ldots\ldots\ldots\

and Lee expect this to be a function of the low confining pressure of the model tests, and not to occur at full scale.

Based on the tests described above, a design method was proposed. It will be described in Chapter 3.

Wood (1982), reported by Nagel (1985), stated some shortcomings of Richardson's testing as follows:

i. Mylar tape has a low friction angle with sand, which is not typical of prototype walls,

ii. the low friction angle meant that longer ties were required (with respect to wall height) than in prototype walls, which may effect the location of the failure surface,

iii. only limited failure surface information was reported, and

iv. very limited information on wall displacements was reported.

Richardson, Feger, Fong, and Lee (1977) describe tests on a full scale 6m. high wall, built by the first three authors. They used concrete facing panels and 4 reinforcing strips per panel, except for the lowest half-panel, where 4 strips per half-panel were used. Steel reinforcing strips were used, probably the smooth strips used at the time, 1974. The wall was instrumented with strain gauges on 2 columns of strips, foundation pressure cells, settlement platforms, extensometers (anchored well back in the backfill) to measure face movements, point strain devices, and several accelerometers. Two methods of dynamic excitation were used: forced vibration with rotating masses, to obtain damping and fundamental frequency data, and blast excitation with explosives. Four commercial walls were also tested to a limited degree with the rotating mass equipment.

Two variable rotation speed vibrators and several rotating masses were used in the forced vibration tests. A number of frequency response curves were obtained for the test wall, from which the natural frequency and damping were obtained. For the commercial walls, only sufficient tests were done to obtain the first two fundamental frequencies, but not the damping in any mode.

For the five walls tested, the resonant frequencies, f_1 and f_2 (in Hertz) in the first two transverse modes were found to be approximately represented by

$$f_1 = \frac{38}{H} \qquad \text{.....(2.4)}$$

$$f_2 = \frac{100}{H} \qquad \text{.....(2.5)}$$

where H is the clear height of the wall, measured from the top of the fill in front of the toe, in metres. Fig. 2.4 shows how these curves fit in the region defined, for shear wave velocity V_s = 120 to 280 m/s, by the Seed and Idriss (1970) equation for the resonant frequency f_n of the n-th mode of vibration in an elastic solid layer of thickness H, above a rigid base:

$$f_n = \frac{(2n-1)V_s}{4H} \qquad \text{.....(2.6)}$$

Note that the data base is quite small (4 points for each curve) for the relations, Eq. 2.4 and 2.5.

The blast excitation tests were done to obtain higher strain levels than the forced vibration tests had produced. 20 explosive tests were done, using a variety of explosive types, detonation rates, and locations and depths of explosives. The maximum accelerations recorded were 1.46g horizontal and 1.25g vertical from the same event, though the vibration period was less than 0.1 sec. The frequency content of all the blast excitations was higher than is usually expected in earthquake ground motions. It was also higher than the wall natural frequencies of vibration. It is perhaps more usual that the earthquake predominant frequency is less than the structure natural frequency. It is thus not clear whether the response to blast accelerations represents real earthquake response, where it might be expected

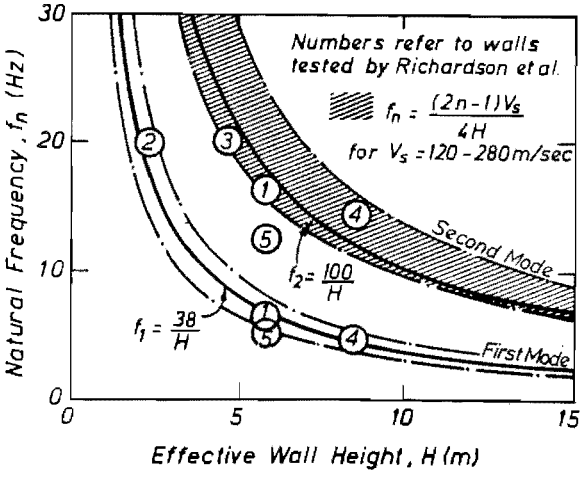

Fig. 2.4. Measured and calculated first and second mode natural frequencies for different height of R/E walls (Richardson, et al 1977).

that strain softening of the structure will lower a wall's natural frequency closer to that of the earthquake.

Single short blasts usually had one initial peak or full cycle followed by several cycles of longer period and lower amplitude accelerations. Four blasts used multiple delayed detonations, though the available delay caps were either too short to produce realistic earthquake frequencies or so long the results were like a series of separate shots.

An acceleration of 1.46g at the toe (1.25g at the wall top in the same blast) was the largest horizontal acceleration measured. It was essentially a single cycle of period less than 0.1 sec. This shock also caused the largest displacement of the wall face, 95mm measured at a point 1.9m down from the wall top. After all the testing on the UCLA wall, it had accumulated a 5.5% "outward tilt", or about 210mm of movement at the measuring point 1.9m below the top. No information was given in the paper about displacements nearer the base of the wall.

Dynamic strain was defined as the ratio of horizontal wall movement (outward and back to the rest position) to the clear wall height. Fig. 2.5 (a) shows the relationship found between the first mode natural frequency and the maximum dynamic strain. Single amplitude strain is used to allow the plotting of a curve interpolated, for sand at relative density $D_r \approx 65\%$, from Fig. 2.5(b) and rescaled by calculating f_1 from the shear modulus using Eqs. 2.6 and 2.3. The calculated curve is in good agreement with the measured data. The figure shows that there is a non-linear decrease in the first mode frequency with increasing dynamic strain. This behaviour was also observed in the small scale walls reported by Richardson and Lee (1975).

The relationship between damping and dynamic strain did not fit the Seed-Idriss predictions anywhere near as well as the natural frequency-strain relation. It was felt that there was a high degree of geometric damping of the forcing function motion between the (effectively) point source excitation and the nearby measuring station, whereas the Seed-Idriss model was only for hysteretic damping.

Dynamic tie forces were plotted together with forces calculated using the Richardson and Lee (1975) design method. The calculated forces grossly overestimated the measured forces. The design method was in fact overhauled and republished in much advanced form by Richardson (1978). (See section 3.4.) It is not clear if there was any permanent increase in the tie forces during the tests.

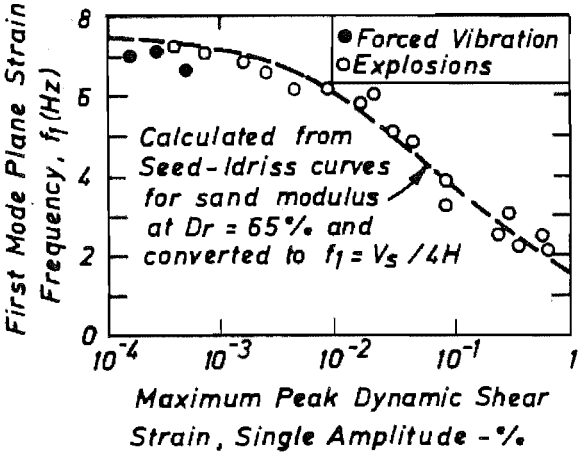

Fig. 2.5(a) Field measured dynamic properties of backfill soil at UCLA test wall compared with published data (Richardson et al 1977).

The authors concluded that a wall designed to purely static criteria could withstand quite severe seismic shaking with only minor movements and no signs of distress. A relationship was found between wall height and the first two modal frequencies of 5 reinforced earth walls, which was in good agreement with simple wave propagation theory and the Seed-Idriss (1970) nonlinear variation of shear modulus with dynamic strain. It was also shown that the earlier design method, derived from a study of small scale models, greatly overestimated the strip forces. It should be noted that the test wall at no time showed any signs of imminent failure, nor was any mention made of a failure surface forming.

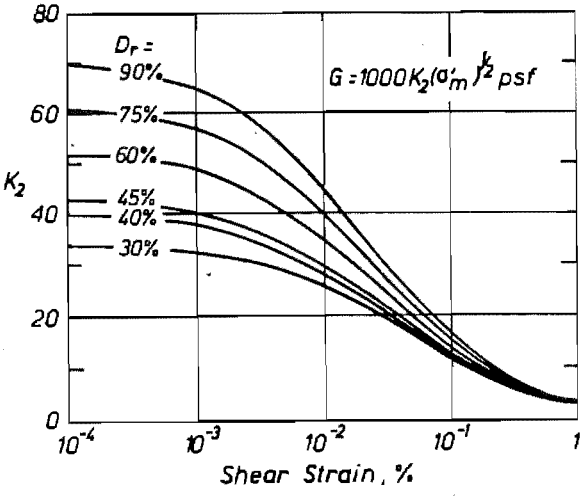

Fig. 2.5(b) Shear moduli of sands at different relative densities (Seed and Idriss, 1970)

Wolfe, Lee, Rea, and Yourman (1978) reported on the effect of vertical motion on the seismic stability of reinforced earth walls. They tested a series of 610mm high walls, with clean fine sand backfill always at the same density. Reinforcing strips were of two types: fibreglass screen mesh (16 threads/25.4mm) cut into 12.7mm wide strips, and mylar recording tape, also

12.7mm wide. All strips in any wall were of the same material and length. The mesh strips were shorter than the mylar in an attempt to cause similar deformations in both types of wall. Mesh strips are likely to be much more extensible than mylar, and while the friction angle with the soil is more like that used in commercial walls, the effect of the extensible strips is not clear. Jewel (1979) says that extensible strips have less strengthening effect on the soil than stiffer strips. Horizontal and vertical spacing of strips was the same in all walls. Base excitation was horizontal, vertical, and combined horizontal and vertical, using sinusoidal and scaled earthquake motions. The sinusoidal motions were ±0.2g, at 30Hz to 5Hz in 1Hz decrements. Earthquake inputs were the Taft (1952) motions scaled to 0.5g horizontal and 0.35g vertical, at a time scale factor of $\sqrt{6} \approx 2.5$.

The geometric scale factor was about 6. The effect of this time scale factor ($\sqrt{6}$) can be easily demonstrated using the constant acceleration formula

$$x = \tfrac{1}{2}gt^2 \qquad \ldots\ldots(2.7)$$

where x is the displacement resulting from the constant acceleration g over time t. If we require

$$x_{prototype} = n x_{model} \qquad \ldots\ldots(2.8)$$

where n is the geometric scale factor, then if $g_{model} = g_{prototype}$ we must have

$$t_{model} = \left(\frac{1}{n}\right)^{\frac{1}{2}} t_{prototype} \qquad \ldots\ldots(2.9)$$

This relationship may be derived in a dimensional study of rigid body motion (Baker *et al*, 1973, p 92), or any other phenomenon in which gravity stresses dominate (Langhaar, 1951; Kerisel, 1967; Schuring, 1977). There is further discussion of modelling in section 5.2.

The 0.2g sinusoidal motions were such that the response levels (dynamic strains) were classed as low. It was found that at excitation frequencies near the fundamental frequency f_1, horizontal inputs caused some vertical response, and vertical inputs caused a relatively large horizontal response.

Sinusoidal vertical input at 15Hz (less than half the vertical f_1, and about 3/4 of the horizontal f_1) resulted in almost no horizontal movement. The conclusion was that vertical harmonic shaking near f_1 may have some effect on dynamic response.

The scaled earthquake motions had frequencies 0.5 to 0.16 of the low strain f_1 of the walls. Much larger strains resulted from the larger inputs with a corresponding lower f_1 of the wall. Combined horizontal and vertical shaking showed that the system responded primarily to the horizontal component. Forces in the strips were slightly higher than from horizontal shaking only. The larger earthquake tests showed much less influence from vertical motion than did the lower level harmonic vibrations.

The study concluded that, within the accuracy and limitations of the test data, the vertical component of ground shaking could be ignored in design.

Rea and Wolfe (1980) reported shaking table experiments on 457mm high walls with mylar tape reinforcements. They also mentioned that they had tested 305 and 610mm high walls. Facing panels were 6x76x762mm, fashioned from plexiglass. Horizontal strip spacing was 152mm at panel mid height, 305mm at panel top and bottom edges. Vertical strip spacing alternated between 38mm and 76mm in the wall. The only variable between walls was the length of the reinforcing strips, which varied from 305 to 762mm. The minimum static length (Factor of Safety 1.0) was said to be 168mm, so the static FS varied between 1.8 and 4.5. The N21E component of the Taft (1952) earthquake was used, with time scale factor 2 and the sub-4Hz frequencies filtered out. This resulted in the power spectral density being concentrated in the 8 to 15Hz band. The low strain first mode fundamental frequency, f_1, was found to be 24Hz. An accelerometer was placed in the top of the fill near the wall face, and displacements of the wall top were measured relative to the containing box. 0.9g was the maximum input acceleration. A sample set of figures was presented for FS = 4.5 walls.

Magnification factors (MF, = response acceleration/input acceleration) were calculated on a pulse by pulse basis, and plotted (Fig. 2.6) against the pulse size (acceleration) for outward (passive forces on the wall) and inward

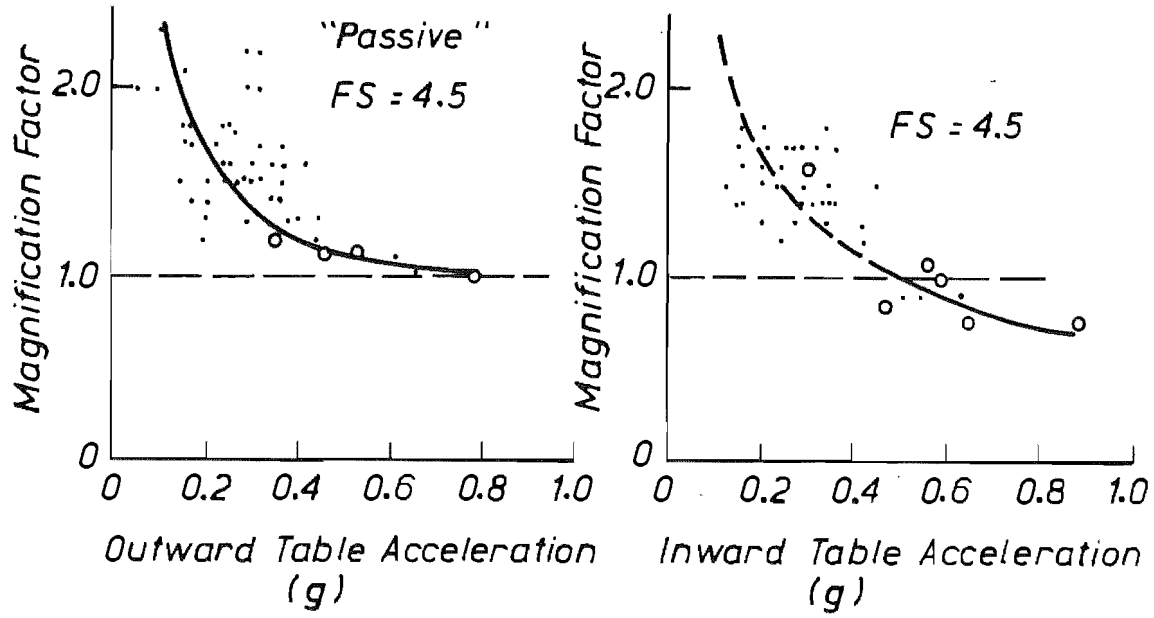

Fig. 2.6. Magnification factors for acceleration pulses (Rea and Wolfe, 1980).

(active forces) table accelerations. The data is quite scattered, especially at low levels, but shows that the MF reduces as the acceleration level increases. Note on the MF vs. inward table acceleration graph (Fig. 2.6(b)) that the fitted curve falls below MF = 1 at about 0.5g. This is identified as a "yield acceleration". The same effect is shown on the plot of dimensionless displacement vs. largest inward acceleration peak, Fig. 2.7, where the curves cross the zero displacement axis at a finite acceleration level. (Dimensionless displacement was defined in a similar way to what Richardson *et al* define as dynamic strain: horizontal displacement / wall height.) Fig. 2.8 shows how the yield acceleration is affected by the factor of safety of the walls. Note that they have assumed that the yield acceleration is zero for FS = 1 and drawn the fitted curve through this point. Permanent displacements were found to be very sensitive to FS when FS was less than 2.

The authors state that at low levels of excitation, the walls vibrated like a continuous elastic body, but at high levels of acceleration they became like a rigid body on a horizontal surface vibrating horizontally (although asymmetrically because the yield accelerations were much smaller in one direction than the other). Such a rigid body was said to have a MF of one up

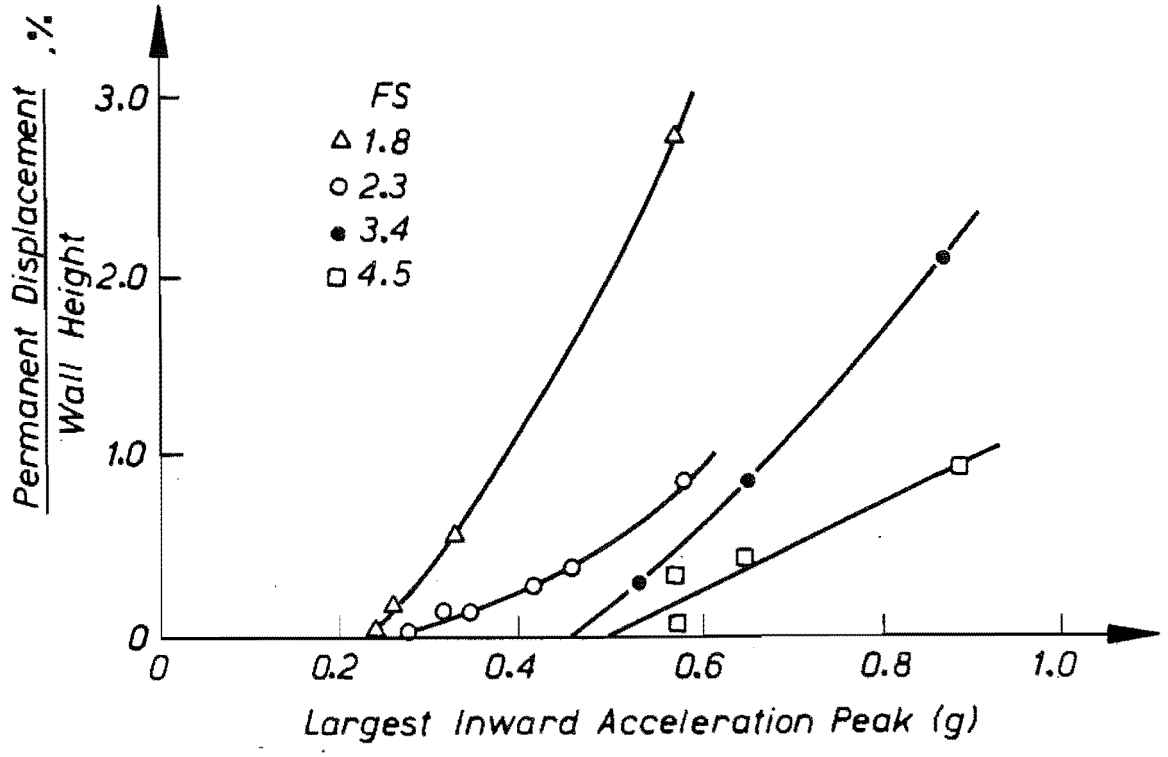

Fig. 2.7. Effect of acceleration intensity on permanent displacements (Rea and Wolfe, 1980).

to a threshold level, and less than one for accelerations greater than this value. The rigid body was identified as the Rankine zone immediately adjacent to the face elements.

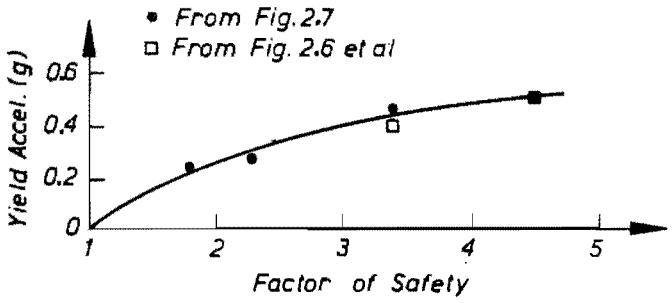

Fig. 2.8. Effect of factor of safety on yield accelerations (Rea and Wolfe, 1980).

The recommendation was that the anticipated peak acceleration in the design earthquake should govern the selection of static FS for design of reinforced earth walls with seismic resistance.

Peak acceleration is not a good characteristic measurement of earthquake severity however. Frequency content and spectral acceleration levels are also important. While this study did produce some information about displacements

related to input acceleration level, it seems the thinking was to try to make the yield acceleration high enough to prevent nearly all permanent movement.

The UCLA approach seems to have been to measure dynamic and permanent displacements and acceleration levels causing them, in an attempt to produce a design method that could prevent any displacement at all from the design earthquake. This is essentially a working stress approach and nothing is known about the ultimate strength or post-elastic behaviour of the structure. Such methods often lead to quite conservative design. Some sort of limit state, or strength and serviceability approach seems much more rational to the design of RE walls. Here, the wall will suffer no displacements under normal working loads, but under abnormal eg. seismic, loads, an allowable, predictable displacement could occur at certain design load levels.

2.3. Ohio State University.

Sommers and Wolfe (1984) report a series of tests designed to investigate the effects of different input motions on measured amplification ratios and displacements of model walls. Their models were similar to those of Rea and Wolfe (1980). Inputs used were the N21E component of the Taft (1952) earthquake, the El Centro 1940 NS component, both scaled with 2 different time scale factors, and 2 of band limited white noise. The El Centro inputs, for example, had their power spectral densities concentrated in the 6 to 15Hz, and 10 to 25Hz bands, and were filtered to remove the sub-4Hz frequencies. All data was recorded on digital tape at faster than 300Hz scan rate. Two accelerometers (input and wall top) and one displacement transducer (wall top) were monitored.

The authors commented that the laboratory tests of Richardson, and Rea and Wolfe (described above) had shown that the loads imposed on model reinforced earth walls by simulated seismic motions are similar in distribution and magnitude to those proposed by Seed and Whitman (1970) for gravity retaining walls. They also refer to the Richards and Elms (1979) class of "deformation walls" where deformation criteria govern design. It is pointed out that Richards and Elms, in assuming the fill to behave as 2 rigid blocks, ignore any amplification of ground motion in the backfill. Sommers and Wolfe

point out that Nadim and Whitman (1983), and Rea and Wolfe (1980) found that amplification factors of 3 or more are possible, and that "passive" displacements had been observed in experiments, contrary to the Richards and Elms assumption.

Wall accelerations were found to be a function of the amplitude of the input motion, and of the ratio of input to wall natural frequency. Wall displacements were found to depend on the type of input motion, and were a function of the base acceleration, with a minimum or yield level necessary to be exceeded to induce permanent displacements. The yield acceleration was relatively insensitive to the specific type or frequency of base motion, and so could be determined from the static factor of safety as proposed by Rea and Wolfe. It was concluded that allowable deformation criteria were appropriate for the design of reinforced earth walls. Rea and Wolfe's parameters (static factor of safety, peak base acceleration, and ratio of fundamental frequency of wall to predominant frequency of input) were confirmed as being important, but different motions had induced different responses even with the same peak accelerations, the same static factor of safety, and the same frequency ratio.

For motions with frequencies much less than the wall natural frequency, similar response was seen at each level of table acceleration. For input frequencies similar to the wall frequency, wall displacement was strongly dependent on the specific motion. There was a correlation between the number of input peaks greater than the yield acceleration and the permanent displacement induced. The band limited white noise inputs gave the largest displacements, and also had the most peaks above the yield acceleration.

There is no information given about the magnification factors near resonance, or how they change as the excitation level approaches and rises above the yield acceleration.

2.4. Japanese National Railways.

In the late 1960's and early 1970's the Japanese National Railway Technical Research Institute carried out some tests on model and prototype

scale reinforced earth walls. Translations of some Japanese-language reports are presented in Cormack et al (1980, Volume 2), which is the source of the following information.

Model walls 235mm high were tested in sinusoidal vibration on a shaking table. Paper tape was used for the reinforcing strips and the facing panels were made from folded paper. Nine cases were tested, with four variations of overall wall geometry, 2 variations of strip density, and 2 tests with surcharge loads. The wall geometries are shown in Fig. 2.9, where it can be seen that the tests were done with a specific use in mind: widening existing embankments. Instrumentation included an accelerometer at the centre of mass of both the embankment and RE wall, a displacement transducer on the wall face, a subsidence measuring device on the surface of the RE, and a displacement transducer on the shaking table, from which accelerations could be calculated. Layers of white sand were used to observe the failure surface.

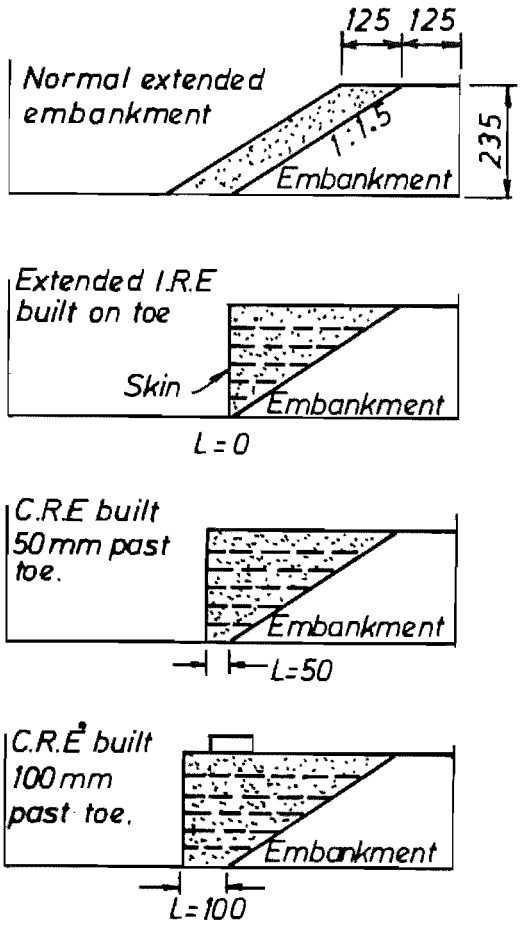

Fig. 2.9. JNR model RE embankment cross-sections (Cormack et al 1980).

The vibration frequency was constant and always close to 6Hz. The time to failure of the walls was noted, with the acceleration level being increased in ramped steps during shaking. Fig. 2.10 shows a typical set of results. Accelerations causing collapse were generally in the range 510 to 800 gal (0.52 to 0.82g), excluding the walls built directly over the toe of the existing embankment. Failure acceleration was 530 gal (0.54g) for the normal extended embankment. The collapse acceleration was found to increase as the distance of the wall from the embankment toe increased. All four L = 100mm walls tested had fairly similar collapse accelerations, leading the authors to conclude that the effect of the surcharge load was negligible. Failure was

usually by slippage along the base, indicating that the RE wall acts as a rigid body when slipping along the base plane.

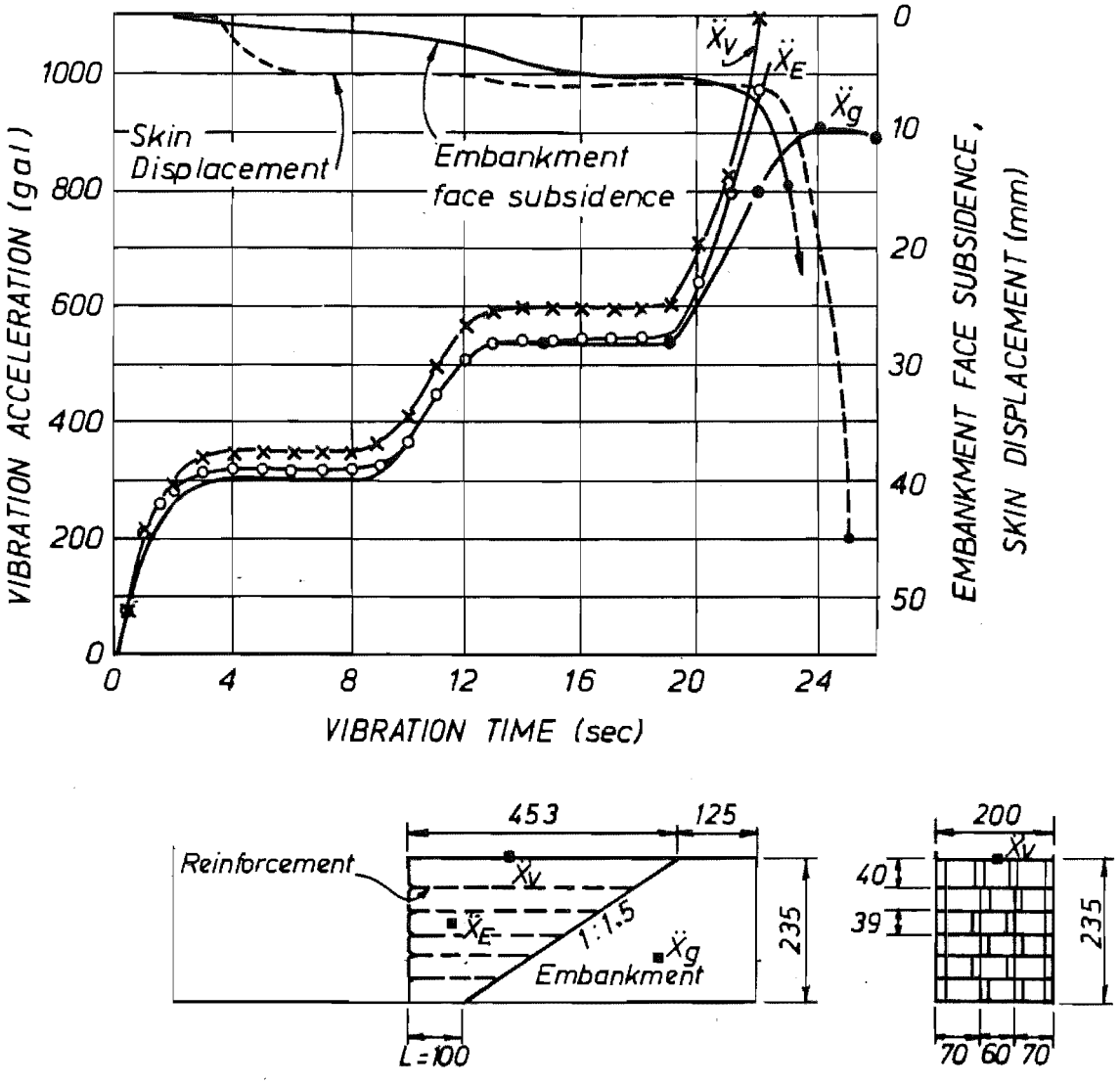

Fig. 2.10. Results of JNR vibration test, configuration shown (Cormack et al 1980).

A test wall 3m high with 3.5m long reinforcing strips and steel skin elements was subjected to vibration testing. The strips were 100mm wide and 0.29mm thick, and sand backfill was used. The static factor of safety of the wall was calculated to be 7. Prior to vibration testing a water sprinkling experiment was done, where 1642mm of water was sprinkled on the surface of the fill over 4 days. 3.9 mm was the maximum displacement measured. 19 days after the end of the sprinkler experiment, a small earthquake (M = 3) struck,

causing a further 1.3mm displacement. 80 days after the water test it was decided that drainage was completed, and a 2 tonne concrete base was placed on the fill surface. A 1.2 tonne oscillator was installed on the concrete base.

Resonance was found at 17 to 20 Hz. (Richardson et al's relation would predict resonance at about 13Hz.) The largest acceleration recorded was 950 gal (0.97g) at the wall top, 240 gal (0.24g) 2 facing panels down, and 120 gal (0.12g) 5 panels down. (The wall was six panels high.) The amplitude at the same places was 1.6mm, 0.2mm, and 0.1mm respectively. It was stated that there was no significant change in the residual stress (in what or where is not clear).

Pullout tests were then attempted. For those strips that did not break, "pullout resistance was high". Pullout tests were abandoned, and many strips were cut at the facing panel. Some 80 out of 118 strips were cut. The wall still stood. Then a further sprinkler test was run, pouring 2060mm of water on in 3 days. 5.2mm of further displacement was measured. Reinforcement tendon strain was also measured, in static conditions.

This work is unusual in that the reinforcing is unusually wide and thin, and placed quite close together. No reference is made about this in the translation. It would appear that the strips used were quite extensible with low tensile strength.

Paper 7.0 in Cormack et al (1980) describes some monitoring of a full scale wall on the Sotobuse railway line in Japan. It was a 3m high wall, with steel facing panels. It was found that the earth pressure due to a train passing along the wall fill "increased only a fraction", and that displacement due to train vibration was "extremely small".

In 1982, the District of Kusuazu Construction Board tested a 3m high wall inside a container connected to a vibrator, as well as a 6m. high wall.

As a result of all these tests the Japanese authorities adopted an active zone, as shown in Fig. 3.10, where the distance of the statically derived line

from the face is increased by an amount related to the horizontal acceleration. (Boyd, 1985)

2.5. University of Canterbury.

Nagel (1985), tested 7 model walls, 320mm high and 810mm long, using 6mm wide satin ribbon for reinforcing. The facing panels were 40mm high, 0.45mm thick aluminium. Instrumentation consisted of an accelerometer in the fill behind the facing at mid height, another 100mm back from and at mid-height of the top facing panel, and one on the containing box. Displacements were measured relative to the box at the centre of panels 4 and 8 (walls were 8 panels high, number 8 being at the top). Tie forces were measured at the wall face for the central tie in each panel. Data was stored on a computer. Layers of white sand were placed in the fill during construction (the backfill was a fine grey beach sand) and columns of white sand were placed against the glass box sides after construction. The failure surface inside the wall was traced by carefully locating the breaks in the white sand layers during dismantling, and for some tests a perspex box was pushed into the fill during dismantling. A column of sand was then visible after removal of the surrounding sand and the coloured layers could be clearly seen. This method was found to be not as reliable in picking up the failure surface as the careful removal of sand layer by layer.

During testing a photographic record of failure surface formation was made from the side. Failure began by the formation of a broad shear band back and up from the toe. After some movement a distinct failure surface was visible forming near the toe. With continuing shaking, it grew towards the surface, eventually outcropping during a pulse. Thereafter a large displacement occurred. Excitation was by sudden release of a compressed spring attached to the box and reacting against a rigid frame. A pair of hydraulic shock absorbers damped the motion, resulting in essentially one large and one small pulse. By compressing the spring to different lengths, the excitation acceleration could be changed.

All walls remained vertical during failure except for the bottom panel, which rotated to lie flat in the same way described by Richardson and Lee

(1975). At no time did a strip break in the tests. Soil shearing was confined to the region of the failure surface. If the wall tilted, it was explained, there would need to be shearing through the entire soil block, clearly requiring much more energy. Failure surfaces not contained within the reinforced volume were bilinear, as determined by Smith and Wroth (1978), while those contained were linear. (For example, see Fig. 2.11 and Fig. 2.12.)

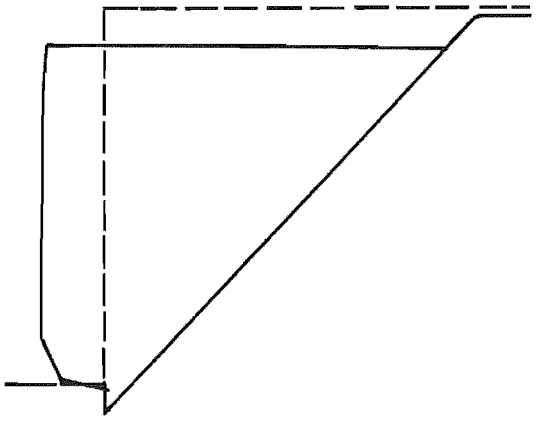

Fig. 2.11. Wall 2 after failure (Nagel, 1985).

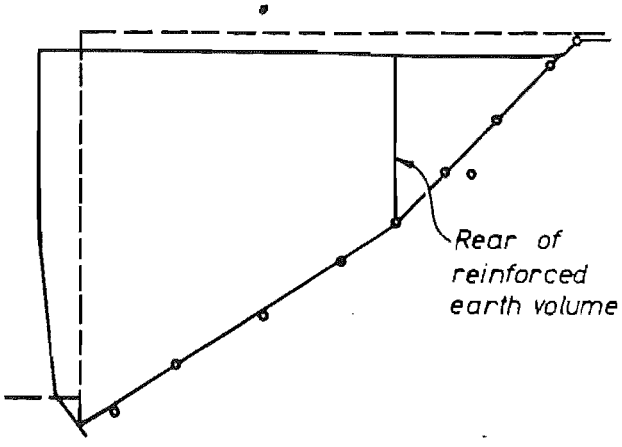

Fig. 2.12. Wall 6 after failure (Nagel, 1985).

Prior to failure, the acceleration level could be maintained for several cycles with relatively small induced displacements. After failure, much larger displacements were induced than before, by the same acceleration level. This is similar to a fatigue failure. There seemed to be a peak strength before failure and a maintainable strength after. It is difficult to quantify the relationship between these peak and maintainable strengths: there is really insufficient data presented in the report, as well as the problems mentioned two paragraphs below. Comparing Fig. 2.13 and Fig. 2.14 however, it appears the peak strength, in terms of yield acceleration, may be about twice the maintainable strength (assuming that Fig. 2.13 is for a run before the failure surface was fully developed). It is perhaps worth noting that Nagel's determination of angle of internal friction, ϕ, for the backfill showed a peak $\phi = 38.4°$ and a residual $\phi = 33.9°$. For seismic design, the peak strength would be of initial interest, and the maintainable strength could be likened to the ductility of the structure.

It was found that the reinforcing tie density (number per square metre of wall face) and length affected the failure surface geometry. Failure displacements of the wall were about 10% of the wall height. (Failure is

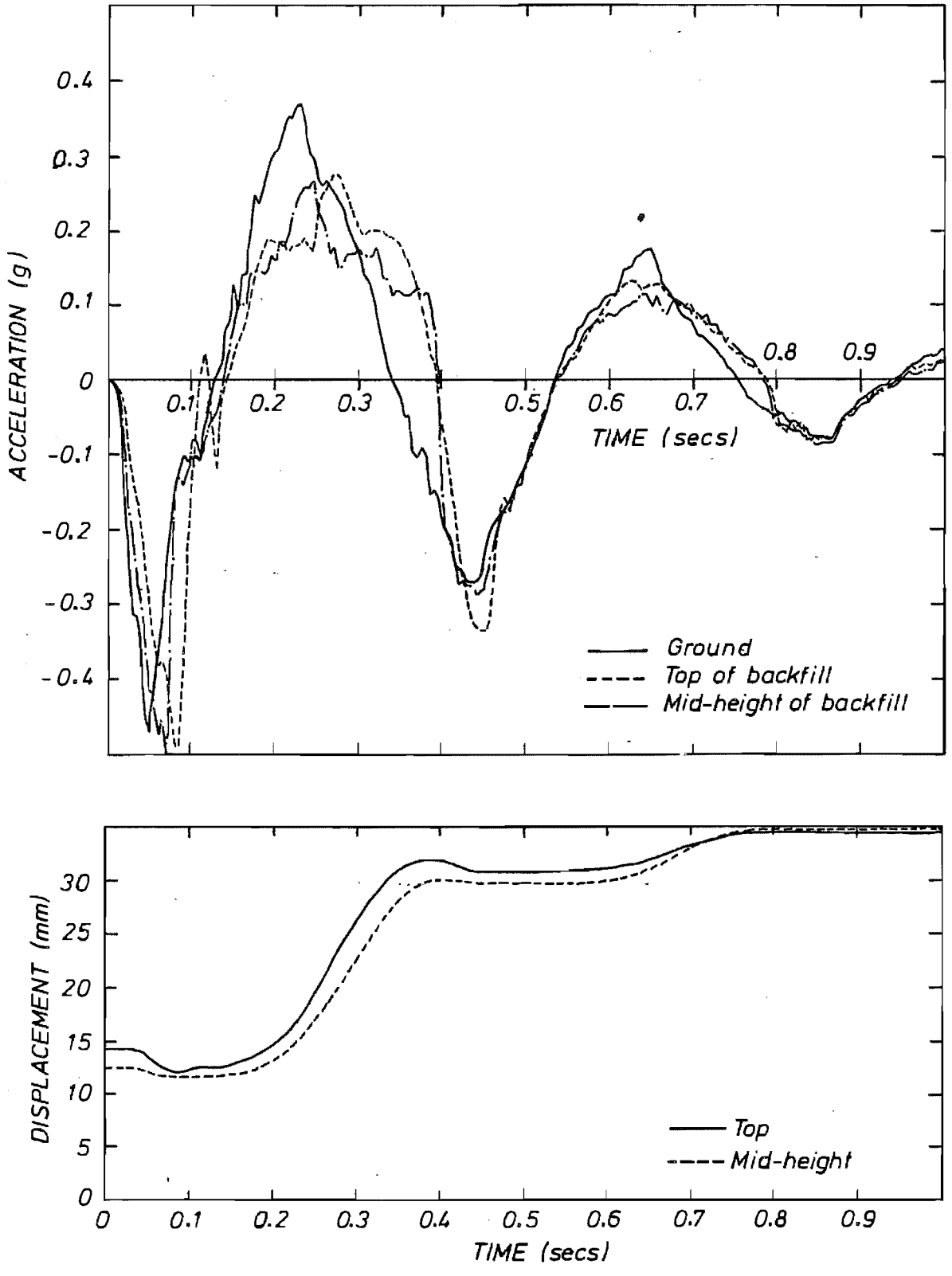

Fig. 2.13. Typical acceleration and displacement time histories, late in test (Nagel 1985).

here defined as when the failure surface first outcrops at the fill surface.) It was seen that there was a cutoff or critical input acceleration, above which permanent displacements were induced in the walls. The response accelerations of the wall during movement were not constant as assumed in the Newmark sliding block analogy (Newmark, 1965). (See Fig. 2.13.)

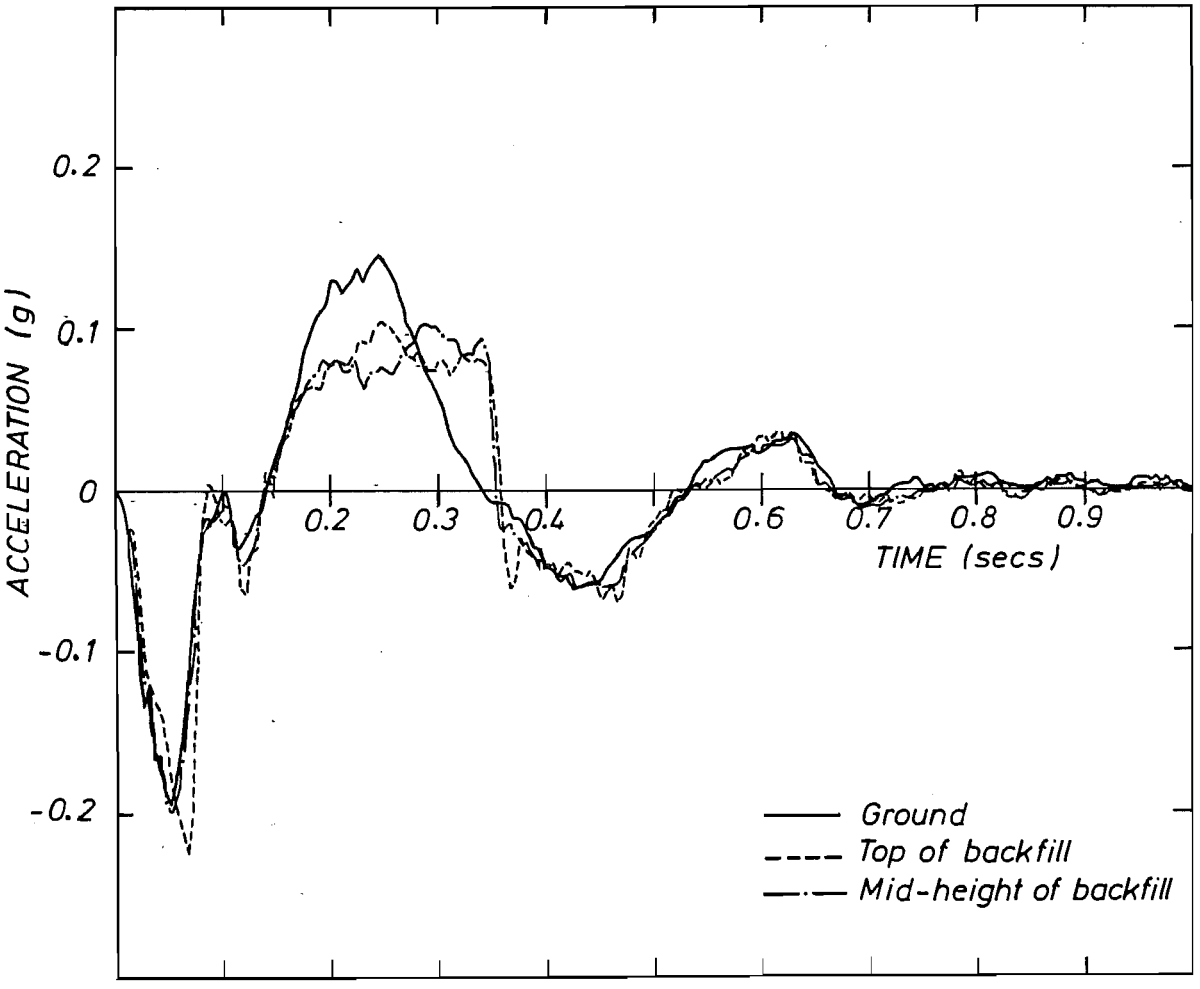

Fig. 2.14. Typical acceleration time history after full failure surface formation (Nagel 1985).

Nagel used a pseudo-static limiting equilibrium approach to try to predict the failure geometry and the critical (limiting equilibrium) acceleration. The approach was proposed by Bracegirdle (1979,1980). Pullout tests were done to obtain a value of pullout resistance vs. depth for use in the formulation. Reasonable agreement was found between the observed and predicted values of failure surface angle to the horizontal. (See Table 2.1.) Only wall 8, which was tested to a much greater degree of failure then the other walls, showed a clear cutoff acceleration plateau, especially after the

failure surface was fully developed. (See Fig. 2.14.) The other walls showed varying degrees of plateau, the best being walls 4 and 7. It was clear, however, that the failure surface only grew when the input acceleration was above a threshold level. (See Fig. 2.13.) The sliding block analogy was said to apply after the complete formation of the failure surface.

Table 2.1.
Predicted and observed yield accelerations and failure surface angles after Nagel (1985).

Wall Number:	2	4	5	6	7	8
Yield Accelerations:						
Predicted (g)	0.07	0.07	0.27	0.27	0.12	0.07
Observed	*	0.09	*	*	0.09	0.08
Failure surf. angle:						
Predicted (degrees)	49	49	34	32	42	49
Observed	47	46	38	33	40	51

* Yield accelerations were not clearly defined.

Elms and Nagel (1987) reported the same work.

CHAPTER 3

DESIGN METHODS

3.1. Introduction.

Most design methods have developed from the assumption that a reinforced earth wall acts as a coherent gravity structure, though some have used the tied-back wall analogy. Evidence supporting the coherent structure approach includes some spectacular foundation failures where walls have moved, sometimes several metres, and remained intact (McKittrick, 1978). In this approach, the structure is checked for "internal stability" (in particular, forces in the reinforcing strips, considering available soil-strip friction and strip durability) and for "external stability" (foundation capacity, overturning, slip-circle failures, sliding on the base).

The Reinforced Earth Company at one time recommended a design method considering gravity loads alone (McKittrick, 1978). Earthquakes in the district of Akita, Japan, in 1983, in Liege, Belgium, in 1983, and in the Frioul area, Italy, in 1976 did little or no discernable damage to reinforced earth walls in those areas (TAI, 1985), although there was no mention of how strong these earthquakes were. No specific allowance had been made in any of the designs for seismic loading (Boyd, 1985). In fact it is often found in Japan that static load cases govern the final design of RE walls (TAI, 1985) - no information is given about how the Japanese design their walls. Nevertheless, seismic design methods are required to check that RE walls are suitably detailed for seismically active areas.

Described below are six design methods.

3.2. Static design method.

The locus of maximum forces in the reinforcing strips coincides approximately with the failure surface under static conditions and thus is assumed to define an active zone in the fill. This boundary is simplified to a bilinear shape. Each strip is assumed to be loaded by the earth pressure over a tributary area (equal to horizontal x vertical spacing of strips) at the facing. This load is resisted by the length of strip in the passive or resistant zone, assuming a value, per metre length of strip, for the friction mobilised between reinforcing and soil. The static earth pressure has been found to vary from about K_o at the surface to about K_a at and below a depth of 6m. The length of strip required to resist the earth pressure load is added to the width of the active zone at that level to obtain the required strip length. (McKittrick, 1978; MWD, 1980; Boyd, 1985.) See Fig. 3.1. Safety factors are incorporated as appropriate.

In a variation of the static method to give some allowance for seismic loads on the wall, Nagel (1985) reports Seed and Mitchell (1980) as suggesting a pseudo-static force on the active zone, brought about by a horizontal acceleration A_{max} acting at its centre of gravity. Nagel calls it the "inertia force on active wedge" method. The distribution of the force is as in Fig. 3.2.

Strip lengths required to resist the pseudo-static earth pressure load on the same tributary area of facing are calculated in a manner similar to that above, and added to the purely static required length.

Using the static active wedge as the dynamic active wedge has no experimental or theoretical basis. It is no doubt an attempt to provide some seismic input to the design in a simple way. Nagel's tests also showed that the dynamic failure surface is much flatter than the static, so the failure volume on which A_{max} acts is somewhat larger than the static active zone.

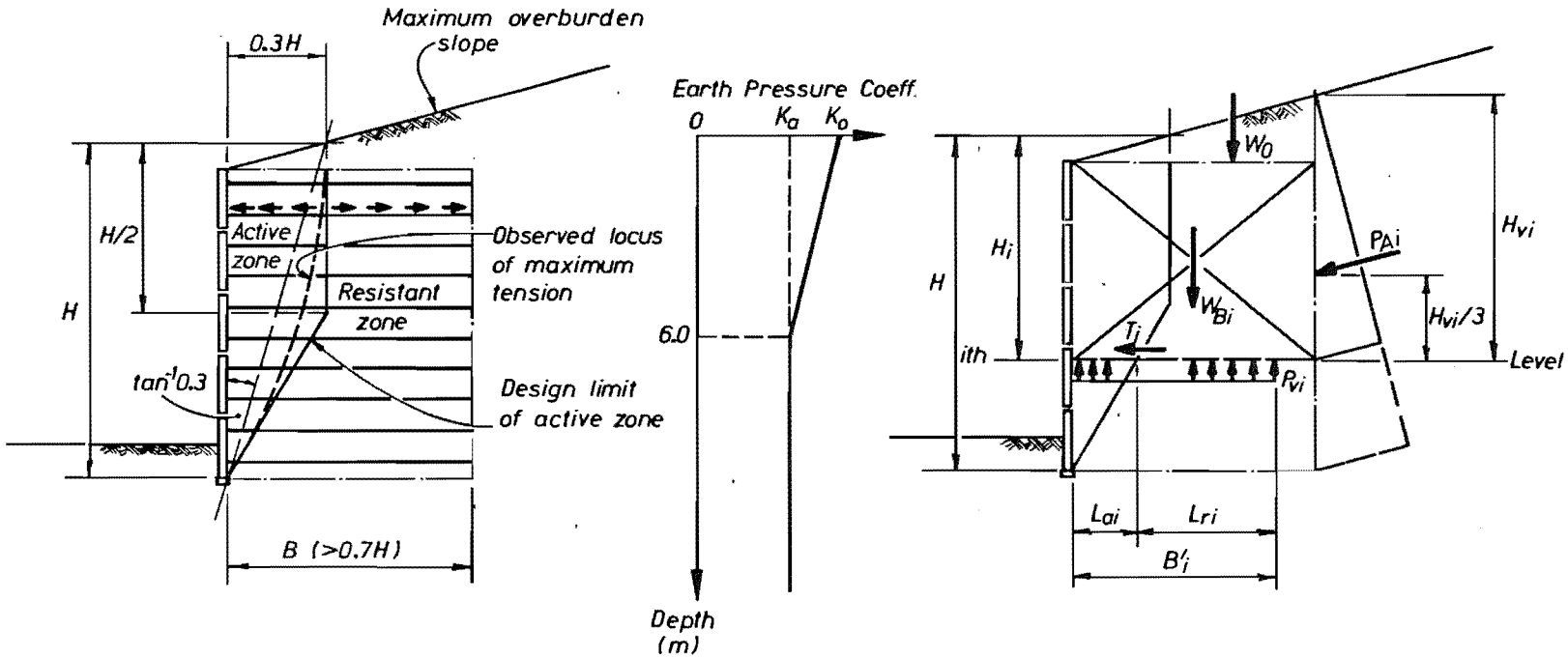

Fig. 3.1. Static design parameters (Boyd, 1985).

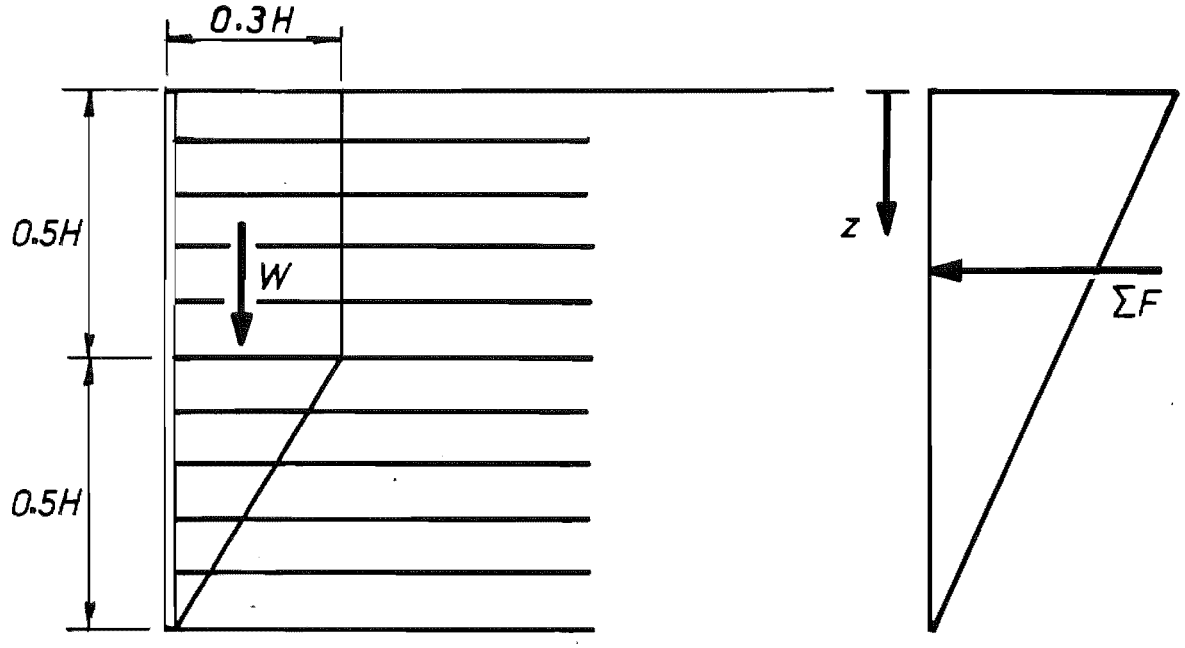

Fig. 3.2. Reinforced Earth Company Design method (Nagel 1985).

3.3. Richardson and Lee (1975)

Richardson and Lee proposed a relatively simple design method based on the results of their tilt-up and shaking table tests (described in section 2.2 above). It was a pseudo-static method of similar application to that of Seed and Mitchell mentioned above. To obtain the design earth pressure, they used response spectra and modal analysis techniques, together with Fig. 2.1. A design acceleration A_{des} was chosen using

$$A_{des} = \Gamma_1 Sa_1 + \Gamma_2 Sa_2 \qquad \text{.....(3.1)}$$

where Γ_1 and Γ_2 are modal participation factors. They were calculated "using structural analysis techniques" to be 1.25 and 0.5 respectively. Sa_1 and Sa_2 are values of spectral acceleration for periods corresponding to the first and second modes of the wall.

To calculate the modal periods of the wall, Eq. 2.2 was used. If a value of G for medium strain levels is chosen (Seed and Idriss, 1970) then T_1 = (0.0018 to 0.003)H, where H is the clear wall height in metres. From wave propagation theory (Idriss and Seed, 1968), $T_2 = T_1/3$. Entering the design spectrum at T_1 and T_2 then gives Sa_1 and Sa_2. Then A_{des} is used in Fig. 2.1

to find the seismic earth pressure coefficient E, and the total seismic-plus-static earth pressure envelope is found as in the first part of Fig. 2.1. The tributary area of each strip was then used to calculate the design strip force.

3.4. Richardson (1978).

Richardson et al (1977) found that the earlier (Richardson and Lee) design method grossly over-estimated the strip forces when applied to the 6.1m high test wall they had built. Richardson (1978) revised and added to the earlier method. The important changes were the inclusion of the effects of dynamic strain and damping levels, and the introduction of a wall relative stiffness concept to determine the magnitude and distribution of dynamic forces and strain. Dynamic strip forces are calculated using this method, and should be added to the static strip forces before obtaining the required strip length.

The method is:

i) From the design earthquake magnitude, M, estimate the peak strain ε from Fig. 3.3.

ii) With ε estimate the design damping λ from Fig. 3.4.

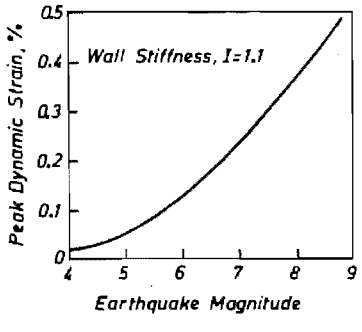

Fig. 3.3. Estimating peak dynamic strains (Richardson, 1978).

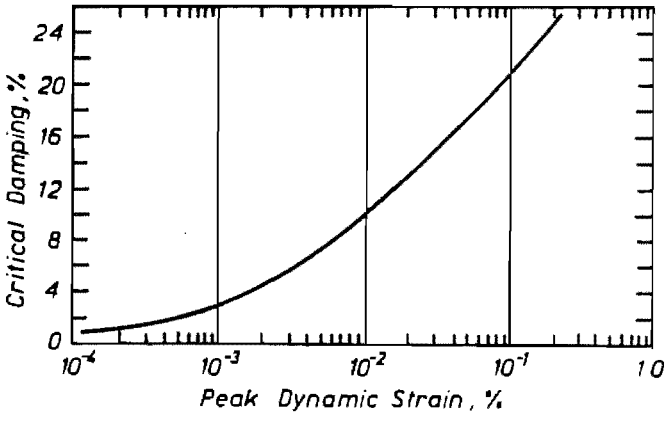

Fig. 3.4. Estimating the level of damping (Richardson, 1978).

iii) With M, λ develop the design response spectra from Fig. 3.5.

iv) With the clear wall height H calculate the undamped low strain natural frequencies $f_1 = 38/H$ and $f_2 = 100/H$.

v) Enter Fig. 3.6 with ε to obtain the frequency correction factor FCF_ε.

vi) With FCF_ε, f_1, f_2 calculate the strained natural frequencies $f_{\underline{1}}$ and $f_{\underline{2}}$ using $f_{\underline{1}} = f_1 * FCF_\varepsilon$, and $f_{\underline{2}} = f_2 * FCF_\varepsilon$.

vii) With $f_{\underline{1}}$, $f_{\underline{2}}$ obtain Sa_1 and Sa_2 from the spectrum derived in step (iii).

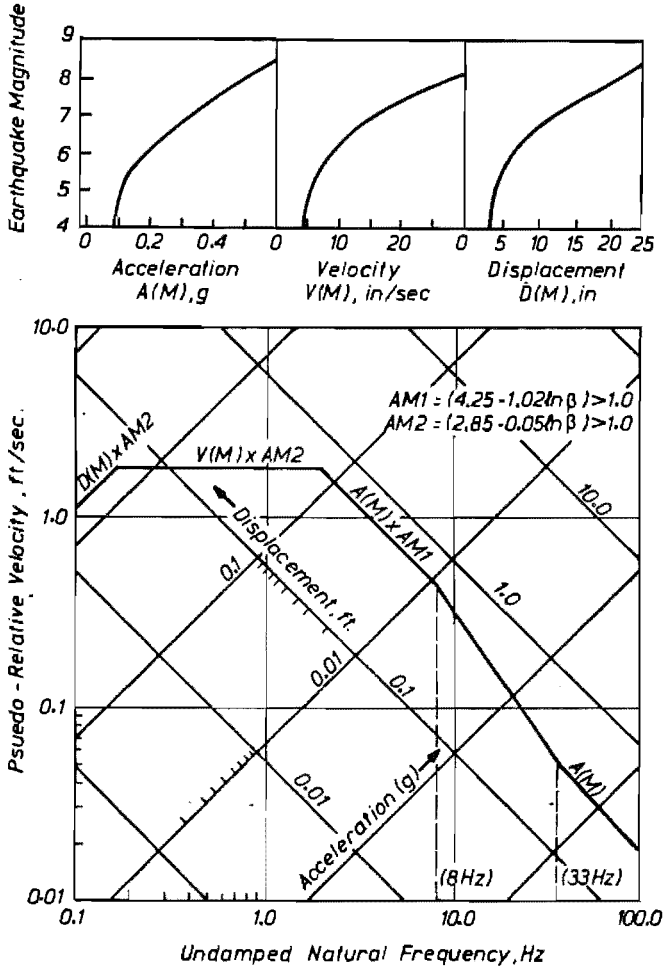

Fig. 3.5. Design response spectra synthesis (Richardson, 1978).

Then the total dynamic force ΣF is

$$\Sigma F = [Sa_1 + 0.2Sa_2]M_{eff} \quad \ldots\ldots\ldots\ldots\ldots\ldots\ldots\ldots\ldots\ldots\ldots\ldots\ldots\ldots (3.2)$$

where

$$M_{eff} = 0.75K_0\rho H^2 \quad \ldots\ldots\ldots\ldots\ldots\ldots\ldots\ldots\ldots\ldots\ldots\ldots\ldots\ldots (3.3)$$

and K_o is the at-rest earth pressure coefficient, ρ is the soil mass density, and H is the wall height. M_{eff} is called the effective mass of the wall. The amplitude and distribution of the force on the wall is a function of the stiffness of the wall. A stiffness coefficient, I, was defined as the second moment of the ultimate tensile strip forces about the base of the wall (eg. see Eq. 3.4), where the ultimate tensile force of a strip is either its tensile strength or pullout force, whichever is the less. Then the distribution of the total dynamic force ΣF on the facing is as in Fig. 3.7. Forces are calculated in each strip using the tributary area assumption (see above), and added algebraically to the static forces.

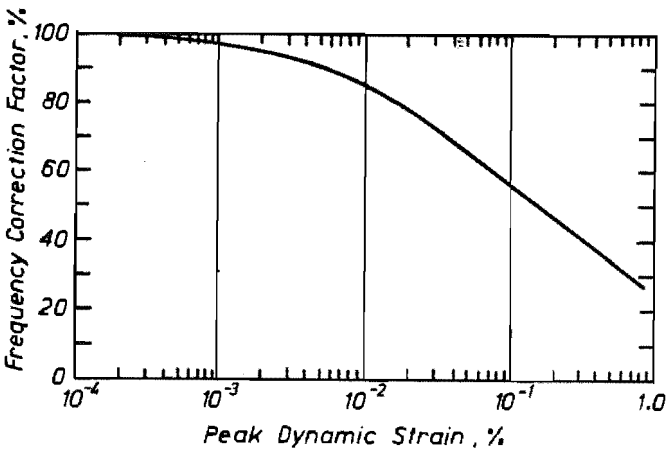

Fig. 3.6. Natural frequency reduction factor (Richardson, 1978).

The stiffness concept was developed from the observation of walls rotating about the toe in vibration, and is central to the whole method. The magnitude and distribution of dynamic forces, and of the peak dynamic strain, is said to be a function of the stiffness coefficient, though relative stiffnesses were found to be more important than the absolute value of I. Thus a reference wall was defined, namely the 6.1m. wall tested with blast vibrations. It had a uniform strip length of 0.8H, uniform horizontal and vertical strip spacing, and a minimum factor of safety against static failure (1.0). (This not a precise definition of the reference wall.) Then the reference stiffness is given by

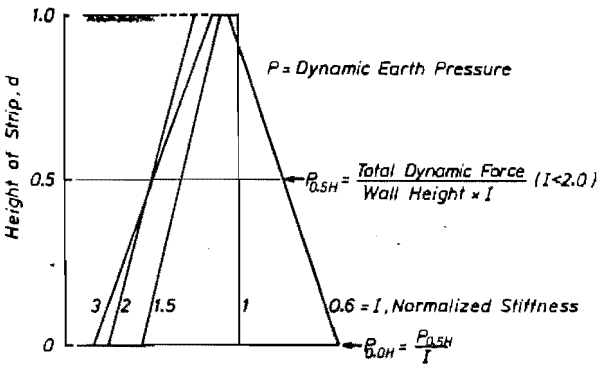

Fig. 3.7. Stiffness vs Dynamic Earth Pressure (Richardson 1978).

$$I_{ref} = \sum_{i=1}^{N} d_i^2 F_i \qquad \text{.....(3.4)}$$

where d_i = height above the base to the i-th strip, N = the number of strips in a tributary width, and F_i = minimum yield strength (force) in the strip, either breakage or pullout. Then the stiffness of the design wall is

$$I' = \sum_{j=1}^{M} d_j^2 F_j \left(\frac{S}{S_j}\right) \qquad \text{.....(3.5)}$$

where S = horizontal spacing of reinforcement in reference wall, S_j = horizontal spacing of reinforcement in j-th layer in design wall, and M = number of strips in design wall. The normalized stiffness is then

$$I = \frac{I'}{I_{ref}} \qquad \text{.....(3.6)}$$

The relationship in Fig. 3.3 (used in part (i) of the method) is derived from a finite element study using a program, LEVSFC, developed by Idriss and Seed (1968). Computed displacements were compared with those measured in the blasting tests at UCLA, and an empirical relationship derived:

$$\varepsilon = \frac{1.1}{I} \varepsilon_{LEVSFC} \qquad \text{.....(3.7)}$$

where ε is the peak dynamic strain of the design wall, I the normalized stiffness, and ε_{LEVSFC} the predicted displacement derived from LEVSFC. Many LEVSFC analyses were said to have been carried out, for wall heights from 5m to 16.75m. One of the inputs of LEVSFC is an earthquake record: actual records were scaled to a range of magnitudes for use. The scaling method used is not clear.

The blasting tests showed a nonlinear decrease in the first mode frequency of the wall with increasing dynamic strain. Fig. 3.4 and Fig. 3.6 are both derived from Seed and Idriss (1970) to account for the change. They are used in parts (ii) and (v), respectively, of the method as outlined above.

Newmark and Blume (1973) and Newmark (1975) are used to develop the response spectra used in (iii) above and shown in Fig. 3.5, which relates to a return period of 100 to 200 years for the design earthquake. Other spectra may no doubt be used, suitable for the area in which the design wall is to be built. Newmark (1975) is concerned with the design of earthquake-resistant facilities to be built in Alaska.

While Richardson's method is quite comprehensive and uses modal analysis techniques to scale model test results to full scale, there are several problems with it:

(a) It is heavily reliant on the output of the program LEVSFC to relate earthquake magnitude and peak dynamic strain. Bracegirdle (1979) points out that the input soil parameters have a marked effect on the result, as does the attenuation law used to scale the earthquake time histories used. The attenuation law used is not defined in the paper. Neither is it clear on the effect of epicentral distance to the site under consideration. Program output is also said to be extremely sensitive to boundary conditions (Bracegirdle, 1979).

(b) It is derived from the blast testing of one wall. Such blast testing may not be representative of earthquake ground motions, especially as it had a very small predominant period of vibration.

(c) Nagel (1985) reports Wood (1982) as pointing out that the increase in pressure with decreasing stiffness (Fig. 3.7) is contrary to conventional results and requires further study.

(d) Static strip forces are difficult to predict, even without the added difficulty of seismic forces. The method may be too complicated in light of this fact. (For example, locked-in compaction stresses can be quite high (Ingold, 1979), and Al-Hussaini and Berry (1978) report that lateral stress on a full scale wall drifted from less than K_a on completion to well above after just two months.)

(e) One of Richardson's assumptions is that the forces in the reinforcing strips return to static pre-earthquake levels at the end of shaking. The present study shows how forces increase quite dramatically with shaking and permanent movement of a reinforced earth wall. The implication is that this method will restrict the response of a wall to merely vibrating elastically. Essentially this would be called a working stress method, and may often lead to conservative design. No advantage is taken of the inherent flexibility and plastic deformation capability of RE walls. Neither is any information available about the ultimate strength or likely deformation of a structure if the design earthquake is exceeded.

(f) Aggour and Brown (1974), in a finite element study of gravity walls showed that the geometry of the backfill (eg. sloping) has a strong

influence on dynamic lateral stress. The stiffness coefficient I is unlikely to account for this.

(g) M_{eff} is derived in Eq. 3.3 without any explanation.

(h) Boyd (1985) points out that the method does not distinguish between the inertia forces of the wall itself and the dynamic forces exerted on the wall by the backfill. It should be pointed out here that the method is applicable to the internal stability analysis of a wall, and the forces Boyd is referring to are perhaps more applicable to external stability analysis.

(i) It is a complicated and detailed method based on relatively crude underlying assumptions, and thus is difficult to justify. This comment is similar in intent to (d) above.

3.5. Prendergast and Ramsay (1980)

Prendergast and Ramsay outline the NZ Ministry of Works and Development design method (see also MWD, 1980). It is essentially a much simplified version of Richardson (1978).

The method was developed while designing the Nauranga Interchange wall in Wellington. A simplified earth pressure diagram is used (Fig. 3.8) which is derived from a Richardson-type analysis, for a magnitude 7.5 earthquake in seismic zone A in New Zealand (NZSS 4203:1984). 75% and 50% of these values would be used in zones B and C respectively. The forces calculated (using the tributary area assumption) are added to the static forces. No information was available about the location of the maximum forces in the strips, so the active zone was assumed to be as shown in Fig. 3.9: an extension of the static active zone. To ensure a ductile failure if one occurs, the minimum probable factor of safety against strip breakage is made greater than the maximum probable factor of safety against pullout.

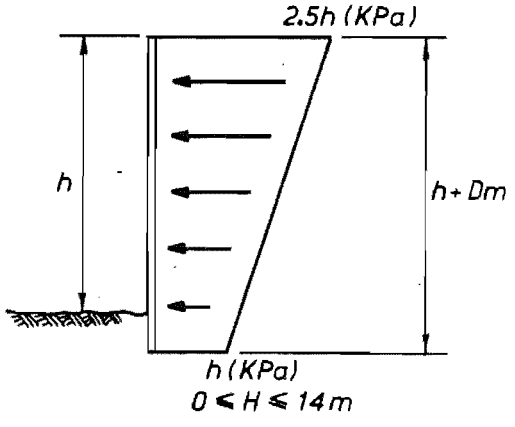

Fig. 3.8. Earthquake earth pressure (MWD, 1980).

The comment was made that seismic design usually only requires longer strips near the top of the wall, when compared with static requirements.

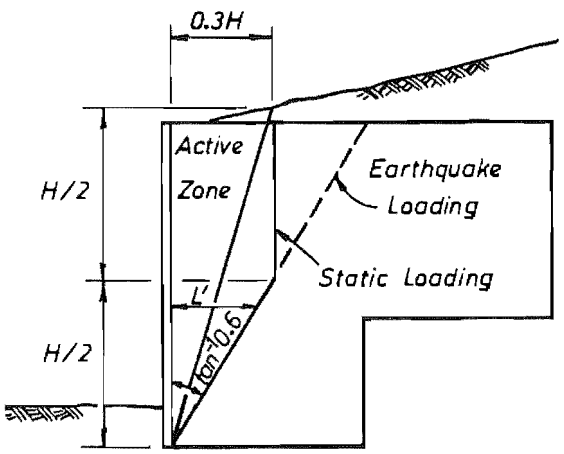

Fig. 3.9. Seismic active zone definition (MWD, 1980).

3.6. Seed and Mitchell.

In a report commissioned by the Reinforced Earth Company in California, Seed and Mitchell (1980) examined previous work and came up with a simple pseudo-static method of design. They identified two main areas of uncertainty: the locus of maximum tension in the reinforcing strips, and the value of the apparent friction coefficient between the soil and the strips (Boyd, 1985). In purely static tests the line of maximum force in the strips coincides with the failure surface, thus delineating the active and resistant portions of the RE block. (McKittrick, 1978.)

TAI (1985) summarizes Seed and Mitchell (1980), with a few modifications. It points out that in the Akita earthquake, 1983, in Japan, serious damage was done to buildings, bridges, and wharves, whereas none of the 24 RE walls in the area seemed to be affected. Thus they conclude that a simple design method is all that is required. No information about the Akita earthquake (magnitude, intensity in the area, epicentral distance) is given, nor is there any about the standard of design or pre-earthquake condition of the damaged structures.

Two kinds of external loads are recognised: dynamic active earth force E_{AE}, from the Coulomb wedge behind the wall, and the inertia force, E_I, from the mass of the wall itself. These loads are analogous to the loads on a gravity wall. There is no reason, they say, that E_{AE} and E_I should both be maximum at the same time, so reduction factors can be used. For gravity

walls, Antia and Whitman (1982) showed, by numerical comparison with an exact formulation in which E_I and E_{AE} were decoupled, that the Richards and Elms (1979) assumption that they acted together and thus were a maximum at the same time introduced very little error.

The dynamic active earth pressure E_{AE} is derived from the M-O equations for K_{AE} and P_{AE}. It was shown that for $\phi = 35°$ and $\delta = \phi/2$, $K_{AE} \approx 0.75a/g$. Thus

$$E_{AE} = 0.5\gamma H^2 0.75a/g = 0.375\gamma H^2 a/g \quad \text{.....(3.8)}$$

acting about 0.6H above the base of the wall (this last from model studies). γ is the unit weight of the backfill, H the wall height, and a the peak ground acceleration.

For a stiff structure, $E_I = Wa/g$, where W is the weight of the wall. But in the case of a RE wall, there is no precise limit between the wall and the backfill. A slice 0.5H wide was proposed. (This might be likened to the line of maximum tension in the strips, by defining the active zone.) Thus $E_I = 0.5\gamma H^2 a/g$. The active zone (0.5H wide) was expected to widen with vibration. TAI prefer the Japanese results, where the active zone is (0.3 + 0.5a/g)H wide. (Fig. 3.10) Thus

$$E_I = 0.75H(0.3+0.5\frac{a}{g})H\gamma\frac{a}{g} = 0.225\gamma H^2\frac{a}{g}(1 + \frac{5a}{3g}) \quad \text{.....(3.9)}$$

applied at

$$\frac{1}{3} \times \frac{H}{3} + \frac{2}{3} \times \frac{3H}{4} = (\frac{1}{9} + \frac{1}{2})H = 0.61H \quad \text{.....(3.10)}$$

Thus E_I and E_{AE} act at the same level.

In keeping with the assumption that E_{AE} and E_I will not be a maximum at the same time, a "reduction factor" is introduced at this point, to keep $E_{AE} + E_I \leq 0.7\gamma H^2 a/g$. Seed and Mitchell suggest reducing E_I by 35%, while holding E_{AE}. TAI choose to reduce E_I by one third, thus

$$E_I = 0.15\gamma H^2 \frac{a}{g}\left(1 + \frac{5a}{3g}\right) \quad \text{.....(3.11)}$$

and the earth pressures are as in Fig. 3.11.

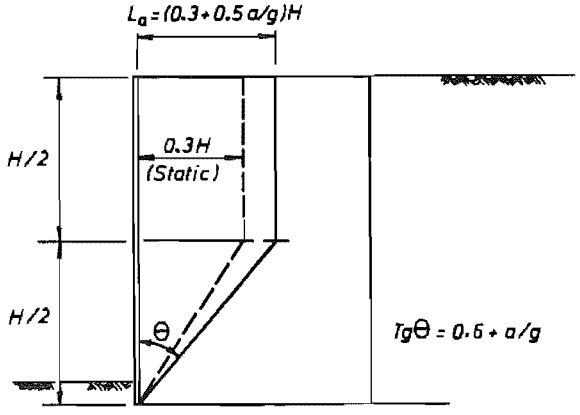

Fig. 3.10. Active zone from Japanese work (TAI, 1985).

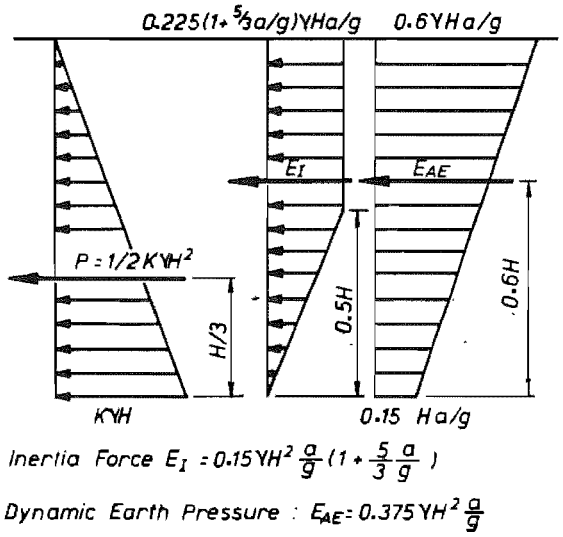

Fig. 3.11. Static, dynamic, and inertia earth pressures (TAI, 1985).

As well as the external loads on the wall, treating it like a gravity wall, there are internal forces generated. Initially, Seed and Mitchell analyzed internal dynamic forces with the Richardson Eqs. 3.2 and 3.3. They conclude that the ground motion, for practical purposes, is not magnified or reduced in the fill, and thus

$$Sa_1 \approx Sa_2 \approx a \quad \text{.....(3.12)}$$

Combining Eqs. 3.2, 3.3, 3.12, and choosing $K_0 = 0.412$ (for $\phi=36°$) and a likely Richardson stiffness of I=1.5, the internal force is

$$E_d = 0.25\gamma H^2 \frac{a}{g} \quad \text{.....(3.13)}$$

In their own intuitive analysis, Seed and Mitchell point out that for an anchored wall, $E_{AE}=0.37\gamma H^2 a/g$. They say that for a RE wall the strips should be less stressed, and thus propose to limit E_d to $0.3\gamma H^2 a/g$, and to adopt a uniform distribution for E_d over the wall height. (See Fig. 3.11.) TAI choose the simple, intuitive, Seed and Mitchell formulation, and thus add to the horizontal static stresses, the uniform dynamic stress

$\Delta\sigma_H = 0.30\gamma H^2 a/g$ .....(3.14).

Strip forces are then calculated using the static plus dynamic earth pressure, as in section 3.2.

A simple analysis of shear in a wall was done to show the level of acceleration at which permanent deformation of a wall can be expected. By summing the values for the inertia force, $E_I = 0.2(1+5a/3g)\gamma H\Delta ha/g$, the dynamic earth pressure force, $E_{AE} = 0.6\gamma H\Delta ha/g - \frac{1}{2}0.45\gamma\Delta h^2 a/g$, and the static pressure force, $P = \frac{1}{2}0.3\gamma\Delta h^2$, (for $\phi=35°$, $K_a \approx 0.3$) for a slice of depth $\Delta h \leq H/2$, and comparing the sum to the shear resistance of the base of the slice (mass x tan ϕ), Seed and Mitchell derive the equation

$$(a/g)^2 + (2.4 - 0.675\Delta h/H)a/g + (0.45\Delta h/H - 1.5) = 0 \quad ...(3.15)$$

and conclude that there is no risk of permanent deformation of a wall, with uniform strip length longer than 0.7H, subject to accelerations of less than 0.5g. This only applies to the top half of the wall. No analysis was done taking the slice as greater than H/2 deep.

The Seed and Mitchell analysis was supposed to be a simple method, making up for complexity with conservatism. It also neglects the flexibility inherent in RE walls. The important issue of the forces in the strips is dealt with in a rather arbitrary way by assuming the strips are less stressed than in an anchored wall. Much of the paper is concerned with external stability (E_I and E_{AE}), hence overturning and bearing pressures, and relatively little on strip force determination. This probably reflects the contention early in the paper that the strip design forces are usually determined by the static load cases in Japan, a very seismically active area, although there is no information given about how the Japanese design their RE walls.

3.7. Bracegirdle (1979,1980).

To take advantage of the plastic deformation available in RE structures, Bracegirdle proposed a limited displacement method of design, or at least analysis during design. A critical (or cutoff) acceleration is defined as that acceleration acting uniformly over the structure that achieves limiting equilibrium. The method assumes a planar (or bi-planar) failure surface, which is not necessarily the locus of peak strip tensions. A pseudo-static seismic force, resulting from the critical acceleration acting at the centre of gravity of the slip mass, is used in the formulation of limiting equilibrium equations. Solution of these equations is to find the failure surface that has the lowest critical acceleration. It is assumed that the slip mass slides rather than rocks, although this can be checked by taking moments about the point at which the failure surface meets the face.

Displacements can then be calculated, using the cutoff acceleration and a design earthquake acceleration, K_m. Bracegirdle suggests the equivalent pulse analogy of Sarma (1976), a development of the Newmark (1965) sliding block method, to calculate displacements (see section 4.6.1). No amplification of the ground motion is assumed. K_m is defined as the maximum inertial force *(sic)* contained within the volume of soil defined by the free surface and the slip surface. What he really means, is that K_m is the maximum acceleration acting on the active (sliding) block in the wall. If the RE is assumed to act as a rigid block, K_m is the maximum base acceleration. Failure must be by strip pullout to ensure ductility.

There are some problems with this method however. There are three equations (in fact, only two: we assume plane strain conditions), and four unknowns:

(1) the cut-off acceleration, k_h,

(2) the failure surface angle to the horizontal, α,

(3) the sum of forces in the reinforcing strips at the failure surface, R, and

(4) the force normal to the failure surface, N.

By solving the two equations simultaneously, we can remove N. We can minimise k_h with respect to α by differentiation. But some other information is necessary for R for a complete solution. A formulation for the strip forces

is given in Chapter 4, where the maximum force obtainable from the soil-strip friction (ie. the ultimate pullout force) is assumed to be what is required.

A second problem is that the failure surface is often not entirely contained in the reinforced volume (it is bi-planar). No information is obtained about the forces in those strips that do not intersect the failure surface. Separate consideration of these strips is necessary. In fact, a separate analysis may be needed for all strip forces.

Not withstanding the problems, this approach seems the most rational of those outlined here. It will give an indication of the ultimate strength of the structure, and of deformations that may be expected in an earthquake. "Ductility checks" can easily be made for earthquakes larger than the design earthquake.

Nagel (1985) has developed Bracegirdle's method a little further, and done some model tests to check the validity of some of the assumptions. (See section 2.4.) The planar failure surface seemed to be confirmed in the tests, though the critical acceleration concept was not clear-cut before the failure surface was fully formed. Nagel did not attempt to calculate displacements.

3.8. About the present study.

This study is concerned with the limited displacement method of Bracegirdle. Nagel's model tests were sufficient to see that the method seemed to work, but too small to instrument the strips to obtain the distribution of forces in the reinforcing strips during seismic shaking. In order to obtain such information, and to verify the idea at a larger scale, a program of testing 1m. high walls on a shaking table was initiated. This would also give the opportunity to use a digitized earthquake record for the ground excitation. With electronic data logging it would be possible to then look at the response of the wall to each pulse of the input, as well as general trends. The logistics of handling the 11-or-so tonnes of sand required for walls of this height were felt to be acceptable. Smaller models could be used to measure forces in the strips, but the problem arises of how to lead the strain gauge wires out of the fill area without themselves acting

as unanchored reinforcement. It was felt that by using a relatively large model, with suitable methods, such effects would be small in comparison with the actual forces in the structure. Also, the force levels being measured would be much larger than the electrical and other noise on the data.

Chapter 4 outlines the mathematical requirements of the theory, and Chapter 5 describes the testing apparatus and systems. More detailed information about some items in Chapter 5 is presented in Appendix A, and the method used to design the test walls is shown in Appendix B. In Chapter 6 the results of the experimental work are discussed.

CHAPTER 4

THE LIMITING DISPLACEMENT APPROACH

4.1. Introduction.

Below is outlined the simple mathematical model that forms the basis of the limiting displacement approach proposed for the design of R/E walls. The original idea was proposed by Bracegirdle (1979,1980), and modified by Nagel (1985) to include a formulation for the strip forces at the failure surface. While Bracegirdle did suggest a method to calculate the displacements, his formulation for the strip forces at the failure surface is not clear. Further, there is no information produced about the distribution of force in the reinforcing strips. Nagel did not attempt to calculate displacements, but did verify experimentally that at least the failure surface angle to the horizontal was predicted with reasonable accuracy.

There are two cases: failure surface contained within the reinforced block (Fig. 4.1), and failure surface not contained (Fig. 4.2). In the first instance the model is for a rectangular block structure (all strips the same length), but is subsequently extended to a stepped block (strips in the lower half of the wall shorter than in the top half, Fig. 4.3 and 4.4). A pseudo-static limiting equilibrium approach is used in each case to derive an expression in which the unknowns are the failure surface angle to the horizontal, and the cutoff or yield acceleration. A search is then made for the value of failure surface angle with the minimum corresponding yield acceleration.

Also shown are three systems, of varying complexity, to calculate the likely displacements. One uses random vibration theory and requires some earthquake characteristics (or a design earthquake time history) as input to

a computer program. The other two systems use prepared charts to predict displacement.

A design process incorporating this approach would be iterative:

a) assuming a first-look design (eg. a static design), calculate the yield acceleration. The limiting equilibrium approach can be readily applied to any configuration of wall.

b) considering some design earthquake(s), or a design spectrum, estimate the displacement likely in the wall. If the prediction is greater than the allowable displacement, change the design and start at a) above again.

Alternatively, an allowable displacement could be used to work backwards to the yield acceleration, and an iterative process of design change and yield acceleration calculation gone through to obtain the final design. This is similar to the Richards and Elms (1979) method for gravity retaining walls.

The assumptions required are:

i) plane strain conditions, which allows analysis of the wall on a per metre length basis,

ii) the backfill soil maintains most if not all of its static strength during and after earthquake shaking. This effectively means that there is little pore pressure rise expected in the soil and thus no liquefaction potential,

iii) vertical accelerations have negligible effect and can be ignored (see Wolf et al, 1978),

iv) transverse accelerations (ie. along the wall) have negligible effect. Sharma (1988) has shown that this is in fact unconservative for the Newmark sliding block approach, but transverse accelerations can be incorporated fairly easily by factoring the yield acceleration;

v) frictionless wall ie. the friction between the wall facing and the backfill is negligible,

vi) the lateral inertia of the face elements is negligible compared to that of the sliding block,

vii) planar (or bi-planar) failure surface. This is compatible with (v) above for the contained case; and

viii) horizontal backfill, with no surcharge.

4.2. Failure surface contained.

Consider the system in Fig. 4.1, which shows a RE wall in a state of limiting equilibrium. For horizontal and vertical force equilibrium respectively,

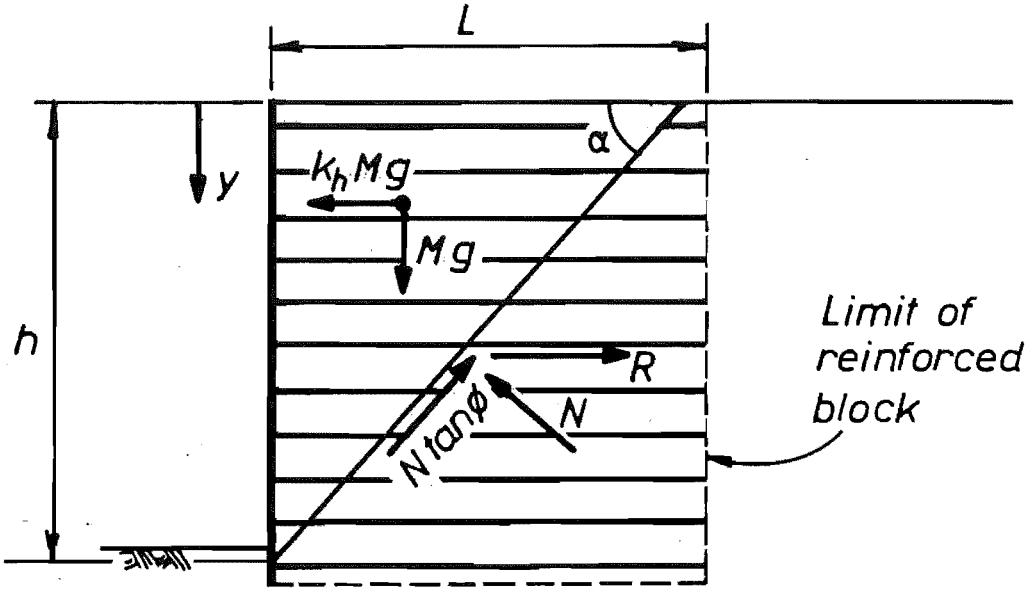

Fig. 4.1 Limiting equilibrium, failure surface contained.

$$k_h Mg = R + N\tan\phi\cos\alpha - N\sin\alpha \qquad \ldots\ldots(4.1)$$

$$Mg = N\tan\phi\sin\alpha + N\cos\alpha \qquad \ldots\ldots(4.2)$$

Solving eq. 4.1 and 4.2 simultaneously eliminates N:

$$k_h = \frac{R}{Mg} + \tan(\phi-\alpha) \qquad \ldots\ldots(4.3)$$

where k_h is the horizontal acceleration coefficient, or yield acceleration, at which failure just occurs for the particular value of α. The weight of the active zone is then

$$Mg = \frac{\rho g h^2}{\tan\alpha} \qquad \ldots\ldots(4.4)$$

where ρ is the mass density of the soil and g the acceleration due to gravity.

It is not clear what formulation Bracegirdle used for the strip forces. Nagel used an integration over the wall height to sum the strip forces, which turned out to provide a force where there was no strip. A summation system is used here. If F_y is the force in a strip at depth y below the top of the wall, and there are n strips per metre run of wall, the total force R of the reinforcing at the failure surface is

$$R = \Sigma F_y = \sum_{i=1}^{m} \left(\left(L - \frac{h-y_i}{\tan\alpha} \right) 2bn\rho g y_i f^* \right) \qquad \ldots\ldots\ldots\ldots\ldots\ldots\ldots\ldots (4.5)$$

where b is the width of the strip and f* is the apparent friction coefficient. The friction coefficient is difficult to quantify. Previous testing, and the results of the work reported here, are discussed in Section 6.7. If we assume, for the moment, that f* is independent of depth, and that all strips are of equal width, then

$$R = 2bn\rho g f^* \left(\left(L - \frac{h}{\tan\alpha} \right) \sum_{i=p}^{m} y_i + \frac{1}{\tan\alpha} \sum_{i=p}^{m} y_i^2 \right) \qquad \ldots\ldots\ldots\ldots\ldots\ldots (4.6)$$

and we should note that if the number of strips per metre width changes at a particular depth, R is calculated in parts for each n with summations over the relevant depths. i is the strip level number, i=1 at the lowest layer of strips in the wall. i = p at the lowest level of strips intercepted by the failure surface, and m is the total number of layers of strips in the structure.

Note that the expressions for Mg (eq. 4.4) and R (eq. 4.6) both have ρg on the right hand side. Thus it is seen in eq. 4.7 (by substituting eq. 4.4 and 4.6 in eq. 4.3) that the value of k_h is independent of the density of the soil backfill.

$$k_h = \frac{2bnf^* \tan\alpha \left(\left(L - \frac{h}{\tan\alpha} \right) \sum_{i=p}^{m} y_i + \frac{1}{\tan\alpha} \sum_{i=p}^{m} y_i^2 \right)}{h^2} + \tan(\phi - \alpha) \qquad \ldots\ldots (4.7)$$

To find the minimum k_h we could set $\frac{dk_h}{d\tan\alpha} = 0$ but this results in a quartic in $\tan\alpha$. It is perhaps easier to use some other method to find the minimum k_h from eq. 4.7. In this work, the minimum k_h was located graphically, after using a computer algorithm with guaranteed convergence for finding a zero of a function (Brent, 1975). The function to be zeroed arises from eq. 4.7 if we subtract k_h from both sides. Usually a value of α was supplied, and k_h calculated, so it is essentially a trial and error method. By including stepping of values of α through a stated interval [a,b] and testing for the minimum, no graphing would be necessary. Parameter sensitivity can be gauged by looking at the shape of the graphs produced by varying the parameters in the equation. This is studied in section 6.11.

4.3. Failure surface not contained.

Consider the system shown in Fig. 4.2. Additional assumptions are required:

ix) bi-planar failure surface, and

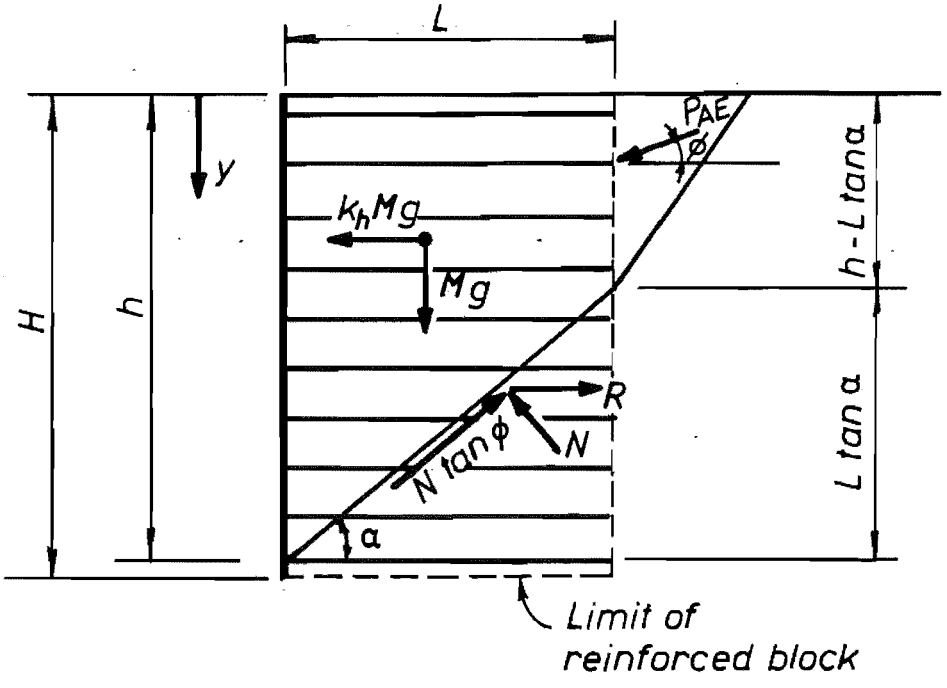

Fig. 4.2 Limiting equilibrium, failure not contained.

x) the angle the resultant dynamic force P_{AE} makes with the horizontal is equal to ϕ.

For horizontal and vertical forces equilibrium respectively,

$$k_h Mg = R + N\tan\phi\cos\alpha - N\sin\alpha - P_{AE}\cos\phi \quad \text{.....(4.8)}$$

$$Mg + P_{AE}\sin\phi = N\tan\phi\sin\alpha + N\cos\alpha \quad \text{.....(4.9)}$$

Eliminating N,

$$k_h Mg = R + (Mg + P_{AE}\sin\phi)\frac{\tan\phi\cos\alpha - \sin\alpha}{\tan\phi\sin\alpha + \cos\alpha} - P_{AE}\cos\phi \quad \text{.....(4.10)}$$

The weight of the active zone of reinforced soil is given by

$$Mg = \rho g L(h - \tfrac{1}{2}L\tan\alpha) \quad \text{.....(4.11)}$$

where ρ is the mass density of the soil. As reinforced earth walls have been found to act as coherent gravity structures, (McKittrick, 1978), we can use Mononobe-Okabe (M-O) theory to calculate the force P_{AE} exerted on a rigid wall by a dynamic active soil wedge:

$$P_{AE} = \tfrac{1}{2}\rho g H_w^2 K_{AE} \quad \text{.....(4.12)}$$

where H_w is the height of the active wedge, and the earth pressure coefficient K_{AE} is given by

$$K_{AE} = \frac{\cos^2(\phi-\theta)}{\cos\theta\,\cos(\delta+\theta)\left(1 + \sqrt{\left(\frac{\sin(\delta+\phi)\,\sin(\phi-\theta)}{\cos(\delta+\theta)}\right)}\right)^2} \quad \text{.....(4.13)}$$

where δ is the friction angle between the back of the wall and the retained backfill and $\theta = \tan^{-1} k_h/(1-k_v)$ (Mononobe-Okabe, see Seed and Whitman, 1970). k_v, the vertical acceleration coefficient, is set to zero.

Assuming that the wedge behind the reinforced block can be represented by the M-O theory, we have

$$P_{AE} = \tfrac{1}{2}\rho g(h - L\tan\alpha)^2 K_{AE} \qquad \text{.....(4.14)}$$

where K_{AE} is found using eq. 4.13.

For the total force R in the strips at the failure surface, eq. 4.6 holds. If we substitute eq. 4.6, 4.11, and 4.14 into eq. 4.10 and simplify, we have

$$\frac{2bnf^*\left(\left(L - \frac{h}{\tan\alpha}\right)\sum_{i=p}^{q} y_i + \frac{1}{\tan\alpha}\sum_{i=p}^{q} y_i^2\right)}{L(h - \tfrac{1}{2}L\tan\alpha)} + \tan(\phi-\alpha)$$

$$+ \frac{(h - L\tan\alpha)^2 K_{AE}}{2L(h - \tfrac{1}{2}L\tan\alpha)}\left(\sin\phi\,\tan(\phi-\alpha) - \cos\phi\right) - k_h = 0 \qquad \text{..(4.15)}$$

where the summation upper limit in eq. 4.6 is now q, the layer number of the highest layer of strips intersected by the failure surface. Note that there is no density dependence in eq. 4.15. Differentiation of this equation will not yield an explicit formulation for k_h or $\tan\alpha$. Brent's (1973) zero-finding algorithm was used in this work to locate the minimum k_h and the corresponding α.

4.4. Extension to two-step block structure.

The case for failure surface contained in the reinforced block for a two-step block structure is the same as that in Sec. 4.2 for the rectangular block structure. There are four other cases as shown in Fig. 4.3: case (2), bi-planar failure surface, running out the back of the top step of reinforcement; case (3), tri-planar failure surface, where there is a small trapped wedge below the

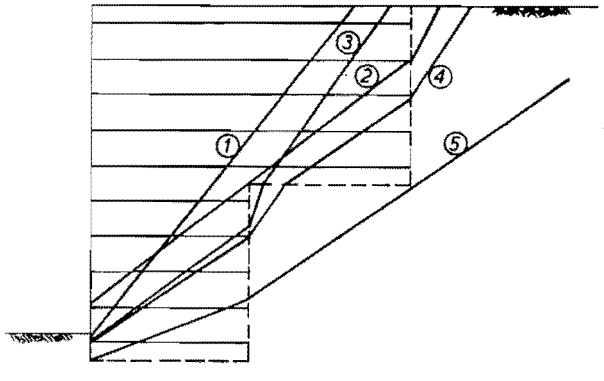

Fig. 4.3 Cases for two-step reinforced block.

top step of the block but the failure surface outcrop is contained in the reinforced block; case (4) where there is a trapped wedge as in (3), but the failure surface runs out the back of the top step as in (2); and case (5), bi-planar where the failure surface runs out the back of the lower step and does not re-enter the reinforced block.

Each case can be analyzed in a similar way to that shown above. Following is a summary of the analysis for case 4 in Fig. 4.3. Assumptions i) to x) above, as well as the following are made (Fig. 4.4):

xi) the trapped wedge ABC can be treated as a M-O active block with a surcharge, in a similar way to the one at the surface behind the reinforced block, and

xii) the failure surface in the upper and lower portions of the failure block make the same angle with the horizontal, α. This is a

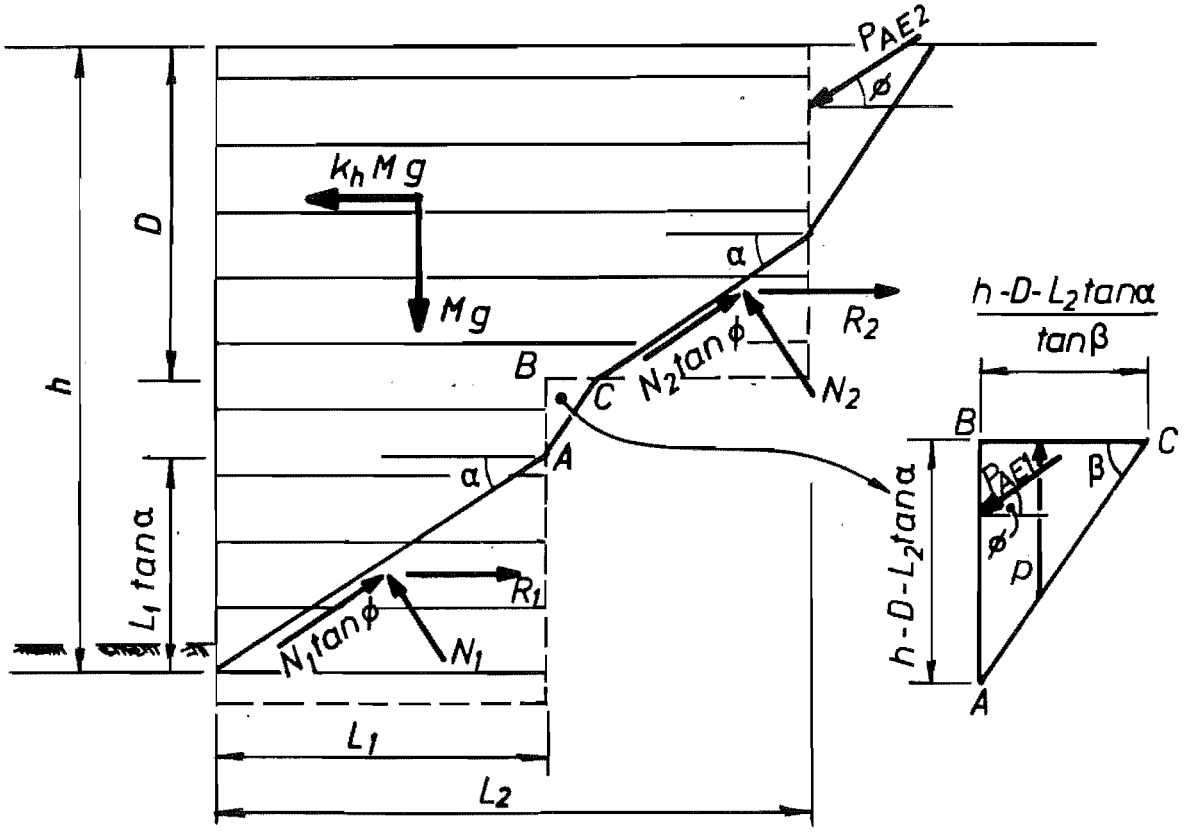

Fig. 4.4 Case 4 (Fig. 4.3) for two step structure.

simplifying assumption that removes a variable from the equations and allows solution. The observations of failure surface in this study support this assumption (see section 6.3.2).

The mass of the reinforced failure block is

$$Mg = \rho g(hL_1 - \tfrac{1}{2}L_1^2\tan\alpha + D(L_2-L_1) - (L_2-L_1 - \frac{h - D - L_1\tan\alpha}{\tan\beta})^2\tfrac{1}{2}\tan\alpha) \quad \ldots\ldots\ldots\ldots(4.16)$$

Assuming the reinforced block acts like a rigid wall, the M-O forces P_{AE1} and P_{AE2} on it are

$$P_{AE1} = \tfrac{1}{2}\rho g(h - D - L_1\tan\alpha)^2K_{AE} \quad \ldots\ldots\ldots\ldots\ldots\ldots\ldots\ldots(4.17)$$

$$P_{AE2} = \tfrac{1}{2}\rho gK_{AE}(D - (L_1-L_2 - \frac{h - D - L_1\tan\alpha}{\tan\beta}\tan\alpha))^2 \quad \ldots\ldots\ldots(4.18)$$

To calculate the vertical force p exerted by the trapped wedge ABC on the underside of the top part of the reinforced block, we can use Meyerhof theory, which has been found to represent foundation pressures in reinforced earth

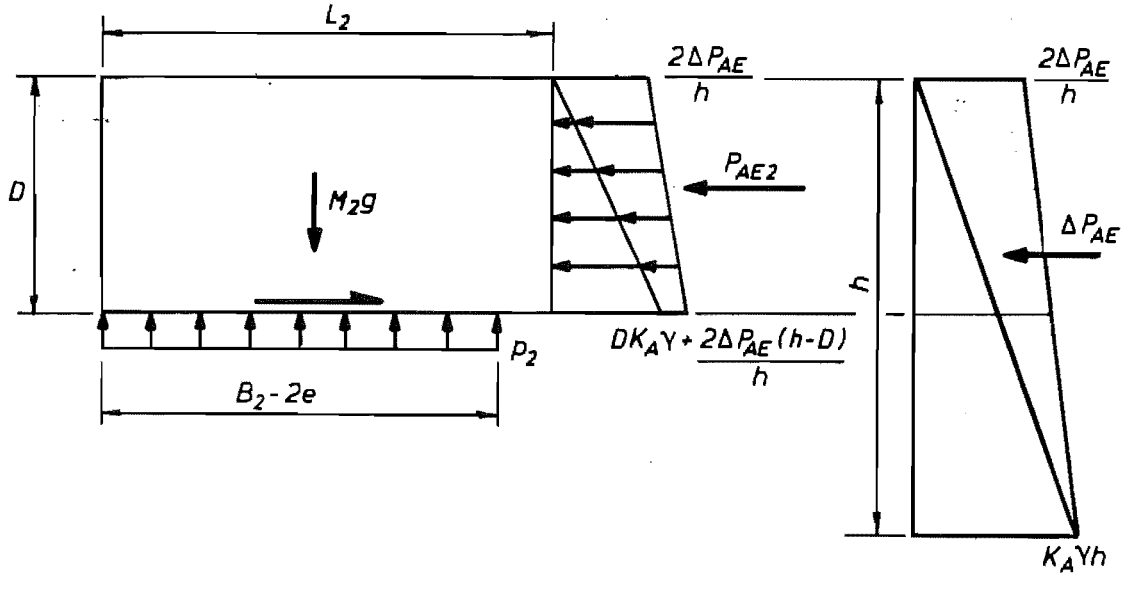

Fig. 4.5 Loads on a slice consisting of the top half of a wall.

quite well (Meyerhof, 1953; Verge and Reid, 1976). Considering a slice consisting of the top half of the wall, Fig. 4.5, the mass of the slice is

$$M_2 g = L_2 D\gamma \qquad \text{.....(4.19)}$$

MWD (1980) in fact limit the L_2 term in eq. 4.19 to the smaller of L_2 and H, the overall wall height. No reason or reference is given, although it is believed to result from observations of full size RE walls. The effect will be to reduce the pressure force p (Fig. 4.4, eq. 4.25 below) for walls with long strips in the top layer. The analyses in §6.11 use this modification. The dynamic active force is

$$\Delta P_{AE} = \tfrac{1}{2}\gamma h^2 (K_{AE} - K_A) \qquad \text{.....(4.20)}$$

Taking moments about the base of the slice at the wall face, $M_2 g$ has moment

$$M(M_2 g) = L_2^2 D\gamma/2 \qquad \text{.....(4.21)}$$

and the active force has moment

$$M(P_{AE2}) = \frac{\Delta P_{AE} D^2}{h} + (DK_A\gamma - \frac{2D\Delta P_{AE}}{h^2})\frac{D^2}{6} \qquad \text{.....(4.22)}$$

Then the width $B_2 - 2e$ is given by

$$B_2 - 2e = \frac{2(M(M_2 g) - M(P_{AE2}))}{M_2 g}$$

$$= \frac{L_2^2\gamma - \frac{2D\Delta P_{AE}}{h} + (K_A\gamma - \frac{2\Delta P_{AE}}{h^2})\frac{D^2}{3}}{L_2\gamma} \qquad \text{...(4.23)}$$

and the pressure p_2 is then

$$p_2 = \frac{M_2 g}{B_2 - 2e} \ \text{N/m}^2 \qquad \text{.....(4.24).}$$

The force p on the element in Fig. 4.4 is thus

$$p = \frac{M_2 g}{B_2 - 2e} \frac{(h - D - L_1 \tan\alpha)}{\tan\beta} \quad \text{N/m run of wall.} \qquad \ldots\ldots\ldots(4.25)$$

Note that ΔP_{AE} is dependent on the density of the soil (eq. 4.21), so every term in eq. 4.23 contains density dependence, which will cancel. Thus eq. 4.24 retains γ in the numerator only.

Considering horizontal and vertical forces equilibrium, and eliminating N_1 and N_2, we get

$$k_h Mg - (Mg - p)\tan(\phi-\alpha) - (P_{AE1} + P_{AE2})(\sin\phi\tan(\phi-\alpha) - \cos\phi) + R_1 + R_2 = 0 \qquad \ldots\ldots(4.26)$$

where R_1 is the total force in the reinforcing strips in the bottom step and R_2 is the force in the strips in the top step of the structure, at the failure surface. Both can be found using eq. 4.6 modified to sum over the relevant part of the structure. K_{AE}, required in the calculation of P_{AE1} and P_{AE2}, can be found using eq. 4.13. Note that eq. 4.13 contains $\theta = \tan^{-1} k_h$. Differentiating eq. 4.26 with respect to $\tan\alpha$ and setting to zero to find a minimum k_h does not produce an equation explicit in k_h. Brent's (1973) zero-finding algorithm can be used on eq. 4.26, with graphical or double iteration (on α) techniques to locate the minimum k_h. Note also that each term in eq. 4.26 contains γ so it can be cancelled out, and again k_h is independent of density.

4.5. Modifications to the formulation.

In the formulation outlined above the effective resistant force in the reinforcing strips at the failure surface is in the direction of the strips before any movement takes place. Once the wall has moved a little the direction of action of R will move towards lying in the failure surface. This can easily be included in the formulation from the horizontal and vertical force equilibrium stage. Bracegirdle (1979) considered this modification.

4.6. Calculation of displacement.

There are several methods proposed in the literature to calculate displacements of earth dams and embankments due to seismic excitation. Most start with the Newmark (1965) sliding block analogy, whereby restraining forces are much larger in one direction than the other (assuming plane strain). Thus the assumption is made that displacement can occur in the outward direction only. Newmark stated that during an event the factor of safety of an embankment may momentarily fall below 1 due to transient stresses. The structure will not fail but all or part of it will develop some permanent displacement during the episodes when the factor of safety is below one, and the displacement during an earthquake event is the sum of all such displacements. It is important to have an estimate of the magnitude of these permanent displacements. In the case of earth dams, displacements will give an indication of the likelihood of overtopping and its attendant damage to property and life downstream. In other cases, provision can be made to accommodate displacements without loss of serviceability. Also, by allowing some displacement, the structure is likely to be less conservative in design and thus usually more economic to build.

Reinforced earth walls behave in a similar way. The resistance to movement into the fill is very much higher than for outward movement, and walls move outwards in small increments during earthquake excitation. Thus the same or similar methods should be applicable to calculate displacements.

Newmark (1965) calculated displacements by integrating the time history of acceleration during an earthquake, assuming that movement occurred when the acceleration in one direction exceeded a yield acceleration. This is still the "exact" method against which other methods are tested. (See, for example, Lin and Whitman, 1986.) To predict displacements for a new facility, several recorded and/or simulated ground motions must be checked. It is then important to consider the uncertainty of the predicted motions as well.

Makdisi and Seed (1978) incorporated an elastic analysis into the method, by saying the displacements should be calculated using the predicted elastic response time history of the structure, assuming no permanent movement. They assume that the elastic and plastic responses of the structure can be

decoupled. Lin and Whitman (1983) examined the effect of the decoupling assumption and found that the displacements calculated were conservative, especially near resonance.

Three methods to calculate permanent displacements are described below and are to be checked against the displacements observed in the testing in section 6.10.

4.6.1. Equivalent pulse technique (Sarma, 1979).

Consider a rigid block sliding on a sloping surface as depicted in Fig. 4.6. When the ground acceleration Kg > k_hg the driving force downslope is

$$D = W[\sin\beta + K\cos(\beta-\theta)] \qquad .....(4.27)$$

and the resisting force is

$$R = W[\cos\beta - K\sin(\beta-\theta) - u_f a/W]\tan\phi' \qquad ....(4.28)$$

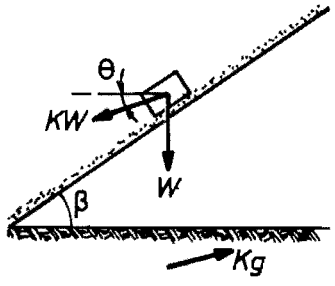

Fig. 4.6 Rigid block on a sloping surface (Sarma 1975).

where u_f is the pore pressure at failure, and a is the base area of the block. Sarma assumes u_f does not change during movement and derives an expression for it, using the Mohr-Coulomb failure criterion, Skempton's equation (1954) ($\Delta u = B[\Delta\sigma_3 + A(\Delta\sigma_1 - \Delta\sigma_2)]$), and limiting equilibrium analysis based on the sliding block analogy (Fig. 4.6):

$$u_f = W\{[\cos\beta - k_h\sin(\beta-\theta)] - [\sin\beta + k_h\cos(\beta-\theta))]\cot\phi'\}/a \qquad .....(4.29)$$

Thus the base area of the block a cancels out of eq. 4.28. The acceleration A_b of the block relative to the plane surface is then

$$A_b = (D-R)g/W \qquad .....(4.30)$$

Substituting eq. 4.27, 4.28 and 4.29 in 4.30, Sarma gets

$$A_b = \frac{\cos(\beta-\theta-\phi')}{\cos\phi'}(K - k_h)g \qquad \text{.....(4.31)}$$

the solution of which depends on the variation of K with time. The equivalent pulse shape of the earthquake pulses will thus have an effect, which was investigated as follows.

For a rectangular pulse of duration T/2 and amplitude K_m (Fig. 4.7), the solution of eq. 4.31 is

$$\frac{4x_m}{K_m g T^2}\left[\frac{\cos\phi'}{\cos(\beta-\theta-\phi')}\right] = \tfrac{1}{2}(K_m/k_h - 1) \qquad \text{.....(4.32)}$$

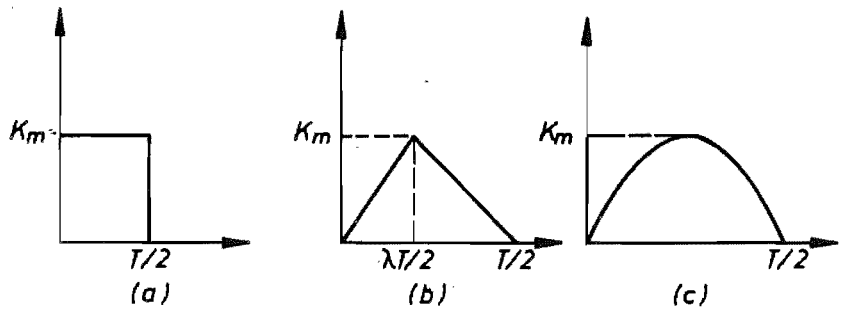

Fig. 4.7 Rectangular, triangular, and half sine pulses (Sarma 1975).

where x_m is the total displacement down the slope.

For a triangular pulse of duration T/2 and amplitude $K_m g$ (Fig. 4.7), solution of eq. 4.31 gives

$$\frac{4x_m}{K_m g T^2}\left[\frac{\cos\phi'}{\cos(\beta-\theta-\phi')}\right] = \frac{4(1-k_h/K_m)(1-\lambda k_h/K_m) - [1-\lambda(k_h/K_m)^2]}{24k_h/K_m}$$

$$= \{(1 - k_h/K_m)^3[2 - 2\sqrt{(1 - \lambda)} - \lambda]\}/6 \qquad \text{.....(4.33)}$$

for $0 \le k_h/K_m \le [1-\sqrt{(1-\lambda)}]/\lambda$

for $[1-\sqrt{(1-\lambda)}]/\lambda \le k_h/K_m \le 1$

and for a half sine pulse,

$$\frac{4x_m}{K_m g T^2}\left[\frac{\cos\phi'}{\cos(\beta-\theta-\phi')}\right] = \frac{(k_h/K_m - \sin q)^2}{2\pi^2 k_h/K_m}$$

$$\text{for } 1 \geq k_h/K_m \geq 0.725$$

$$= [k_h/K_m + \alpha - \pi + \cos^2(\alpha/2)\cot(\alpha/2)]/\pi^2 \qquad \ldots.(4.34)$$

$$\text{for } 0.725 \leq k_h/K_m \leq 0$$

where $q = \alpha + k_h/K_m(\cos\alpha - \cos q)$ and $\alpha = \sin^{-1}(k_h/K_m)$.

The solution for earthquake records is obtained by assuming piecewise linear acceleration, with movement only allowed downhill. By piecewise linear acceleration it is meant that an earthquake record can be assumed to consist of many pulses, which can be further assumed to be of one of the shapes shown in Fig. 4.7 and that there are no discontinuities (it is linear). By adding the displacements calculated for each such pulse inducing downhill movement, the displacement for the earthquake can be found. T is the predominant period obtained from the earthquake acceleration spectrum, and K_m is the maximum acceleration. Fig. 4.8 shows values for eqs. 4.32, 4.33, 4.34 and several earthquakes plotted. For the triangular pulse, λ is chosen as 0.5 (eq. 4.33). It is seen on Fig. 4.8 that for higher k_h/K_m, the earthquake records are close to the triangular pulse curve. For small k_h/K_m the number of pulses in the earthquake record seems more important, though the displacement calculated is still bounded by the rectangular pulse curve. Thus for $k_h/K_m > 0.5$, Sarma recommends the triangular pulse curve, and for $k_h/K_m < 0.5$, the rectangular pulse curve, to predict displacements. How to handle the discontinuity at k_h/K_m is not stated. Use of the pulse shape curves seems

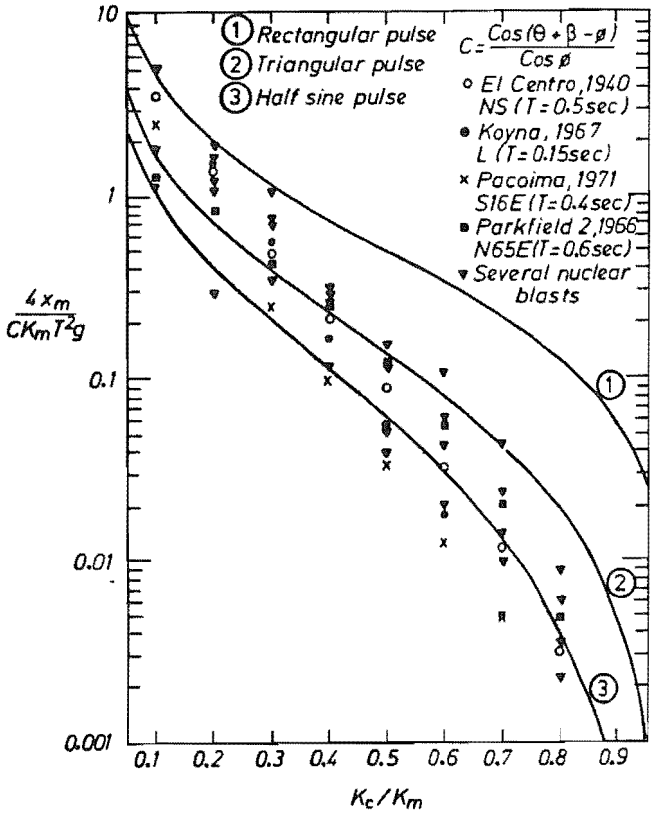

Fig. 4.8 Variation of dimensionless displacement with k_h/K_m (Sarma 1975).

to be an attempt to make the method independent of any actual earthquake records by, in effect, simulating earthquake pulses of different shapes.

The effect of θ, the direction of the inertia force, in eqs. 4.32, 4.33 and 4.34 was investigated by Sarma, and found to be minor. Thus vertical acceleration can be ignored and the inertia force taken as horizontal. Also given is a treatment of the effect of excess pore pressures. For reinforced earth structures, however, it is assumed (and indeed required for the development of friction between the soil and backfill) that the structure is well drained and thus the development of excess pore pressures during seismic shaking should have little effect. The validity of this assumption is something that needs investigating further.

4.6.2. Standardized displacements by double integration (Newmark, 1965).

Franklin and Chang (1977) extended the database for Newmark's charts (1965). Newmark had used double integration of four earthquake records to calculate displacements. The displacements were then standardized by scaling them to the value expected from the various earthquakes if they had a maximum acceleration A_{max} of 0.5g and maximum velocity V_{max} of 30 in/sec (762mm/sec). Such standardization was said to allow direct comparison of displacements calculated from records with a wide variety of A_{max} and V_{max}.

Scaling could be done in two ways: scale the earthquakes before integration, or multiply the calculated displacements by a factor. There is less work if we scale the displacements. Franklin and Chang explain that scaling is equivalent to (referring to an earthquake velocity record):

i) transforming the velocity axis, by scaling it such that the highest peak equals the desired maximum, and

ii) transforming the time axis such that the slope of the line representing peak acceleration has the desired value (ie. the desired maximum acceleration).

Thus using $V = At$ (velocity = acceleration x time),

$$\frac{V_s}{V} = \frac{A_s}{A} \cdot \frac{t_s}{t} \qquad \text{.....(4.35)}$$

where the subscript s indicates the scaled value. Then from u = Vt (displacement = velocity x time) and eq. 4.35,

$$\frac{u}{u_s} = \frac{V}{V_s} \cdot \frac{t}{t_s} = \frac{V^2 A_s}{V_s^2 A} \qquad \text{.....(4.36)}$$

and by rearranging eq. 4.36 and substituting for V_s (30 in/sec) and A_s (0.5g),

$$u_s = u \cdot \frac{1800A}{V^2} \qquad \text{.....(4.37)}$$

where A and V are the actual maximum values of acceleration coefficient (fraction of g) and velocity (inches/sec) in the earthquake record being integrated, and u is the displacement (in inches) calculated in the integration. u_s is then the standardized displacement, which Newmark plotted against k_h/A on log-log scales. (K_h is the yield acceleration of the sliding block, and A is the peak acceleration in the earthquake record being considered.)

Franklin and Chang extended the database of Newmark's charts using 169 horizontal and 10 vertical strong motion records from 27 earthquakes, and 10 synthetic accelerograms. Resistance to sliding was assumed rigid-plastic and non-symmetrical. That is, no movement occurred until the yield acceleration had been reached, then movement continued until the acceleration dropped below the yield acceleration, when movement stopped. Non-symmetrical resistance simply means that there is much greater resistance to movement in one direction than the other. Franklin and Chang in fact assumed that the resistance in the "uphill" direction was infinite, and thus there could be no reduction of permanent movement once it had occurred. This was said to represent the worst case. They computed velocities and displacements using the trapezoidal rule of integration. The earthquake records used were California Institute of Technology (CIT) baseline-corrected accelerograms.

With the results of their analyses they plotted u_s vs. k_h/A, as Newmark had done. They produced separate plots for rock sites, stiff-soil sites, and soft-soil sites, as well as for the synthetic accelerograms. Upper bound

curves from these plots were aggregated on one chart, which is reproduced in Fig. 4.9. They found that maximum displacements calculated from various accelerograms from the San Fernando earthquake of 1971 were about 1.5 times Newmark's maximum, and from synthetic records, about 1.7 times Newmark's upper bound. They also found that u_s was proportional to the duration of shaking (and hence the earthquake Richter magnitude), but the trend was weak and there was considerable scatter. u_s at rock sites were about 75% of that at soil sites for the same magnitude, A_{max} and V_{max}.

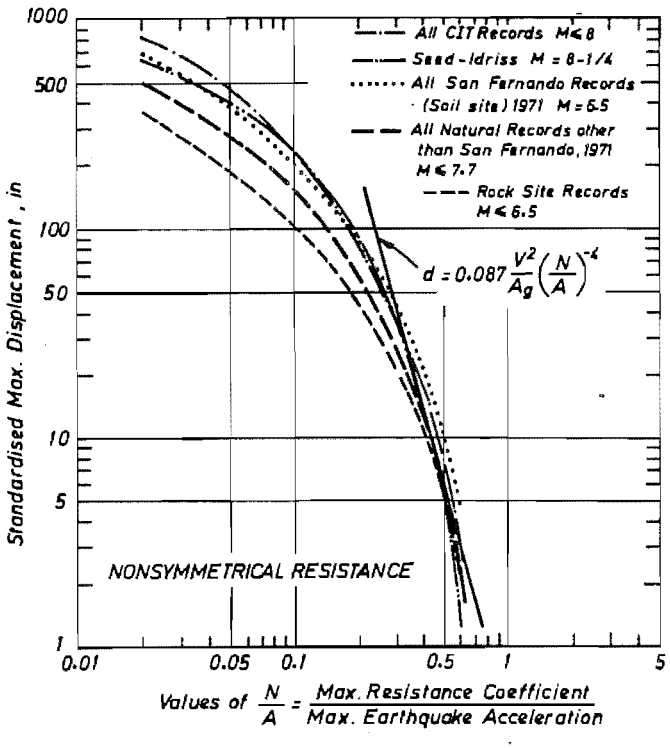

Fig. 4.9. Newmark's chart after Franklin and Chang (1977).

Richards and Elms (1979) took this chart (Fig. 4.9) and drew a suggested upper bound curve on it for the displacements of gravity retaining walls. Thus to obtain the maximum displacement expected of a design wall just enter the chart with a value of k_h/A, go up to the upper bound line, then across to the displacement scale and read off the displacement. This could then be scaled to the design earthquake characteristics A_{max} and V_{max} if necessary.

This same system should be usable for RE walls. The yield acceleration k_h would be calculated as in section 4.2, 4.3, or 4.4, and the displacement obtained off the chart would be scaled as necessary. See section 6.10.2 for discussion of the fitting of data from the present study on the chart, Fig. 4.9.

4.6.3. Random vibration theory (Lin and Whitman, 1986).

Lin and Whitman (1986) attempted to incorporate ground motion characteristics, as well as the physical mechanism of the displacement buildup, into their formulation. They point out that Franklin and Chang (1977) showed that even normalised motions resulted in widely scattered calculated displacements. The paper in fact derives the probability distribution of the expected displacement. Here we are only interested, in the first instance, in the expected displacement formulation.

First, we will obtain some characteristics of ground motion. Lin and Whitman draw heavily on Vanmarcke and Lai (1980) who described a model whereby a true non-stationary ground motion is transcribed into a fictitious zero-mean, Gaussian stationary motion of duration S. The Vanmarcke and Lai method decomposes an earthquake into the product of a stationary process with constant frequency content and a time-varying intensity function. The intensity function is taken as the simple case of a box function, so is characterised by a single parameter: the strong motion duration S (Lin, 1982). The power spectral density function, which describes how the energy per unit time, or power, of a ground motion is distributed over frequency, is used to calculate the characteristics of the motion, which are: the equivalent duration of strong motion, S; the predominant frequency, Ω; a bandwidth measure, δ; and the root-mean-square acceleration, σ_x.

The moments λ_i of the spectral density function $G(\omega)$ are:

$$\lambda_i = \int_0^\infty \omega^i G(\omega) d\omega \qquad \text{.....(4.38)}$$

where ω is the circular frequency at which the spectral density function takes the value $G(\omega)$. A measure of where the spectral density is concentrated on the frequency axis is

$$\Omega = \sqrt{(\lambda_2/\lambda_0)} \qquad \text{.....(4.39)}$$

(also called the central or predominant frequency) and a measure of the spread of frequency, or bandwidth, about Ω is

$$\delta = \sqrt{[1-\lambda_1^2/(\lambda_0\lambda_2)]} \qquad \ldots\ldots(4.40)$$

(Vanmarcke, 1976). Also,

$$\sigma_x = \sqrt{\lambda_0} \qquad \ldots\ldots(4.41)$$

Ω corresponds to period $T_0 = 2\pi/\Omega$.

The squared Fourier amplitude spectrum $A^2(\omega)$ of the ground accelerations shows how the total energy in the earthquake motion is spread over frequency. Its integral over frequency is a measure of the total motion energy, the Arias intensity I_o (Arias, 1970):

$$I_o = \int_0^{t_o} a^2(t)dt = \int_{-\infty}^{\infty} a^2(t)dt = \frac{1}{2\pi}\int_{-\infty}^{\infty} A^2(\omega)d\omega = \frac{1}{\pi}\int_0^{\infty} A^2(\omega)d\omega \qquad \ldots(4.42)$$

where $a(t)$ is the time history of acceleration of ground motion (zero for $t < 0$ and for $t > t_o$) and the third equality is Parseval's Theorem. The fourth equality is true since $a(t)$ is real, thus $A(\omega)$ is even ($A(-\omega) = A(\omega)$).

Note that Parseval's Theorem states

$\int_{-\infty}^{\infty} a^2(t)dt = 2\pi d_1^2 \int_{-\infty}^{\infty} A^2(\omega)d\omega$, where d_1 depends on the definition requirements. If we require that the energy computed in the time domain (from $a^2(t)$) is equal to the energy computed in the frequency domain (from $A^2(\omega)$), then $d_1 = 1/\sqrt{(2\pi)}$. If, however, we require that the Laplace transform, usually defined as

$$L[a(t)] = \int_{-\infty}^{\infty} h(t)e^{-st}dt = \int_{-\infty}^{\infty} h(t)e^{-(\alpha+jw)t}dt, \quad j = \sqrt{(-1)},$$

reduces to the Fourier transform when $\alpha = 0$, then $d_1 = 1/2\pi$, which is in contradiction to the previous definition (Brigham, 1974). Vanmarcke and Lai (1980) appear to have adopted the Laplace transform definition with Eq. 4.42. It seems more reasonable in this instance, however, that the equal-energy definition should be used. As the power spectral density is usually calculated from the squared Fourier transform of the data, there will be a difference of $1/2\pi$ between values calculated in the two ways. Looking at Eq.

4.39, there will be no effect as the constant of proportionality will cancel out between λ_0 and λ_2. The same will occur in Eq. 4.40, as it appears twice in the numerator (λ_1^2) and twice in the denominator ($\lambda_0\lambda_2$). There may be some bias in the value of σ_x arrived at from Eq. 4.41, though. This is further discussed in Appendix D, along with details concerning calculation of the spectral density function.

Now we assume that the total ground motion intensity I_o is distributed uniformly at constant average power σ_x^2 over the duration of strong motion S, thus:

$$I_o = S\sigma_x^2 \qquad \text{.....(4.43)}$$

To estimate S and σ_x, we assume a relationship exists between the actual maximum acceleration A_{max} and σ_x, which will be probabilistic in nature. From the theory of stationary Gaussian random processes, there is a prediction of the most probable value of the peak factor $r=A_{max}/\sigma_x$ which is exceeded once on the average during the interval S. This corresponds to a probability of e^{-1} of not being exceeded during S:

$$r = \frac{A_{max}}{\sigma_x} = \begin{cases} (2\ln(2S/T_o)) & S \geq 1.36T_o \\ 2 & S \leq 1.36T_o \end{cases} \qquad \text{.....(4.44)}$$

where S/T_o is the number of cycles during S. Eq. 4.44 is derived on the assumption that the crossings of a specific relatively high threshold occur as a Poisson arrival process (Vanmarcke, 1975). The lowest peak factor permitted is 2, the ratio between the amplitude and the rms value for a simple sinusoid.

Assuming T_o is known, we can solve eq. 4.43 and 4.44 simultaneously, giving an implicit expression for S:

$$S = r^2\frac{I_o}{A_{max}^2} = \begin{cases} [2\ln(2S/T_o)](I_o/A_{max}^2) & S \geq 1.36T_o \\ 2I_o/A_{max}^2 & S \leq 1.36T_o \end{cases} \qquad \text{....(4.45)}$$

The relation I_o/A_{max}^2 can easily be computed for any earthquake record, remembering that A_{max} is determined for one direction only. An approximate explicit solution for S can be obtained assuming that the peak factor r is constant. Vanmarcke and Lai (1980) found that $r=2.74$ is a reasonable value, from a study of some 140 recorded ground motions. Then

$$S = (2.74)^2 I_o/A_{max}^2 \approx 7.5 I_o/A_{max}^2 \qquad \text{.....(4.46)}$$

and substituting eq. 4.46 in eq. 4.45,

$$S = 2\ln\left(\frac{15 I_o}{T_o A_{max}^2}\right) \frac{I_o}{A_{max}^2} = [5.42 - 2\ln T_o + 2\ln(\frac{I_o}{A_{max}^2})] \frac{I_o}{A_{max}^2} \qquad (4.47)$$

Use of the less exact formulation for S is generally acceptable because the probability of exceedance of the peak factor r is chosen somewhat arbitrarily as e^{-1}. If it was 0.5, the top part of eq. 4.45 would become $(2\ln(2.8S/T_o))$ (provided it is not smaller than 2). Within the range of S/T_o of practical interest (1.3-500), this would lead to an increase in S of about 10%. (Vanmarcke and Lai, 1980.)

We now have sufficient information to calculate the earthquake ground motion characteristics. We could do this for simulated motions as well. For example, Lin and Whitman suggest the Kanai-Tajimi spectral density function, $G_x(\omega)$, for a site with ground damping λ_g and ground natural frequency ω_g:

$$G_x(w) = \frac{G_0 [1 + 4\lambda_g^2 (\frac{\omega}{\omega_g})^2]}{[1 - (\frac{\omega}{\omega_g})^2]^2 + 4\lambda_g^2 (\frac{\omega}{\omega_g})^2} \qquad \text{.....(4.48)}$$

where G_0 is a constant. It can be found from a knowledge of σ_x using, for example, (compare eq. 4.38 and 4.41)

$$\sigma_x^2 = \int_0^\infty G(\omega) d\omega \qquad \text{.....(4.49)}$$

and effectively scales the function to match the energy in the ground motion.

We can now return to Lin and Whitman's formulation for the conditional expected permanent displacement. For the rectangular pulse shown in Fig. 4.10 sliding will start at time t=0 and stop at t=t_0 where $t_0 = AT/(k_h+A)$, and the displacement d_i for cycle i is

$$d_i = \frac{A^2T^2}{k_h+A} - \frac{A^2T^2}{4A} - \frac{A^2T^2}{\frac{2(k_h+A)^2}{A}} - \frac{A^2T^2}{2(k_h+A)^2/k_h}$$

$$= \frac{A^2T^2}{2k_h} g_1\left(\frac{k_h}{A}\right)$$

$$= \frac{A^2}{2k_h\Omega^2} g_2\left(\frac{k_h}{A}\right) \qquad \text{.....(4.50)}$$

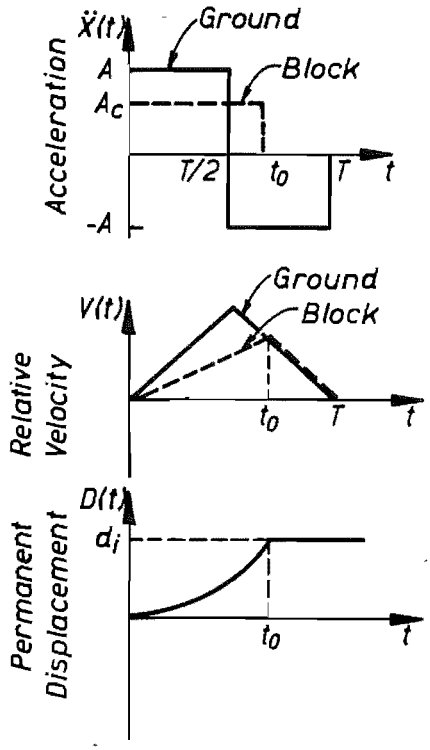

Fig. 4.10 Permanent displacement caused by one cycle of excitation (Lin and Whitman, 1986).

where only g_1 depends on the shape of the pulse and $g_2 = (2\pi)^2 g_1$. If the probability density function of the pulse amplitude A is $f_A(A)$ then the expected value of d_i is

$$E(d) = \int_0^\infty \frac{A^2}{2k_h\Omega^2} g_2\left(\frac{k_h}{A}\right) f_A(A)\,dA \qquad \text{.....(4.51)}$$

where the subscript i is dispensed with as all displacements d_i are equal. Since $f_A(A)$ decays rapidly, we can integrate this numerically (ie. in a finite number of steps with little loss of accuracy). Using the Gaussian integration scheme, and choosing the integration points A_i in terms of σ_x and combining g_2 and f_A into g_3,

$$E(d) = \frac{\sigma_x^2}{2k_h\Omega^2} g_3\left(\frac{k_h}{\sigma_x}\right) \qquad \text{.....(4.52)}$$

where g_3 remains to be determined.

If the excitation is narrow-band there will be slip every time there is an upcrossing at the k_h level in the excitation. Hence the expected number

of slip events E[N(S)] is found by multiplying the upcrossing rate ν_{r}^{+} at $r=k_h/\sigma_x$ by the duration S. For Gaussian excitation (which we have transformed our earthquake motion into), the upcrossing rate is

$$\nu_{r}^{+} = (1/2\pi)\sqrt{(\lambda_2/\lambda_0)}\exp\{-k_h^2/2\lambda_0\}$$

$$= \frac{\Omega}{2\pi}\exp(-\frac{r^2}{2}) \qquad \text{.....(4.53)}$$

We still need to identify the pulse shape (and hence g_s) which is quite difficult, and $\nu_{r}^{+}.S$ may not be a good representation of the expected number of slippage events. An intuitive corrective factor $f(\delta)$ is introduced, because the bandwidth δ affects both the pulse shape and the upcrossing rate. The expected number of slip events, E[N(S)], is kept intact assuming decoupling. Hence

$$E(d) = \frac{\sigma_x^2}{2k_h\Omega^2}\, g(\frac{k_h}{\sigma_x})\, f(\delta) \qquad \text{.....(4.54)}$$

Using simulations Lin and Whitman found that

$$f(\delta) = 1 + 7.11(\delta - 0.2)^2 \qquad \text{for} \quad 0.2\leq\delta\leq0.8 \qquad \text{.....(4.55)}$$

and that the function g is as in Fig. 4.11. For k_h/σ_x between 0 and 0.1, they suggest linear interpolation. Thus the expected conditional permanent displacement can be expressed as

$$E(D\,|\,k_h,\sigma_x,A_{max},\Omega,\delta) = \nu_{r}^{+}S\frac{\sigma_x^2}{2k_h\Omega^2}\, g(\frac{k_h}{\sigma_x})\, f(\delta) \qquad \text{.....(4.56)}$$

This model was derived using simulated motions. To check its accuracy, Lin and Whitman calculated the displacements for 140 recorded ground motions, and compared them with displacements calculated directly with time domain double integration. A_{max} for each record was scaled to 0.5g (σ_x was scaled accordingly). Two levels of yield acceleration were used, k_h/A_{max} = 0.1 and k_h/A_{max} = 0.5. Prediction was good with points scattered evenly on both sides of the 45° line in both graphs (Fig. 4.12 and 4.13). One point in Fig. 4.13 (circled) is well away from the line, and it turned out that that motion had

only one peak greater than the yield acceleration, whereas the Gaussian assumption in the ground motion modelling assumes there are 3.2.

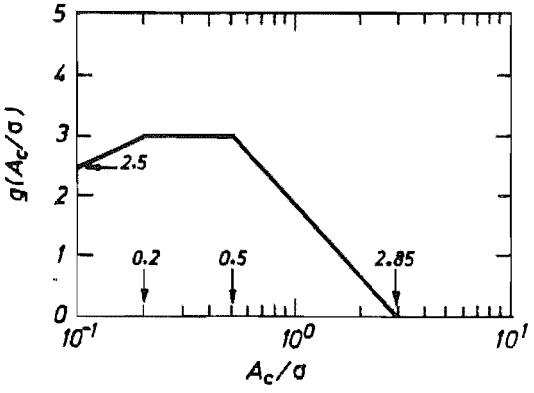

Fig. 4.11 Plot of function $g(k_h, \alpha)$ (Lin and Whitman 1986).

If we draw two lines on Fig. 4.12 and 4.13 parallel to the 45° line and including most of the plotted points, they will provide an indication of the spread exhibited in the predicted displacements compared to the calculated displacement (which is assumed to be "correct"). The lines on Fig. 4.12 show that the displacement may easily be a factor of about 1.6 different from the predicted value, for k_h/A_{max} = 0.1. On Fig. 4.13 they show that the range is the predicted value times or divided by a factor of about 2, for k_h/A_{max}=0.5. So we could use the upper lines as an upper bound on the conditional expected displacement.

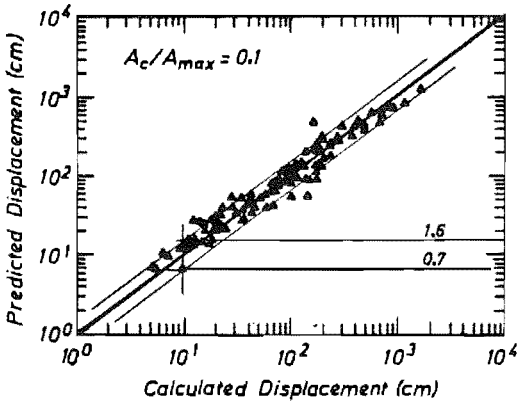

Fig. 4.12 Comparison of predicted and calculated permanent displacements at k_h/A_{max} = 0.1 level (after Lin and Whitman, 1986).

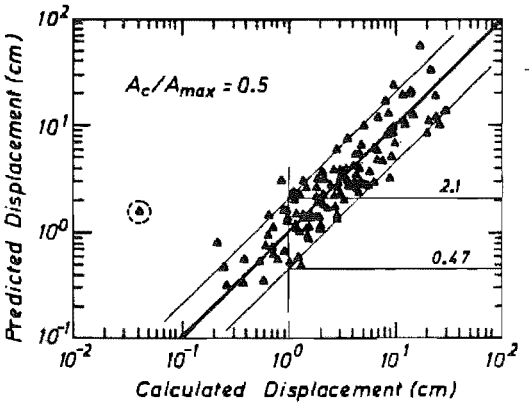

Fig. 4.13. Comparison of predicted and calculated permanent displacements at k_h/A_{max} = 0.5 level (after Lin and Whitman, 1986).

4.7. Requirements to verify the system.

There are essentially four areas that need verifying with test or field evidence:

i) failure mode and geometry. Nagel (1985) found that the method seemed to be able to predict the failure surface angle to the horizontal reasonably

well, at his small model scale. The failure mode (planar failure surface) was also verified, and others (see Chapter 2) have found that R/E walls move outwards while remaining more or less vertical. Japanese work apparently indicated an active block like that shown in Fig. 3.10, which is different to that found by Nagel and assumed in this analysis. The actual Japanese paper has not been seen so it is not known what the test conditions were that indicated such a surface.

ii) force distributions in the strips. There is no information about the location of the maximum forces in the strips under seismic loading. In the static case the locus of maximum forces coincides more or less with the failure surface observed in model tests (McKittrick 1978). The method outlined above ignores the force in the strips between the failure surface and the wall facing, but does tacitly assume that the force distribution in the resistant zone is linear and maximum at the failure surface. Allied with force distributions is the lack of information about the force in the strips within the active zone, and especially in those strips high in the wall that do not intersect the failure surface. Separate consideration needs to be given to these forces.

iii) cutoff (or yield, or critical) acceleration. Nagel did not observe a clear-cut yield acceleration in many of his tests. Mostly, although the response acceleration was less than the input acceleration during movement, it was not constant as predicted in the Newmark (1965) sliding block analogy. Plateaux of sorts could be seen in 3 tests, but only in one test, the last, did he observe a clear acceleration plateau in the wall response, and that was after the failure surface had completely formed. (See Table 2.1.) Where there was a cutoff acceleration observed it was in reasonable agreement with the prediction.

iv) magnitude of displacements vs. input accelerations. Sommers and Wolfe (1984) concluded that displacements depended on the static factor of safety, the peak base acceleration, the ratio of wall fundamental frequency to input frequency, and the type of motion, specifically on the number of acceleration peaks greater than the yield acceleration. They also found that the yield acceleration was a function of the static factor of safety (and hence the reinforcement geometry, roughness and quantity, and backfill shear strength), and could be determined independently of the earthquake ground motion (for their model tests using dry sand backfill).

Lin and Whitman (1980) give an approximate method relating k_h to the static factor of safety for an earth dam, taken from Sarma and Bhave (1974): $k_h = (FS - 1)g/3.33$. It is used in the context of finding the probability distribution of k_h. In the displacement formulations above, Lin and Whitman consider all the other important variables identified by Sommers and Wolfe, except the frequency ratio. If the Kanai-Tajimi spectral density function is used, rather than some recorded or synthetic earthquake motions, there is input of the ground natural frequency and damping which could be set to those of the structure to wall, according to Lin and Whitman. The effect of ω_g, however, is that it acts rather like the derived Ω in the Lin and Whitman method, and is the approximate central frequency of the K-T spectral density function. Thus it is more for positioning the spectrum on the frequency axis than for including site parameters.

Sarma (1975) considers only the peak acceleration (his K_m factor), although by using some recorded motions there is some effect from the type of motion (number of peaks greater than the yield acceleration). His yield acceleration is calculated from an expression derived using limit equilibrium principles, assuming a factor of safety of one on the failure surface. There is provision for the Skempton pore pressure parameters A and B, and there is a possible experimental set-up outlined to find the effect of earthquake shaking on A in particular, and hence on k_h. The input base acceleration can be calculated using a relationship from Ambraseys and Sarma (1967). Fundamental period and depth in the embankment were found there to affect the distribution of maximum accelerations (or conversely, of magnification factors) in a dam. No such analysis has been done for R/E walls.

CHAPTER 5

DESCRIPTION OF TESTING

5.1. Introduction.

The purposes of the testing were to:

i) verify the failure surface shape (planar or bi-planar) at a larger scale than Nagel (1985) had used, ie. check for scale effect;

ii) verify the existence of the yield acceleration, the level of input base acceleration above which the wall will move relative to the ground. Nagel's testing was inconclusive in that the yield acceleration before the failure surface outcropped at the fill surface was not clear;

iii) observe the response of walls to earthquake motions. This was not possible with the system used by Nagel;

iv) observe forces in the reinforcing strips; and

v) observe the magnitudes of wall displacements caused by base accelerations.

In other words, the testing program was, most importantly, designed to verify the applicability of the limiting equilibrium formulation at a larger scale than was used in previous testing. Measuring the strip forces would allow checking of the force formulation proposed in Chapter 4, and would also allow investigation of the soil-strip friction mobilised during seismic shaking of a model RE wall. Observing wall permanent displacements would allow comparison with the three displacement prediction systems outlined in Chapter 4. And by chosing to use a shaking table, the response of model walls to recorded earthquake motions could be observed pulse by pulse.

With these objectives in mind, it was decided to test a series of 1m. tall walls on the Department of Civil Engineering shaking table. The primary

criteria in the choice of this size were the requirement to measure the reinforcing strip forces, and also that it was close to the maximum that could be handled with existing facilities. The strip forces should be well above the levels of noise on any electronic data recording system. The scale of the instrumentation would be small compared to the elements they are attached to so should not effect the measured forces. Use of the shaking table was necessary to enable tests with digitized earthquake motions, and also to handle the load of the test rig: some 15 tonnes with a model in place. This scale was 2.5 times that used by Nagel, thus satisfying objective i) above. Finally, the logistics of handling the quantity of sand necessary for a model of this size (some 11 tonnes) was felt to be acceptable.

An important consideration in dynamic modelling in soil mechanics is that of dynamic similitude. It is discussed in the next section (5.2), along with the only attempt at a similitude study seen for RE walls (Hornbeck, 1982). Section 5.3 outlines the equipment, methods and procedures used in the testing of six model reinforced earth walls in this study. More detail on some items is contained in Appendix A. Section 5.4 discusses testing for shear strength parameters for use in the limiting equilibrium formulation described in Chapter 4. The tests were to establish values for soil angle of internal friction ϕ and the coefficient of soil-strip friction f^*.

5.2. Dynamic modelling and similitude.

5.2.1. Introduction.

The primary reason for using scale models to study the behaviour of systems is that of economics. It costs only a small fraction of the amount to test a model as it does to test a full size system. In laboratory tests of scale models we thus try to predict quantitatively the behaviour of the prototype from measurements on the model (Kerisel, 1967). To do this the model must be scaled down correctly from full size.

The method of scaling is through the use of dimensionless products, called Pi-numbers. The process of arriving at these products is called di-

mensional analysis. Langhaar (1951) says that the application of dimensional analysis is based on the assumption that the behaviour of a system is governed by a specific set of independent variables, and all others (except the dependent variable) are redundant or irrelevant. Langhaar also points out that it is based on the hypothesis that the solution of a problem can be expressed in terms of a dimensionally homogeneous equation in terms of the specified variables.

In dimensional analysis, first the laws affecting behaviour of the prototype are identified, and the variables involved specified. The second step is to form a set of dimensionless products from the specified variables. Once a set of dimensionless products has been formed, any other set can be derived from the first set. Each product is independent of the others, which means that it cannot be derived from powers of the others in the set. This usually means that each Pi-number contains one particular variable that does not appear in any other Pi-number. Langhaar gives a matrix-based algorithm to derive dimensionless products from a set of specified variables. The net result of dimensional analysis, Langhaar says, is a reduction in the number of variables, which effectively amplifies the information that can be obtained from a few experiments.

If there are n variables in a problem, there are $n-r$ dimensionless products among them. Langhaar points out that usually r is the number of fundamental dimensions in the problem, but is better defined as the maximum number of the n variables that will not form a dimensionless product.

With reference to modelling, Langhaar defines completely similar as meaning that all the dimensionless variables have the same value for model and prototype. He describes three further divisions of similarity: geometric similarity, where model and prototype have the same shape; kinematic similarity, literally "similarity of motions", which means that corresponding components of acceleration or velocity are similar; and dynamic similarity, where homologous parts of systems experience similar net forces. It was shown that dynamic similarity exists if systems are kinematically similar and mass distributions are similar. "Homologous" is used to mean "corresponding", hence homologous points means points on the model and prototype that correspond,

and homologous times are instants that occur at the same fraction of a cycle in model and prototype.

Scale effects are said to arise when forces that have no effect in the prototype have a significant effect in the model, or vice versa. The best guard against scale effect is thus to build large models.

"Model laws" are the relationships between dimensions derived by equating Pi-numbers. They can also be derived as the relationships between dimensionless products. An example used by Langhaar is that of an elastic system with a specified shape and loading. The stress σ at a specified point is then a function of a single force F, a single moment M, a length L, and Young's modulus E and Poisson's ratio ν: $\sigma = f(F,M,L,E,\nu)$. The single force and moment are used to represent the loads on the system. Similarly, the deflection u is a function of these variables: $u = f(F,M,L,E,\nu)$. Dimensional analysis of the relationships yields:

$$\sigma = \frac{F}{L^2} f_1\left(\frac{F}{EL^2}, \frac{M}{FL}, \nu\right), \qquad u = \frac{F}{EL} f_2\left(\frac{F}{EL^2}, \frac{M}{FL}, \nu\right)$$

From these equations the following general model law for statically loaded elastic structures is derived:

$$K_\nu = 1, \quad K_F = K_E K_L^2, \quad K_M = K_F K_L$$

$$K_\sigma = K_F / K_L^2 = K_E, \quad K_u = K_L$$

in which the K's are scale factors for the subscripted variable eg. K_F = force in the model / force in the prototype.

The first part of the following section discusses the theory of similitude relating to this study of RE walls. The second looks at the only attempt at a similitude study seen for RE walls, that of Hornbeck (1982).

5.2.2. Similitude theory and discussion relative to dynamic testing of model RE walls.

5.2.2.1. Similitude theory.

Schuring (1977)* states that there are six basic soil considerations in dynamic model studies of soil-structure systems:

1. the inertia of soil particles,
2. the friction between soil particles,
3. cohesion between soil particles,
4. soil weight,
5. soil elasticity, and
6. adhesion between soil and structure.

Schuring seems to ignore the effects of the pore fluid and the strength of the soil particles. Pore fluid effects may be extremely important in some instances, for example in seismic liquefaction of sands. In RE walls we try to ensure that the structure is well drained, and hence ignore pore fluid effects. Soil particle strength is ignored as well: it only becomes an issue for very weak soils or for very tall walls with high stresses in the soil. Looking at the six "basics", inertia must include the mass of the soil particles plus the accelerations they experience. Soil friction and cohesion have obvious implications, while the soil weight must include the density and acceleration due to gravity. Soil elasticity would include Young's modulus and Poisson's ratio, as well as whether the soil behaviour is linear or not. Adhesion between soil and structure seems to be meant to include friction between soil and structure if the soil does not stick to the structure.

Schuring points out that elastic and strain rate effects can be neglected if displacements are large ie. well into the inelastic range. Adhesion can be ignored if it is assumed that a layer of soil is stuck to the structure. Then only items 1 to 4 survive, plus compaction effects (quite large compaction-induced stresses can be "locked in" to the soil: Ingold, 1979, Aggour and Brown, 1974). Schuring derives the following dimensionless ratios, or Pi-numbers, for these 4 "basics", ignoring compaction effects:

from Newton's law of inertia, force $F \stackrel{d}{=} \rho L^3 L/t^2$, and because time $t \stackrel{d}{=} L/v$,

$$\pi_i = F/\rho L^2 v^2,$$

from Newton's law of gravitation, $F \stackrel{d}{=} \rho g L^3$, or $\pi_g = F/\rho g L^3$,
from Coulomb's law of cohesive force, $F \stackrel{d}{=} cL^2$, or $\pi_c = F/cL^2$, and
from Coulomb's law for internal friction force, $F \stackrel{d}{=} F\phi$, or $\pi_\phi = \phi$,

where F is a representative force, v is velocity, L is a representative length, ρ is the soil density, c is the soil cohesion, and ϕ is the soil angle of internal friction. The $\stackrel{d}{=}$ means "is dimensionally equal to". Note that ρ appears in π_i and π_g, and is difficult to separate from the acceleration of gravity in these relationships as given.

The following analysis generally follows that of Schuring. Let the length ratio $L_p/L_m = n$, where the subscript p means prototype and subscript m refers to the model. For soils, ϕ, c and ρ apply as a group to a particular soil, and cannot be separated, and hence for similar soils (model-prototype) π_g and π_c are in conflict ($F_p/F_m = n^3$ from π_g, and n^2 from π_c) and some violation of the modelling laws is necessary. For clay soils, with high cohesion, we can often breach π_g. Such soils also show little internal friction so π_ϕ can be neglected as well.

For cohesionless soils, we can neglect π_c. We can make a new π-term $\pi_2 = \pi_i/\pi_g$ which gives $L_p/v_p^2 = L_m/v_m^2$, or $t_p/t_m = \sqrt{n}$, ie. time runs $\sqrt{n}$ times as fast in the model as in the prototype. This is the time scale factor used by Wolfe et al (1978), as shown in section 2.2. Accelerations, with dimensions L/t^2, are then equal in prototype and model scales. From π_g, for similar soils under normal gravity, we have $F_p/F_m = L_p^3/L_m^3 = n^3$, and hence the stress ratio $\sigma_p/\sigma_m = n$. If strains are similar in the model and prototype (geometric similarity) this means that the ratio of Young's moduli is $E_p/E_m = n$, which is clearly impossible in a similar soil. Hence there is non-similarity in stresses, when gravity effects are dominant and modelling is done under normal gravity. If strains were kept small (well inside the linear elastic range), then strains in the prototype would scale at n as well, with a resulting loss of geometric similarity. This is why we must ensure elastic effects are small in modelling gravity-dominant situations.

If we consider elastic effects, ie. when external loads and forces are dominate over mass and inertia loads (Kerisel, 1967), we must have the stresses (and hence the various moduli, including Young's modulus E and the shear modulus G, which have units of stress) equal in a same-soil model and prototype. If stresses are the same, we are at the same point on the stress-strain curve at homologous times. This would then give us the scaling relationships shown in Table 5.1 (from Kerisel, 1967). All of these relationships can be

Table 5.1.
Scaling relationships, gravity neglected.

All significant dimensions	L	$L_p = nL_m$
Masses	m	$m_p = n^3 m_m$
Stresses and moduli	σ	$\sigma_p = \sigma_m$
Forces	F	$F_p = n^2 F_m$
Acceleration	a	$a_p = a_m/n$
Times	t	$t_p = nt_m$

derived from n_1 above, if it is first stated that $\sigma_p = \sigma_m$, or $F_p/L_p^2 = F_m/L_m^2$. Note that the forces are now scaled at the ratio n^2, and accelerations (and hence gravity) by 1/n. Thus to accurately scale stresses in a same-soil model, we must increase gravity in the model. This requires use of a centrifuge, which Canterbury University does not have. An alternative, when gravity is not important, is to use, for example, stressed tie-down wires, or percolation forces, to increase the model stresses up to prototype levels (Kerisel, 1967).

5.2.2.2. Modelling of reinforced earth.

There are 3 distinct phases in the seismic response of RE walls. They are the initial small-strain elastic response, the formation of the failure surface up to "failure" when the surface outcrops at the fill surface, and post-failure displacement by sliding on the failure surface. There will also be some elastic behaviour during the second and third phases. Modelling is discussed below appertaining to each of these phases, followed by some more general comments.

5.2.2.2.1. Small-strain elastic response, and the natural frequencies of vibration.

To correctly model elastic response in a same-soil model, we require the stresses in the model and the prototype to be equal (Kerisel, 1967; Langhaar, 1951). This will maintain geometric similarity. Otherwise, if the stresses are scaled at 1/n, then strains will be too if Young's modulus is the same. If strains in the model become greater than 1/n times the yield strain then we can expect the prototype to exceed the yield strain and similarity is lost. In situations where the stress strain curve is non-linear, we cannot expect to obtain good results from elastic modelling when stresses scale at 1/n, because we are at different points on the stress-strain curve. As stated above, it is not possible to equate stresses in a normal-gravity (1-g) model. For seismic response of RE walls, though, it is felt that the small-strain elastic response of the wall has a minor effect on the overall response of the wall, once some displacement has occurred.

Wolfe (1979) reported that to measure the low-amplitude natural frequencies of RE walls, excitations used must be small enough not to cause permanent displacements of the wall. Accurate determination of the natural frequencies was said to involve three steps: finding the mode shapes of the wall at various frequencies, measurements of the phase differences between shaking table acceleration and wall face acceleration, and calculating the ratio of the wall surface (top) motion to the input motion (acceleration ratios). Wolfe also reports that the natural frequency is a function of wall height, and is almost independent of the density of reinforcement, which indicates that the elasticity of the strips contributes little to the vibration characteristics of RE walls.

We expect the natural frequencies of RE walls to be an elastic phenomenon. If we look at some published natural frequency data, however, an interesting relationship emerges. Richardson et al (1977) proposed that the first mode natural frequency of a RE wall (in Hertz) was given by the empirical relationship 38/H, where H is the wall height in metres. If this relationship was to hold at model scale, natural frequency would scale at n from prototype to model, in keeping with elasticity-dominant modelling. Richardson and Lee (1975), however, found that their 380mm tall wall had a

low-strain natural frequency of about 22Hz (whereas 38/0.38=100Hz). Wolfe et al (1978) found that their 610mm high walls had a natural frequency of about 20 Hz (38/0.61=62Hz). Wolfe (1979) reported 610mm and 305mm walls with natural frequencies of 18 and 34Hz respectively (38/0.305=125Hz). Rea and Wolfe (1980) determined a natural frequency of 24 Hz for 457mm high walls (38/0.457=83Hz). A Japanese National Railways 3m. high test wall had a natural frequency of 17 to 20 Hz (section 2.4). None of the above obey the 38/H rule although the 3m. high wall comes closest (38/3≈13). If we assume they were all modelling a 6m. high wall, which according to Richardson's relationship would have a natural frequency of 38/6 = 6.33 Hz, then:

i) For a 610mm wall (scale factor 10), $\sqrt{10}$ x 6.33 = 20, which is the natural frequency determined by Wolfe et al for 610mm walls, and close to Wolfe's 18 Hz result.

ii) For a 457mm wall (scale factor 13.1), $\sqrt{13.1}$ x 6.33 = 23, which is very close to the natural frequency of the 457mm walls determined by Rea and Wolfe (24Hz).

iii) For a scale factor of 15.8 (380mm wall), $\sqrt{15.8}$ x 6.33 = 25, which is close to the natural frequency of the 380mm wall tested by Richardson (22Hz).

iv) For a scale factor of 19.7 (305mm wall), $\sqrt{19.7}$ x 6.33 = 28, which is a little below the natural frequency of the 305mm walls tested by Wolfe (34Hz).

It would appear that time is scaled in keeping with the same-soil, 1g, gravity-dominant modelling formula (ie. $t_p/t_m = \sqrt{n}$), even for what might be expected to be elasticity-dominant phenomena, in RE walls. From Table 5.1, $t_p = nt_m$ when elasticity dominates. Richardson's formula is closer to the observed natural frequency for the 3m. tall wall, the difference perhaps reflecting the empirical nature of the relationship (it removes the dependence on the shear wave velocity from the formula for the natural frequency of a soil layer, see §2.2) and the small data base from which it was derived.

It appears, then, that 1-g modelling is acceptable even for natural frequency studies of RE walls.

5.2.2.2.2. Formation of the failure surface.

Failure surface formation begins as a broad band of shearing soil growing upwards and inwards into the fill. Just behind the leading edge of this zone, the failure surface forms, with the result that the shear deformations quickly become localised in a narrow zone of the soil (Nagel, 1985). Displacements are quite large in comparison to the grain size of the soil.

The predominant parameter affecting the formation of the failure surface is felt to be the soil angle of internal friction ϕ, including its effect on the reinforcing strip-soil friction coefficient. Gravity and inertia Pi-numbers are also involved - it is the seismic inertia of the sliding block that causes the displacement, and gravity pulls the block down as it moves outwards. There are no other external loads. As the failure surface grows, the soil in the shear zone would move along the q'-ε_a curve, Fig. 5.1. (The effective deviatoric stress $q' = \sigma'_1 - \sigma'_3$ when $\sigma'_2 = \sigma'_3$; ε_a is the axial strain, and ε_v is the volumetric strain. σ'_1, σ'_2, and σ'_3 are the effective principal stresses. The ϕ-ε_a curve is the same shape as the q'-ε_a curve since σ'_3 is held constant. In RE walls, it is required that the structure is well drained, so the pore pressure u is approximately zero and $q' = q$.) In the zone ahead of the failure surface, the soil would be moving up the curve at point A on Fig. 5.1. Immediately ahead of the failure surface the soil would be at point B, the peak of the curve, and once the failure surface forms it would be in the residual strength area near point C.

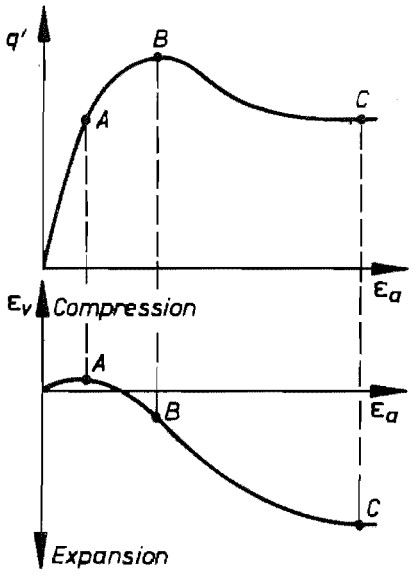

Fig. 5.1 Typical curves from a drained triaxial test on a dense sand (from Atkinson and Bransby, 1978)

While elasticity is important in the generation of strip forces, it is felt to be of minor importance as long as the strips are relatively inextensible and their elongation is very small compared to the shear strains in the soil immediately adjacent to the strip during pullout.

It is probably not possible to obtain true geometric similarity with a same-soil 1-g model, however, because:

i) The soil angle of internal friction ϕ may increase at low stress levels, with a concomitant increase in soil-strip friction f* for rough strips. (An increase in ϕ at low stress levels was demonstrated by Ponce and Bell (1971). Fukushima and Tatsuoka (1984), however, found that the effect was quite small if membrane forces and sample self weight in the triaxial tests used were properly accounted for. They also used lubricated platens at the ends of the samples.)

ii) In critical state soil mechanics, it is found that dense sands behave like heavily overconsolidated clays (Atkinson and Bransby, 1976). The critical state line, shown in Fig. 5.2, defines where the soil fails in shear. If we have the same soil at the same specific volume v but at two different mean effective normal stresses p'_A and p'_D, then the dilatancy rate is larger for the sample at p'_A than for that at p'_D. It can also be seen in Fig. 5.2 that sample A fails at a somewhat higher deviatoric stress q' than sample D.

iii) Grain-breaking cannot be modelled properly at low stress levels.

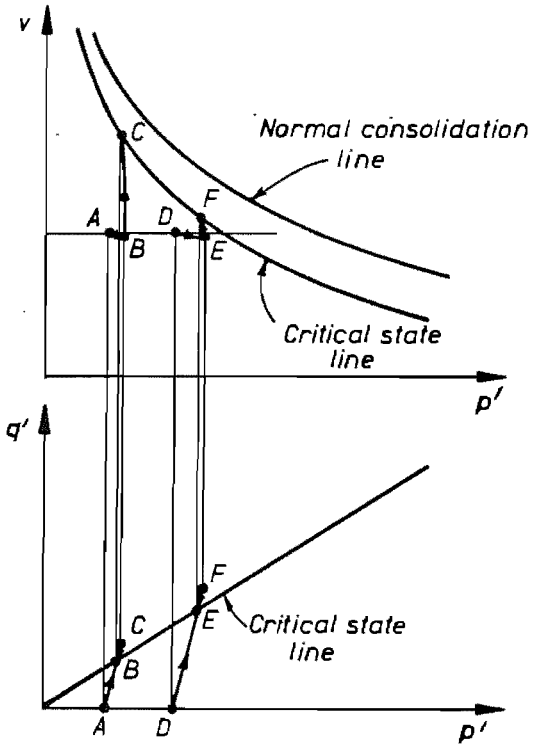

Fig. 5.2 Failure of dense sands in drained triaxial tests (after Atkinson and Bransby, 1978)

These effects, plus the fact that the stress distribution is scaled incorrectly, lead to the major problem with such model studies, that the failure mechanism may be incorrect and should not be applied to prototype structures without verification in centrifuge tests (Schlosser, Jacobsen, and Juran, 1983).

It is encouraging that in many static model tests, the failure surface and locus of maximum strip forces (which are approximately the same line) have been observed in an analogous position to the locus of maximum forces in full size structures. The first reason given above for doing model tests was to verify that the failure geometry was similar, at larger scale, to what had

been observed before. Accordingly, the scale of the models chosen for this testing is 2.5 times that used by Nagel. While a different sand was used, the grading was similar. In very small models there may also be a scaling effect from grain size, so the increased size should show if grain size contributes to any scaling effects as well.

5.2.2.2.3. Post-failure displacement.

After the failure surface is fully formed, displacements should be the same, no matter how big the structure is, as long as the yield acceleration is the same. The only effect the structure has on the displacement is in the value of the yield acceleration k_h. This can be seen by considering the Newmark (1965) sliding block analogy: displacements are calculated by time domain double integration of the part of the earthquake acceleration record with accelerations greater than the structure's yield acceleration, remembering that the yield acceleration is asymmetric and applies to one direction only. That in the opposite direction (for movement of the wall back into the fill) is much larger. Thus sliding block displacement is related mainly to the earthquake characteristics, in particular to the number of times the acceleration is greater than the yield acceleration, and the duration of each exceedence, or more specifically the predominant frequency of the earthquake excitation.

5.2.2.2.4. Analysis Comments.

It was seen in the displacement calculation methods in section 4.6 that displacements are often normalized or standardized to a certain size of earthquake. For such scaling to be valid for model test results as well, it must include some adjustment of the time scale: it was shown above that when gravity is dominant, $t_p/t_m = \sqrt{n}$. Scaling for both acceleration and velocity levels, as done by Newmark (1965) and Franklin and Chang (1977), accomplishes this. So by scaling to a standard earthquake using this method we can scale displacements of model walls to the same earthquake. This is done in section 6.10.4 below.

Richardson and Lee (1975) used "strains" (displacement divided by wall height) rather than standardized displacements. Their "strains" are perhaps more correctly dimensionless displacements, as the reference distance used in the "strain" ratio is perpendicular to the displacement. They used the wall height as the representative length for calculation of "strains". Richardson et al (1977), Richardson (1978), and Rea and Wolfe (1980) do the same. Design strip lengths are also compared to the wall height, and many design rules are related to the strip length / wall height ratio (TAI IR 15;1985). As a RE wall is characterized by its height, the wall height is a good representative length to use. Dimensionless displacements calculated like this can also be standardized to a standard earthquake using the Newmark method.

When considering the forces in the strips we cannot directly scale from model to prototype, because of the conflict: forces scale at n^2 when gravity effects are neglected, and n^3 when they are important. This may be part of the reason that the (static) strip forces in full size walls are so difficult to predict from one wall to another: design theory is assumed to be applicable to any wall, whether it is 3m. or 18m. high. In fact, the 3m. wall can be thought of as a distorted 1/6-scale model of the 18m. wall: it is 1/6 the size, but uses full size facing components and the strips are of equal cross-section but approximately scaled length. As gravity and elastic effects are both important in static analysis of RE walls (the load on the facing is due to the soil under gravity, there are small outward displacements of the wall face, and the reinforcing strips elongate during construction), there are difficulties in using the same theory to calculate the strip forces. It is assumed in design that stresses are related to the wall height, so in fact the gravity-dominant assumption is made. But then the same soil is used and we imply use of the same values for Young's and the shear modulus, which is contradictory. Modelling laws are ignored in design. Safety factors are chosen to cover the high degree of scatter in data measured in full size walls.

Another problem is that residual compaction stresses in the backfill may be larger than gravity induced stresses in the early life of an engineering fill, such as that in an RE wall (Ingold, 1979). In the method of sand placement used in the tests reported here (raining through air), we are unable to model this phenomenon. The soil friction angle may be affected by these

increased stresses, and hence the soil-strip friction coefficient. The effects may also be quite localised and varied, especially since in construction of commercial walls heavy plant is not allowed close to the facing because it causes unsightly bulging - compaction of a region about 1.5m. wide behind the facing is done by hand-operated equipment.

5.2.2.2.5. About the present study.

Two of the most important variables in RE are the friction coefficient f^* and the soil friction angle ϕ. Both are dimensionless. In derivation of modelling laws we should then be able to equate them for the model and prototype. The problems pointed out above, however, arise in that at the low stress levels in a 1-g model, ϕ and hence f^* (which is closely related to ϕ for roughened strips) may be different, and that the rate of dilatancy is certainly different in model and prototype. This *may* cause the failure mechanism to be different also. Because of these problems, there seemed little point in trying to obtain complete similarity. Other problems arise, for example, in scaling the ridged reinforcing strips. The difficulty of making a fill at uniform density also causes departures from similarity. Foundation conditions and construction compaction effects are very difficult to model and were not attempted to be modelled. Both may affect the failure mechanism by changing the stress regime within the reinforced block. In addition edge effects at the box side walls may affect the failure mechanism if the box is too narrow (see §A.1).

Initially, decisions were made on a practical basis. These included the method of preparing the fill to obtain uniform density, the surface preparation of the strips (although attempts were made at methods of placing ridges on thin strips), and the general shape of and sealing between the facing panels. Panels were made full width of the testing box, along the lines of the previously used steel facings for full size structures - there is no distinction in design rules for steel and concrete-faced walls (McKittrick, 1978). Final sizing of the strips was made during design of the test walls using the MWD (1980) design method. The method of attaching the strips to the facing panel was chosen after considering several methods, including scale models of the prototype detail. (The problem with those was

that they were subject to tearing failure of the strip at the bolt hole. Failure by strip breakage was avoided as far as possible.)

In the final analysis, the strips were 1/6 as wide as prototype strips, and about 1/10 as thick. Vertical spacing was 1/7.5 times and horizontal spacing ranged between 1/4.7 and 1/2.3 times (assuming 750mm horizontal spacing in full size structures). Young's modulus for aluminium is about 1/3 that for steel. The steel facing panels used in the past were 6mm thick, so the facings at 1.2mm were 1/5 as thick.

5.2.3. Hornbeck's study.

Hornbeck (1982) attempted to carry out a similitude study of reinforced earth walls. He was concerned only with static testing. Unfortunately his main analysis omitted a force shown on his definitive freebody diagram, and his mathematics was flawed.

Hornbeck proceeds by setting the factor of safety for a wedge sliding on a planar failure surface to be equal in model and prototype. The wedge is treated as a Culmann-type wedge, part of a retained embankment. Unfortunately, the retaining force on the embankment face is omitted from the analysis, even though it is shown on the freebody diagram. It is then really an unbraced cut, and indeed he compares the solution to that case (and it is of course the same). There is geometric similarity between model and prototype. A cohesive resisting force is included in the formulation. In the course of the analysis, he "collects terms" in a mathematically illegal way. The problem, as he has it, is only tractable if one of his results is used as an assumption or requirement, to overcome the bad mathematics. If the omitted force is included, and cohesion set to zero, then for a same-soil model ($\phi_m = \phi_p$, $g_m = g_p$), the formulation results in the requirement that the retaining force on the embankment face is equal in model and prototype, which is clearly impossible.

Essentially this part of Hornbeck's analysis shows up the conflict between cohesion, gravity and ϕ Pi-terms mentioned in section 5.2.1.1. If the

omitted force is included in the formulation, it is intractable without further assumptions.

Hornbeck then looks at the problem of variation in the apparent coefficient of soil-strip friction. He comments that several authors have noted that strip forces have been higher than expected from direct shear friction tests, and have postulated that the high forces were due to undulations in the strips. To take soil-strip rigidity into account Hornbeck proposes to use the relative stiffness factor R_s from the theory of beams on elastic foundations: $R_s = \sqrt[4]{(k/4EI)}$, where k is the equivalent spring stiffness, E is Young's modulus and I is the moment of inertia of the strip cross section about the longitudinal axis of bending. R_s has units of (1 / length), so the ratio of R_{sm}/R_{sp} should be n, the geometric scale factor. From this it follows that geometric similarity of the strip cross section is necessary, and that the equivalent spring stiffness k should be the same in the model and prototype.

It is uncertain whether this argument is valid. When a strip pulls out of the backfill in a model, the displacements are large compared to the grain size of the soil. The loading regime on the strip is quite different to that on a foundation beam as well. Furthermore, putting the blame for strip forces being greater than expected from direct shear tests entirely on undulations in the strips is perhaps not realistic. It ignores completely the effect of dilation of the sand during shearing. (Section 6.7 looks more closely at the effects of dilation on the apparent strip-soil friction.) It is unlikely that elastic beam theory is applicable.

An analysis of deformations of the wall facing is done next. Hornbeck assumes that all earth pressure on the facing causes reinforcing strip elongation. This is only the case immediately adjacent to the wall facing. He requires that deformations in the model and prototype are geometrically similar, and derives that the earth pressure in the model should be n times the earth pressure in the prototype. Hornbeck states that this means that the angle of internal friction must vary directly with density, and considerably so. Such soils are rare. It can also be interpreted that gravity must be scaled up in the model. He used elastic theory to derive this relationship.

Without actually stating it, Hornbeck shows the conflict between the cohesion and gravity Pi-numbers, and also the difficulty of scaling forces and stresses when both elastic and gravity considerations are important. He attempts to set up a series of model tests based on the conclusions of his analysis. Really they are little different to many other model tests done on the static strength of RE walls.

5.3. Testing procedures and methods.

In the following sections is described the equipment, procedures and methods used in the testing. Further detail on some sections is available in Appendix A.

5.3.1. The containing box.

The box inside which the tests were carried out was plywood-lined and steel framed. Fig. 5.3 shows a view of the box from one end. The design

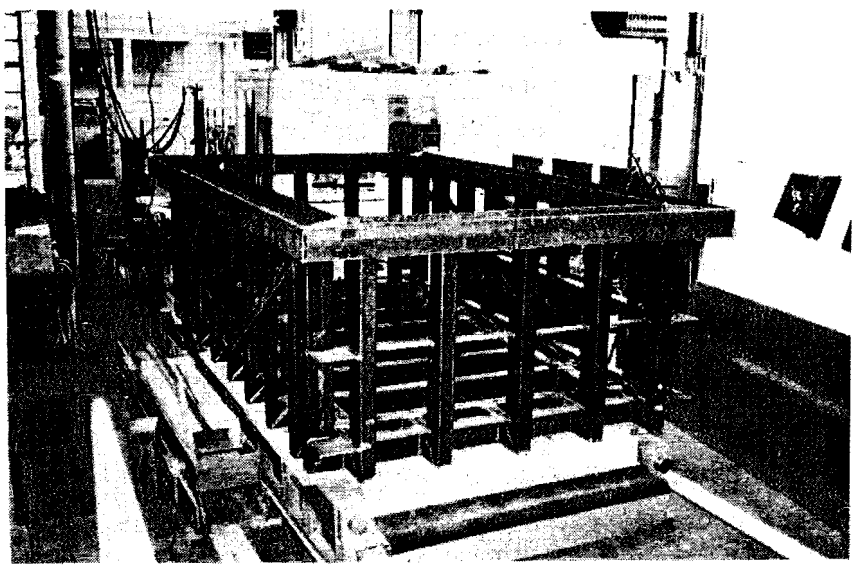

Fig. 5.3 The steel frame of the test box on the shake table, prior to lining with plywood.

criterion for stiffness was that there should be no active failure wedges in the contained sand at the side or end walls under any foreseeable conditions. Thus deflection was limited to 0.5mm maximum at any point, including under the load imposed on the end walls by the sand under 2g acceleration.

A finite element computer program was used to design the highly statically indeterminate steel frame. Main members were heavy RHS with a substantial ring beam (flanges vertical) around the top. Flats were used for the diagonal and horizontal bracing. 30mm thick plywood was bolted inside to provide the lining. The floor and the walls were each one piece.

Interior dimensions of the box were 3785x2000x1200 mm. It was bolted to the shaking table through the RHS in the floor of the box. Bolt holes in the plywood floor were filled and taped over to prevent sand leakage. The entire floor was then covered with P40-grade sandpaper, stapled down, to reduce sliding of the sand on the floor of the box. Interior side walls were filled and sanded smooth before test 1, and painted before test 4. In tests 1 to 3, only the portion of the side walls visible after construction was painted.

It was decided not to put a transparent wall in the box to view the failure surface forming. The heavy RHS uprights and the diagonal bracing would have substantially obscured the view. More importantly, it was felt that the failure surface formation history was understood. Edge effects render the failure surface slope seen at the side walls irrelevant for the analysis of the structure. Mapping of the failure surface using coloured sand, well away from the side walls, was felt to be more useful. Discussion of edge effects can be found in Appendix A.

In one end of the box a 400mm square hole was cut for emptying. A steel vertically-sliding door was fitted over the opening. Adjacent to the test box was a steel tank to store the sand between tests. Sand was poured through the door into a skip, which was then raised using an overhead crane and the sand emptied into the storage tank.

During test 1, the wall top accelerometer (see section 5.3.9) recorded a 50Hz vibration (see also section 5.3.10). The 50Hz noise was recorded in the shake table input signal as well, though at a very much lower level of

acceleration. After that test, two sheets of 25mm thick polystyrene were nailed to the inside end wall of the box. It was felt that there might be reflection of compression waves, in the sand, off the end wall during testing, so the polystyrene was an attempt to absorb the wave energy. It appeared to make no difference to the recorded motions at the model RE wall.

Because the sand raining (see section 5.3.3) produced a lot of dust, the whole test rig was enclosed in a plastic-covered tent. A roller blind was fitted on one end to allow easy access for the sand raining trough and trolley.

5.3.2. The sand.

Mt Somers sand, an air-dry medium white quartz sand was used for all testing. Its grading curve is shown in Fig. 5.4. The coefficient of uniformity was 2.32; D_{60} = 0.36mm, D_{10} = 0.155mm. It had a specific gravity of 2.66. The grains could be described as angular to sub-angular. Fig. 5.5 is a scanning electron microscope photograph of the sand.

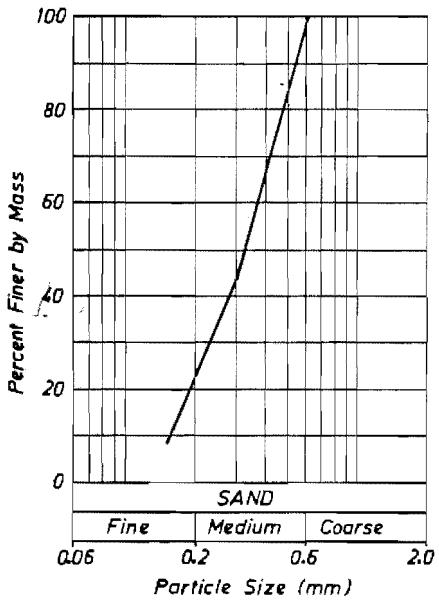

Fig. 5.4 Grading curve of Mt Somers sand.

5.3.3. Sand raining.

Backfilling of the test walls was by raining the sand from a V-shaped trough, through 4mm dia. holes at 10mm centres (Fig. 5.6). Opening and closing of the holes was accomplished using a lever-operated sliding panel. The trough was mounted on a trolley which ran on the outside flange of the ring beam at the top of the testing box and was towed at a constant speed during raining. For test 1, towing was uni-directional, with the raining

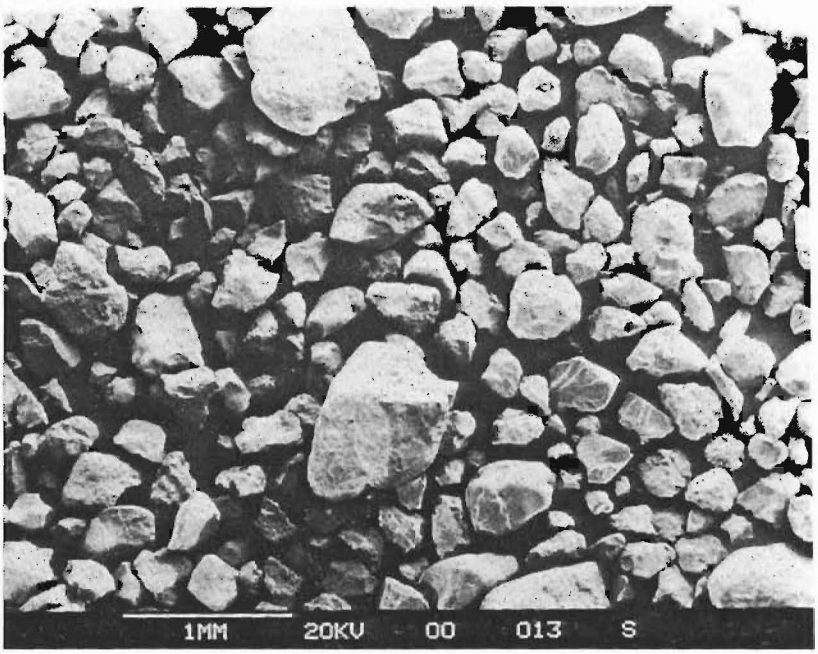

Fig. 5.5 Scanning electron microscope photograph of Mt Somers sand.

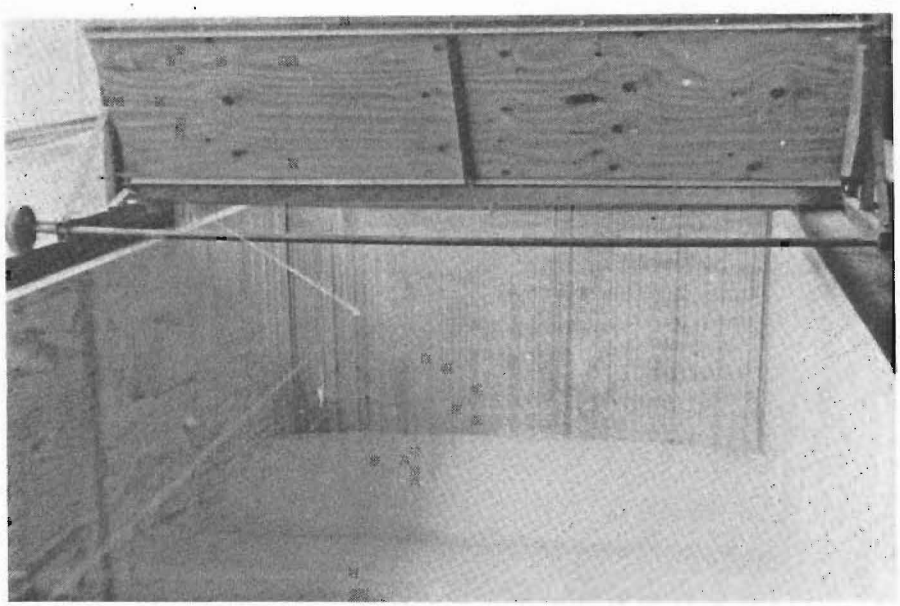

Fig. 5.6 Sand raining during filling for test 1.

holes being opened at the remote box end wall and closed at the RE wall, and the trough being pulled back to the starting position by hand. Subsequent tests used a bi-directional towing system, where the electric motor rotation was reversed at each end of towing. At the turn, raining was in general not stopped unless a trough fill or wall construction activity was required. The turn was made just after the test wall was passed, to avoid a build up of

material in the fill area adjacent to the wall during the instant the trough was stationary. In the case of tests 2 and 3, there was a consequent build-up of sand at the toe of the wall, some of which had to be removed to provide the Reinforced Earth Company recommended burial depth of 8.5% of the total wall height. Removal in these cases was by vacuum cleaner using a special end piece to obtain a smooth surface. For tests 4 to 6, a cardboard cover was used to prevent this buildup of material at the toe during construction (Fig. 5.7).

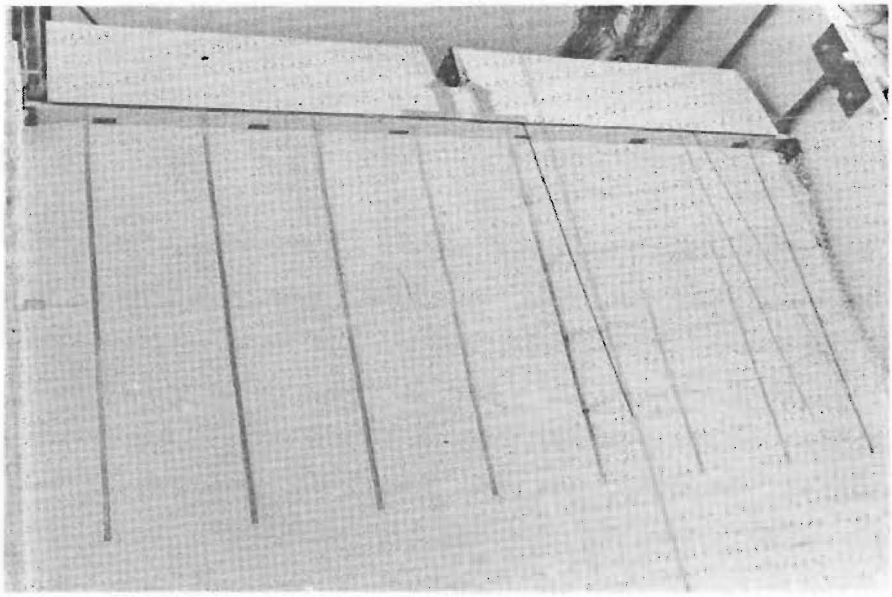

Fig. 5.7 Cardboard cover in place to protect the toe area from sand placement before the completion of construction.

A constantly-variable-ratio gearbox was used to adjust the speed of towing so that four runs along the fill would almost empty the trough. Trial runs were done before construction of the test walls began to obtain the optimum speed. The increase in fill height gained per run at this speed was about 12 to 15 mm, so one trough-full was sufficient between construction activities on the test walls (50mm depth of rained fill). There were always small undulations in the fill surface, so prior to reinforcing strips being laid out, the hollows were filled by raining small quantities of sand by hand, with a fall height similar to the trough raining height.

Near the sides of the box, and the end especially, the surface of the sand was always lower than it was some distance (300-400mm) away. Very close to the box walls there was probably a slightly higher density in the sand.

However, the main effect causing the lower fill level near the walls was air currents caused by the wall of raining sand moving along over the fill (Fig. 5.6). This was most pronounced as it approached the end wall of the box, where the advancing sand wall was subject to quite severe disturbance. Increased densities result from the reduction in intensity of the rained sand curtain (see Appendix A). Some form of air bleed through the walls would prevent most of these turbulence effects, though there would then be leakage and rigidity problems. The low areas were filled by hand raining, and also using a bucket pouring through a lid drilled in the same hole pattern as in the bottom of the raining trough. Raining height in these cases was similar to the trough height. The area in front of the test walls (at the toe) was filled from the trough (hand towed), and from the bucket, after completion of the rest of the wall.

At the beginning of construction of a test wall, the raining height was about 1300mm. This was allowed to reduce to about 800mm by increase in fill height, and then kept fairly constant at that height by raising the trough in the trolley after each fill. The trough was kept above the top of the containing box, so the maximum raining height was about 1300mm when the sand surface was at the bottom of the box. For a discussion of methods of obtaining a uniform density of sand, see Appendix A (section A.2).

As part of the trough refilling process, the sand was run through a wire mesh sieve of about 2mm opening. This removed any coarse objects and prevented blockage of the raining holes in the trough.

5.3.4. Density determinations.

One density determination was done in each test. Table 5.2 shows the results of them. The determination was done by placing a 1 litre Proctor mould in the fill during sand raining, and by weighing it (full) after testing. The density determined would then reflect the condition of the sand after testing, including the effect of any settlement or expansion during testing.

Table 5.2.
Density determinations for sand fill.

test	position in fill	density, tonne/m^3
pre test trial	(3mm holes in trough):	
	bottom, near box end wall	1.664
	" middle of fill area	1.671
	near RE wall position, 200mm up	1.672
	middle of fill, 200mm up from floor	1.660
	(4mm holes in trough):	
1	@ bottom (cyl on floor)	1.651
2	mid-height of fill	1.642
3	base @ level of strip 8: 250 down	1.583
4	as above	1.615
5	base @ level of strip 9; 150 down	1.595
6	base 220 below top	1.622

5.3.5. Facing panels.

The ten facing panels were fashioned from 1.2mm thick aluminium sheet (alloy 1200-H14). They were 100mm high, and ran full width of the containing box (2.0m). Fig. 5.8 shows the cross-section. Upstands on the outer facing side gave them some longitudinal stiffness. Slots were punched at mid-height for the reinforcing strips to pass through for attachment. There was no fixity between panels.

Sealing between panels was by a flap of PVC sticky parcel tape stuck to the upper panel and folded back on itself, and thus held against the lower panel by sand pressure. Sealing of the ends at the box side walls to prevent sand leakage was by a flap of synthetic material glued to the panel, and taped very lightly to the wall (Fig. 5.9). Also, two layers of synthetic knit fabric were wrapped around the ends of the panels to try to prevent binding on the wooden side walls (Fig. 5.10). Test 1 however, used brown PVC sticky parcel tape folded back on itself as the end seals, which was not successful. Large craters formed as a result of sand leakage (Fig. 5.11). Neither was there any knit fabric padding around the ends of the panels in test 1.

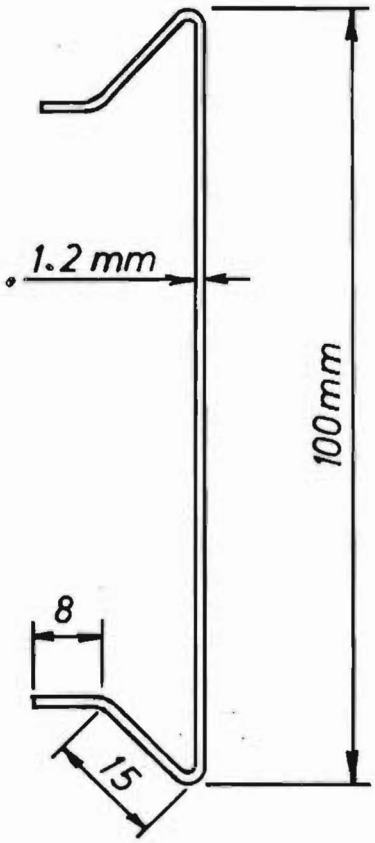

Fig. 5.8 Cross section of facing panels.

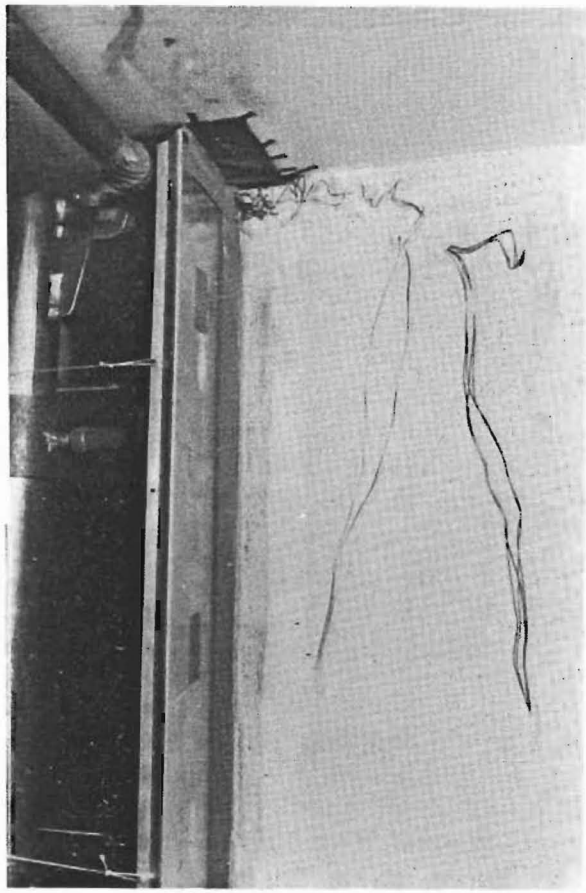

Fig. 5.9 Panel end sealing in place, tests 2 to 6. Usually only three small pieces of tape were used.

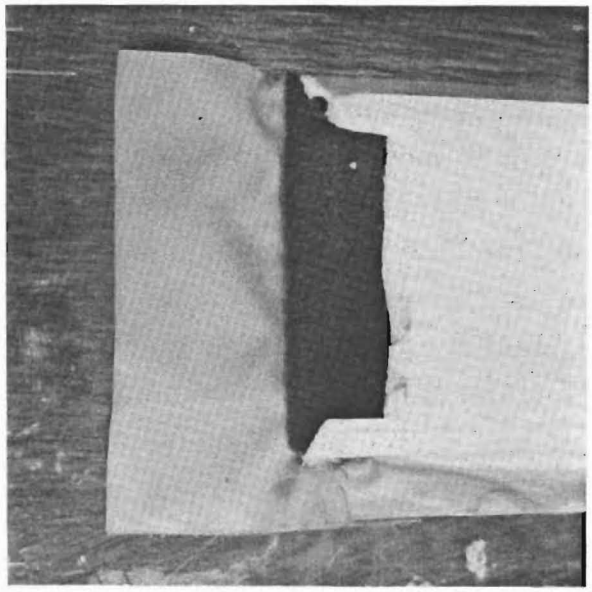

Fig. 5.10 End sealing details, tests 2 to 6. Visible are the end of the facing panel, the knit fabric (dark colour), the synthetic flap at the end, and the PVC parcel tape along one edge of the panel.

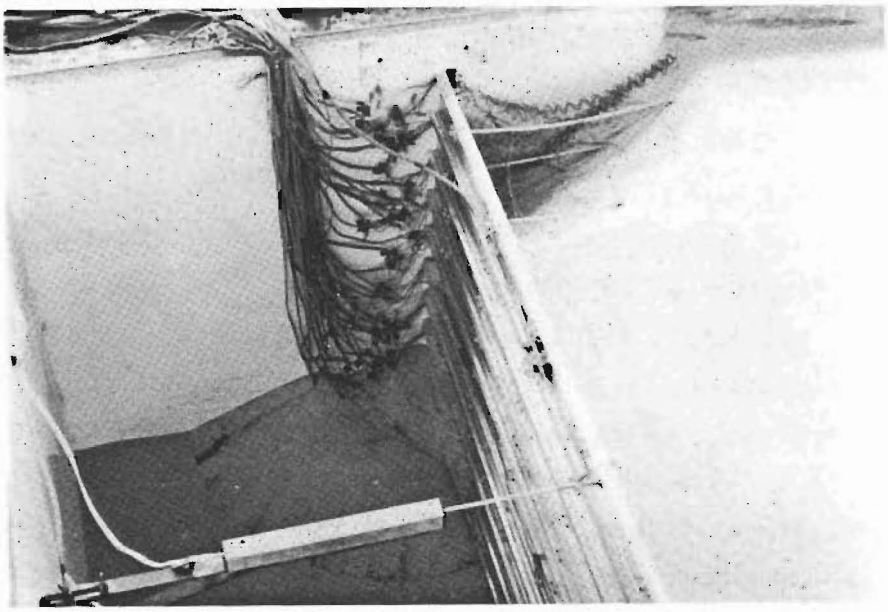

Fig. 5.11 Leakage crater in test 1. A similar crater formed at the other end of the wall.

5.3.6. Reinforcing strips.

5.3.6.1. Introduction.

The reinforcing strips used were 10.0mm wide x 0.45mm thick aluminium (alloy 1200-H14), with sand glued to the surface. Aluminium was chosen because it was felt that it was cleaner, easier to work with, and easier to obtain the high grade of surface preparation required for sand and strain gauge attachment than with steel. At the time it was chosen, the sand to be used had not been decided, and it was possible a beach sand would be used. The salt content in such a sand could cause rapid corrosion of steel strips if they were left in it for long. It was not known at the time how a long a model would be standing before testing, so aluminium was chosen as it was thought to be less affected by corrosion.

Strips were cut from a sheet of aluminium in a guillotine. This created a very slight curve in the horizontal (or wide) plane of the strips, as the blade cut from one end to the other. It was not possible to completely remove this curve by gentle stretching of the strips. Great care was needed to set the guillotine up to cut the strip width accurately.

5.3.6.2. Surface preparation of reinforcing strips.

An attempt was made to increase the soil/strip friction angle above the plain-surface value. This was because smooth strips are no longer used in construction, and because research has found that smooth and ribbed strips (with a high friction angle) behave in different ways (see section 6.7 for a discussion of soil-strip friction in reinforced earth.) Ribbed strips tend to have a friction angle close to or the same as the angle of internal friction of the soil: it is thought that the pullout failure surface is in fact in the soil adjacent to the strip rather than along the strip/soil boundary (Mckittrick 1978). By attaching sand to the strip surface, there would be some interlock with the backfill soil and the friction angle should be close to ϕ of the soil. Other ideas were tried with preliminary pullout tests: ridges pressed into the aluminium, either plain or filled with a piece of wire glued on. It was very difficult to obtain a good fix of the wire pieces, and pressed ridges tended to pull out. The section of the strips was chosen to give measurable forces, limited to less than 40% of the nominal yield force for the material, so it could not be increased without reducing the measured elongation. Another idea was to press many small raised "rat-tails" into the surface, but this also required an increase in the section. Gluing sand on to the surface was a relatively simple process and gave good results.

The best "glue" found for attaching the sand was a zinc chromate primer paint, formulated for aluminium. Strips were first brush painted, then the sand rolled on with a heavy steel hand roller. Coating was generally quite even with this method when done with care. Once the initial tack of the paint was reached, the "feathers" of sand along the edges were removed with a knife.

5.3.6.3. Instrumentation of reinforcing strips.

Ten strips in each wall were strain gauged, one at each panel level. The instrumented strip was placed as close as possible to the middle of each panel. Five pairs (top and underside) of electrical resistance strain gauges were used on each strip. For the first three tests, the gauges were clustered around where the maximum force in the strip was expected (Tables A.1, A.2, and

A.3 in Appendix A). For tests 4 and 5 gauges were attached evenly spaced along the strip. (Table A.4.) In test 6 the instrumented strips from test 1 were reused, though in slightly different order. (Table A.5.)

To prevent the strain gauge wires acting as unanchoured reinforcement and themselves taking tension forces, they were led up 50mm, then sideways to the box side wall, then forward and through a hole near the top and end of the facing panel to which they "belong". The upward- and forward-running lengths of wire were bent into a tight zigzag (except in test 1, where only the forward-running wires were zigzagged), so that if there was any extension in the sand they would just straighten a little and offer no resistance (Fig. 5.12). Where they passed through the failure surface there should have been enough straightening capacity available to prevent any tension development in the wires.

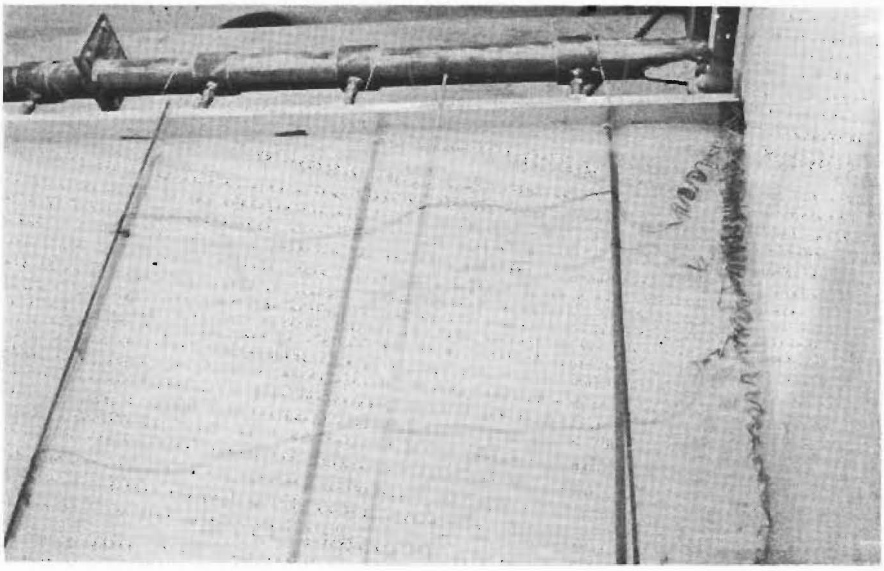

Fig. 5.12 Strain gauge wiring laid out on the sand surface.

5.3.6.4. Attachment of strips to the wall facing.

Attachment of the strips to the wall facings was by a pin and friction mechanism. A piece of viscose satin ribbon was glued in a loop to the end of the strip (Fig. 5.13). This was passed through the slot in the facing panel and between two short pieces of aluminium angle (Fig. 5.14). The lower piece of angle was glued to the panel. A 2.5mm dia. wire pin was passed through the

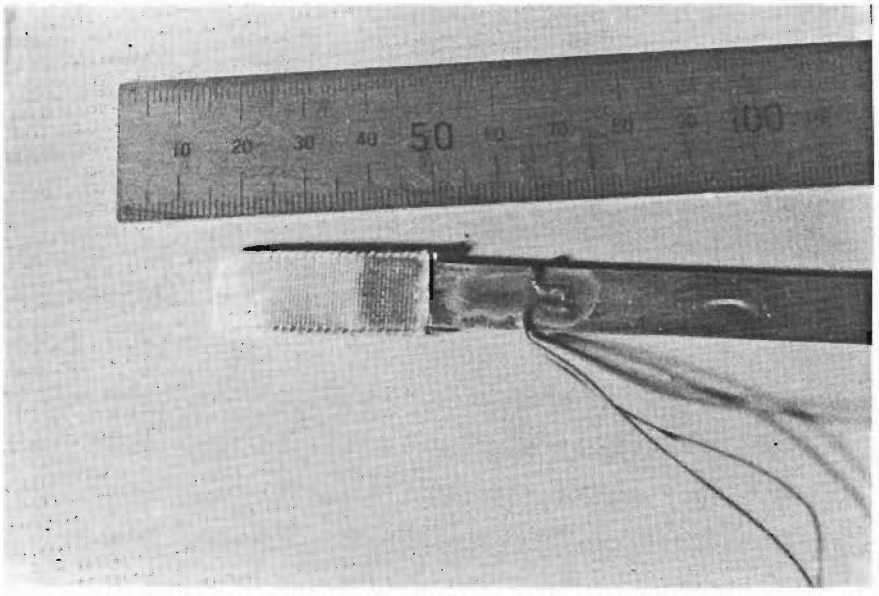

Fig. 5.13 Strip attachment cloth loop. Also shown is the strain gauge closest to the facing panel.

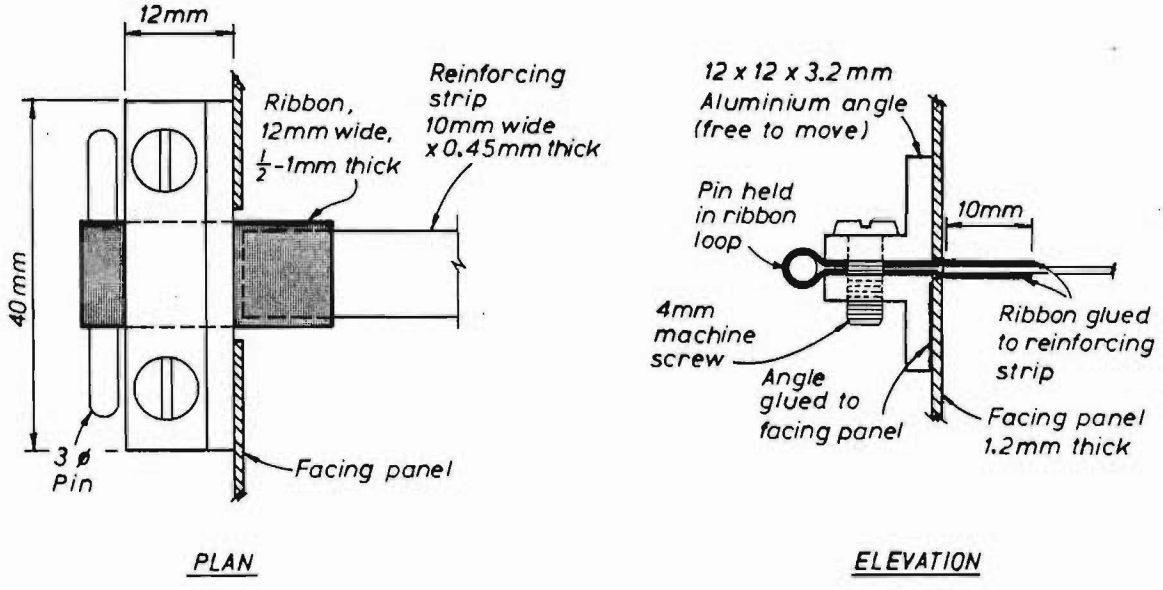

Fig. 5.14 Strip attachment detail: a) plan view, b) elevation.

end of the loop of ribbon, and the screws tightened while a gentle backpressure was applied to the strip. Thus the strip was prevented from slipping out by the pin and the friction grip of the tightened screws (Fig. 5.15). This arrangement also effectively provided a pin joint in the strip at the wall facing. There was no sign of distress in any strip as regards the strip

pulling off the ribbon loop. To make it easier to push the loop through the slot in the facing panel, it was ironed to put a sharp bend in the end.

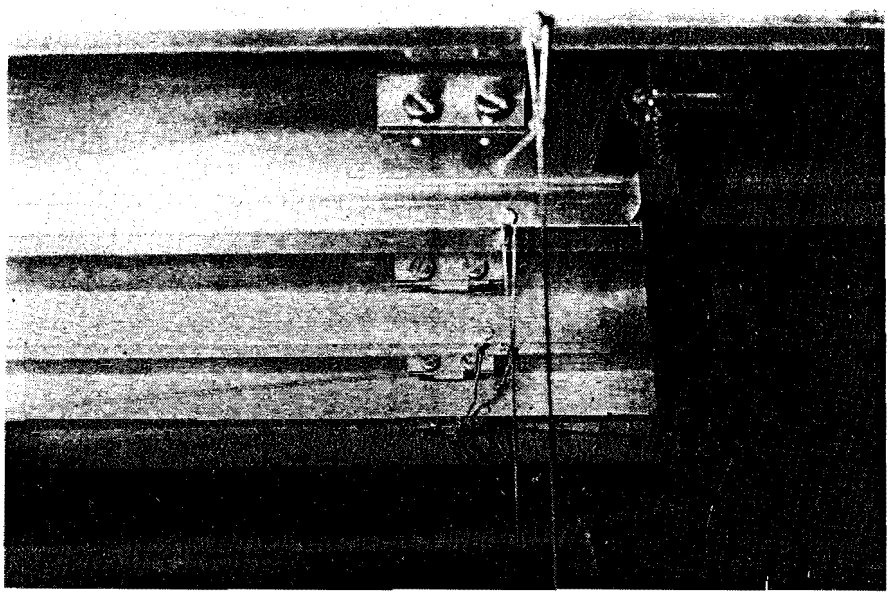

Fig. 5.15 Strip attachment detail at wall outside facing.

5.3.6.5. Strip placement.

To introduce the strips to the slot in the facing panel, each was supported in a cradle made of two loops of cotton hanging from a piece of light steel rod. Using this cradle it was possible to try the strip on the surface of the fill, and remove it if necessary to fill and smooth hollows in the fill surface, without significantly disturbing the surface. After final placement, the cotton loop was cut and pulled out from under the strip.

The strips could be made quite straight in the vertical direction (as laid out on the fill) before placement by holding up by one end, sighting along the strip, and pulling it between the fingers to remove any undulations. It was less easy to obtain a perfectly flat fill surface on which to place the strip, even with hand raining small quantities of sand. While every effort was made to attain complete flat contact between strip and sand surface, it was usually necessary to accept small gaps of up to about 0.5mm between them, over small areas.

5.3.7. Displacement measurements.

Two 200mm-travel linear potentiometers were used to measure wall displacements relative to the containing box. One was attached to the top facing panel, the other to panel number 5 (panel number 1 was at the wall toe). In tests 1 to 3, the potentiometers were mounted inside the box and connected to the panel with a piece of flexible plastic hose. They needed lowering several times during a test, as the wall moved out and down (Fig. 5.16). For tests 4 to 6, they were mounted outside the box, and connected to the facing panel using a 600mm long piece of aluminium tube with a small simple universal joint at each end. With this arrangement the potentiometers did not need lowering during a test, which was quite important for the longer-duration earthquake tests. A small error was introduced proportional to the outward (hence downward) movement of the wall. To reduce the average magnitude of the error, the potentiometers were mounted some 50mm below the wall connection starting position, and thus finished the test some 40 or 50mm above the wall connection point. A hole was drilled in the box end wall for the aluminium tube to pass through.

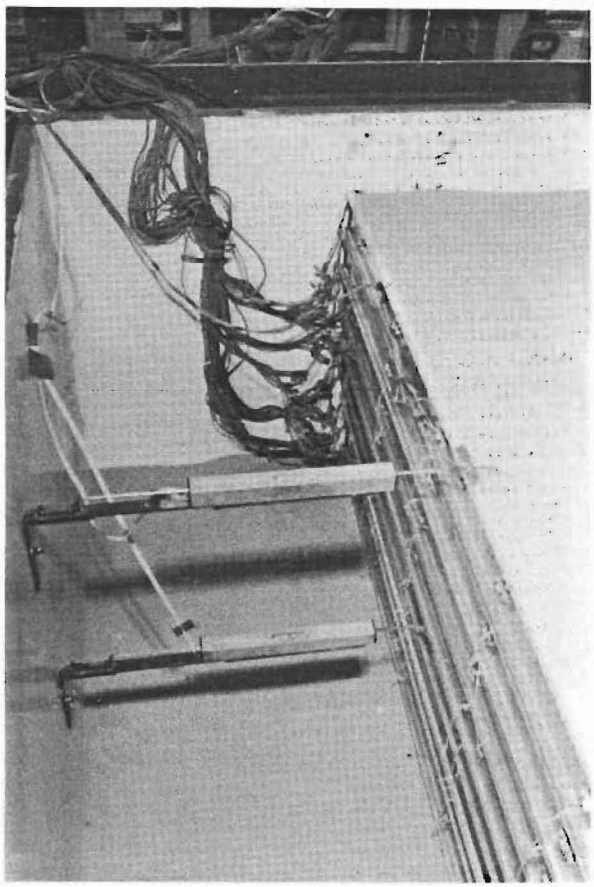

Fig. 5.16 Test 2 near end of test, showing displacement transducers and exit of wiring loom.

5.3.8. Wall construction.

100mm depth of sand was rained into the box before wall construction started. Then the first panel was placed, and 50mm of sand rained in, up to the level of the first layer of strips. A layer of strips was placed, the

zero readings taken of the instrumented strip, and a further 50mm of sand rained in. At that point, the panel holding mechanism was released, raised, and another panel placed. Construction continued in this way until the wall was competed.

The panel support mechanism consisted of tubular steel uprights bolted to the box side walls. A larger steel tube was bolted horizontally between collars sliding on the uprights. Inverted-L shaped supporting brackets were attached to the horizontal tube. The panel was restrained on the supporting brackets using a loop of elastic string. Details of this system can be seen in Figs. 5.12, 5.15, and 5.17. To release the mechanism, the elastic was released, the horizontal tube split at the mid-length flange provided for the purpose, and "opened" away from the panel. After raising to the level of the next panel, the flanges were rejoined, and the new panel fitted and attached by new elastic loops. Each new panel was carefully levelled so that it barely touch the one below.

Small pieces of brown PVC parcel tape were used to hold the end-sealing flap in place against the sidewall (Fig. 5.9). These tapes were sufficient to hold the fabric in place while sand raining was going on, but offered very little resistance to the fabric being pulled out along the wall, and were of no effect after the first movement of the RE wall.

Prior to the fitting of a new panel, a wedge of sand was removed from the top of the last panel, to provide space for the tape sealing flap attached to the bottom of the new panel. The sand was removed with a vacuum cleaner using a special annulus-shaped nozzle. Fig. 5.17 shows a wall ready to have the next panel fitted, with the wedge of sand removed.

5.3.9. Acceleration measurement.

At the levels of panels 5 and 10, accelerometers were placed in the fill 75mm behind the wall facing, except in test 1 where the top accelerometer was taped to the facing panel. During test 1, this top accelerometer registered quite large (compared to the input levels) 50Hz resonant oscillations. 50Hz noise was often present on the observed input accelera-

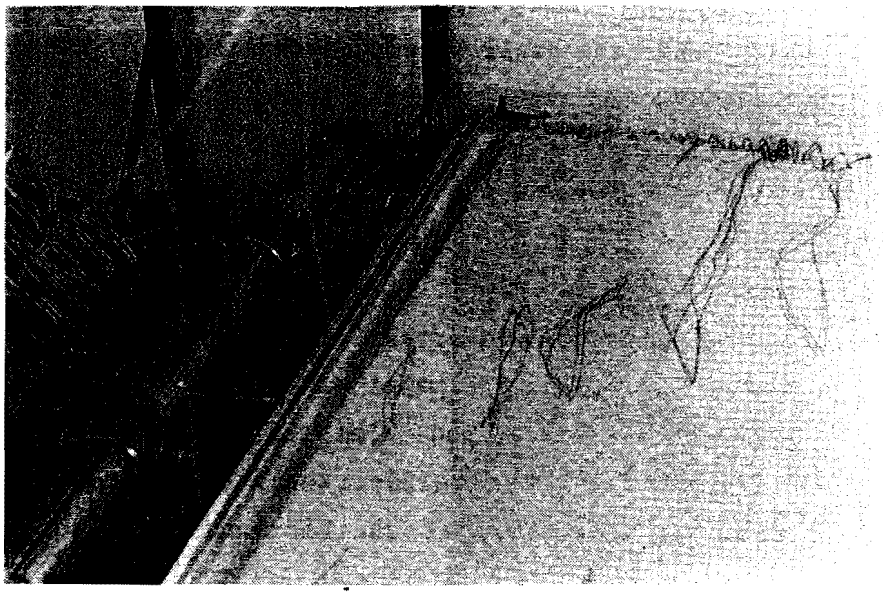

Fig. 5.17 A wall ready for the fitting of a new panel, showing the wedge of sand removed for the sealing flap.

tions, though at low levels (less than 0.01g; see section 5.3.10). It was felt that the panel could be vibrating horizontally, and that there could be some reflection of waves in the sand off the box end wall. So subsequent tests had both accelerometers sitting in the fill, and as mentioned in section 5.3.1 a 50mm thickness of polystyrene was nailed to the box inside end wall. These precautions did not stop the recording of highly magnified 50Hz accelerations in some subsequent test runs.

Input acceleration levels were measured using an accelerometer taped to the shake table surface between the box uprights, near the actuator-table connection point. This and the wall top instrument were 2g capacity Showa model BA-2L accelerometers, while the mid-height instrument was a Kyowa AS-1C of 1g capacity.

5.3.10. Shake table inputs.

Four "earthquake" records were used as input to the shaking table. Two of them, FARLS2 and EQCV1D, were artificial, single-pulse sinusoidal inputs (tests 1 to 4), the third was El Centro 1940, north-south component run at 10 times natural speed (test 5), and the fourth was El Centro 1940, north-south component at 3 times natural speed (test 6) (Table A.7).

FARLS2 was calculated from

$$a = A\cos(\omega t/2) - A\cos(\omega t) \qquad \ldots\ldots\ldots\ldots\ldots\ldots\ldots\ldots (5.1)$$

where a is the acceleration, A is the maximum amplitude of acceleration, ω is the circular frequency of the excitation, and t is the time in seconds. For one cycle, $0 < t < 0.3333$ sec. For a 3Hz wave form, $\omega = 12\pi$, and the maximum acceleration required was 1g. As the shaking table is displacement-controlled, we must integrate eq. 5.1 twice to obtain the displacement values to be output to the shake table:

$$d = \frac{1}{144\pi^2}\cos 12\pi t - \frac{4}{144\pi^2}\cos 6\pi t \qquad \ldots\ldots\ldots\ldots\ldots\ldots (5.2)$$

There are also additive and multiplicative constants to convert the actual displacements into the integer data format required by the Apple IIe computer program that reads the data to the shake table driver. Plots of the displacement and acceleration functions are shown in Fig. 5.18.

The record actually used consisted of three parts: a slow ramp from the actuator resting place (mid-travel) to the starting displacement, the generated "earthquake", and a slow ramp back to the resting place. The ramps were in the form of half-cycle cosine curves and sufficiently long to induce only very small accelerations.

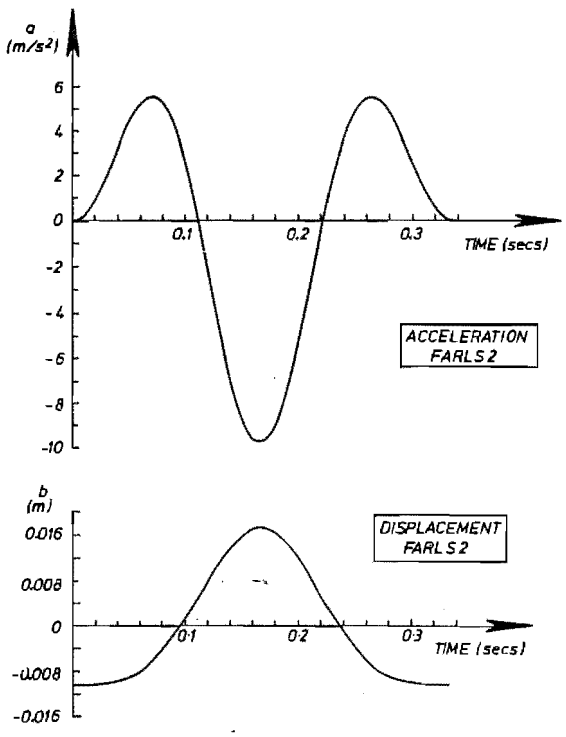

Fig. 5.18 a) Acceleration, and b) displacement traces of FARLS2. The displacement zero is mid-travel of the table top, its normal resting place.

Acceleration response of the shaking table was not as good as expected, especially at low acceleration amplitudes. The problem seemed to be at the change in direction, probably due to lack of stiffness in the actuator-table

connection. EQCV1D was derived to counteract this problem by adding FARLS2 to a uniformly increasing displacement (ie. a constant velocity). Thus there is no change in direction in the record, except in the low-acceleration-amplitude ramps (Fig. 5.19). Additional ramps were required: from zero to constant velocity at the beginning, and from constant to zero velocity at the finish of the record. It turned out that the change in direction problem diminished above about 0.4g acceleration, and the maximum acceleration possible with EQCV1D was about 0.37g, so the range of accelerations of interest (0 to 0.6g) were covered.

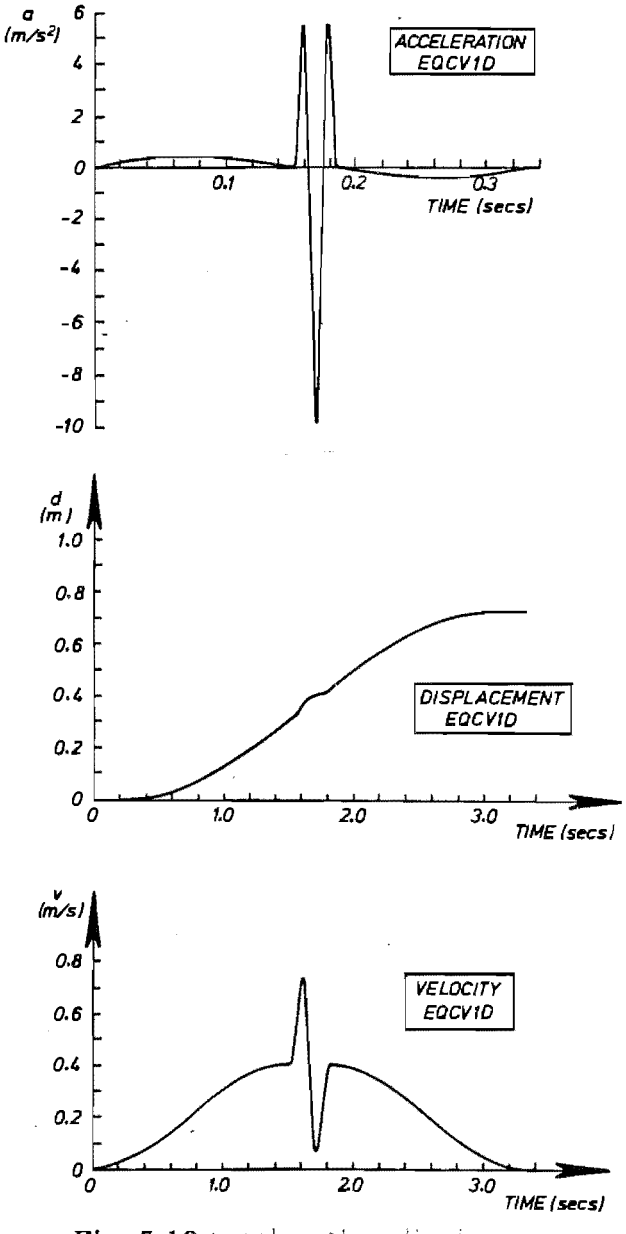

Fig. 5.19 Acceleration, displacement, and velocity traces of EQCV1D.

FARLS2 (both stand alone and inside EQCV1D) was always run at 3Hz. Unfortunately, there was often 50Hz noise on the input signal, which showed on the acceleration traces. The recorded 50Hz oscillations are believed to have been correctly measured, rather than introduced as noise during the data-logging process. Comments were made by observers that the table motion felt "gritty" rather than smooth during the sinusoidal test runs, which would be expected if there were 50Hz vibrations included. It was also possible to hear the vibrations in the hum made by the shaking table operating system hydraulic pump. When the vibrations were not present, the pump sounded different, and they were not recorded on the accelerometers. The exact source of this noise is unknown, though it is most likely to be in the power supply. It was not possible to tell before starting the pump whether the noise was present. When it was present on the input there was strong resonance shown in the wall top accelerometer readings, and much less so in the wall mid-

height readings. Because the acceleration levels of the 30Hz noise were very low, there was no apparent effect on the performance of the test walls.

In test 5 El Centro 1940 NS was run at 10 times natural speed in an attempt to move the predominant frequency up near the expected natural frequency of the wall (38Hz using the Richardson (1978) 38/H rule). Fig. 5.20 shows the power spectral density of the El Centro 1940 north-south component

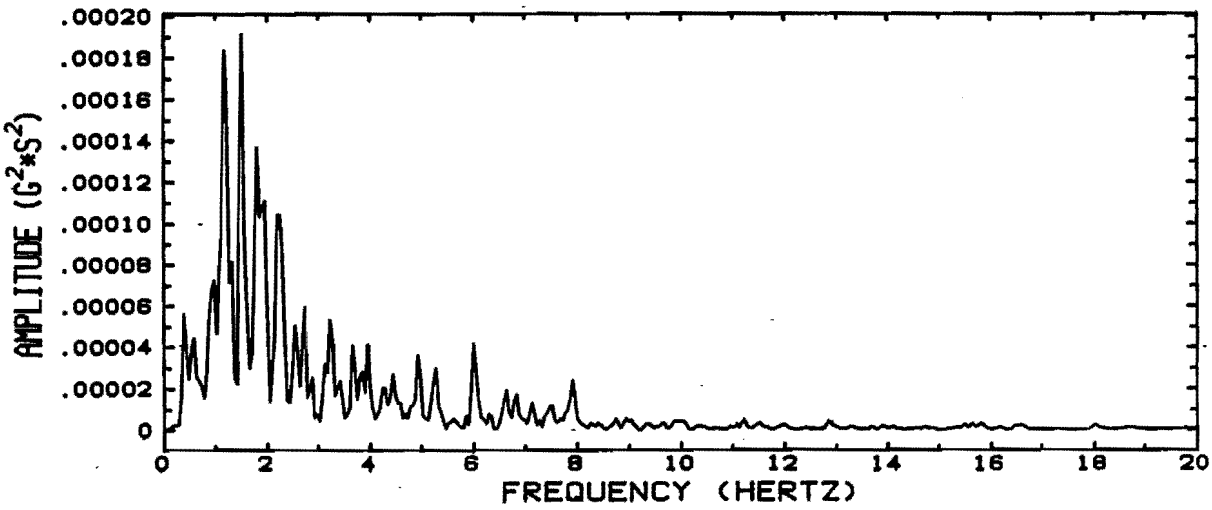

Fig. 5.20 Power spectral density function of El Centro 1940 NS. at natural time scale.

at natural time scale. The energy of the motion is seen there to be mostly in the 0.8 to 3 Hz band. Table response was disappointing however, in that the response was much slower than expected. The effective time scale factor in test 5 was only about 3. Fig. 5.21 shows the power spectral density for test 5 run 6, where it can be seen that the energy of the signal is concentrated in the 3 to 10 Hz band. Thus in test 6 El Centro was run at 3 times natural speed. Fig. 5.22 shows the power spectral density function of the input acceleration for test 6 run 2, where the energy is seen concentrated in the 2 to 8 Hz band.

5.3.11. Data logging.

Data was captured using an IBM-PC-driven analog-to-digital converter. Scan rates were usually 247Hz (maximum speed with 55 channels), although in

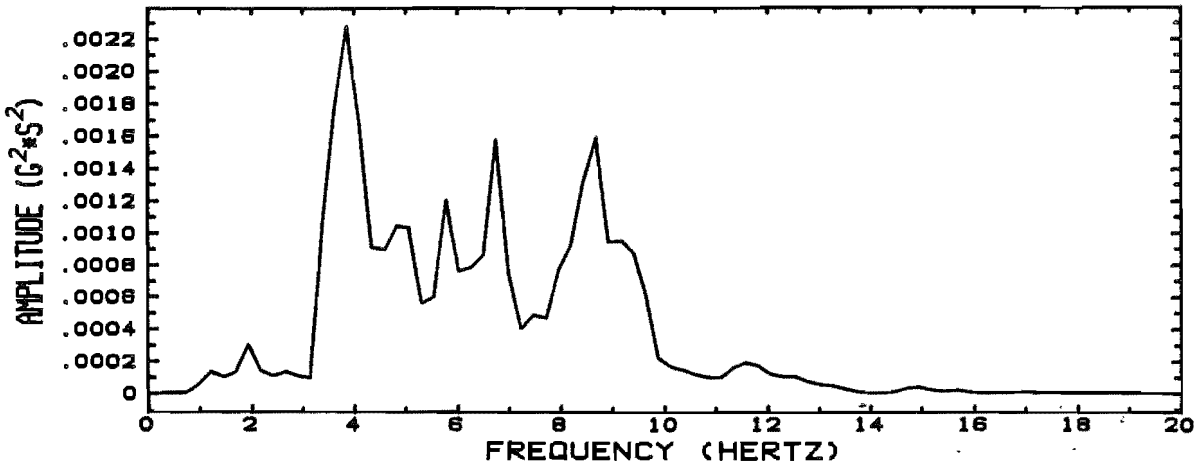

Fig. 5.21 Power spectral density function of Test 5 run 6: El Centro 1940 NS at time scale factor 10.

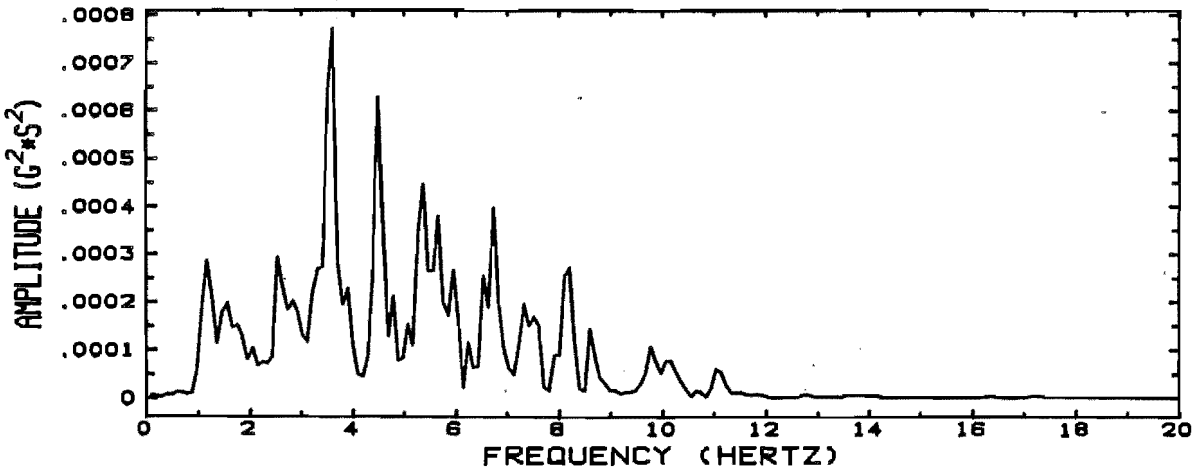

Fig. 5.22 Power spectral density function of test 6 run 2. El Centro 1940 NS, at time scale factor 3.

test 6, 100Hz was used to keep the data files to a manageable size (duration of test was much longer than in test 5). Data was saved in memory during each run, and written to a floppy diskette in binary integer format afterwards.

Discussion of problems of dynamic data logging and the pre-treatment of the data is in section 6.2.

5.3.12. Failure surface measurements.

In tests 1 to 3, no method of logging the failure surface was employed apart from mapping the failure surface outcrop. In test 2, bends were noted and measured in some of the reinforcing strips during dismantling of the wall after testing.

A grey sand was spread over one portion of the fill every 50mm or so of fill height in tests 4 to 6 to allow mapping of the failure surface, Fig. 5.23. (The main sand was white.) During dismantling of the walls after testing, a perspex box, machined to a knife-edge at the bottom edge, was pushed into the fill ahead of excavation (Fig. 5.24). By sitting weights on top of the box, it went down as the surrounding sand was removed. There was a limiting height of sand inside the box at which the weight used was not sufficient to push the box down against the sand-inside wall friction. The breaks in the darker sand layers could then be clearly seen and their position mapped. Also, as a result of careful dismantling, bends in all strips passing through the failure surface were noted and their position measured (Fig. 5.25).

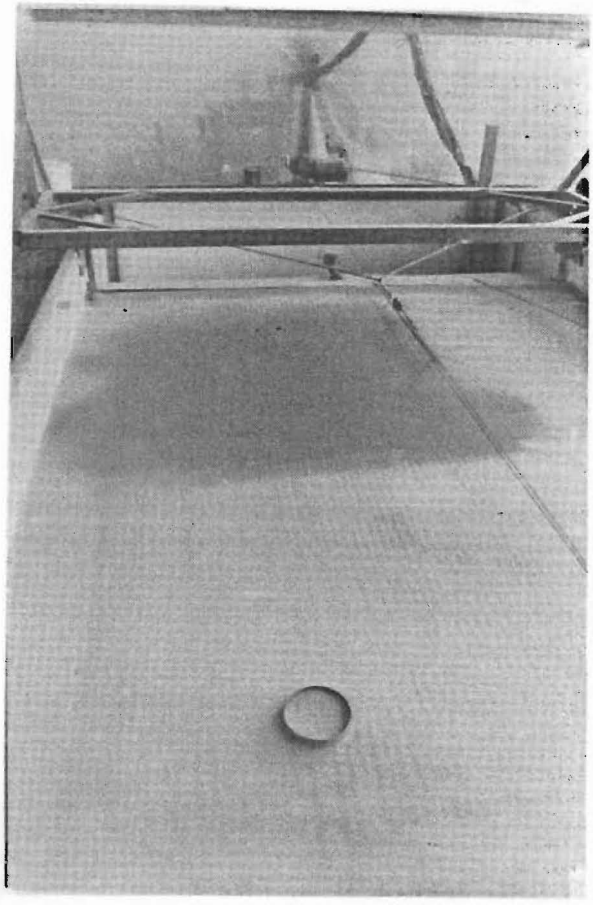

Fig. 5.23 Dark sand in preparation for mapping of the failure surface during dismantling. The greater mass of sand for density determination is also seen in place.

These methods are not as accurate as locating the failure surface with layer-by-layer removal of sand with a vacuum cleaner (Nagel, 1985). They were sufficient for this work, however, especially as the failure surface seemed to be less well defined than in Nagel's tests, at the advanced stages of

failure existing at the ends of these tests. Also, the failure surface had in fact split into several surfaces in test 5.

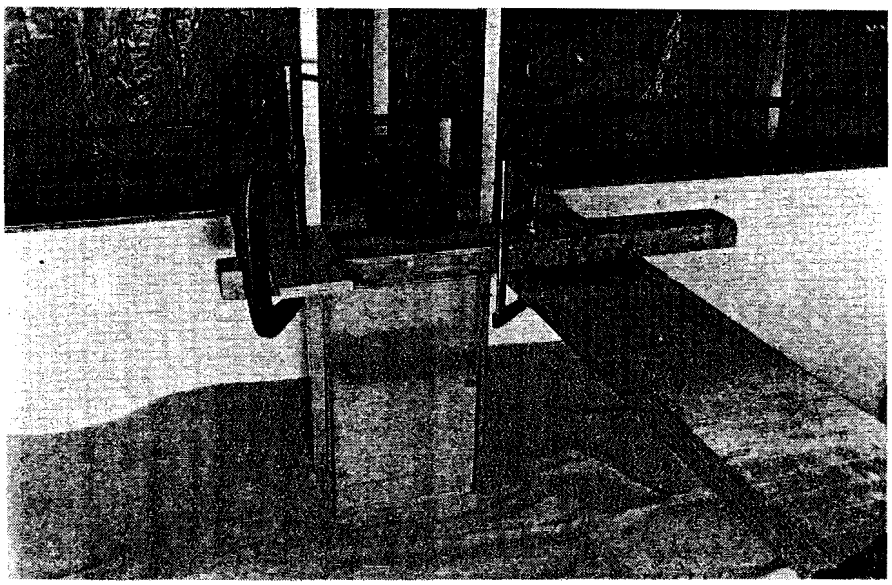

Fig. 5.24 Perspex box used for logging the failure surface. Discontinuities in the dark sand show the position of the failure surface.

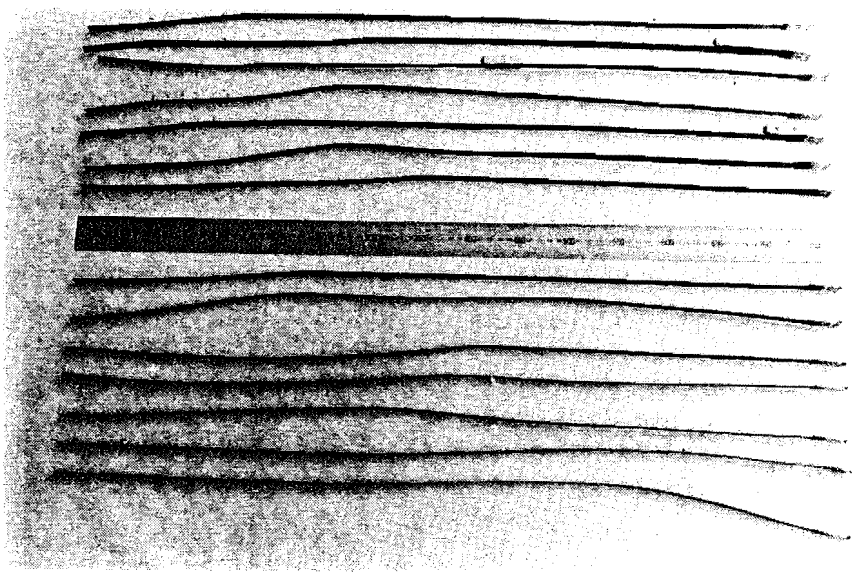

Fig. 5.25 Strips from test 6. Bends were logged to help determine the failure surface position.

The end-of-test position of walls 2 to 6 was measured after each respective test. It was noticed at the end of test 5 that there was a fine, barely visible line of dust on the side walls at what was the position of the sand surface at the start of the test. Hence it was possible to map the sand surface shape change fairly accurately. The fine dust line was also visible at the end of test 6.

5.3.13. Test configurations.

Table 5.3 shows the test wall configurations. Vertical spacing of strips was always the same. New slots were punched in the facing panels for the different horizontal spacings. Slots not being used were taped over to prevent sand leakage. Strip horizontal positions were always symmetric about the vertical wall centreline.

Table 5.3.
Test configurations. Top is the top half of the wall (5 strips), bottom is the bottom half of the wall (5 strips). N is the number of strips per metre length of wall.

Test	Excitation (see Table A.7)	Strip spacing mm Horiz.	Vert.	Length mm	N /m. of wall
1	FARLS2 & EQCV1D	250	100	750	4
2	FARLS2 & EQCV1D	330	100	1000	3
3	FARLS2 & EQCV1D	330	100	750	3
4	FARLS2 & EQCV1D	250 top	100	900 top	4
		160 bottom	100	500 bottom	6.25
5	El Centro 40 NS	250 top	100	900 top	4
	(time SF =10)	160 bottom	100	500 bottom	6.25
6	El Centro 40 NS (time SF = 3)	250	100	750	4

5.4. Testing for shear strength parameters.

The following sections outline the testing done to establish shear strength parameters for use in the limiting equilibrium calculations. They are, in order, apparent coefficient of soil/strip friction f*, and the angle of internal friction ϕ of the soil. There are two common methods used to find

f^*, the pullout test and sliding shear test. Both of these tests were done. There is further discussion of soil/strip friction in section 6.7.

5.4.1. Pullout tests for soil/strip coefficient of friction.

Preliminary pullout tests were done early in the project to try to find a suitable surface treatment for the reinforcing strips. A wire rope mechanism was used in those tests to pull the strips. It was not successful due to slip in the gearbox used. Testing to establish the value of f^* to use in the calculations therefore used a threaded pulling device, described below.

The maximum depth of fill possible above a strip was about 370mm. To obtain results applicable to greater depth, a surcharge of steel was placed on top of the fill in a second series of tests.

All pullout tests were done in Nagel's (1985) tank. A one-piece plywood wall facing was used, drilled as shown in Fig. 5.26. It was fully supported throughout. In an attempt to reduce edge effects due to the proximity of the wall during pulling, 14mm inside diameter PVC pipe sleeves 110mm long were fitted to the back (soil) side of the wall, and the strips pulled through the

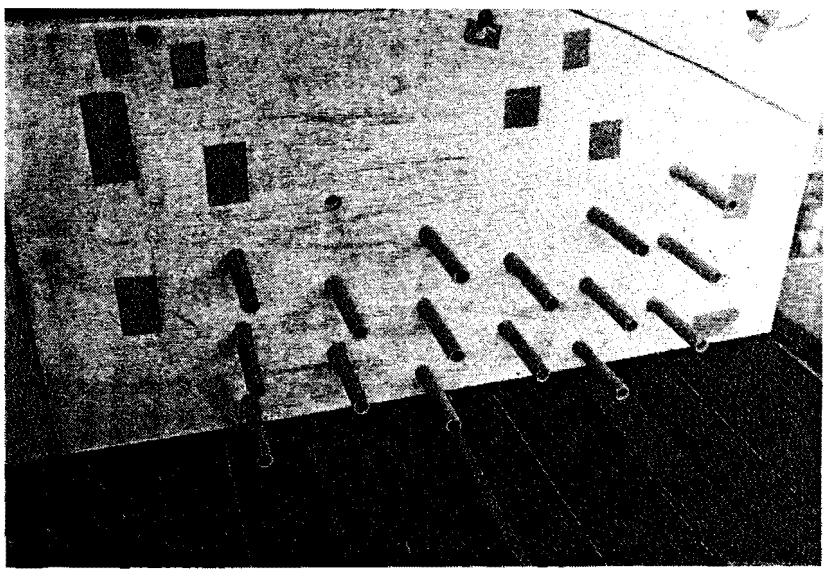

Fig. 5.26 The pullout wall, showing PVC sleeves fitted.

sleeves. Nagel's raining trough was used to build the fill. Strips were 1m. long (those used in test 2). Once the fill was up to the top of the wall, the pulling device was connected. It consisted of an electric motor connected through a gearbox to the end of a threaded rod (Fig. 5.27). A fixed-end-beam load cell was connected to two large nuts running on the threaded rod, and attached in turn to the end of the strip being pulled. To prevent the load cell from rotating during pulling, a small idler wheel was clamped to it such that the wheel ran on the floor of the tank.

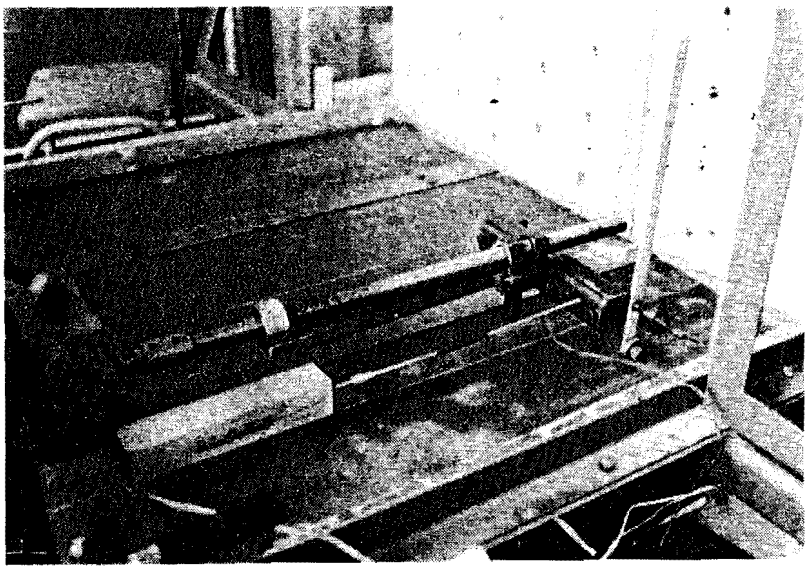

Fig. 5.27 The pulling device.

Data was captured using a Hewlett Packard X-Y plotter, connected through a high-quality amplifier. The X-axis was connected to a linear potentiometer which measured the displacement of the load cell. The load cell was calibrated before and after the test. Pulling commenced at the bottom of the wall. Speed of pulling was set arbitrarily at 30mm / minute.

To simulate greater depth, a surcharge of steel weights was placed on top of the fill in a second test (Fig. 5.28). 280mm extra fill height was obtainable in this way. A different wall was used, with the strip positions spaced further apart (Fig. 5.29): it was felt that there may have been interference between strips with the earlier arrangement. A higher capacity fixed-end-beam load cell was also used.

The apparent coefficient of friction was calculated from

$$f^* = \frac{T}{2bLy\gamma} \qquad \ldots\ldots\ldots(5.3)$$

where T is the pullout force, b is the strip width, L the resistant length, y the depth of the strip from the fill surface, and γ the unit weight of the soil. Fig. 5.30 shows all values determined. It is seen there that there is a substantial reduction in f^* with increasing depth. This is probably due to the effects of dilation in the sand. At small depths, the increase in confining stress due to dilation is significant compared to the pre-existing confining stress, whereas at greater depth it is less significant. It is also clear on Fig. 5.30 that there is severe scatter in f^* values determined in the tests. It is not reasonable, on the basis of the limited data, to postulate a formulation of how f^* varies with depth.

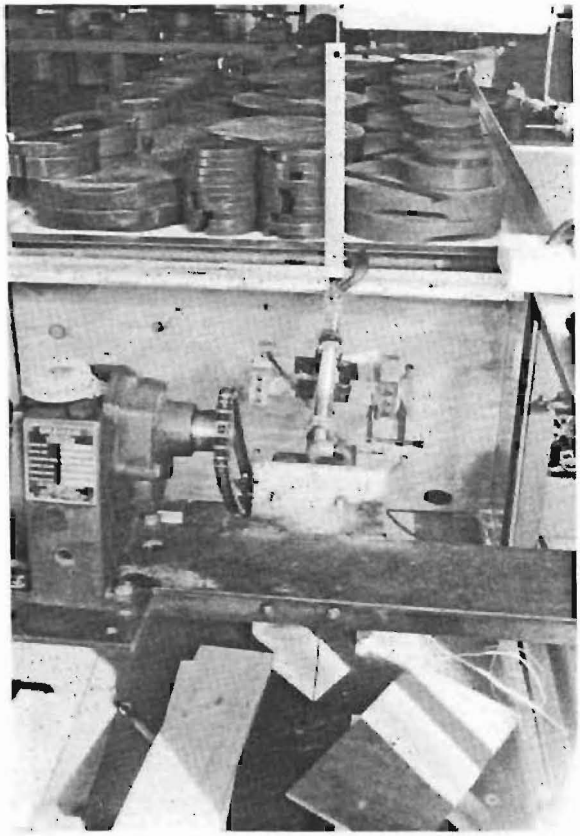

Fig. 5.28 Steel surcharge in plane strain pullout test.

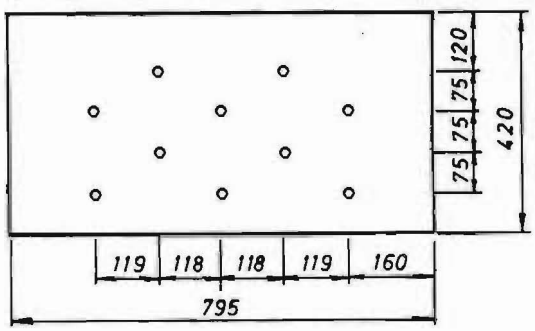

Fig. 5.29 Surcharge-test wall strip spacings.

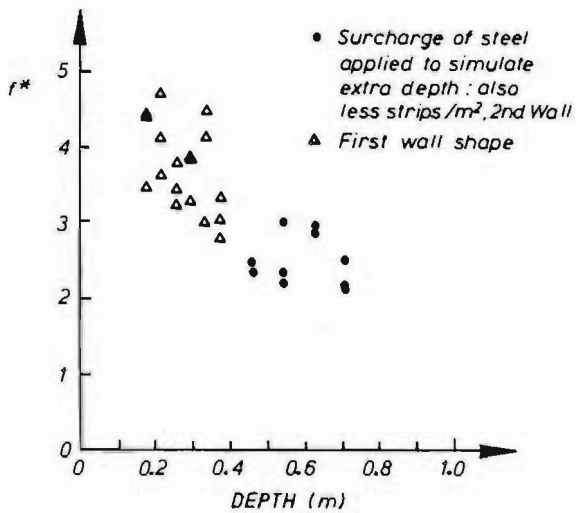

Fig. 5.30. f^* vs depth from pullout tests.

Fig. 5.31 shows how f* varies during pulling. There is an apparent relationship between f* and strip length. This does not necessarily mean that there is such a relationship though. It may be that as pulling progresses there is a decreasing effect from dilation of the sand, together with a very slight reduction in confining stress, as a small quantity of sand is removed through the sleeve with the pulled strip. Also possible is a "far end effect", where the effects of dilation reduce toward the interior end of the strip, and as the strip is pulled the overall effect of dilation is reduced as the region affected by the "far end effect" becomes a more significant part of the overall strip length. This effect would be in keeping with what others have found: that f*, determined from full scale pullout tests, is directly related to length for strips up to about 8m. long (McKittrick, 1978).

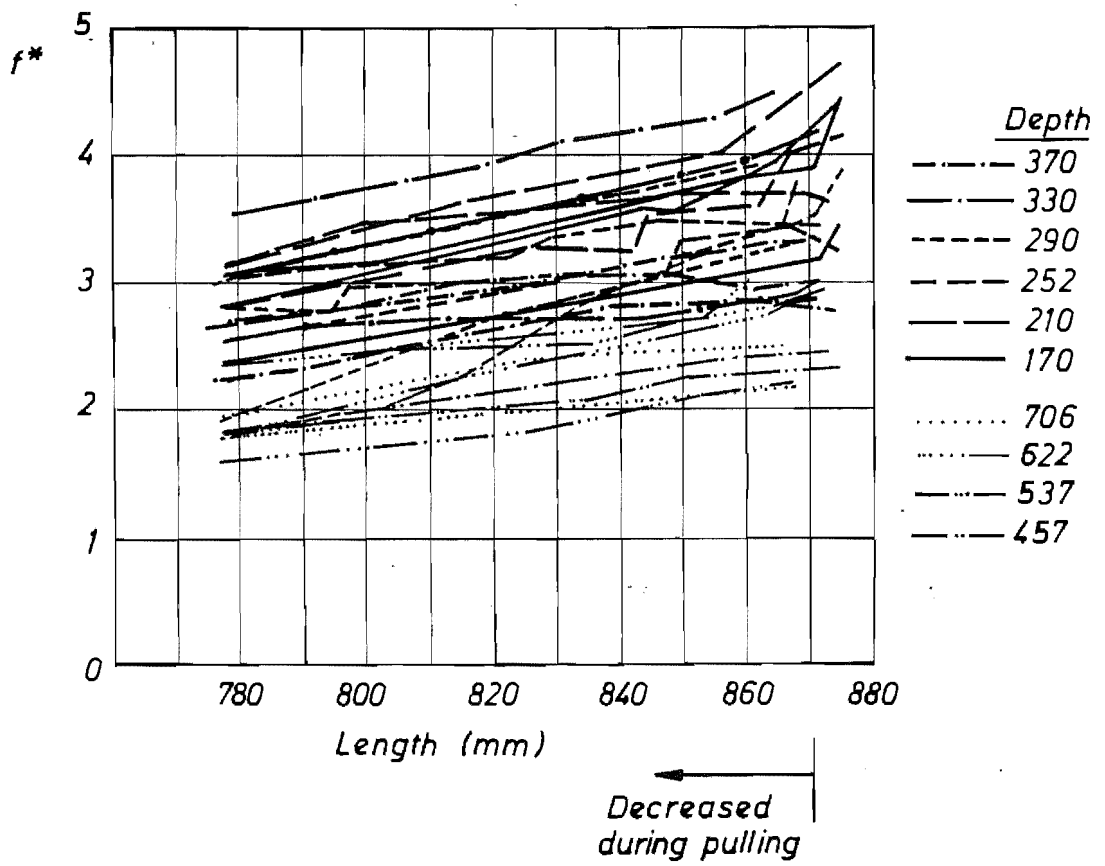

Fig. 5.31 f* vs resistant length of strip remaining in pullout tests.

5.4.2. Sliding shear tests.

The pullout test value for f* was thought to be unrealistically high. As a check on the values of f* derived, sliding shear tests were done in the direct shear apparatus.

A 100mm square shear box was used. A 25mm thick block of aluminium was machined to fit in the bottom of the carriage in place of the bottom part of the shear box. To the top of the machined block a sheet of the aluminium used to make the strips was attached with double sided tape. The surface of the sheet of aluminium had been prepared in the same way that the strips were: painted with zinc chromate primer, and sand spread and rolled on. An electronic load cell was used to record the shear force directly on an X-Y plotter, with an LVDT measuring displacement attached to the X-axis. Prior to the test the machine was run with no sample to measure the friction in the water-tight gland in the carriage.

Two tests were carried out. The first consisted of one forward and one reverse cycle (1.4mm travel each way). The second was three forward and three reverse cycles. The confining stress in both tests was 16.2kPa. Table 5.4 shows the values determined from the graphs for f*, the apparent coefficient of soil-strip friction.

Comparison of Fig. 5.30 and Table 5.4 shows that the values of f* determined in the two tests are widely divergent. The residual sliding shear values of f* are equal to about tan 40°. In the next section, it is found that the low stress value for ϕ of the sand is about 45°, so the sliding shear value of f* is close to tan ϕ, as it is for full size structures using ribbed strips (McKittrick 1978). Further discussion of soil-strip friction is in section 6.7

Table 5.4.
f* determined from direct shear tests.

Position of determination.	f*
test 1:	
Peak, forward run	1.32
lowest point, forward	0.95
same position, reverse	0.87
test 2:	
Peak, forward run 1	1.49
0.5mm, forward run 1	1.05
0.5mm, forward run 3	0.81
0.5mm, reverse run 3	0.77

5.4.3. Angle of internal friction of the sand.

The only soil parameter in the limiting equilibrium formulation is the angle of internal friction ϕ. Nagel (1985) used a value determined by multiple reversal direct shear at quite high confining stress (relative to his model test). Several tests were done in this study, initially at fairly high confining stresses, subsequently at confining stresses relevant to the 1m. tall wall models tested. It was found that the values determined at high confining stress were much too low to give satisfactory solutions of the equations 4.7, 4.15 and subsequently, 4.26.

Three test methods were used. First, multiple-reversal direct shear tests were done, using 2.5 inch (62.5mm) diameter circular samples. It seemed that the test did not give a good residual ϕ value, as the shear force varied very little during cycling: on each forward run it increased to a flat peak, then slowly reduced, and was still reducing at the same rate when the limit of travel of the machine was reached. On the reverse runs, a similar phenomenon was observed. It was felt that the travel was insufficient to reach the residual ϕ value: in each cycle the sand grains were just rolling back and forth.

To increase the actual displacement of the sand, a ring shear test was tried. Unfortunately the machine was new, and there was quite large clearance between the top platen and the surrounding carriage. There were rapid losses of sand as the test progressed. The shear stress reached an early peak and subsequently reduced as expected, but then started to rise again. This happened in all four tests done. It was felt that the increase was due to the sand forced up between the top platen and the carriage causing an increased friction area. A new top platen was made, with small clearance to the carriage. In addition, the sides of the new platen were tapered so that any material that did come between the platen and the carriage would rise easily into a wider area and cause only a very small increase in friction force. Two tests were done with the new top platen. Table 5.5 shows the results of all the shear tests, both direct and ring shear. All shear tests were done dry, as in the RE wall tests.

Table 5.5.
Results of tests for determination of angle of internal friction of Mt Somers sand. max means maximum, res means residual.

Confining pressure (kPa)	Friction angle ø (degrees)	Test.
98	32	Ring shear, new top platten.
49	34	as above
122.5	33 max 31 res	Ring shear, high losses.
49	37 max 32 res	as above
24.5	41 max 36 res	as above
24.5	42 max 36 res	as above
20.9	43 max 40 res	Multiple reversal direct shear
48.14	43 max 37 res	as above.
10.1	57 max 50 res	Vacuum triaxial
15	52 max <46 res	as above
22.2	47 max <42 res	as above

It was felt that the ø values determined in the above tests were not particularly reliable, especially those from the direct shear tests. They did show, however, that ø seemed to increase at low confining stresses. So three vacuum triaxial tests were done. A vacuum pump was used to partially evacuate the triaxial cell, and a large mercury manometer was used to measure the vacuum created. Condoms were used as membranes, to reduce membrane effects to a minimum. The samples were prepared (dry) by raining from a 4mm aperture funnel, held about 500mm above the sample. 0.9% / minute was the strain rate used. Fig. 5.32 shows the test results, and Fig. 5.33 shows how ø was found to vary with confining stress. A value of ø = 40° was chosen for use in the limiting equilibrium calculations.

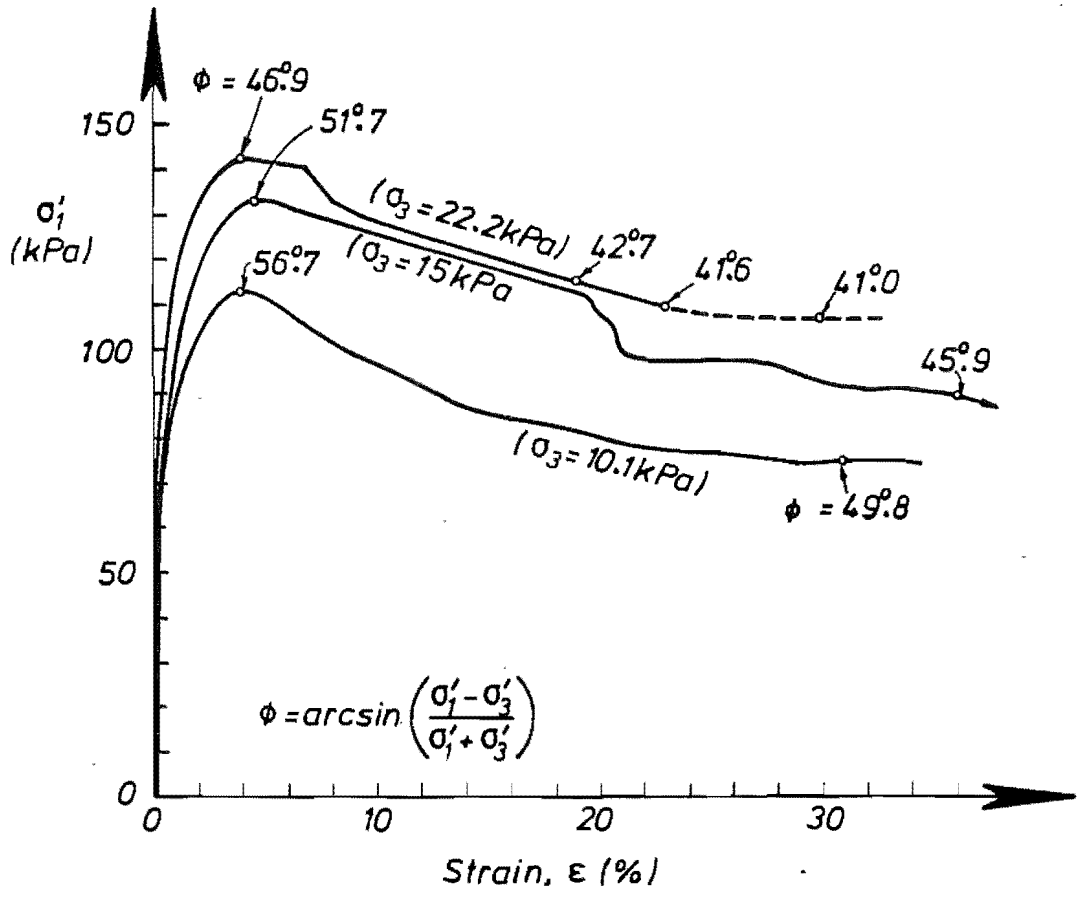

Fig. 5.32. Vacuum triaxial test results.

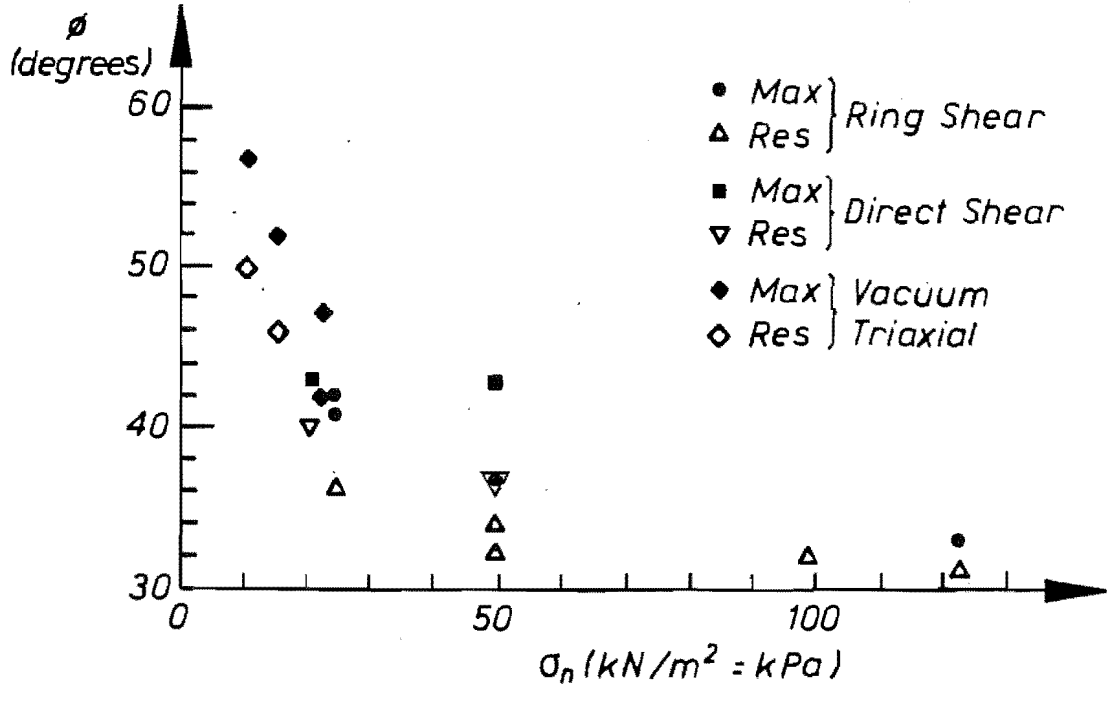

Fig. 5.33. Angle of internal friction vs. normal stress for Mt Somers sand.

CHAPTER 6

RESULTS AND ANALYSIS

6.1. Introduction.

This chapter presents and discusses the results of the testing. First, though, an overview of the data pre-analysis procedures and problems is given. Computing problems, wild point removal, dimensional scaling, removal of scanning slew (the time delay between channels), and filtering (smoothing) are included in the pre-analysis discussion. There is then discussion of the aliasing problem inherent in discrete digital sampling of time series. To complete the data treatment methods section, the overall analysis and graphing methods are outlined.

In the analysis of the results, the yield acceleration and failure geometry are studied first, and compared to predictions from the limiting equilibrium formulation derived in chapter 4. Next, the strip forces are presented, with forces during the excitations and distributions at specific times being considered. Then the observed forces are used in the limiting equilibrium formulation in place of the expression for R, the aggregated resistant force at the failure surface. Back-calculations of f^* and ϕ are done using observed k_h, α, and forces.

The mean mobilised f^* is back-calculated as above. Mobilised f^* is also calculated for each strip, at various locations along the strips, and compared to the pullout and sliding shear values. Other researchers have put forward different ways of deriving a design f^*, and some of those are discussed in the light of the test results.

Mobilised ϕ is then back-calculated, using k_h, α, and both observed forces and observed f* values, and compared to the test values. Dimensionless tension, which is similar to earth pressure, is calculated for the strip forces at the face and for the maximum strip forces, and compared to K_a, K_o, and the Mononobe-Okabe K_{AE}.

Measured displacements are discussed, and compared to the values predicted by Sarma's, Lin and Whitman's, and Newmark's methods.

A sensitivity analysis is presented for the parameters in the limiting equilibrium formulation, which indicates which parameters must be determined most carefully.

6.2. Data treatment methods.

6.2.1. Computing methods and problems.

Almost all computing (data reduction, displacement predictions, calculations using the limiting equilibrium formulation, etc) was done on an IBM PC-XT-compatible machine. Programs were written in Borland International Ltd's Turbo Pascal, versions 3.02 and 4.0.

Problems encountered were mainly due to the operating system. Firstly, the maximum data segment size is 64 kilobytes, and secondly, the largest data element (such as an array) allowed by the system is 64 kilobytes, which is quite small. To circumvent these restrictions, a special Pascal programming technique was used, namely a dynamic or linked list data structure. In this structure, several items (for example, 64 kilobyte arrays) can be linked in a list format, by attaching a pointer to the end of each item in the list to point to the starting memory address of the next one. List items can only be accessed sequentially, but the method does allow full use of the memory available. A "bug" was also found in one version of the operating system (PC-DOS 3.1), so a more recent version was used for the remainder of the project.

6.2.2. Wild point removal.

Various numbers of wild points, also called outliers, were present in the data. If left in the data, serious problems may arise in analysis. A single wild point occurring at a digitizer maximum value can seriously bias a power spectral density function by raising the overall noise level. Two such points close together introduce a number of spurious frequencies into the power spectral density (Bendat and Piersol, 1971). Filtering (smoothing) may not remove these spurious frequencies and hence the wildpoints will remain. There is no completely satisfactory general method for automatic removal of outliers (Otnes and Enochson, 1978; Bendat and Piersol, 1971).

Bendat and Piersol state that usually a first-difference check can be used to check for wild points, but manual correction is recommended for good results. There is too much data in this work for manual checks to be satisfactory. Otnes and Enochson give two methods for removing wild points, one of which was used here. The "Tukey 53H" procedure uses the fact that the median is a robust estimator of the mean. The median concept is applied twice, to compute an estimate of the smooth part of the signal, as follows (x(i) are the data points) :

1. Obtain a new sequence x'(i) from x(i) by finding the median, x'(3), of x(1),...,x(5). Delete x(1) and add x(6) to the set. The median of this new set becomes x'(4). This is continued until all points are exhausted. Thus there are four less x'(i) terms than there are x(i) terms. The median is always selected from a group of five adjacent points.
2. The sequence x"(i) is constructed from x'(i) in much the same manner, except that the span over which the medians are computed is of length three.
3. Compute the sequence x"'(i) from x"(i) using a Hanning smoothing filter:
   $x"'(i) = \frac{1}{4}x"(i-1) + \frac{1}{2}x"(i) + \frac{1}{4}x"(i+1)$
4. Analyse the sequence x(i)-x"'(i) to see if
   $|x(i) - x"'(i)| > eps$, where *eps* is a predetermined value. If it is, the point x(i) is deleted and a new point interpolated.

For the interpolation, a cubic spline procedure was used (see section 6.2.4). Points x(i-3), x(i-1), x(i+1), and x(i+3) were used to interpolate the new

point x(i). This was done because the interpolation procedure (described in section 6.2.4) had been already programmed for equally spaced data points.

During the preliminary trials of the CEDACS II data logger (it was new at the beginning of testing), it became clear that the normal scatter in the logged data was of the order of about 9 bits. (See §A.4 for an explanation of this.) For relatively smooth data, such as that from the sinusoidal excitations in tests 1 to 4, the test criterion *eps* was usually set to 9. This gave good results, although when there was 50Hz noise on the input (see §5.3.10) *eps* was usually set to 35 for the acceleration channels. If *eps* was left at 9 in these cases, the process acted as a smoothing filter, especially for the wall top acceleration readings. Displacement and strain gauge (force) readings did not display the high degree of oscillation that the acceleration channels did and so *eps* = 9 was usually suitable for them.

In tests 5 and 6 (El Centro 1940 north-south excitation), the data showed sharp peaks and rapid changes in the numerical value of the readings. For these tests, *eps* = 9 was too restrictive, causing the procedure to clip the peaks. This was especially so for the acceleration readings and for some, apparently critical, force channels. *Eps* was relaxed to 35 for the three acceleration channels, and sometimes 15 for all the other channels. The peaks in the displacement and force readings were generally less sharp, although for some runs other channels were equally as spiky as the acceleration channels. For example, channels 9, 22, 52 etc in Table 6.1.

Table 6.1 shows the number of wild points removed from each channel for test 5 run 8, for two values of *eps*. There were 1604 points in the data file.

The Tukey53H procedure is not completely satisfactory. If there are two wild points adjacent, one at greater distance from the likely smooth function value than the other, one of them may be actually increased in distance from the "smooth value", and the other greatly reduced. Fig. 6.1 shows a part of test 1 run 9 input acceleration, where there are two such points, as well as the same data after application of the Tukey53H procedure with *eps* = 9. It can be seen there that point number 336 has actually moved further from the "smooth function" value, and number 337 has moved closer.

Table 6.1
Number of wild points removed from each channel of test 5 run 8 data, for *eps* = 9 and 35. There were 1604 points in the data file.

Ch. No.	No. wild points for *eps* = 9	35	Ch. No.	No. wild points for *eps* = 9	35	Ch. No.	No. wild points for *eps* = 9	35	Ch. No.	No. wild points for eps = 9	35
1	18	2	15	16	1	29	14	0	43	10	2
2	301	18	16	10	1	30	17	1	44	8	0
3	32	1	17	14	0	31	12	2	45	7	0
4	21	3	18	10	0	32	483	2	46	5	1
5	17	5	19	16	1	33	667	1	47	7	0
6	13	0	20	11	1	34	14	1	48	10	1
7	5	1	21	8	0	35	19	2	49	9	2
8	23	1	22	875	1	36	8	2	50	18	0
9	1054	5	23	10	0	37	50	0	51	103	0
10	11	4	24	13	0	38	10	0	52	972	7
11	9	3	25	17	3	39	13	1	53	61	1
12	940	2	26	12	7	40	11	0	54	15	4
13	170	1	27	12	4	41	8	1	55	4	0
14	16	1	28	15	5	42	11	0			

The problem arises in the interpolation procedure where if either x(i+1) or x(i+3) are themselves wildpoints, the new point is placed some distance away from the "smooth" function value. An alternative is to extrapolate the new point from the previously tested and possibly extrapolated data. Unfortunately this procedure can lead to a completely new function being produced, if certain conditions exist. An extrapolation counter must be used, and the routine stopped if more than a set number of points in a row are replaced.

A better alternative would be to calculate and test all the x"'(i) before doing any interpolation. Then if the points x(i+1) or x(i+3) are themselves wildpoints, then some other points should be used for the interpolation (x(i+2), x(i+4), etc). In this case the interpolation procedure would be working with non-equally spaced points, which is perfectly possible with the cubic spline procedure that was used. Unfortunately, with the large number of data points in the "earthquake" data files (tests 5 and 6) it was not possible to keep all the data required in memory at once, so the Tukey53H tests were done "in a bubble" with just enough points considered to derive one x"'(i) at a time. The new point was interpolated at that time, before testing the forward points. In hindsight it would have been better to test all points

before interpolating new data points. This could still be done "in a bubble" with an array to store the point numbers of the bad data.

These problems apart, the Tukey53H procedure seemed to give quite good results.

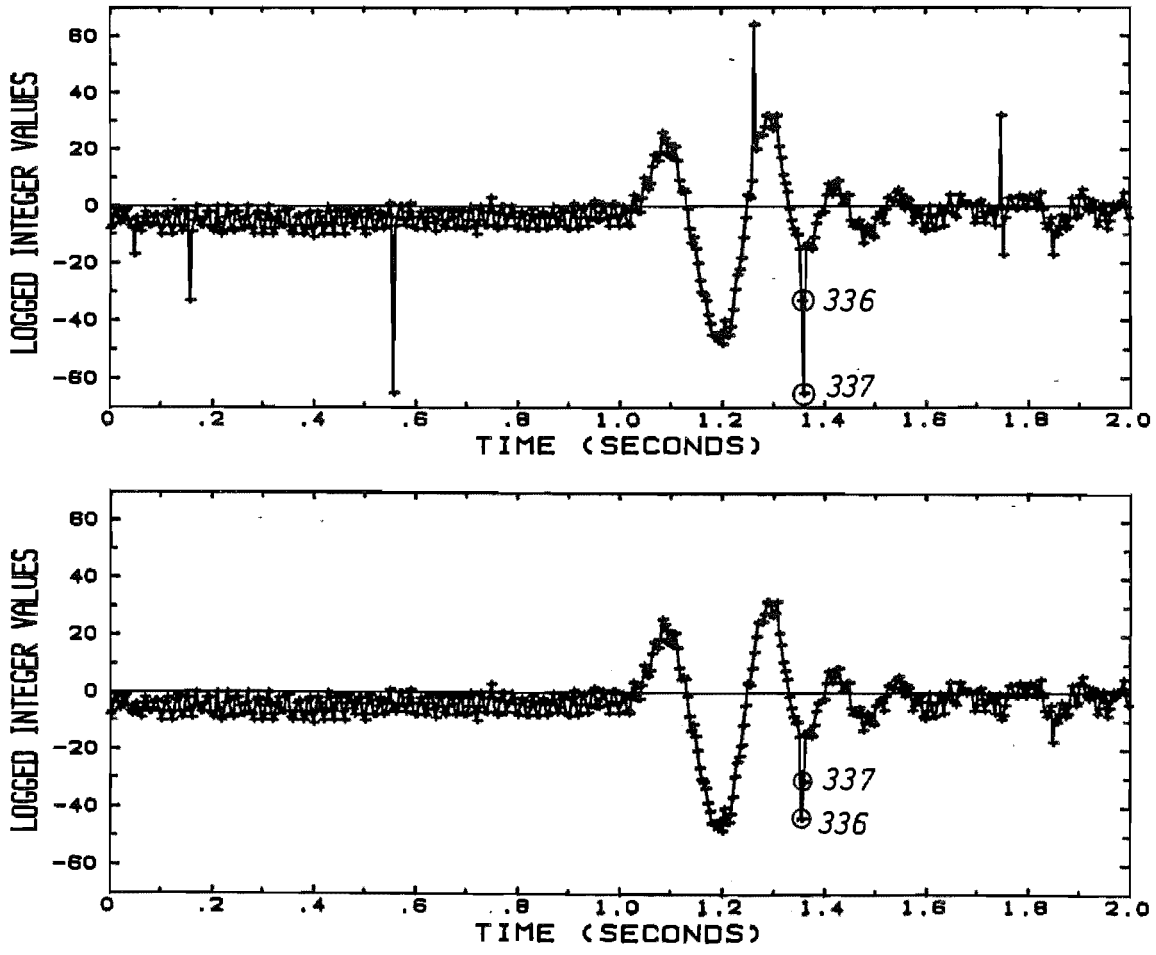

Fig. 6.1. Test 1 run 9 input acceleration: with wild points (top), and after running through the Tukey53H procedure, *eps* = 9.

6.2.3. Dimensional scaling.

As described in section A.4, the data values were stored as two-byte integers in the range -2047 to +2048. To convert to a dimensional number (Newtons, g's acceleration etc), it was necessary to subtract a zero reading from the integer data values, and then to multiply by a scaling factor. The multiplicative factor was found by calibration of the relevant transducer. Zero readings were taken before testing, and for the strain gauges, zeros were

read before any sand was deposited over the strips. Scaling was done after removal of wild points.

6.2.4. Scanning slew removal.

Scanning slew refers to the delay between the time of scan for each channel. They were scanned sequentially, starting at channel 1 and stepping through to channel 55, then starting at channel 1 again. In order to make comparisons between channels at the same time instant, it was necessary to interpolate new points between the measured points. All channels (except the first) were interpolated to bring them to the same time origin as channel 1, the base excitation accelerometer. Thus each channel had a different time step for interpolation.

The cubic spline method of piecewise polynomial interpolation was used (Johnston, 1982, §3.1.2). The boundary condition at the beginning of the data was that the third derivative was set to zero, thus forcing the first two polynomial pieces to coincide. That at the end of the data was similar. After return from the cubic spline procedure, the new points were calculated using the returned spline coefficients. This interpolated data was used for all subsequent analysis.

6.2.5. Smoothing the data.

For the sinusoidal-excitation data, it was felt that smoothing would aid the study of force distributions in the reinforcing strips. With smoothed data, graphing a force distribution at a specific time would give a better representation of the underlying shape of the distribution. This was especially so for those test runs with the 50 Hz noise present (see section 5.3.10), where a small time shift may make quite a difference in the distribution shape.

In tests 5 and 6, the earthquake excitation tests, forces were expected to be much more transitory. In that case, the relationship of the magnitude of the peaks to the residual forces is important, because it is most likely

that a strip will break suddenly at a high peak. So smoothing was not used at all in those tests.

Smoothing was done in the frequency domain. A fast Fourier transform algorithm was used to derive the Fourier amplitude spectrum of the sampled data. The amplitude spectrum was then truncated at the required frequency, and set to zero for all points corresponding to larger frequencies. The inverse transform then produced the smoothed data. At the frequency truncation, a short (usually 5Hz) half-cycle cosine function (with ½ added to make it positive) was used to smooth the truncation. Appendix D outlines some of the problems encountered in discrete Fourier transform computations for spectral density functions; the comments apply equally to derivations of the Fourier amplitude spectrum.

In Appendix D there is mention of the Parzen window used for leakage suppression. In the smoothing program a simple cosine window was used, whereby the first and last quarter of the data array were multiplied by rising and falling half-cycle cosine functions respectively. This window is not particularly good at reducing the height of the sidelobes of the transformed box-shaped truncation function (see Appendix D), so the leakage suppression was not particularly good. With truncation usually at 40Hz, and most of the frequency content of the data in the 2 to 15Hz range, the distorted frequency spectrum truncated above 40Hz should contain little of the power in the data from the lower (sub-30Hz) frequencies. Comparisons between the smoothed and unsmoothed data showed that the smoothing was satisfactory: the amplitudes were similar and the unwanted high frequency ripples were removed quite well.

Note that the windowing for leakage suppression is done before the forward Fourier transform is performed. Thus after completing the inverse Fourier transform to produce the smoothed data, the data will still be factored by the tapering window used for leakage suppression. With the window used in the smoothing program, though, the end portions of the data which were factored were usually not critical - they were part of the slow displacement ramps used to move the shake table actuator out to its starting displacement and back to its resting place after the test run. The excitation of interest was rarely in the area affected by the windowing function.

All transforms done for smoothing were with 2048 points, the data being padded with zeros to make that number of points. With 247Hz scanning of the data channels, this gave a resolution bandwidth in the frequency domain of 0.24Hz (247/1024). The 40 Hertz frequency truncation value effectively removed the 50Hz noise sometimes present on the data.

6.2.6. Data file format.

In the course of the above operations (wild point removal, scaling, slew removal, and filtering) the data was broken up into units of like data. The three acceleration channels were stored as one file, as were the two displacement channels. The force data for each strip (5 channels) was stored as a file, making ten strip force files for each test run. All data was stored in binary real format to save space on disk.

6.2.7. Aliasing.

One potentially serious problem with dynamic data logging is that of aliasing. The maximum frequency of wave form that can be defined unambiguously is one-half of the scanning frequency. This is because there must be at least two points logged per wavelength to define a wave; anything less is interpreted as defining a lower frequency wave. Such a wave will have frequency less than half the scanning frequency. Hence one-half the scanning frequency is called the folding, or Nyquist frequency, as waves of higher frequency are effectively folded around the Nyquist frequency into the lower frequency domain. This effect is called aliasing. Such folded frequencies can only be removed at the analog stage, before digitizing (Bendat and Piersol, 1971). On a Fourier amplitude spectrum, aliasing (ie. time domain sampling interval too large) shows up as small ripples in the spectrum.

Anti-aliasing filters were ordered but were not available in time for use. Thus there may be some frequency content in the logged data that is in fact folded from the band above the folding frequency. In tests 1 to 5 the scan rates were more than ten times the maximum excitation frequency (excluding the 50Hz noise sometimes present), and in test 6 the scan rate was

five or more times the maximum input frequency. Thus it is felt that there should be very little folded frequency content, although there is no way to tell how much there is. (Prevention of aliasing was an important reason for using the fastest scan rate that the data logger was capable of, although in test six the data file size - because of storage and processing requirements - was the limiting criterion.) Power spectra, Fourier spectra, and even response spectra, are all distorted by any aliased frequency content (Bendat and Piersol, 1971).

6.2.8. Graphing systems.

Study data was graphed using the Turbo Pascal Graphix Toolbox from Borland International. This allowed rapid preparation of graphs, and their "dumping" to a dot matrix printer. The ability to look at the logged data immediately after each test run greatly expedited the testing program, as well as allowing good control of the testing parameters (mainly the maximum acceleration) for the following run. Generally during testing only the acceleration and displacement channels were checked.

It should be pointed out that the graphs shown in this report rarely start at time = 0. Data logging was started manually, and there is nearly always a little of the slow table displacement ramps logged (see section 5.3.10). This portion of the data is omitted from the graphs.

Programming for graphs of force distributions in the reinforcing strips allowed several distributions, at different time instants, to be taken from a data file. This allowed changes in shape of the distribution to be observed, as well as peak values to be shown by taking several cuts around the expected peak. With the non-smooth data from tests 5 and 6 the ability to take such multiple cuts was particularly useful. The force distributions shown in section 6.4.2.2 where drawn from study of these computer-graphed distributions.

6.3. Observed k_h and α in the limiting equilibrium formulation.

In the following sections the observed yield accelerations and failure surface geometries are shown, and then tested against the predictions of the limiting equilibrium formulation. The values of ϕ and f* used are those derived in the testing described in section 5.4.

6.3.1. Observed yield accelerations, k_h.

Observed yield accelerations were found to decrease at the time the failure surface became fully developed, that is, outcropped at the fill surface. Such a decrease is expected in the case of a dense sand, as the peak shearing resistance is somewhat higher than the residual resistance. Before the failure surface is complete, a part of the area being sheared still has higher (peak) strength. Once the failure surface outcrops, the entire zone in shear has a lower resistance, characterised by the residual angle of internal friction. Hence the yield acceleration is lower than before the failure surface is fully developed. Table 6.2 shows observed yield accelerations for selected test runs. (Recall that tests 1, 2, 3, and 6 were rectangular block structures, 4 and 5 stepped blocks. Tests 5 and 6 used "earthquake" excitation.) Table A.7 in Appendix A shows the excitation of each run.

There were several earthquake-excitation runs where the yield acceleration seemed to decrease during the run. It is understandable that this should happen during runs before and when the failure surface became fully developed. In those cases the resistance would be reducing as the proportion of the failure surface not developed is decreasing and hence the average resistance to shear in the sand is also reducing. T6r6, however, had a fully developed failure surface. It could be that the yield acceleration is proportional to some characteristic of the excitation peak at which it is measured, but Rea and Wolfe (1980) and Sommers and Wolfe (1984) showed that it is independent of the excitation. This variability may be due in part to the stick-slip nature of strip pullout. More likely is the temporary sticking and release

of one end of a facing panel in the plywood box sidewall. A restrained panel would cause an increase in the resistance of the RE wall to deformation.

Table 6.2
Yield accelerations for selected test runs. Italic run numbers are those at which the failure surface became fully developed.

test/ run	yield acceln (g)	test/ run	yield acceln (g)	test/ run	yield acceln (g)	test/ run	yield acceln (g)
t1r13	0.28	t2r1	0.36	t3r3	0.20	t5r2	0.28
t1r14	0.30	t2r3	0.32	t3r4	0.21	t5r3	0.32
t1r15	0.31	t2r6	0.34	t3r5	0.23	t5r4	0.32
t1r19	0.36	t2r8	0.28	t3r8	0.26	*t5r6*	0.21-0.17
t1r20	0.37	t2r9	0.33	t3r10	0.20	t5r7	0.22
t1r23	0.34	t2r10	0.30	*t3r11*	0.13	t5r8	0.22
t1r25	0.35	t2r11	0.32	t3r12	0.08	t5r9	0.17
t1r27	0.27	t2r12	0.27	t3r14	0.09?		
t1r28	0.25	*t2r13*	0.24	t3r16	0.06	t6r1	0.38-0.29
t1r30	0.26	t2r16	0.20			t6r2	0.38
t1r32	0.24	t2r17	0.20	t4r8	0.30	*t6r3*	0.37-0.18
t1r34	0.24	t2r20	0.21	t4r12	0.36	t6r4	0.23-0.18
t1r37	0.23	t2r23	0.19	t4r14	0.36	t6r6	0.26-0.20
t1r40	0.22			*t4r17*	0.23	t6r8	0.22
t1r43	0.23			t4r20	0.20		
				t4r24	0.19		

Some actual response accelerations are presented and discussed in section 6.9.1, along with displacements.

6.3.2. Observed failure geometry.

Fig. 6.2 shows the failure surface outcrop shapes in plan view. It can be seen there that the effect of the side walls are that the outcrop is generally concave toward the retaining wall. The apparent width of the most affected region is about one-quarter of the box width at each side. In Appendix A (§ A.1) it is shown that a box twice as wide as the wall is high should introduce only small (≈5%) errors in active earth pressure determinations, with glass sidewalls. From the shapes of the failure surface outcrops, it is difficult to say whether the effect is so small; it could be greater than that in this testing. Certainly the side walls were painted filled plywood rather than glass.

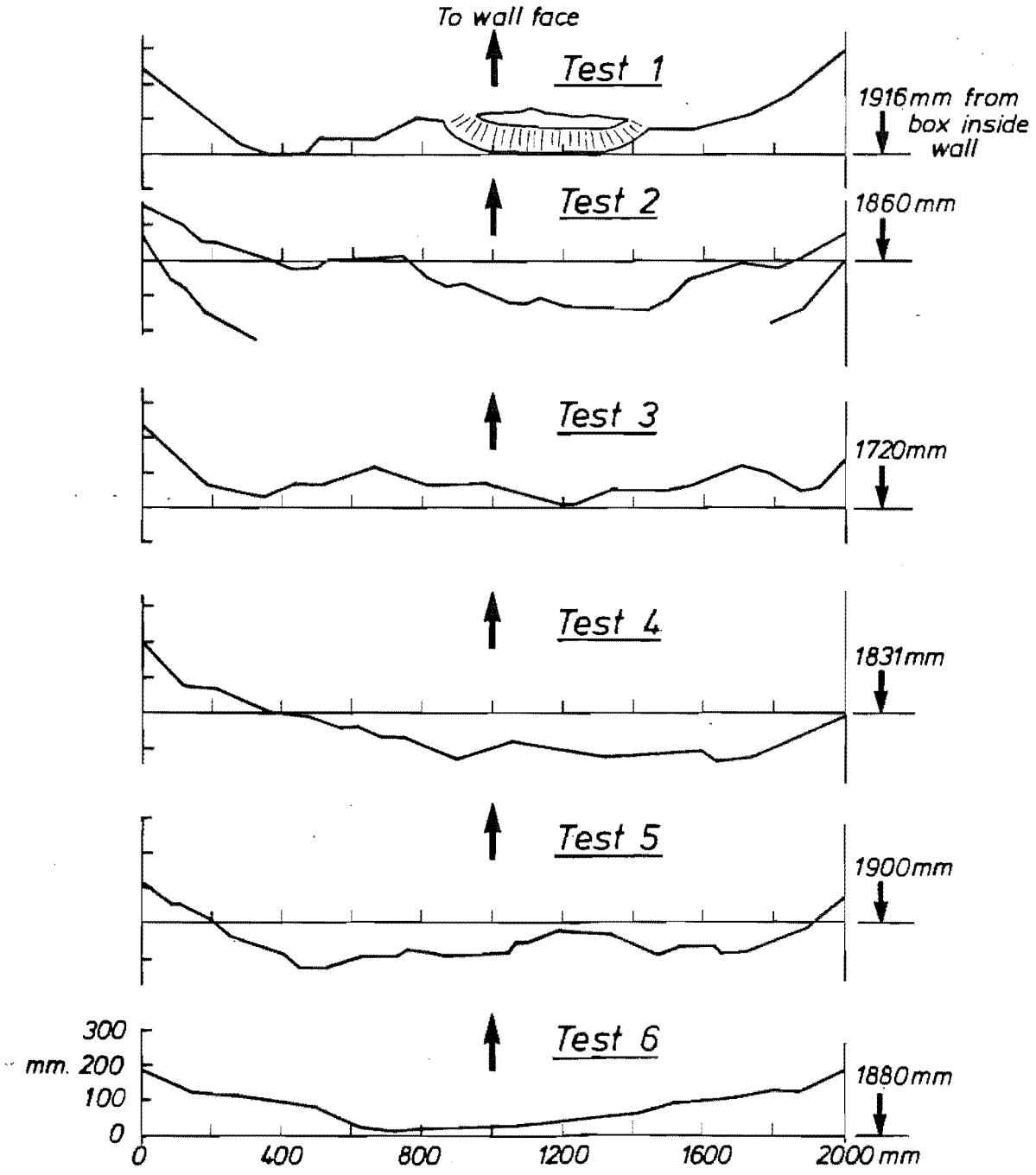

Fig. 6.2. Failure surface outcrops, plan views, test 1 to 6. The arrows point outwards toward the walls.

Figs. 6.3 - 6.8 show the failure geometries of each test, and the line assumed to represent the failure surface for the purpose of calculations.

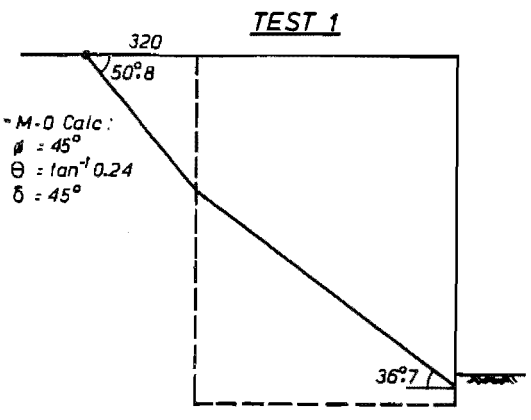

Fig. 6.3. Failure geometry, test 1. Wall final position not measured.

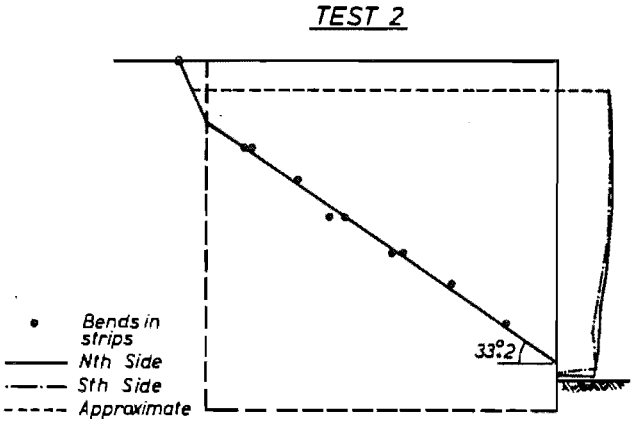

Fig. 6.4. Failure geometry, test 2.

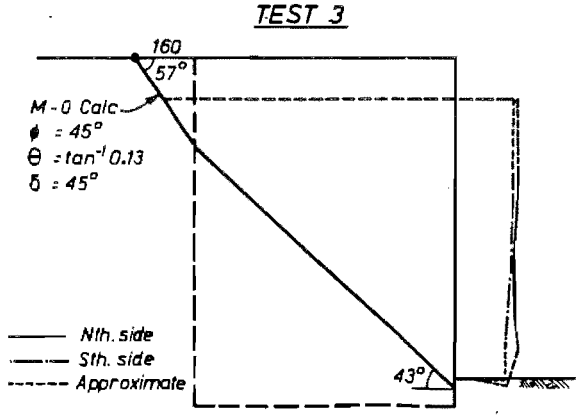

Fig. 6.5. Failure geometry, test 3.

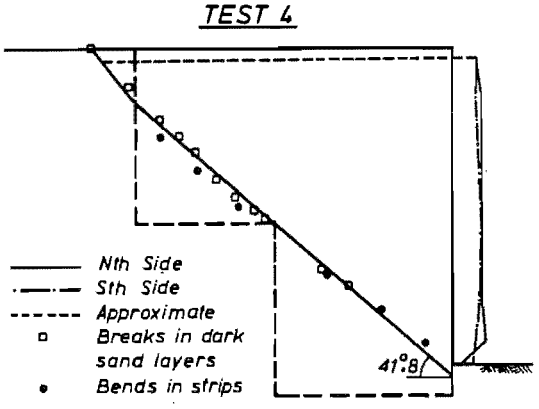

Fig. 6.6. Failure geometry, test 4.

As mentioned in section 5.3.12, there was no measurement of the failure surface location in tests 1 to 3, although bends in the strips were logged during dismantling of wall 2 - Fig. 5.25 showed some similar bent strips from test 6. With the lack of data for the failure surface in tests 1 and 3, an attempt has been made to calculate the failure angle in the retained wedge behind the reinforced block, assuming that Mononobe-Okabe (M-O) theory is applicable. The equation used was (MWD, 1973)

$$\cot(\alpha - i) = -\tan(\phi+\delta+\beta-i) + \sec(\phi+\delta+\beta-i)\sqrt{\left(\frac{\cos(\beta+\delta+\theta)\sin(\phi+\delta)}{\cos(\beta-i)\sin(\phi-\theta-i)}\right)} \qquad \ldots\ldots\ldots(6.1)$$

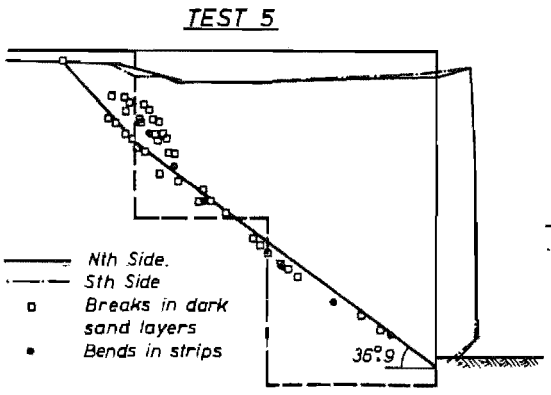

Fig. 6.7. Failure geometry, test 5.

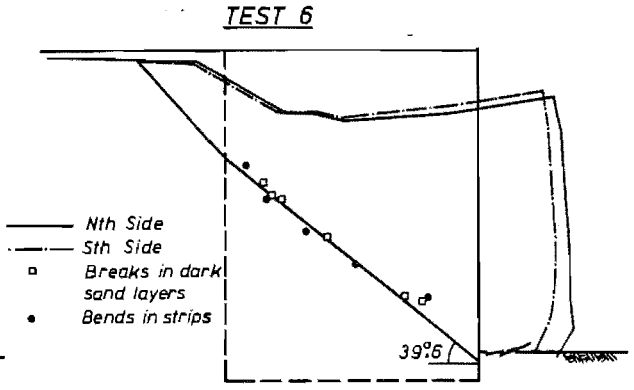

Fig. 6.8. Failure geometry, test 6.

where α is the failure surface angle to the horizontal, i is the slope angle of the backfill measured against the horizontal (in our case, always 0), δ is the friction angle at the back of the wall, β is the slope of the rear of the wall measured from the vertical and positive when the heel of the wall is further into the fill than the top rear (in our case, always 0), and $\theta = \tan^{-1} k_h$. As shown in Figs. 6.3 and 6.5, the friction angle δ of the wedge on the rear of the wall was taken as 45°, the same as ϕ. For the wall 1 calculation, if δ is taken as 0°, the angle the rear slope of the wedge makes with the horizontal increases from 50.8° to 58°. Once the retained wedge was estimated, its base (ie. at the rear of the reinforced block) and the observed failure surface position at the wall facing were joined on the diagram (Fig. 6.3 and 6.5) and this line assumed to represent the failure surface. Shown on each figure is the information used to map the respective failure surface, namely bends found in the strips during dismantling, discontinuities in the coloured sand layers, and the failure surface outcrop. Where the deformed fill surface was measured (tests 5 and 6), it is also shown on the relevant figures.

The failure surface shapes in Fig. 6.3 and 6.5 are thus assumed bilinear. In Fig. 6.4 the shape is also bilinear, using the bends logged in the strips to define the failure surface. Note that in this figure the surface seems to meet the wall facing at about 865mm below the wall top, which is 15mm below strip 2. In all the other walls the failure surface intersected the facing at a point just above the lowest strip in the wall. Where the failure surface was carefully logged with coloured sand layers, it is slightly curved (Fig. 6.6, 6.7, and 6.8), concave upward. Fig. 6.6 shows that the failure surface

in test 4 was barely bilinear, very nearly contradicting one assumption of the limiting equilibrium formulation. In Fig. 6.7 (wall 5) it is a little more curved, but also splits into several branches at about 400mm depth. There is slightly more deviation in the direction of the top part (retained behind the reinforced block), compared to the failure surface inside the block, then in wall 4. The failure surface logging for wall 6 was less certain because of the very advanced state of failure at completion of the test. The coloured sand layers had been dispersed and could not be identified closer than about 350mm from the fill surface.

The dispersion of the coloured sand layers near the rear of the sliding block in test 6 is thought to be caused by the same phenomenon as the failure surface branching seen in wall 5. Wall 6 was in a more advanced state of failure than wall 5 at the end of the test, as can be seen by comparing the total outward movement of the facings in Fig. 6.7 and 6.8. If the failure surface was bilinear one would expect to observe a confused deformation pattern around where the change in slope of the failure surface occurs, developing as the wall outward displacement increased. It is felt that the scarp pattern seen late in test 3 (shown in Fig. 6.9) arises in the same way. The deviation between the directions of the failure surface in the retained and reinforced blocks is similar in test 5 and 6 (Fig. 6.7 and 6.8).

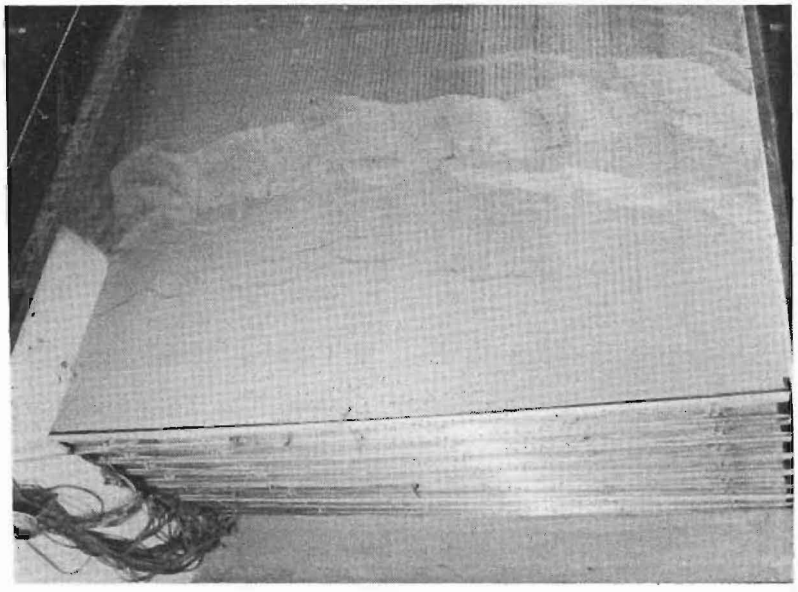

Fig. 6.9. Surface outcrops of graben-like structures seen late in test 3.

From these figures, it is clear that the planar failure surface approximation adopted in the limiting equilibrium formulation is acceptable, although M-O theory probably predicts that the wedge of retained soil behind the reinforced block has a steeper "rear" surface than in fact it does. The effect of this is that the mass of soil in the active block is a little greater than assumed in the limiting equilibrium formulation.

There were other differences in the failure shapes observed. In test 1 the bottom facing panel rotated outwards to lie nearly flat at the end of the test. In all the other tests, the second panel rotated to lie flat at the end of the tests. The bottom panel stayed vertical, although it was bent along a horizontal axis. Fig. 6.10 shows an end view of the lowest panel after test 6, where the longitudinal bend can be seen. Such bending indicates that the failure surface actually starts below the top of the bottom panel, and that the lower part of the panel is held quite firmly by the burial depth of sand in front of the wall. With the geometry used here, the 8.5% burial depth covers the lowest 85mm of the bottom panel, so the top part of the panel provides less resistance to the moving sand in the bottom of the failure block, and is thus bent over. It is not clear why the bottom panel in test 1 should rotate as it did. It may be that for some reason the density of the fill in front of that wall was lower than in other walls, and was more easily displaced by the rotating panel. It may also be the case that the 8.5% burial depth was not strictly observed, and the fill was in fact a little lower than required by the rule.

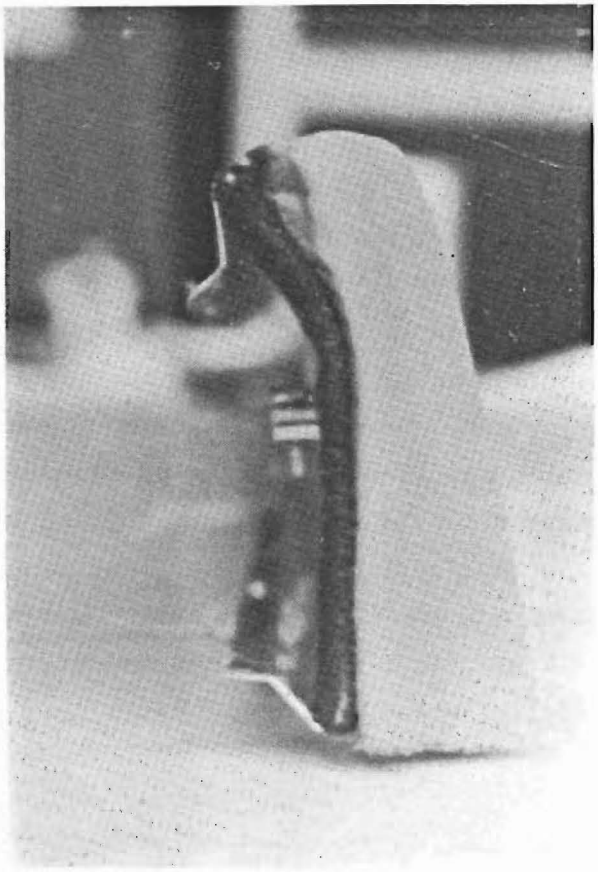

Fig. 6.10. End view of the bottom panel after test 6. On the right is the nylon sealing flap attached to the panel.

In test 1, the fill in front of the wall was built after the wall was otherwise finished. In walls 2 and 3, the burial fill was placed during construction. In tests 4 to 6, the burial fill was placed after construction. (Section 5.3.3 described how the fill was placed.) Walls 4 to 6 behaved similarly to walls 2 and 3. It appears unlikely that the method of fill placement caused the different wall behaviours. The density of the fill varied between tests (see section 5.3.4, and Table 5.2) but is not thought to have affected behaviour that much. Indeed, the highest density was measured in test 1, and that test was the only one where the bottom panel rotated during the test.

The only other differences between test 1 and subsequent tests were the craters at the side walls during test 1, caused by sand leakage, and the panel end-sealing details. For wall 1 brown PVC parcel tape was used for end seals, whereas walls 2 to 6 used a synthetic fabric, as well as a knit fabric wrapped around the panel ends to try to prevent them from digging into the plywood and catching. The end sealing details should have negligible effect. We would expect the leakage craters in test 1 to have reduced the sidewall friction, and thus a slightly lower yield acceleration to be observed, but it appears from a study of Table 6.2 that this is not the case. Test 6 values are fairly similar (wall 6 had the same configuration as wall 1, 750mm strips at 250mm centres horizontally).

6.3.3. Comparison of observed k_h and α, with limiting equilibrium formulation predictions.

Fig. 6.11 shows plots of yield acceleration k_h vs failure surface angle α for the 4 test configurations used. This was the sort of plot produced from all calculations using the limiting equilibrium formulation. Brent's (1973) zero-finding algorithm was used to iterate on k_h using Eq. 4.15 or 4.26. To

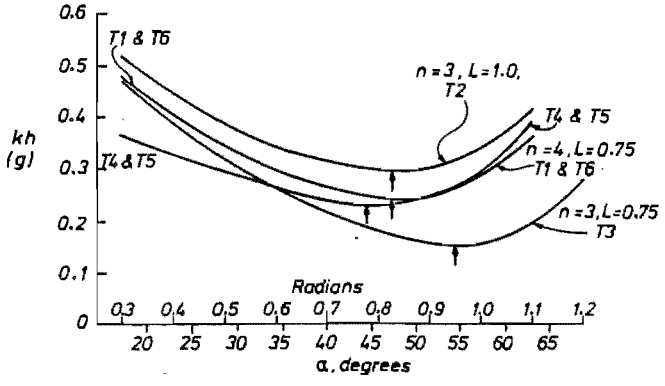

Fig. 6.11. Yield acceleration k_h vs failure surface angle α.

obviate the necessity to draw a graph, an algorithm to iterate on two variables to find the zero of a function could be used. Brent's algorithm could be used for this in a nested fashion. Table 6.3 shows a comparison of the calculated minimum k_h, and the value of α at which it occurs, from Fig. 6.11 and the observed k_h and α from Table 6.2 and Figs. 6.3 to 6.8 respectively. The observed yield acceleration shown for each test is the mean found for the runs during which the failure surface outcropped, and for subsequent runs.

Apart from tests 2 and 3, the observed yield acceleration agrees quite well with the predicted value. Test 2 and 3 observed k_h values were somewhat smaller than predicted. The failure surface angle agrees much less well: the observed failure surface was without exception flatter than predicted. Table 6.4 shows the same comparison as Table 6.3, except that the calculations used $\phi = 40°$ instead of 45°. The effect of the change is to reduce the predicted yield acceleration, but the failure surface angle remains much the same. Table 6.5 shows results of the same calculation again, for $\phi = 38°$ and $f^* = 1.4$. Using a larger value for the friction coefficient is seen to predict an increased yield acceleration but a decreased failure surface angle. The value of the friction coefficient affects both the yield acceleration and the failure surface angle, whereas the soil friction angle affects mainly the yield acceleration. In Table 6.5 the predictions for α are generally quite close to the observed failure surface angle. Comparing Table 6.5 and Table 6.4, it appears that the average mobilised ϕ may be about 38°, or slightly less.

Table 6.3
Calculated and observed yield accelerations k_h and failure surface angles α, for $\phi = 45°$ and $f^* = 0.85$.

Test	k_h (g)		α (degrees)	
	Calc'd	Obs'd	Calc'd	Obs'd
1	0.24	0.24	47.0	36.7
2	0.30	0.21	47.0	33.2
3	0.16	0.09	54.4	43.0
4	0.23	0.21	44.7	41.8
5	0.23	0.20	44.7	36.7
6	0.24	0.22	47.8	39.5

Table 6.4
Calculated and observed yield accelerations k_h and failure surface angles α, for $\phi = 40°$ and $f^* = 0.85$.

Test	k_h (g)		α (degrees)	
	Calc'd	Obs'd	Calc'd	Obs'd
1	0.16	0.24	47.0	36.7
2	0.21	0.21	48.7	33.2
3	0.06	0.09	54.4	43.0
4	0.14	0.21	47.0	41.8
5	0.14	0.20	47.0	36.7
6	0.16	0.22	47.0	39.5

A value of f* of 1.40 is in the region of the peak friction angle measured in the sliding shear tests reported in section 5.4.2. This is in keeping with what other researchers have found, that the peak friction angle can be used in design. Friction is discussed more fully in section 6.7, where it is shown, from study of measured forces, that the maximum mobilised friction coefficient in the walls is in the region of 1.5 to 1.8.

ϕ = 38° is the residual value derived in the tests described in section 5.4.3 at a normal pressure of about 25kPa, whereas the maximum normal stress in the test walls, assuming hydrostatic earth pressure, is about 16kPa. It may be that dilation of the sand causes an apparent or real increase in the confining stress in the soil, and/or it may be that the test values from §5.4.3 are incorrect. Fig. 5.33 shows a rapid rise in ϕ as the confining stress drops below about 50kPa, whereas Fukushima and Tatsuoka (1984) showed, by very careful triaxial tests, that a significant rise in ϕ at low stress did not occur, even below 10kPa.

Table 6.5
Calculated and observed yield accelerations k_h and failure surface angles α, for ϕ = 38° and f* = 1.40.

Test	k_h (g)		α (degrees)	
	Calc'd	Obs'd	Calc'd	Obs'd
1	0.26	0.24	35.5	36.7
2	0.34	0.21	32.7	33.2
3	0.18	0.09	43.0	43.0
4	0.21	0.21	36.7	41.8
5	0.21	0.20	36.7	36.7
6	0.26	0.22	35.5	39.5

Another point that should be made here concerns the variability of the observed yield acceleration and especially of the observed failure surface angle. In Table 6.3, it can be seen that walls 1 and 6, which had the same geometry, had slightly different yield accelerations (0.24 and 0.22g), and also α values (36.7° and 39.5°). Similarly for walls 4 and 5: k_h values are similar, but the α values are different (41.8° and 36.7°). It is difficult to say whether these differences are inherent in 1-g modelling, reflecting small differences in the model. More information is needed before we can say whether such differences would be seen in the behaviour of similar prototype structures. Certainly static case studies of RE walls do show large variations in some aspects of their behaviour; in strip forces, for example.

The data presented in this section gives a first look at the average mobilised friction in the wall, both within the soil and between the soil and the reinforcing. It was shown that the limiting equilibrium formulation does

predict the yield acceleration and the failure surface angle, within the limits of the observed variability of k_h and α. In section 6.5, observed forces are used in the limiting equilibrium formulation to determine mobilised ϕ and mobilised f^*. The apparent mobilised ϕ is found to decrease as permanent displacement of the test walls increases. Section 6.6 looks in detail at the mobilised friction coefficient f_*, using the resistant force formulation to obtain an average for the test run, and also the simple pullout force equation to obtain a value for each strip. Section 6.7 looks at friction in more detail and compares the observed values to what has been recommended for design use.

6.4. Observed strip forces.

As stated in chapter 5, strains were measured at 5 positions on 10 strips in each test wall. Forces were calculated from those strains using a linear stress-strain relationship. Sections 5.3.6 and A.5 give information about the strip force-measuring instrumentation.

Forces were measured from the time each strip was put in position on the surface of the fill, except for test 1. In that test the data logger was not available at the time the wall was built, so there are no construction forces. To obtain gross forces, the construction forces for test 6 were subsequently added to the measured (dynamic) forces from test 1. (Walls 1 and 6 had the same configuration.)

Two types of force graph were used in the study: time histories of forces at five positions on each strip, and force distributions along each strip effectively obtained by taking a cut across a time history graph at a particular time instant. (Recall that the scanning slew has been removed by interpolation of new points at the same time instants for all scanned channels.) The time history graphs show how the strip forces develop during a run. They were used only to choose the times at which to take a distribution of forces in the strips eg. to choose the time at which the maximum forces were measured. In the next section 2 sets of typical force time history graphs are presented, along with the acceleration and displacement

traces for the test run to which they refer. Then there is a section looking at force distributions.

6.4.1. Time histories of strip forces.

Figs. 6.12 and 6.13 show the acceleration and displacement recordings for test 2 run 1, and Figs. 6.14 to 6.23 show the corresponding forces. The time axes are the same for Figs. 6.12 to 6.23. These drawings show smoothed data, and are typical of the sinusoidal-excitation test runs. Figs. 6.24 and 6.25 show acceleration and displacement data for test 5 run 4, and Figs. 6.26 to 6.34 show the related force data (the data for strip 8 was bad and is not shown). Test 5 run 4 is typical of the earthquake excitation test runs.

The single-pulse sinusoidal excitations were used because it was felt that it was necessary, and easier, to see what happens on a pulse-by-pulse basis before using a more complicated earthquake excitation. Once the single-pulse behaviour of the walls had been studied, and it had been found that the limiting equilibrium formulation seemed to be applicable, it was necessary to check the effect of a recorded earthquake motion. As mentioned in §5.3.10, an attempt was made to have the predominant frequency of the earthquake motions near the expected natural frequency of the test walls, but the shaking table turned out to be incapable of meeting that requirement. The same effects were noted in the earthquake runs as in the sinusoidal runs: forces increased on the pulses causing outward (active) displacement, reduced on pulses causing passive displacement, and there was a general permanent rise during shaking causing permanent displacement.

It can be seen on Figs. 6.14 and 6.15 that the forces in the lowest two strips increase quite dramatically with the first acceleration pulse experienced by the wall. This was the case in all tests. At the time that the failure surface first appeared over the full width of the fill surface (run 13 in test 2), strip 1 forces were almost the same at the end of the run as they were at the beginning. The strip took no more load. Strip 2, on the other hand, showed a net increase in force during run 13, as did strip 3. (See Fig. 6.39). These two strips were then taking the additional load imposed on the lower part of the wall by permanent displacement of the facing

during the run. This indicates that the failure surface starts to form low down, and grows upwards, as observed by Nagel (1985). It also shows that the failure surface starts above the lowest strip, as shown in Figs. 6.3 to 6.8.

It can also be seen on all the test 2 force graphs that the peaks are a little after the excitation peak. Peaks occur on different strips at slightly different times. It appears that the lowest strip experiences the effects of deformation first, followed by the second lowest, and then all the other strips have peaks at similar times. The acceleration graphs show that there are small delays between the excitation and mid-height, and mid-height and wall top acceleration traces, reflecting oscillatory motion of the wall, like a single-degree-of-freedom oscillator, about the base. Such motion was noted by Richardson and Lee (1975), Richardson et al (1978), Rea and Wolf (1980), and Sommers and Wolf (1984) (see § 2.2 and 2.3).

Variation in strip force during an excitation pulse is usually greatest near the wall facing. Fig. 6.31 shows a case where this is not true: the greatest variation was at gauge number 3, 360mm from the wall facing. This perhaps illustrates that most of the dynamic load is being applied somehow at some distance behind the facing. The static failure surface and maximum force in the strip would be at about 300mm (0.3H) from the facing, so it could be that this loading reflects the static failure surface, and the portion of strip outside the static active block is still acting as the resistant length of strip. At this stage of the test the failure surface is still partially developed, and is unlikely to be extending up this far in the fill (350mm deep, or 650mm from the base of the wall).

A similar effect to that noted above in Fig. 6.31 can also be seen in the time history graph for test 6 run 2 strip 9 forces (Fig. 6.35), where only gauges 1, 3 and 5 are shown in the figure for clarity. There, gauges 3 and 5 experience much larger force variations during the earthquake than gauge 1 (at the facing). Gauges 2 and 4, while not shown, are similar. The failure surface is unlikely to be this far advanced up through the fill during run 2 of test 6.

Forces reach peak values and begin reducing before the displacement reaches the maximum outward value in the run.

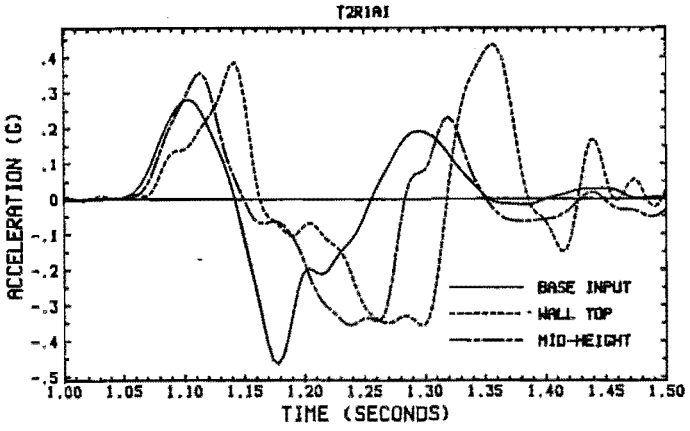

Fig. 6.12. Acceleration traces for test 2 run 1.

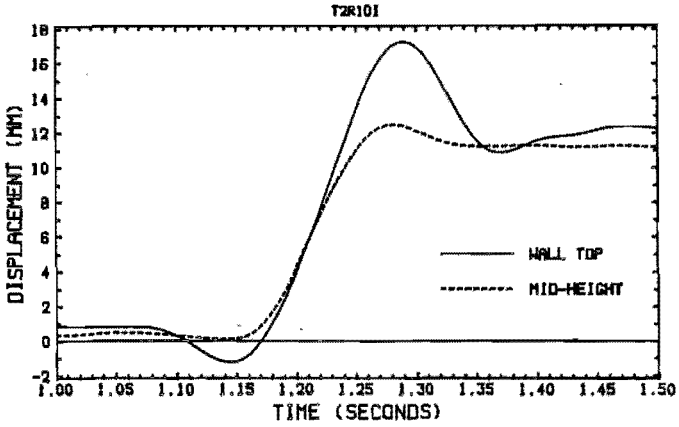

Fig. 6.13. Displacement traces for test 2 run 1.

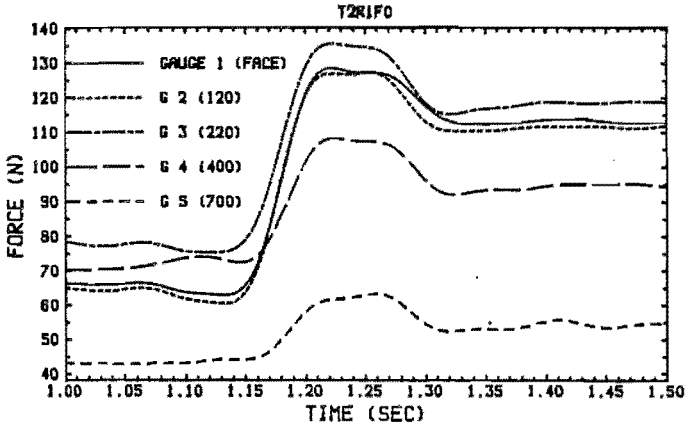

Fig. 6.14. Forces, strip 1 (bottom of wall), test 2 run 1.

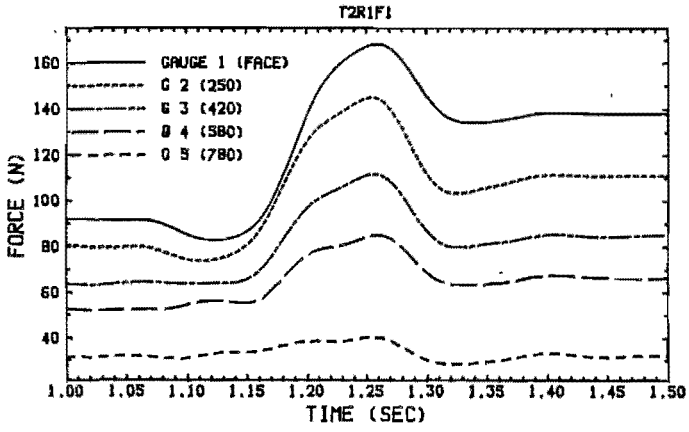

Fig. 6.15. Forces, strip 2, test 2 run 1.

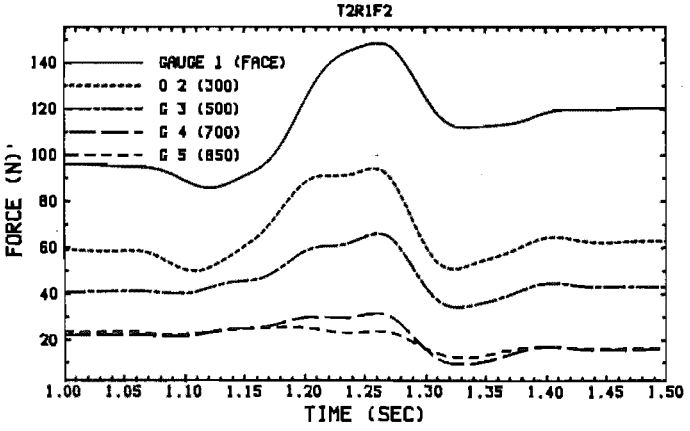

Fig. 6.16. Forces, strip 3, test 2 run 1.

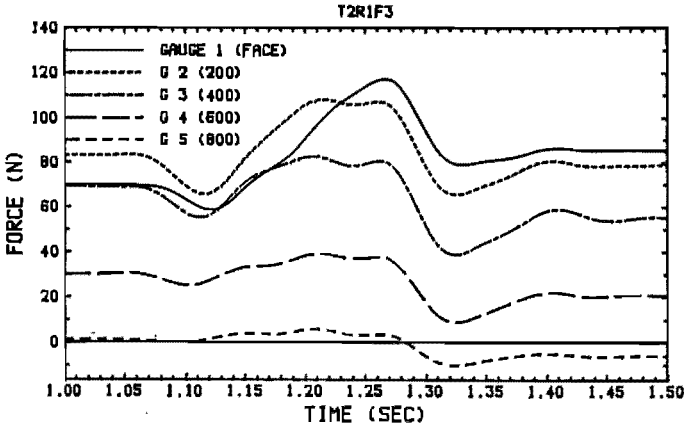

Fig. 6.17. Forces, strip 4, test 2 run 1.

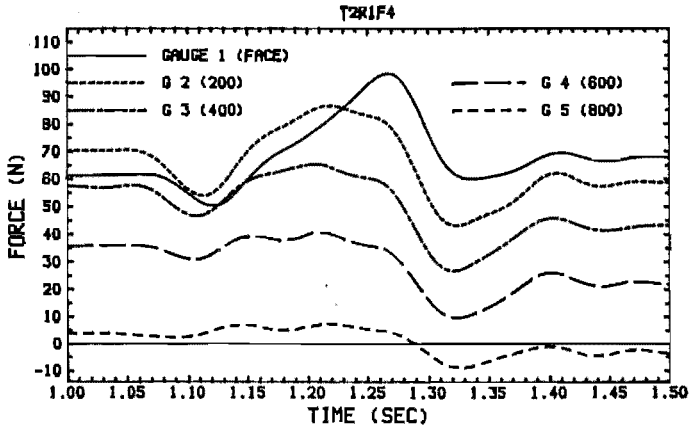

Fig. 6.18. Forces, strip 5, test 2 run 1.

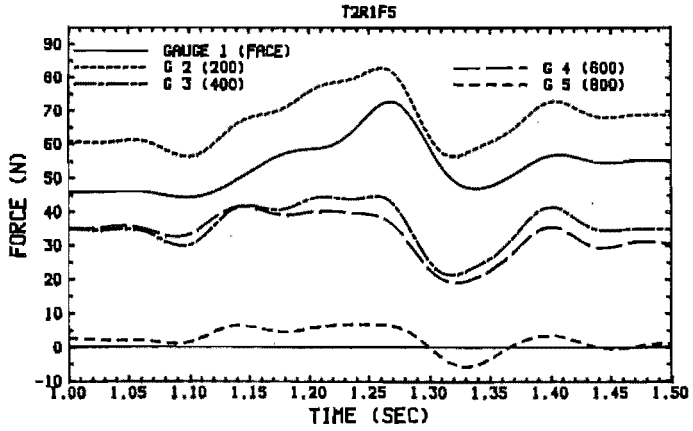

Fig. 6.19. Forces, strip 6, test 2 run 1.

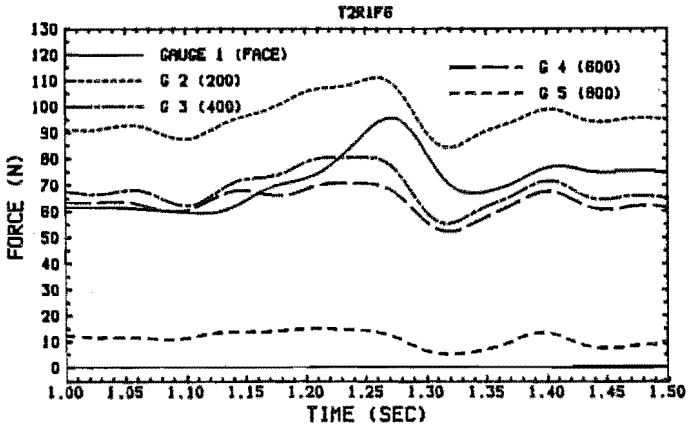

Fig. 6.20. Forces, strip 7, test 2 run 1.

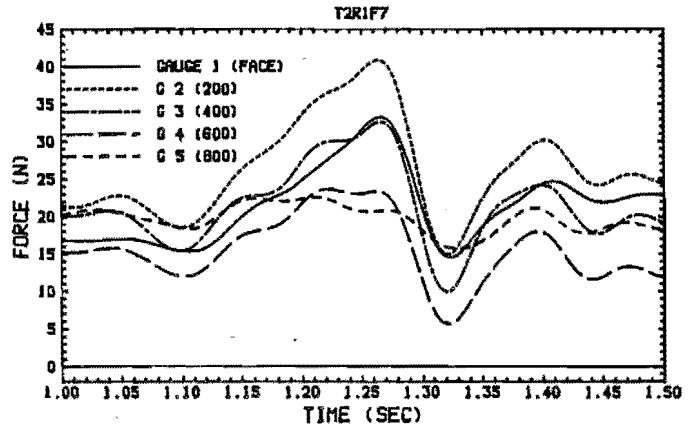

Fig. 6.21. Forces, strip 8, test 2 run 1.

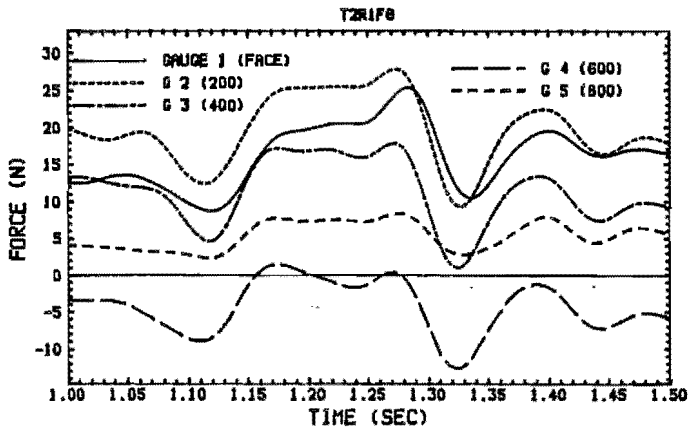

Fig. 6.22. Forces, strip 9, test 2 run 1.

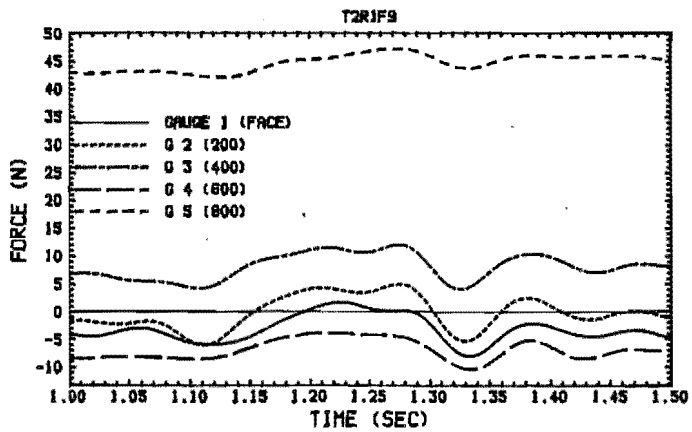

Fig. 6.23. Forces, strip 10, test 2 run 1.

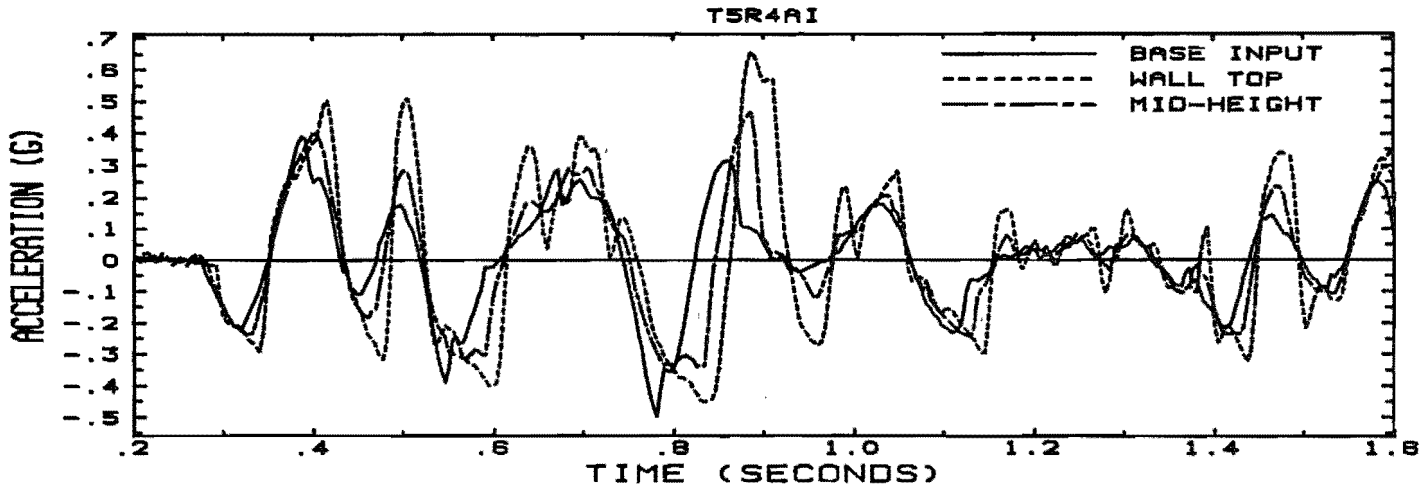

Fig. 6.24. Acceleration traces for test 5 run 4.

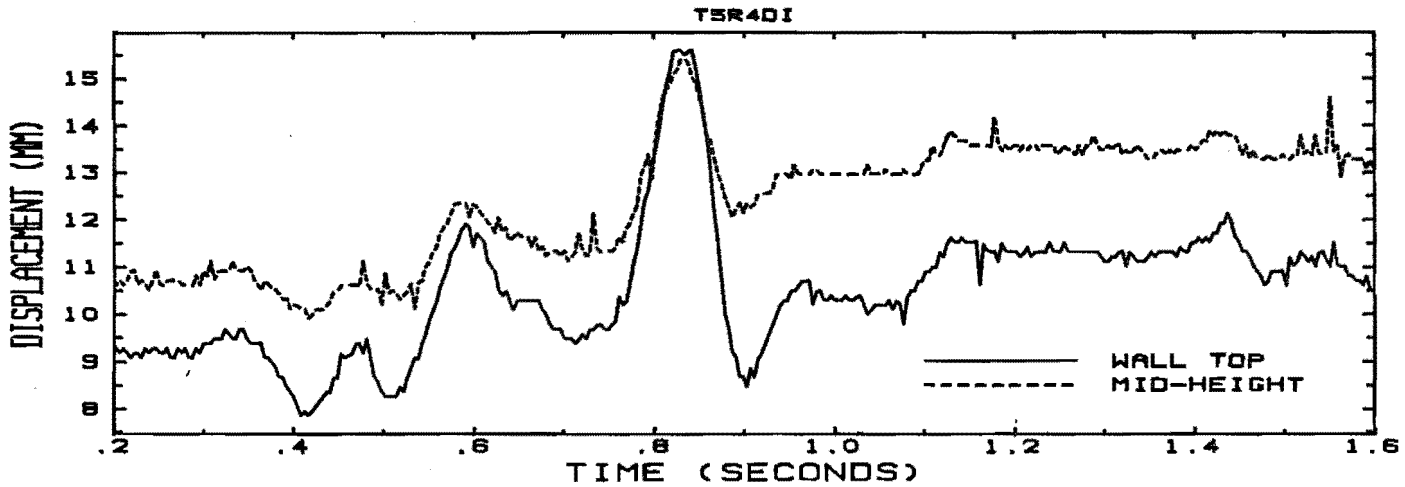

Fig. 6.25. Displacement traces for test 5 run 4.

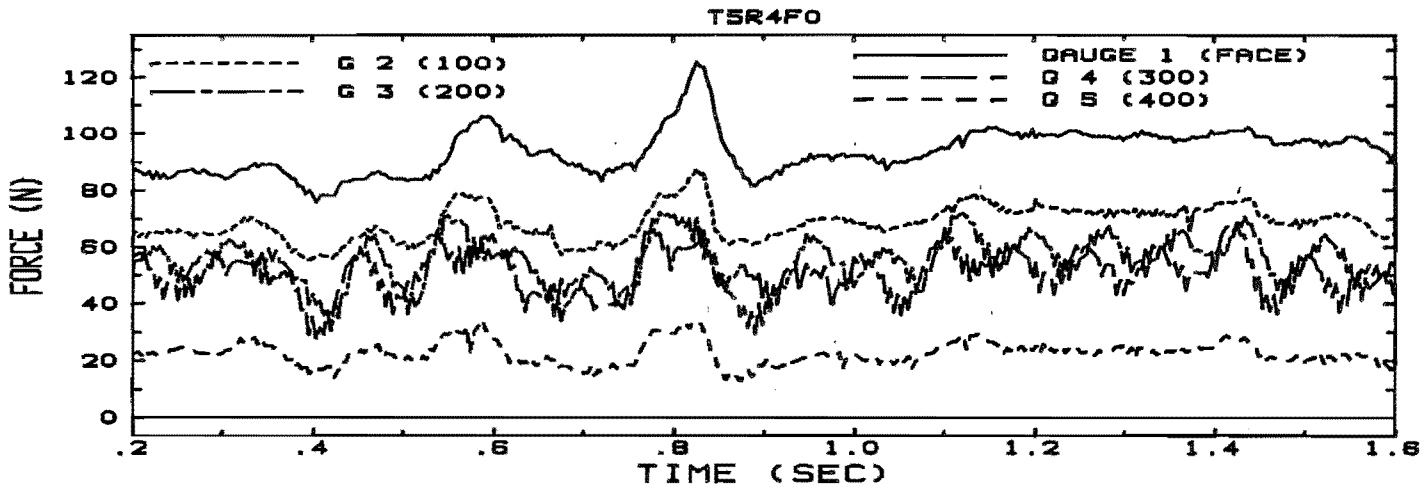

Fig. 6.26. Forces, strip 1 (bottom of wall), test 5 run 4.

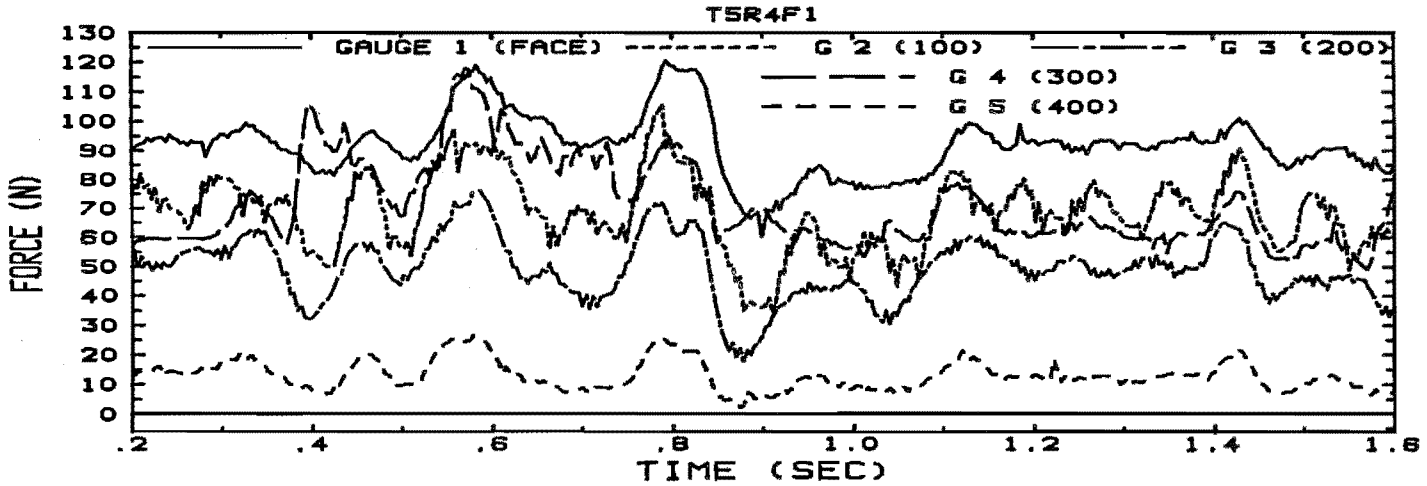

Fig. 6.27. Forces, strip 2, test 5 run 4.

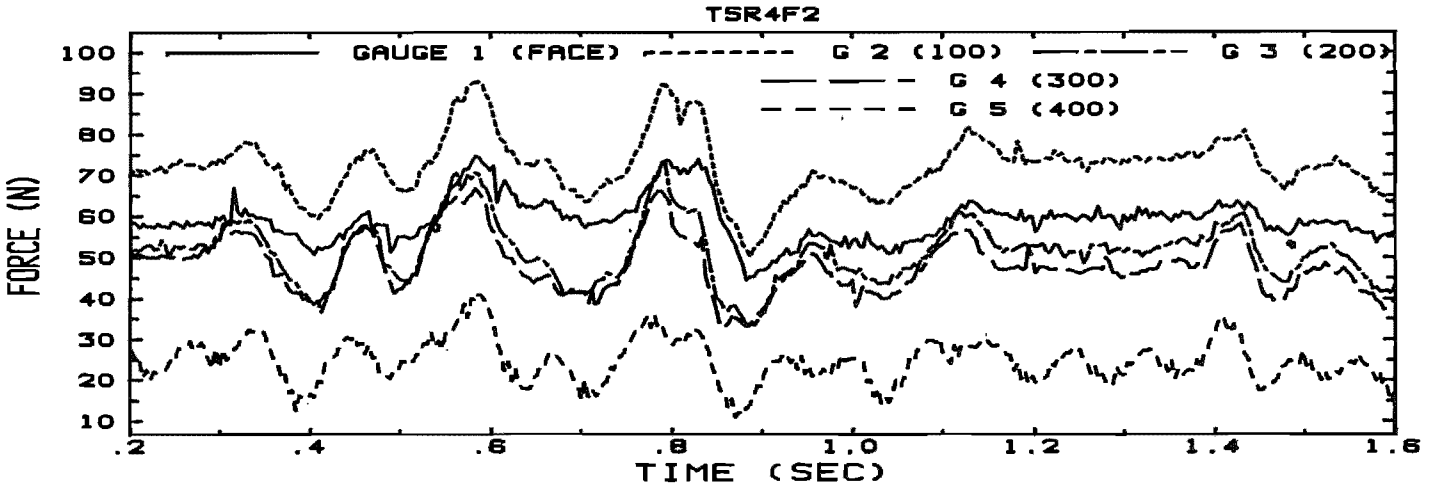

Fig. 6.28. Forces, strip 3, test 5 run 4.

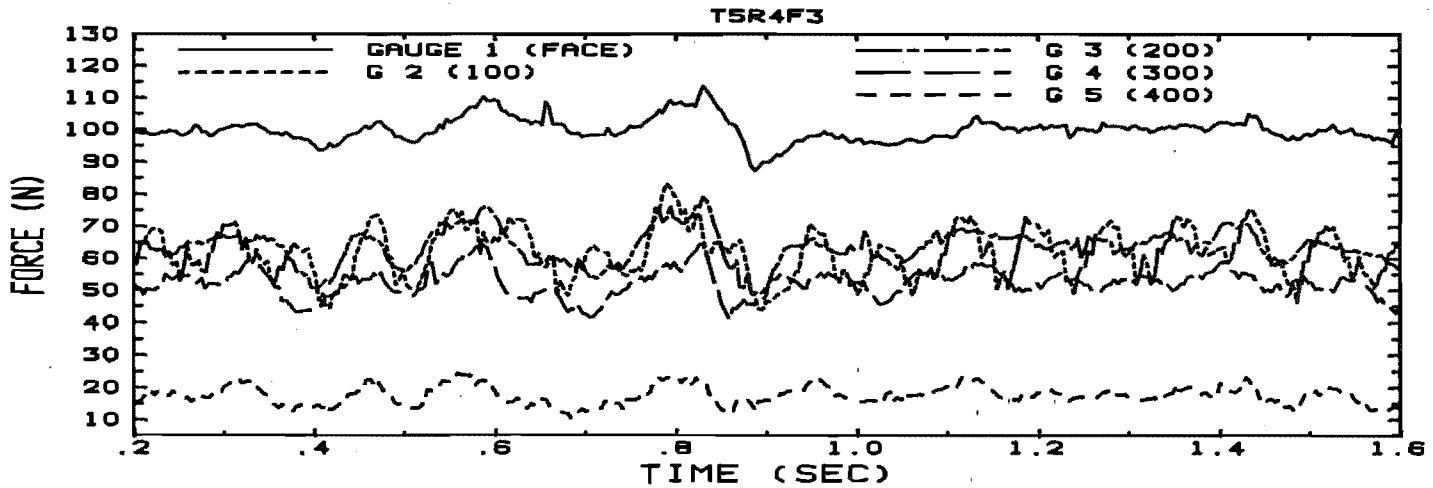

Fig. 6.29. Forces, strip 4, test 5 run 4.

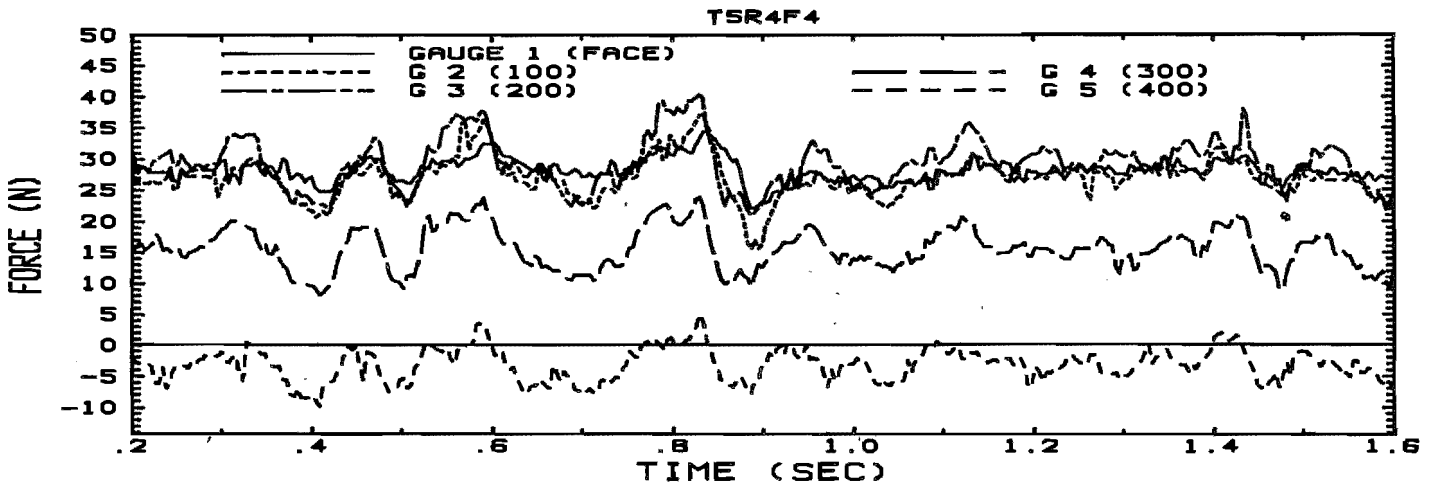

Fig. 6.30. Forces, strip 5, test 5 run 4.

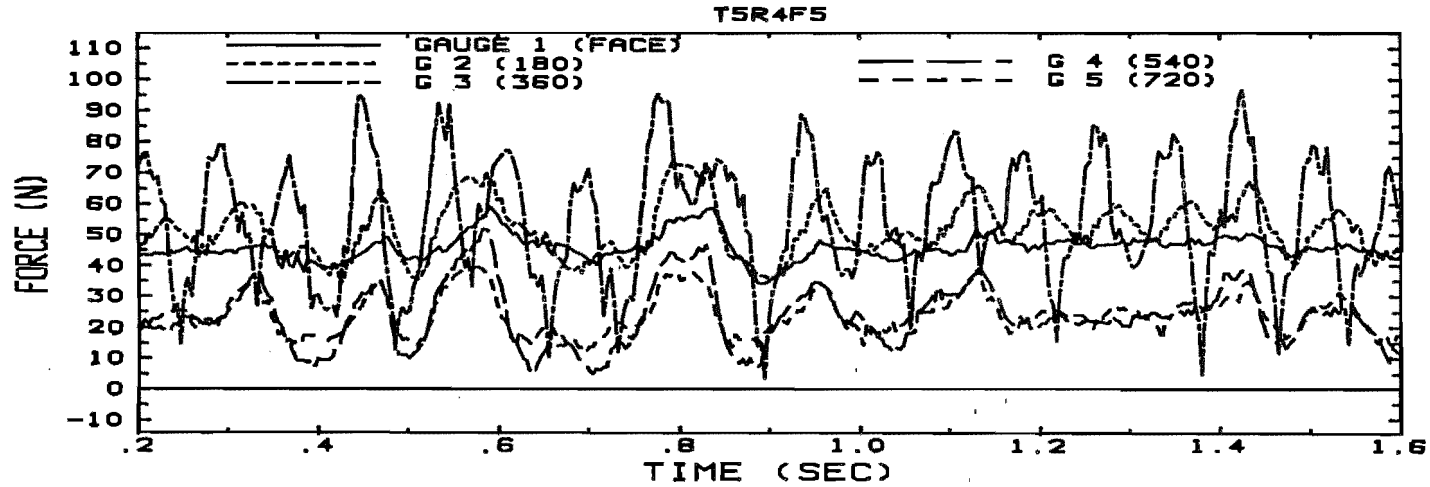

Fig. 6.31. Forces, strip 6, test 5 run 4.

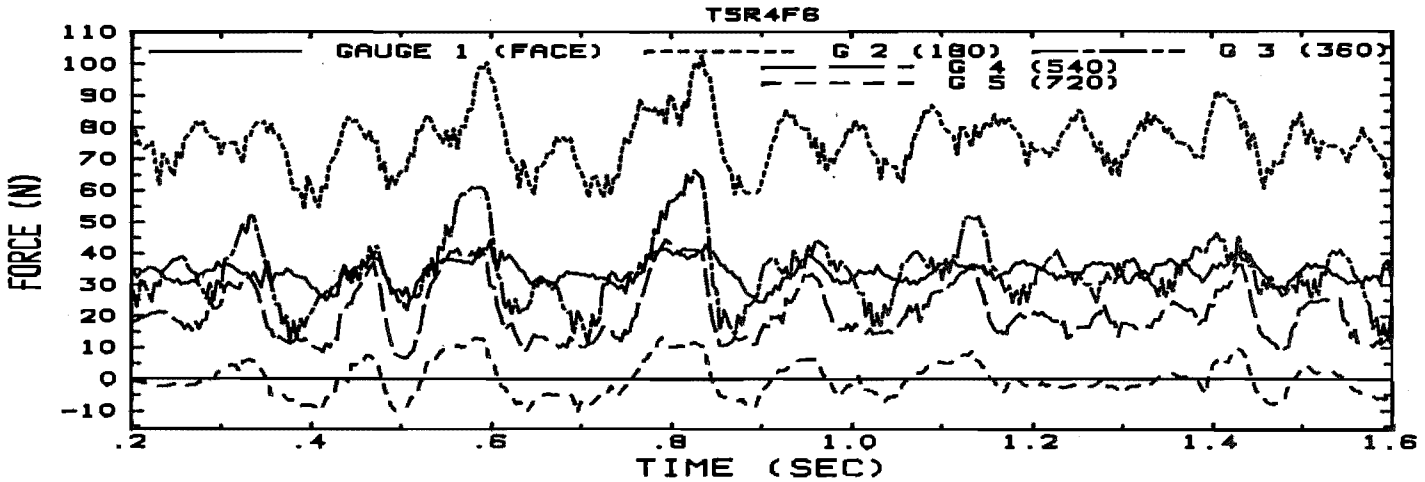

Fig. 6.32. Forces, strip 7, test 5 run 4.

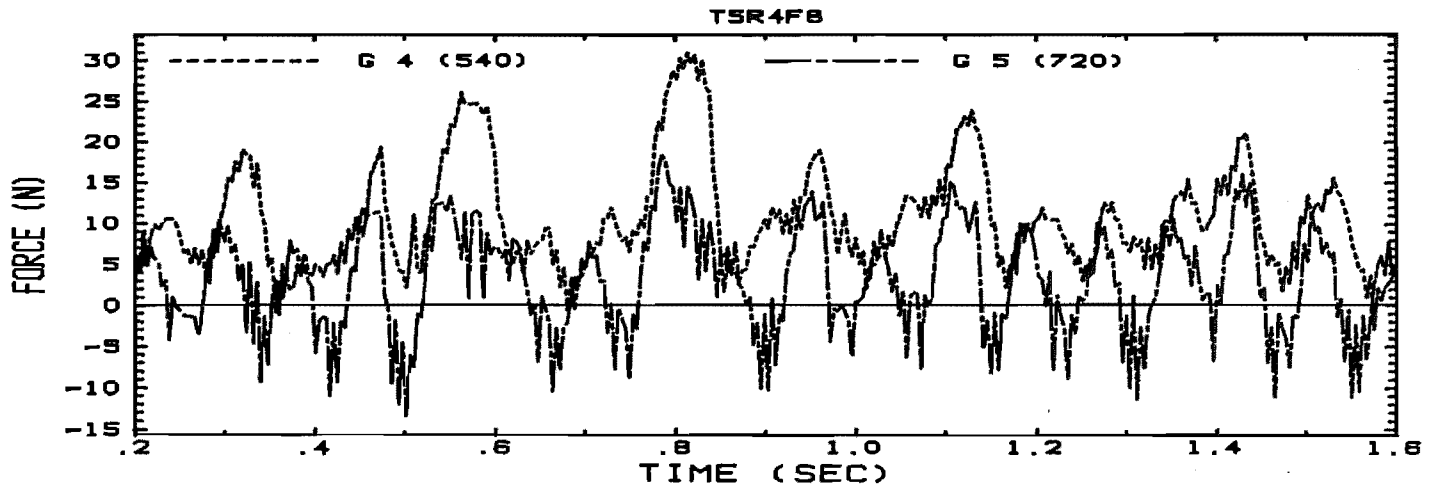

Fig. 6.33.

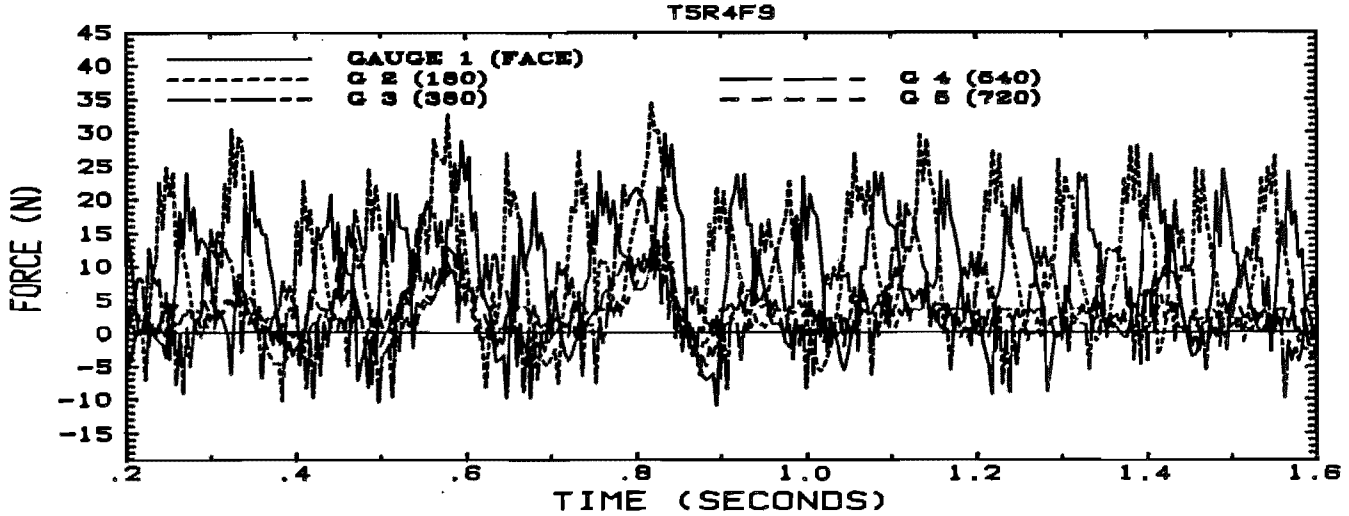

Fig. 6.34. Forces, strip 10, test 6 run 4.

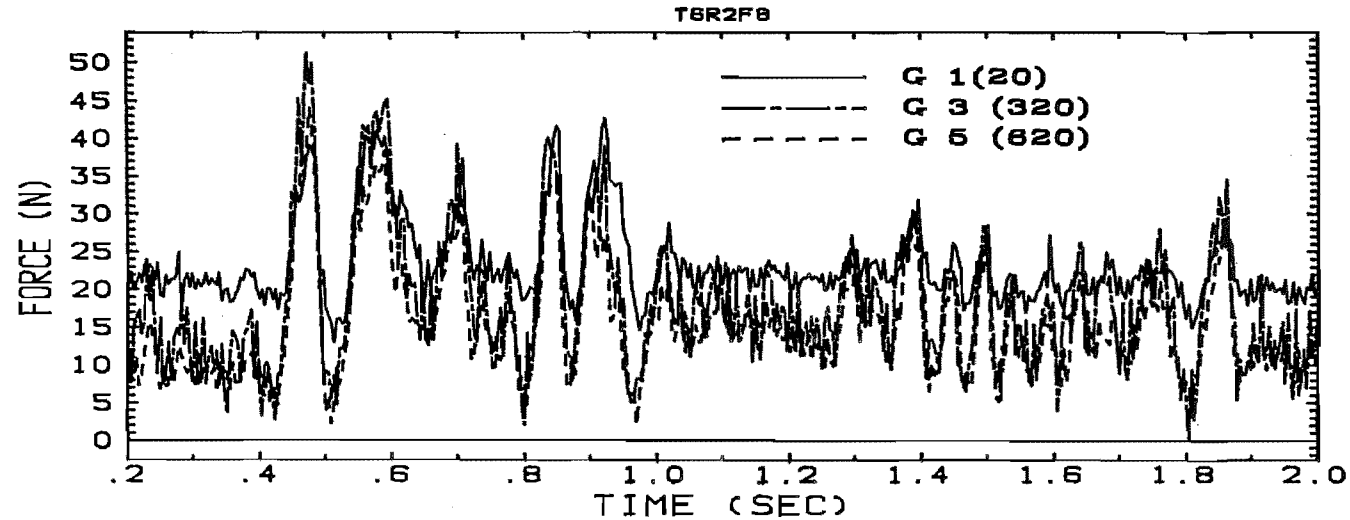

Fig. 6.35. Forces, strip 9, test 6 run 2.

The test 5 graphs (Fig. 6.26 to 6.34) show more clearly the effect of the magnitude of the individual acceleration peaks (Fig. 6.24) on the strip forces. In Fig. 6.24 it can be seen that the mid-height acceleration is limited at about 0.55sec. and 0.8sec. The level of the limitation is taken as the observed yield acceleration. Those acceleration peaks that are above the yield acceleration (eg. at 0.55 and 0.8 sec.) produce marked increases in the strip forces, with equally as marked rebounds with the "passive" pulse following. Permanent increases in strip force seem to occur more with excitation pulses that are a little below the yield acceleration magnitude eg. at 1.11 sec. Unfortunately the data for 8 channels (strip 8 and 3 gauges on strip 9) was lost due to a suspected earth loop on one data logger input board.

For design purposes, the transient maximum forces are more important than the residual forces, because of the necessity to provide protection against strip breakage. The residuals are important because they are the ambient force levels before any subsequent shaking. In the next sections both residual and maximum force distributions are discussed.

6.4.2. Strip force distributions.

6.4.2.1. Construction forces.

Fig. 6.36 shows final construction forces for all strips where they were measured, aggregated on one set of graphs. It is not particularly useful in this format. The data was replotted for Fig. 6.37 where the position of the gauges at which the various forces were measured is normalised against the relevant strip length. On both these figures, the construction forces for each test are shown as run 0 (R0). The same convention is used throughout the following discussion and anywhere construction forces are shown in figures.

The most obvious point to be made from a look at Fig. 6.37 is that the force distribution shapes are quite variable. Slight trends can be seen, however. Strip 1 forces tend to have the maximum near the facing. There is a tendency for the maximum to move away from the facing on strips 2 and 3. Strip 5 has the most repeatable shape ie. only T4R0 really deviates from the

humped shape, with the maximum at about 0.2 times the strip length away from the facing. In the higher strips, especially 8, 9 and 10, the distribution tends to be more flat with a very weakly defined maximum.

The test 4 force data might not be particularly good, judging from the odd construction force distribution shapes eg. strips 3 and 5. One peculiar observation about the stepped-block structures (walls 4 and 5) is that both T4R0 and T5R0 have a steep decrease in force away from the wall facing in strip 4. It is difficult to explain, assuming that the data is good.

A point of concern is the apparent negative forces sometimes measured eg. T4 strips 3, 7 and 9; T6 strips 8 and 10; T3 strip 9. While it is possible that there could be compressive forces in parts of some strips in some situations, it is felt that most, if not all, of the apparent negative forces are in fact bad readings. The reason is not known, although it is suspected that quite a lot of noise was picked up by the data logger set-up. Subsequent work, in the same area of the building and with the same equipment, has experienced problems when people move around near the apparatus.

6.4.2.2. Dynamically induced forces.

Distributions of maximum total forces for each strip, aggregated for several runs in each test, are shown in Figs. 6.38 to 6.43 for tests 1 to 6 respectively. The values of force for these charts were taken at a suitable time instant in the run in question, at the same instant for all strips eg. for the T2R1 data, values at time 1.25 sec. were taken from Figs. 6.14 to 6.23.

Note that construction forces were not measured in test 1, so the measured dynamic forces were added to the construction forces for test 6. The excitations each wall was subjected to are listed in Table A.7. Vertical lines on the graphs show where the failure surface force readings have been taken for the discussion below (§6.4.3).

In studying these charts, it is useful to know the runs during which the failure surfaces became fully developed. They were as follows:

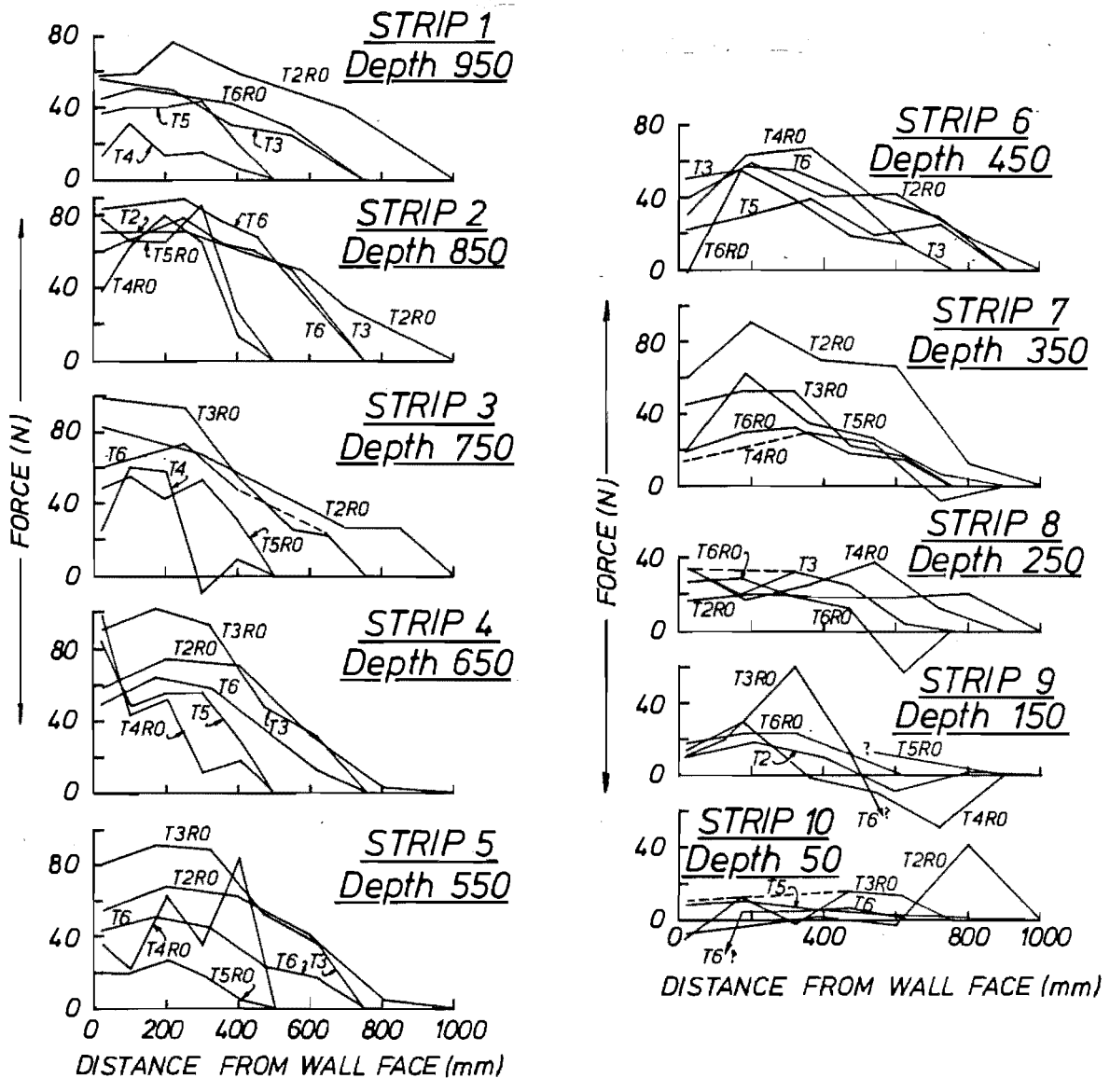

Fig. 6.36. Construction forces in the reinforcing strips.

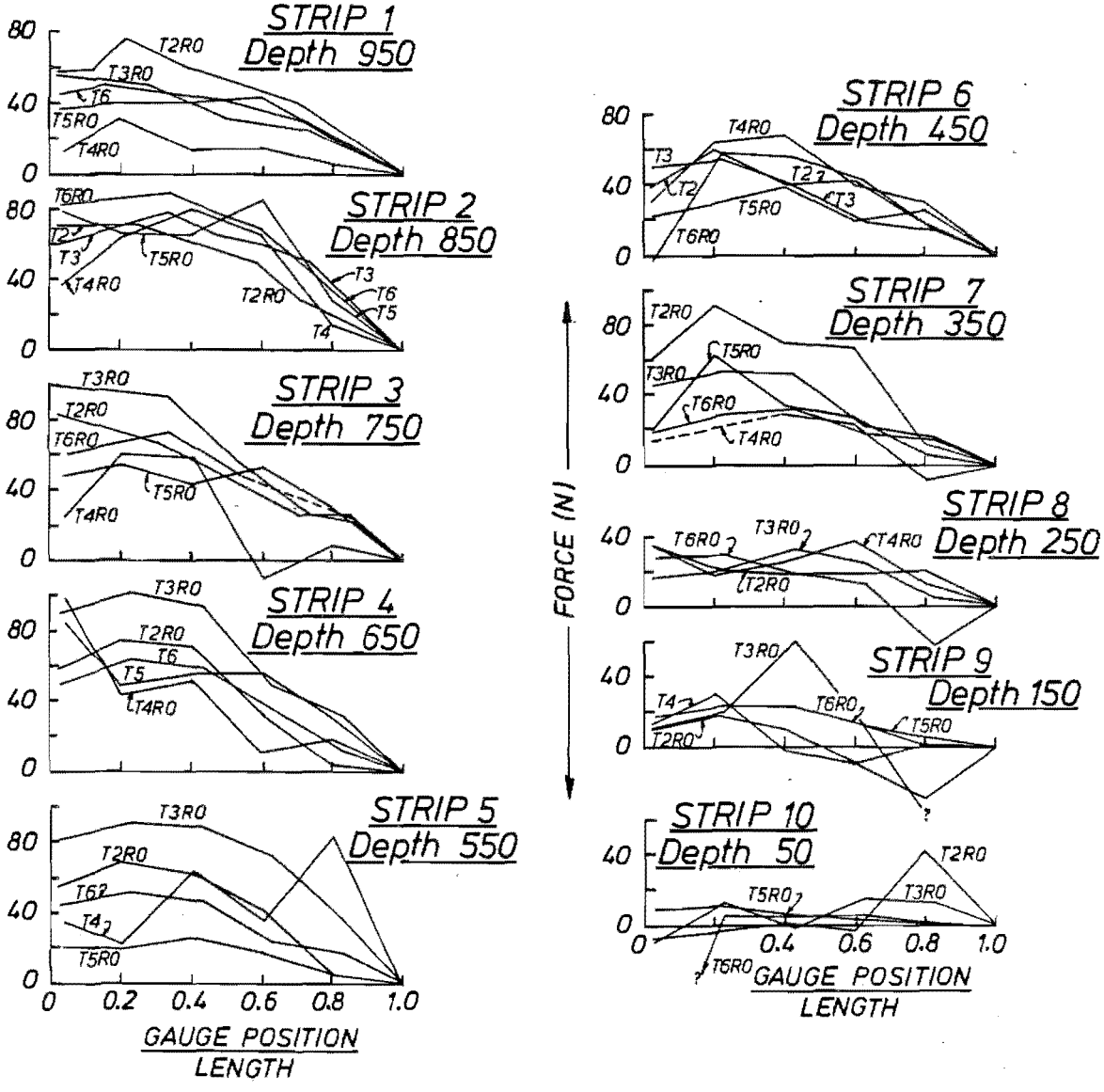

Fig. 6.37. Construction forces in the reinforcing strips, with position in the strip normalised against strip length.

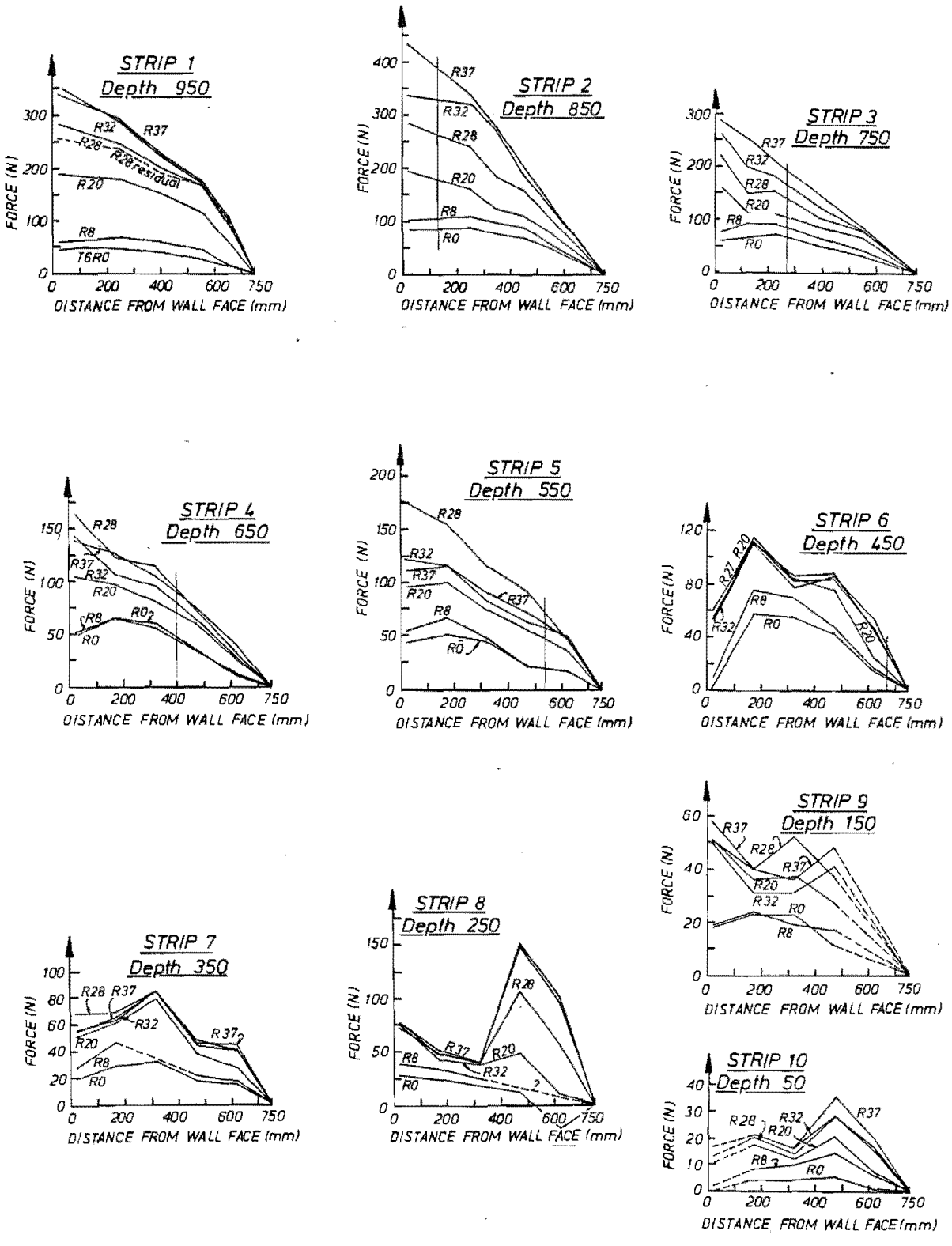

Fig. 6.38. Forces in the reinforcing strips for several runs in test 1.

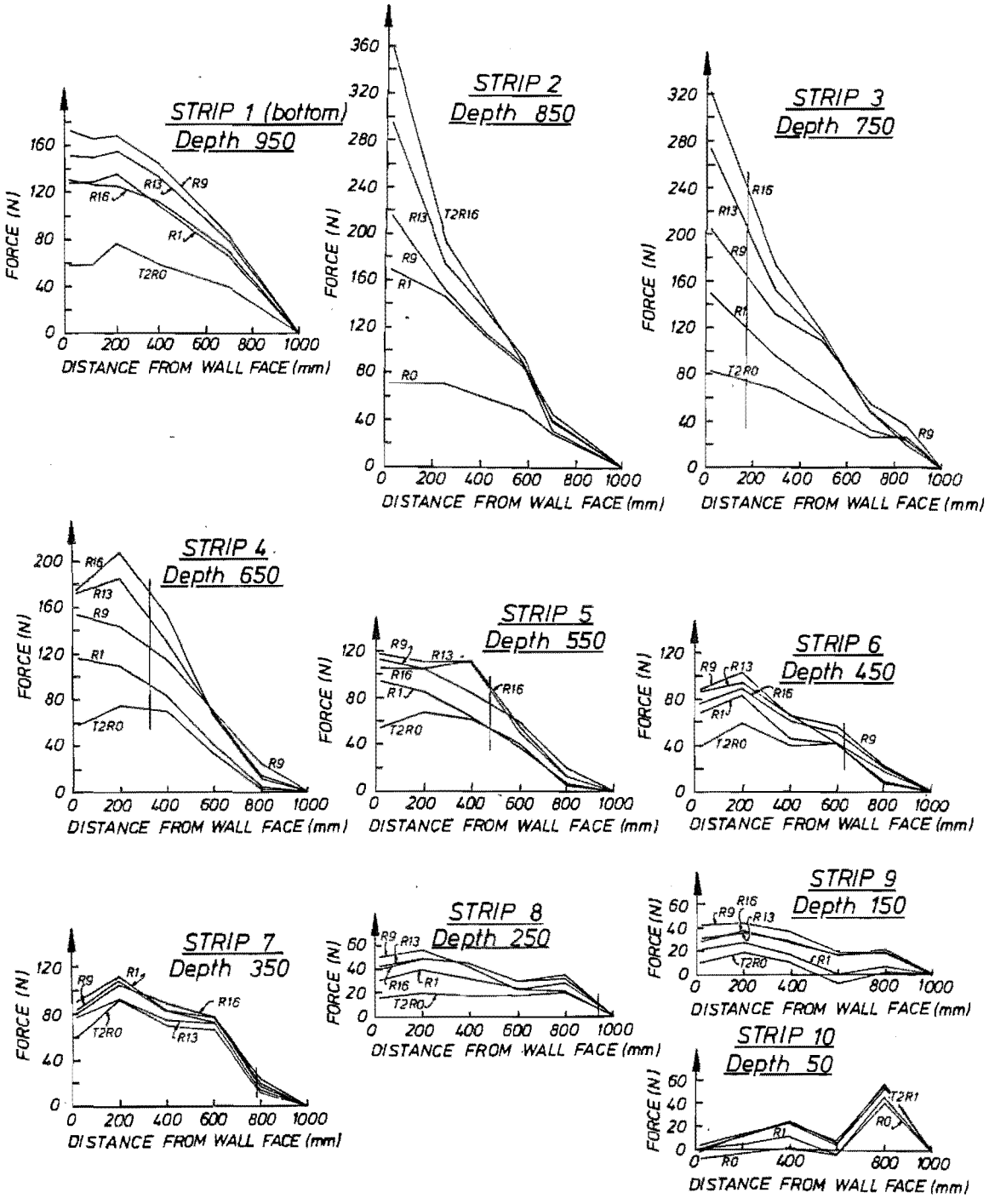

Fig. 6.39. Forces in the reinforcing strips for several runs in test 2.

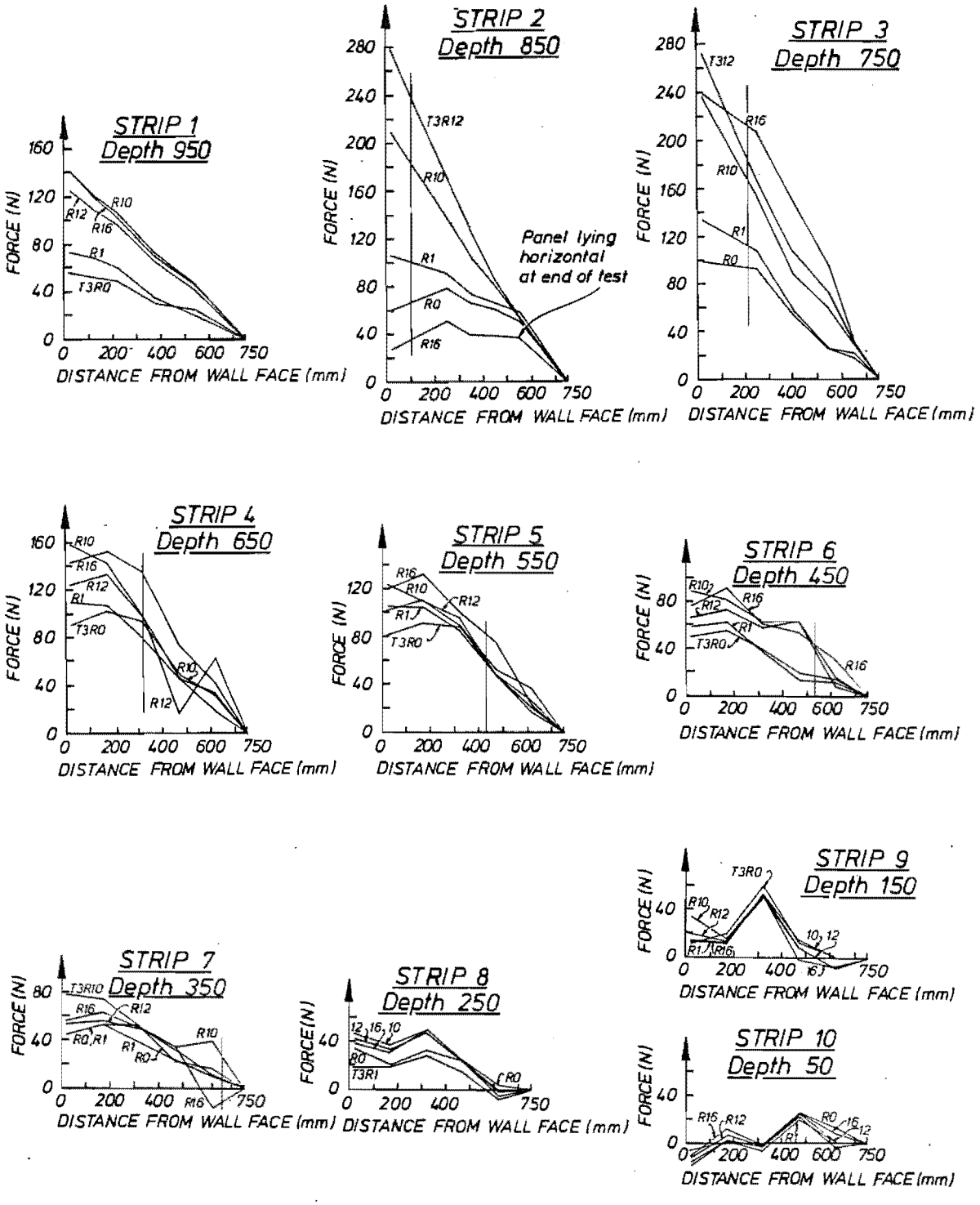

Fig. 6.40. Forces in the reinforcing strips for several runs in test 3.

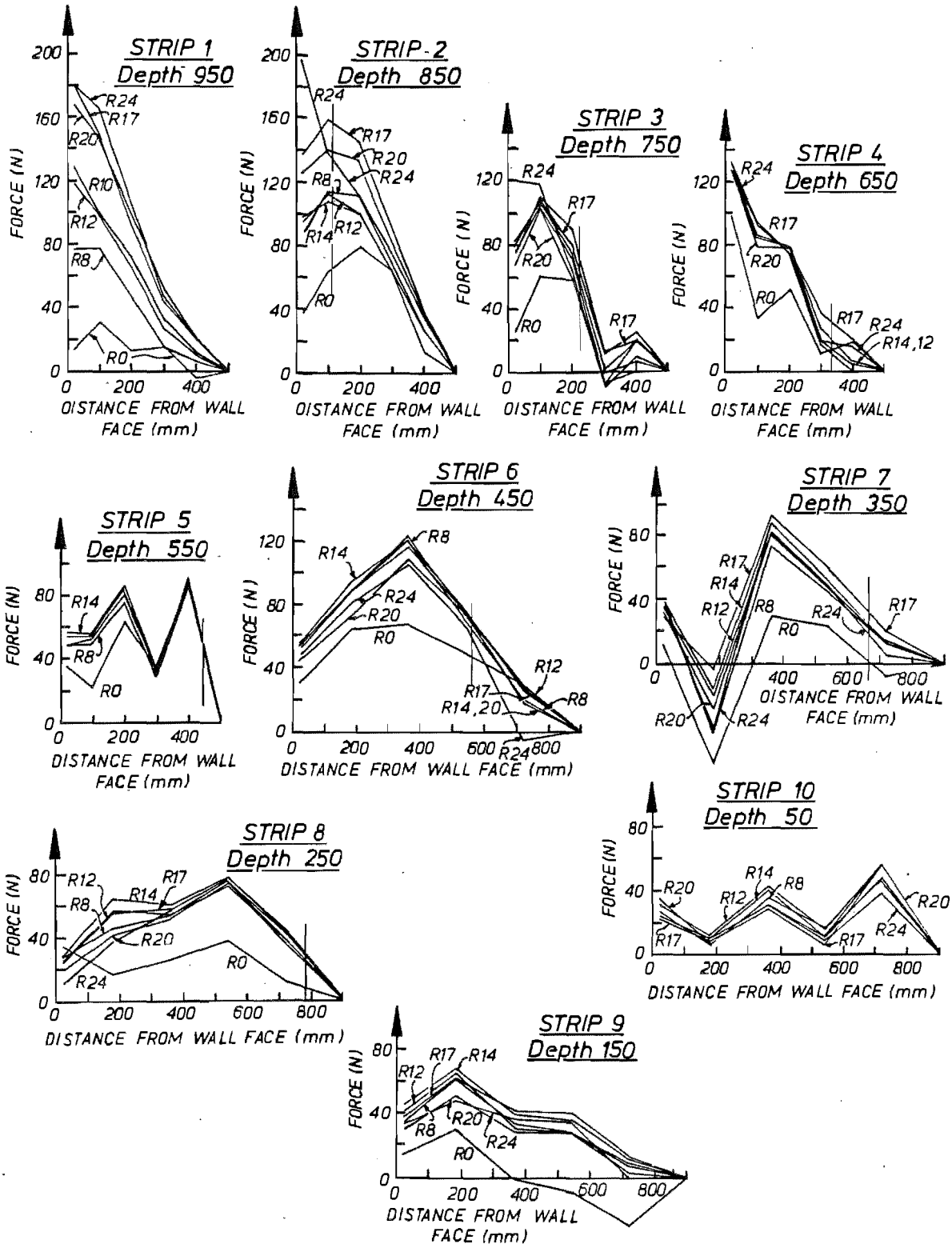

Fig. 6.41. Forces in the reinforcing strips for several runs in test 4.

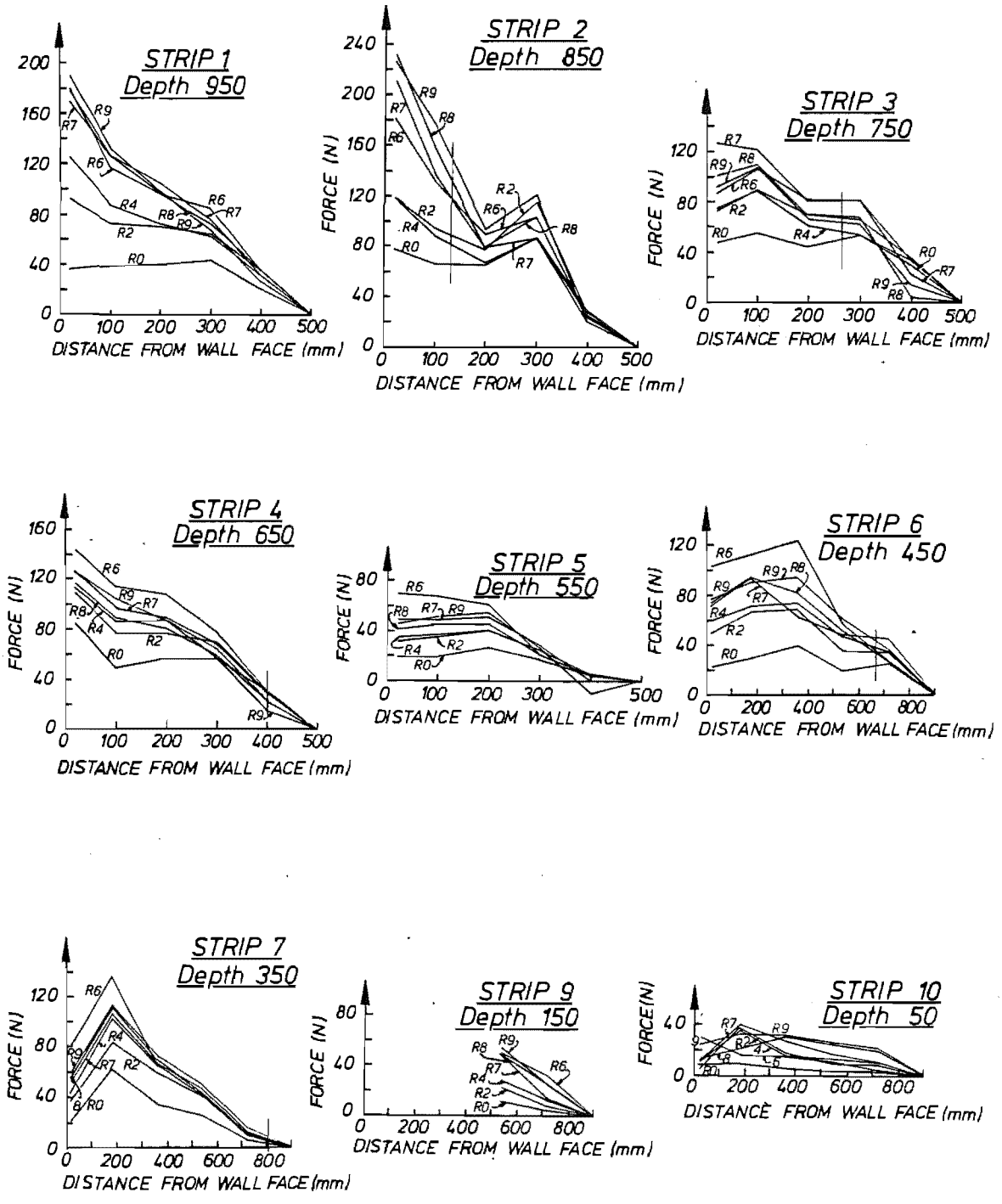

Fig. 6.42. Forces in the reinforcing strips for several runs in test 5.

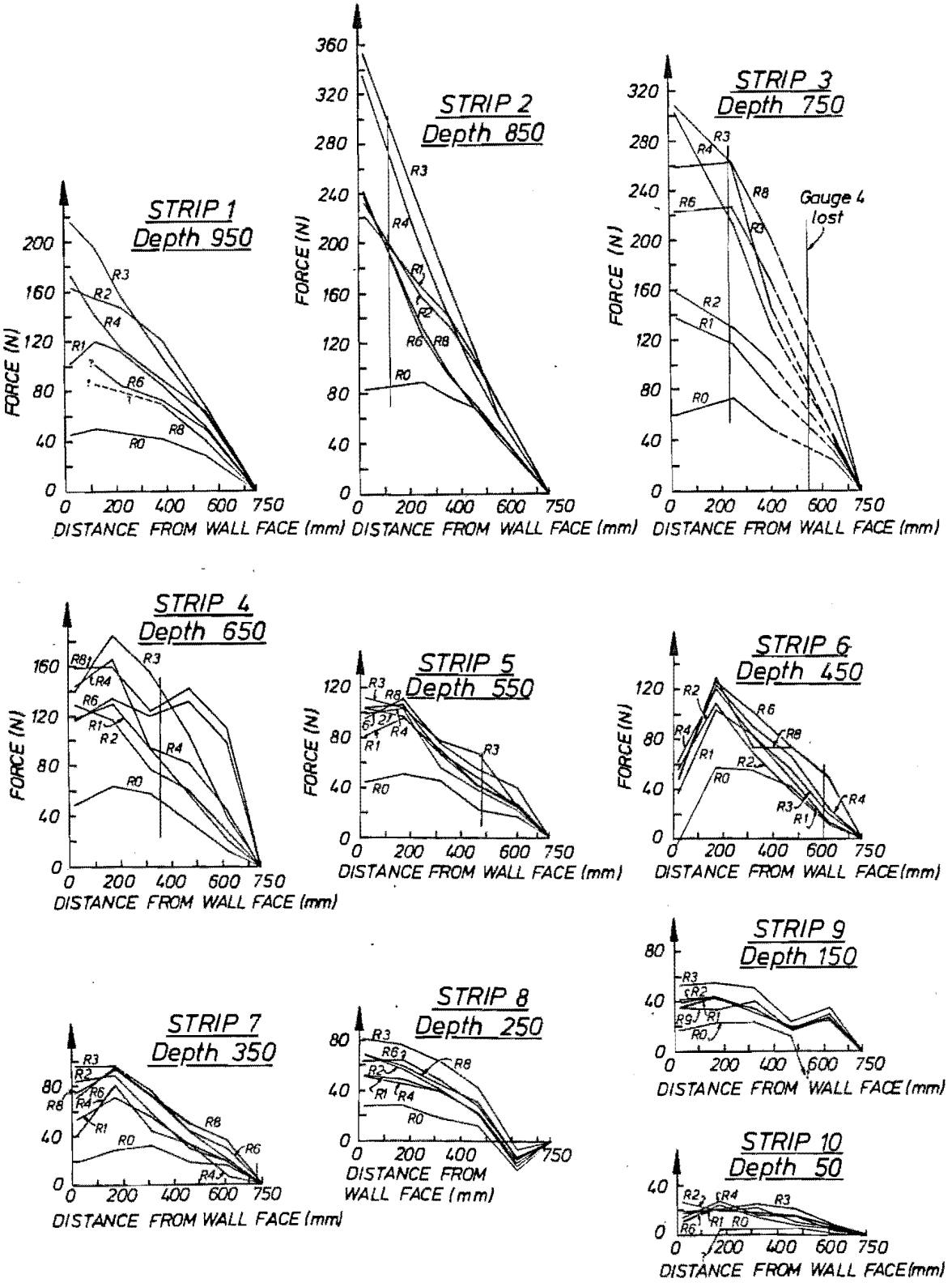

Fig. 6.43. Forces in the reinforcing strips for several runs in test 6.

Test 1 run 28 (T1R28)
T2R13
T3R12
T4R17
T5R6
T6R3.

The first point to note is that the post-failure forces may be 6 or more times as large as the construction forces eg. test 1 strips 1 and 2, test 3 strip 2, test 4 strip 1. The strip forces at failure (the outcropping of the failure surface is here used as a definition of failure) may be 4 or 5 times as large as the construction forces. Generally it seems to require a very advanced stage of failure before the forces in the critical strips (those near the bottom of the wall) cease to increase with further base excitation eg. in test 3, the failure block started to form a series of graben-like structures near the failure surface scarp (shown in Fig. 6.9). Permanent displacement by this stage was quite large, equal to some 15% of the wall height. Similarly in test 6, where total permanent displacement after run 8 was some 20% of the wall height, the forces in the lower strips actually decreased a little as higher strips took more of the load. By this stage the 2nd facing panel up from the bottom was lying horizontal and offering no resistance to further outward movement of the wall.

The position of the maximum force in the lowest 4 strips (1 to 4) generally moves towards the wall facing with earthquake loading of the model walls. In the other 6 strips the maximum does not really move at all with earthquake excitation. There is a general increase in force in those strips with only a slightly greater increase near the facing than further away. The lowest 4 strips appear to be the most important in resisting earthquake-induced displacements.

In the rectangular block walls (1, 2, 3, and 6) the largest forces were measured in strips 2 and 3, whereas in the stepped block walls (4 and 5) the maximum forces were measured in strips 1 and 2. It is not clear why this should be so. The different foundation conditions of the two geometries could contribute to the difference. Or it could be that different modes of

vibration are more significant in the stepped block, with a sharp change of section and hence stiffness at the change in strip length.

As expected, the shorter strips of the stepped block walls experienced significantly lower forces than similarly placed strips in the rectangular block walls. Forces in wall 2 strips, however, were not significantly larger than wall 1 strips, even though there were only 2/3 as many strips in wall 2 as in wall 1, and they were 1/3 longer in wall 2.

Wall 2 also seemed to behave in a different manner to all the other walls: it was shown above (eg. Table 6.5) that the limiting equilibrium formulation was least applicable to this wall, the yield acceleration being predicted as much larger than was observed. The horizontal strip spacing for that wall, at 0.33, was the largest used. The same spacing was used in test 3, although the strips were shorter in that test. It could be that the spacing was large enough that the group effect reported by some researchers (see also §6.7) did not occur between horizontally spaced strips. In prototype structures, the strip spacings are fairly uniform horizontally and vertically. Another aspect is that at the model strip spacings, in general, there may be significantly more interference between strips than there is in prototype structures. This type of scale effect needs investigation.

There are some apparently anomalous results in the force distributions. For example, strip 8 of test 1 (Fig. 6.38), where there is a rapid rise in force near the inner (free) end of the strip. How such a rise could occur is not clear: if the strip was acting as a pin across the failure surface, we might expect an increase around the failure surface position. But in test 1, the failure surface was behind the reinforced block at the depth of strip 8. Thus such a rise is discounted as probably being bad data. A similar effect is seen in strip 10 of test 1. The shape of the strip 10 distribution for test 2 (Fig. 6.39) also is difficult to believe. There is a fairly uniform rise in force along the entire strip with shaking, so it is felt that the zero readings for that strip were not good. Similar comments may be made about strips 9 and 10 of tests 3 (Fig. 6.40) and 4 (Fig. 6.41). Strip 5 of test 4 had 2 bad gauges, and the zero readings for gauge 2 on strip 7 and gauge 4 on strip 3 of that test are felt to be bad.

Where there is one gauge on a strip that appears to have a bad zero reading, but subsequent readings appear good in relation to the original reading, it is possible that the distribution could be "smoothed" by linearly interpolating a new zero reading between the adjacent gauges and adding the dynamic forces to this new zero. Gauge 2 on strip 7 of test 4, and gauge 4 on strip 3 of test 4, would perhaps be more believable if this were done. Such smoothing is not done in this report, however.

6.4.2.3. Force distributions adjacent to the wall face.

Figs. 6.44 to 6.49 show the maximum total forces adjacent to the wall facings, taken from Figs. 6.38 to 6.43. Also shown on Figs. 6.44 to 6.49 are the at-rest and active earth pressure lines for $\phi = 40°$, and the Mononobe-Okabe active earthquake earth pressure line for $\phi = 40°$ and $\theta = \tan^{-1} k_h$ for each test. These lines were calculated by assuming that all the earth pressure on the facing indicated by K_a, K_o, and K_{AE} was transferred to the strips, considering the tributary area of each strip to be equal to the rectangle around it defined by the horizontal and vertical strip spacing.

In all the rectangular block structures (Figs. 6.44 to 6.46 and Fig. 6.49) the 2nd and 3rd strips up from the base of the walls are by far the most heavily loaded by dynamic excitation of the wall. The 2-layer stepped block walls, however, do not show this exaggerated loading in those 2 strips. Both Fig. 6.47 and 6.48 show reductions in the force level in strip 3 (depth 750mm) from the level in strip 2, and an increase again in the force in strip 4. If the data correctly shows the forces in these strips ie. strip 3 in both walls did not have bad construction force readings, then the sawtooth shape of the force distribution with position up the wall is difficult to explain. Strip 5, the topmost of the short strips, has a reduced force level in both walls, and strip 6, the lowest of the long strips, showed larger forces than strip 5. Such a step in force level would be expected at an increase in stiffness of the wall section, as stiffer elements of most structures tend to attract more load than less stiff elements. It could be that the load shedding from strip 5 goes downwards more than upwards.

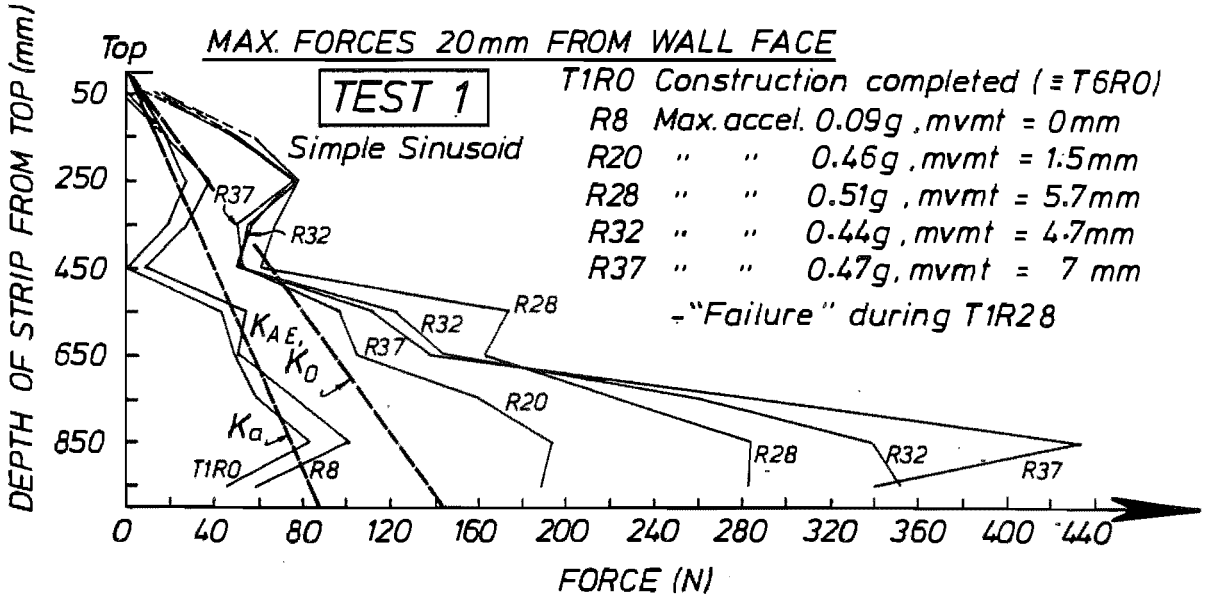

Fig. 6.44. Maximum forces adjacent to the wall facing, test 1.

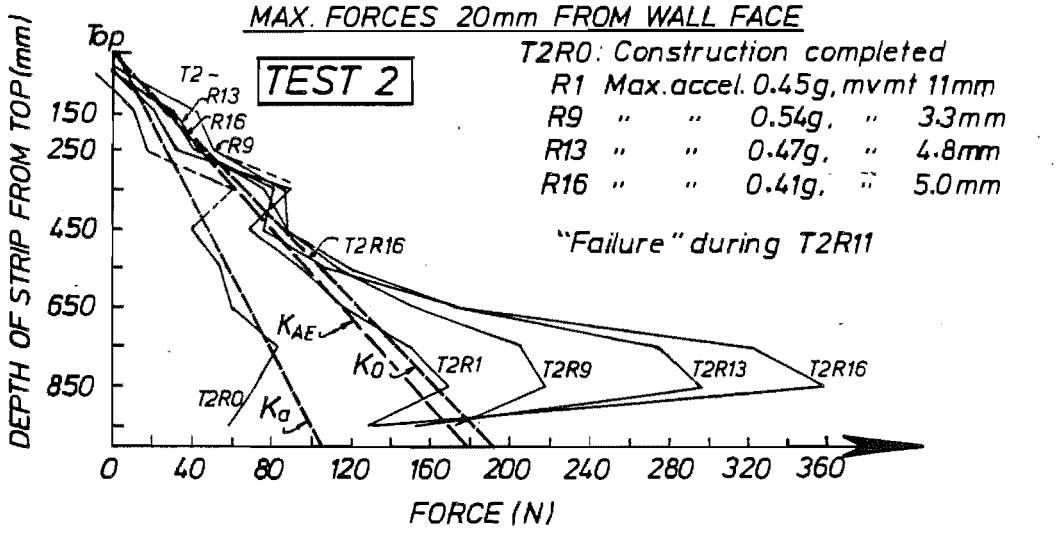

Fig. 6.45. Maximum forces adjacent to the wall facing, test 2.

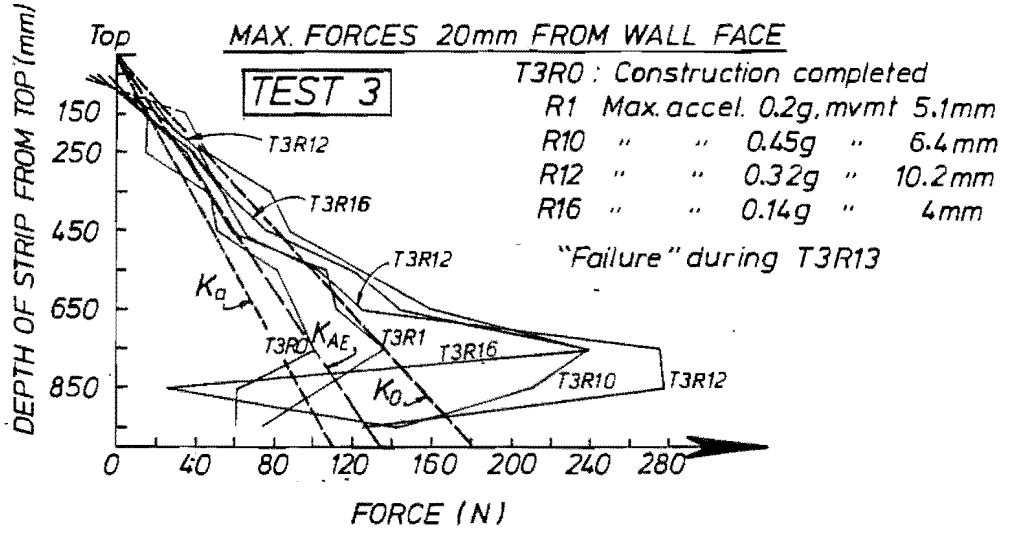

Fig. 6.46. Maximum forces adjacent to the wall facing, test 3.

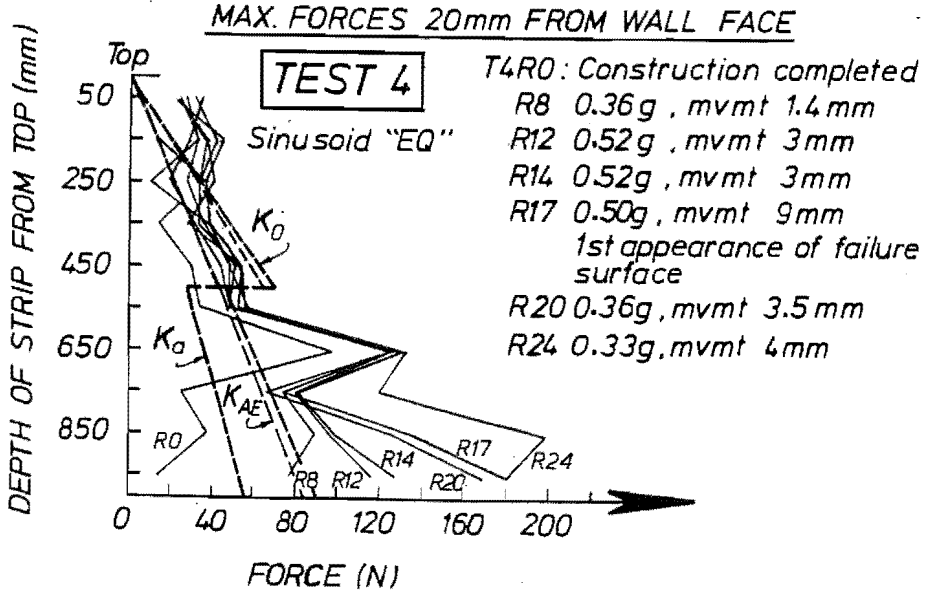

Fig. 6.47. Maximum forces adjacent to the wall facing, test 4.

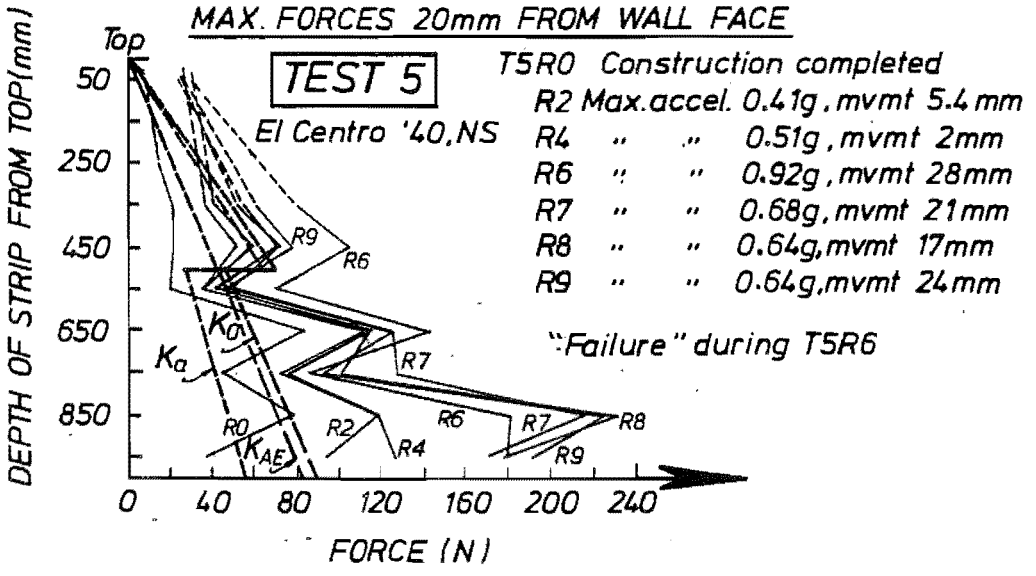

Fig. 6.48. Maximum forces adjacent to the wall facing, test 5.

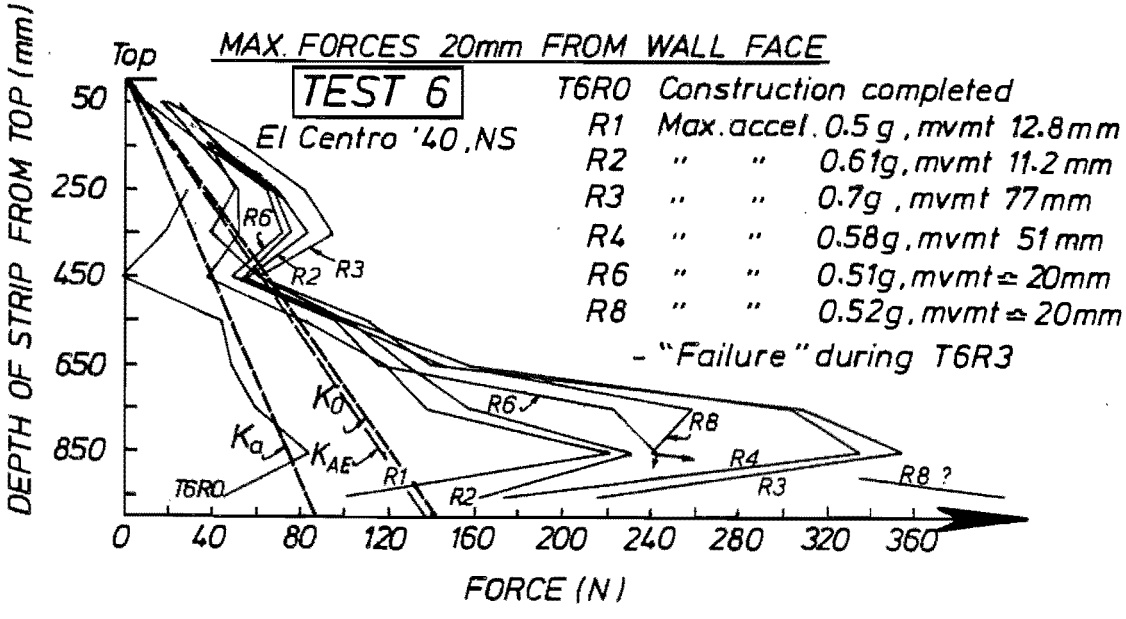

Fig. 6.49. Maximum forces adjacent to the wall facing, test 6.

The M-O earthquake earth pressure K_{AE} line is generally similar to the at-rest earth pressure K_0 line, and much less than the forces in Fig. 6.38 to 6.43. Maximum forces are more than twice those predicted using K_{AE} or K_0. The relationship between the earth pressure coefficient and the maximum forces is studied further in §6.9.

Figs. 6.50 to 6.55 show the distributions of residual forces adjacent to the wall facing. Residual forces are the forces in the strips at the end of the relevant test runs. They are in effect the post-earthquake forces. It can be seen that these forces are often significantly less than the peak forces, but still also much larger than the construction forces. The residual forces are also much larger than K_{AE} and K_0 forces, particularly in the critical strips numbers 2 and 3.

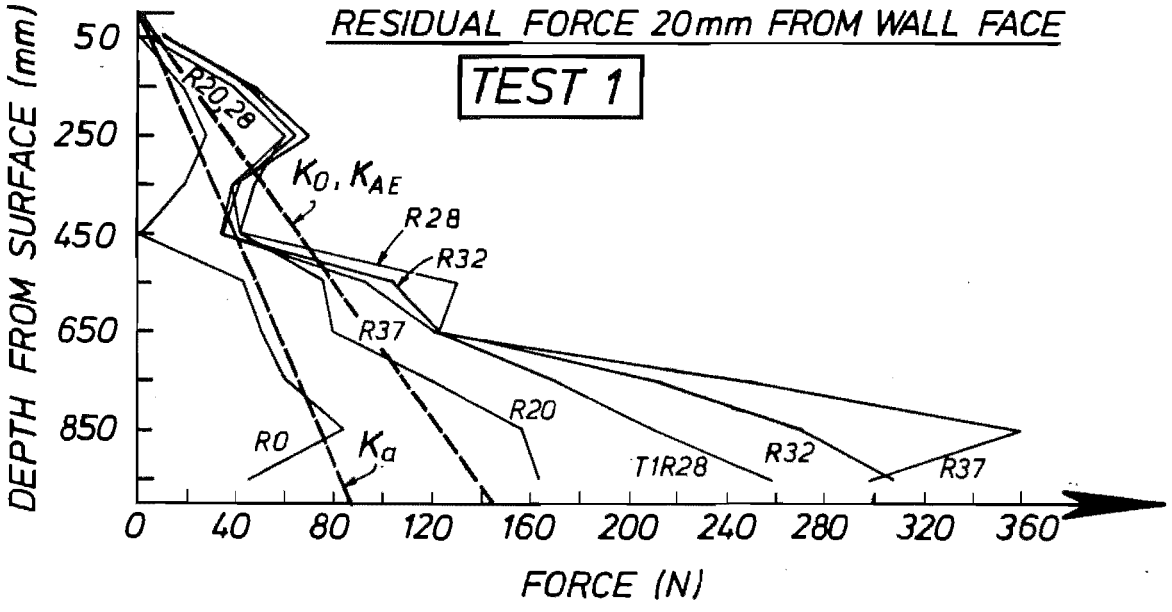

Fig. 6.50. Distribution of residual (end of run) forces at the wall facing, test 1.

6.4.2.4. Forces observed at the failure surfaces.

Using the observed failure surface geometries (Figs. 6.3 to 6.8 summarised in Table 6.3) the position at which the relevant failure surface intersects each strip can be easily calculated. Then the force at that position can be read off the graphs of maximum force distribution, and the

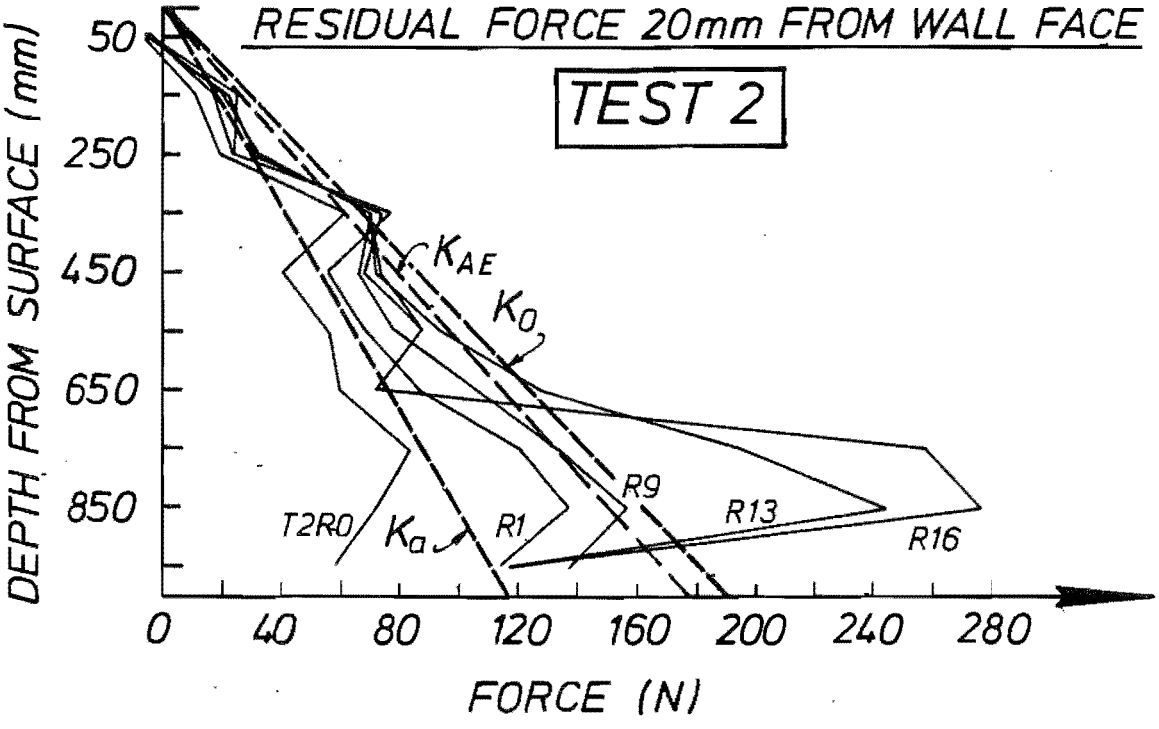

Fig. 6.51. Distribution of residual (end of run) forces at the wall facing, test 2.

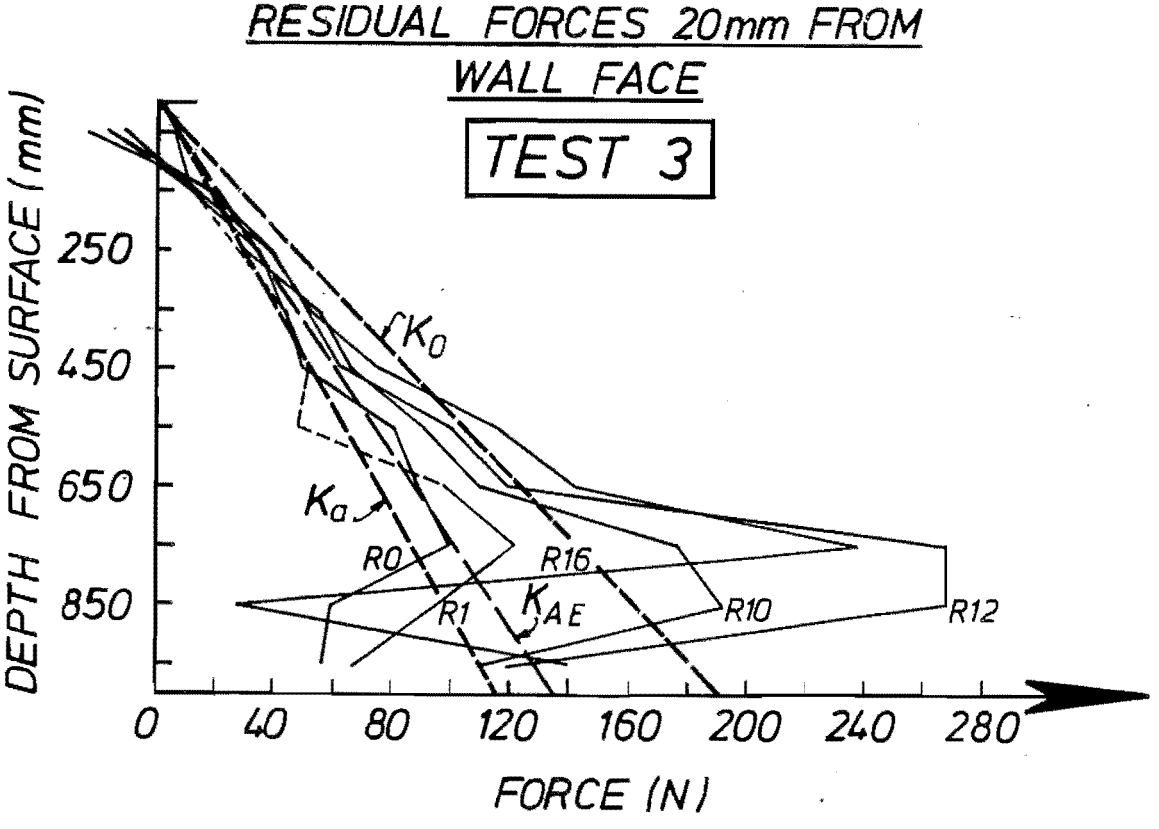

Fig. 6.52. Distribution of residual (end of run) forces at the wall facing, test 3.

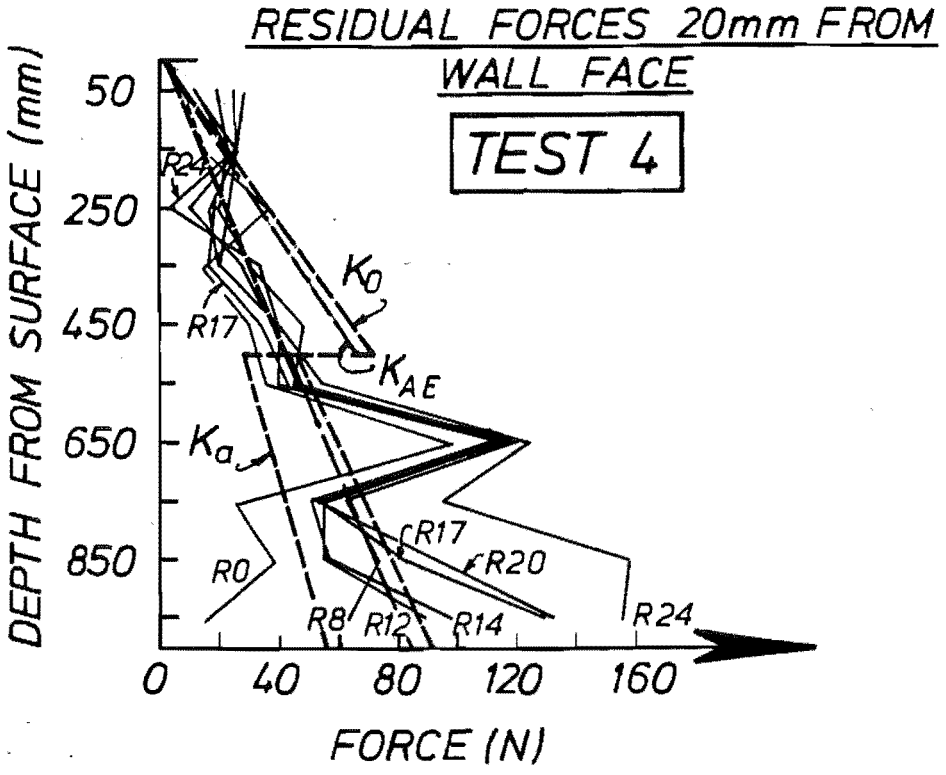

Fig. 6.53. Distribution of residual (end of run) forces at the wall facing, test 4.

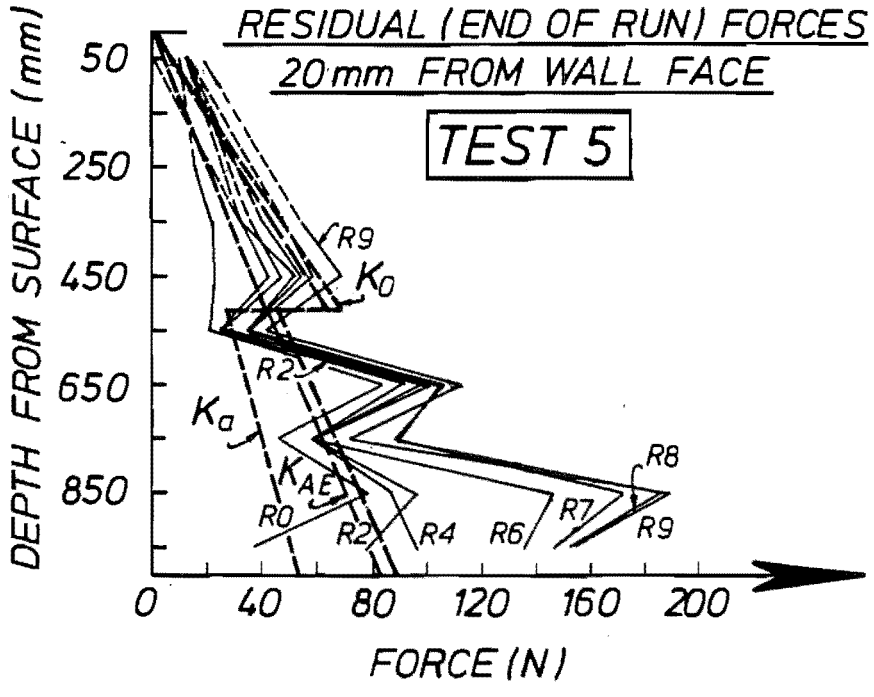

Fig. 6.54. Distribution of residual (end of run) forces at the wall facing, test 5.

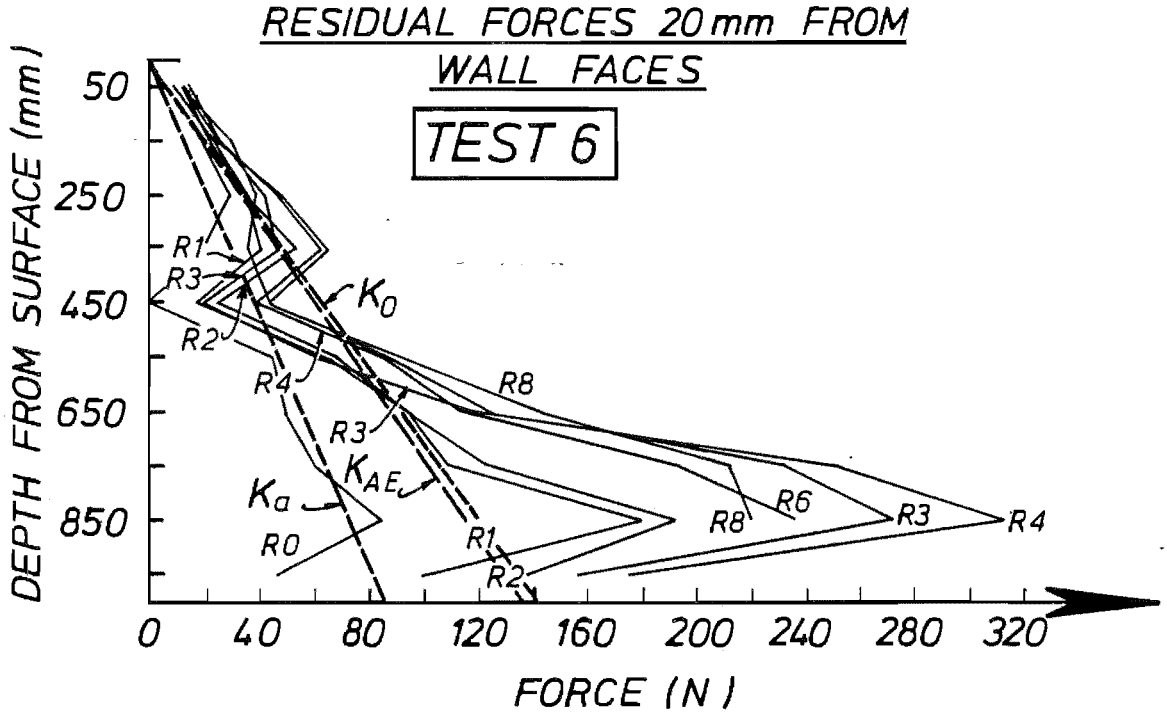

Fig. 6.55. Distribution of residual (end of run) forces at the wall facing, test 6.

total force R in the strips found. R is a parameter in the limiting equilibrium formulation, and can then be substituted into the equations. Thus the observed maximum force at the failure surface is used instead of calculating it using equations derived from Eq. 4.6. Table 6.6 to Table 6.11 show some observed forces derived in this way.

There are some trends in the data shown in Table 6.6 to Table 6.11. Forces in the rectangular reinforced block structures (walls 1, 2, 3, and 6)

Table 6.6
Observed forces at failure surface, and the geometry used, test 1.

Strip	Dist. from face (mm)	Forces at fail. surf. (N) R8	R20	R28	R32	R37
6	669	11	15	34	29	29
5	535	20	47	71	57	62
4	400	45	70	92	79	89
3	266	85	105	142	166	194
2	132	105	178	263	330	386
Sum of forces:		266	415	602	681	760

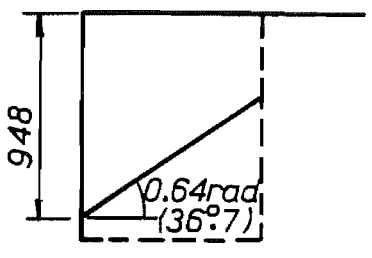

generally increase with continuing dynamic excitement. Test 1 and 2 data show no reduction in strip forces at the failure surface after failure (run 28 and run 13 respectively) whereas test 3 and test 6 data do show a reduction after failure (t3r11 and t6r3), with the largest forces found during the run at which the failure surface became fully developed. The reduced value is still larger than the earlier-measured forces. The two stepped block structures, on the other hand, have fairly constant levels of strip force at the failure surface, except during the run when the failure surface becomes fully developed (t4r17 and t5r6). This also shows in the data shown in Table 6.12 in the following section, where the calculated k_h is fairly constant.

Table 6.7
Observed forces at failure surface, and the geometry used, test 2.

Strip	Dist. from face (mm)	Forces (N) R1	R9	R13	R16
8	938	7	9	11	10
7	786	24	18	24	21
6	633	36	51	38	46
5	480	54	74	86	90
4	328	92	124	149	172
3	176	119	161	206	239
2	23	169	216	296	358
Sum of forces:		501	653	810	936

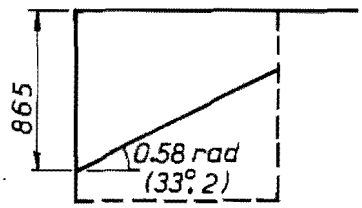

Table 6.8
Observed forces at failure surface, and the geometry used, test 3.

Strip	Dist. from face (mm)	Forces (N) R1	R10	R12	R16
8	749	0	0	0	0
7	642	7	27	11	-11
6	535	12	40	42	43
5	427	59	60	61	82
4	320	99	139	122	147
3	213	84	123	139	180
2	105	100	183	240	36
Sum of forces:		361	572	615	477

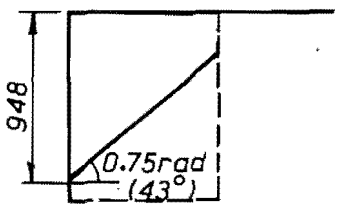

Table 6.9
Observed forces at failure surface, and the geometry used, test 4.

Strip	Dist. from face (mm)	Forces (N) R8	R12	R14	R17	R20	R24
9	892	1	1	1	1	1	0
8	780	26	29	29	31	30	28
7	668	22	24	24	32	22	18
6	556	68	68	68	72	68	58
5	445	49	49	49	49	49	49
4	334	10	14	14	30	19	18
3	221	72	59	53	65	44	47
2	110	114	111	108	157	139	135
Sum of forces:		362	365	346	437	372	353

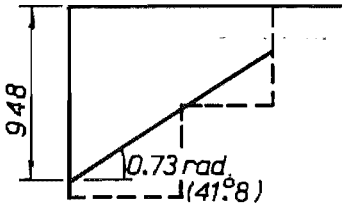

Table 6.10
Observed forces at failure surface, and the geometry used, test 5.

Strip	Dist. from face (mm)	Forces at failure surface (N) R2	R4	R6	R7	R8	R9
7	803	6	6	6	6	8	5
6	669	34	38	35	46	36	43
5	-	-	-	-	-	-	-
4	400	29	22	30	28	22	15
3	266	68	56	82	81	68	63
2	132	88	81	117	118	132	149
Sum of forces:		225	203	290	279	266	275

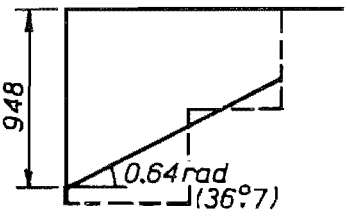

Table 6.11
Observed forces at failure surface, and the geometry used, test 6.

Strip	Dist. from face (mm)	Forces at failure surface (N) R1	R2	R3	R4	R6	R8
7	725	1	3	3	3	5	6
6	603	14	12	21	25	53	53
5	482	40	40	64	36	54	46
4	361	83	72	141	90	123	129
3	240	116	130	263	215	207	263
2	119	198	200	297	274	192	193
Sum of forces:		452	457	789	643	634	690

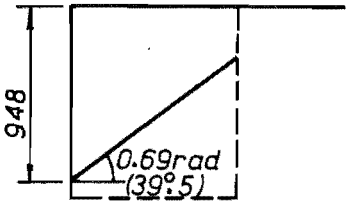

Looking more closely at test 3, the reason for the drop in the sum of forces at the end of the test is a major drop in force in strip one in run 16. The second facing panel up is lying horizontal, and the attached strips are offering no further resistance to outward movement of the wall. Hence the force in strip 2 has dropped to almost zero. There is still a general rise in force in the other strips, though.

In test 6, however, there is an overall drop in force in almost every strip passing through the failure surface, after failure (run 3). Why this should be is not clear. Test 6 was different from the other tests in that failure was in only the third "earthquake", so was subject to somewhat stronger motions prior to failure. While walls 6 and 1 had the same geometry, the forces at the failure surface at failure in wall 6 were some 27% greater than in wall 1, although the forces in wall 1 approached the wall 6 maximums with continued shaking after failure. Development of the maximum force possible (ie. when the maximum soil-strip friction is mobilised) is probably related in some way to the strength and predominant frequency of shaking. Note also that the forces at the failure surface in wall 4 are some 50% greater than in wall 5 at failure - walls 4 and 5 have similar geometry - although some of the force data for wall 4 may be unreliable. How the predominant frequency and strength of shaking affect the development of strip-soil friction needs investigation.

6.5. Observed forces in the limiting equilibrium formulation.

In this section the observed forces shown in Table 6.6 to Table 6.11 are used in the limiting equilibrium formulation. Firstly, they are used with the observed failure surface angle α to calculate yield acceleration, k_h, values (§6.5.1). Secondly, observed k_h and observed α are used to calculate the apparent mobilised f* at the failure surface and in the resistant zone (§6.5.2). Values of the force R derived in the calculations for f* are compared to the observed forces. Finally, observed forces and the observed k_h and α are used to find the mobilised soil internal friction ϕ (§6.5.3). When they are not being tested, ϕ and f* are 40° and 1.4 respectively, as

before. All calculations were done using computer programs written for the purpose.

6.5.1. Calculated k_h using observed failure surface angle α and observed forces.

Recall that in the general equations for the limiting equilibrium formulation (Eqs. 4.7, 4.15, and 4.26), the unit weight of the soil cancels out of all terms. Thus the sum of observed forces R must be divided by the soil unit weight before using it in the equations. The observed failure surface angle must be used as well, as the forces derived are only relevant to one failure surface angle. A value for k_h can then be calculated. k_h values derived in this way are shown in Table 6.12.

Table 6.12
Yield accelerations calculated using observed forces and failure surface geometry, for ϕ=40°.

test/ run	calc. k_h	obs. k_h	test/ run	calc. k_h (g)	obs. k_h	test/ run	calc. k_h (g)	obs. k_h
t1r8	0.15	none	t2r1	0.29	0.36	t3r1	0.09	none
t1r20	0.22	0.37	t2r9	0.34	0.33	t3r10	0.18	0.20
t1r28	0.30	0.25	t2r13	0.39	0.24	t3r12	0.19	0.08
t1r32	0.34	0.24	t2r16	0.44	0.20	t3r16	0.14	0.06
t1r37	0.37	0.23						
t4r8	0.21	0.30	t5r2	0.19	0.28	t6r1	0.21	0.34
t4r12	0.21	0.36	t5r4	0.17	0.32	t6r2	0.22	0.38
t4r14	0.20	0.36	t5r6	0.22	0.20	t6r3	0.37	0.24
t4r17	0.26	0.23	t5r7	0.22	0.22	t6r4	0.30	0.20
t4r20	0.22	0.20	t5r8	0.22	0.22	t6r6	0.30	0.20
t4r24	0.21	0.19	t5r9	0.22	0.17	t6r8	0.32	0.22

The increasing values of calculated k_h for tests 1 and 2, and to a lesser extent tests 3 and 6, indicate that some other parameter(s) in the formulation must be changing in value with continuing dynamic excitation of the walls, and/or with the development of permanent displacements. This effect is not observed in the stepped block structures, walls 4 and 5, although the forces measured during the run at which the failure surface became fully developed were larger, resulting in a larger calculated value for k_h. Forces measured

in the following runs dropped back to levels not far from the pre-failure values. Behaviour of rectangular and stepped block structures would seem to be fundamentally different.

The calculated values for k_h late in tests 4 and 5 are close to the observed values. The ϕ value used in the calculations (40°) is probably close to the mobilised value in those tests. Of the parameters in the limiting equilibrium formulation, only ϕ and f* values could conceivably change during dynamic excitation of a RE wall, causing over-estimation of the yield acceleration. This effect is investigated in the following sections.

6.5.2. Mobilised f* using observed α, observed k_h, and observed forces.

Table 6.13 shows values of f* calculated with the limiting equilibrium formulation using observed failure surface angle α and observed yield acceleration k_h. For these calculations the value of the soil angle of internal friction ϕ was maintained at 40°.

Table 6.13
Calculated f* and total force R, for ϕ=40°, using observed k_h and α. Observed forces are shown for comparison.

test/ run	calc. f*	calc. R	obs. R	test/ run	calc. f*	calc. R	obs R	test/ run	calc. f*	calc. R	obs R
t1r8	k_h not	obs.	266	t2r1	1.32	712	501	t3r1	k_h not	obs.	361
t1r20	1.85	762	415	t2r9	1.16	625	653	t3r10	1.32	633	572
t1r28	1.16	478	602	t2r13	0.68	367	810	t3r12	0.71	340	615
t1r32	1.12	461	681	t2r16	0.47	253	936	t3r16	0.61	292	477
t1r37	1.06	436	760								
t4r8	1.57	480	362	t5r2	1.65	380	225	t6r1	1.62	719	452
t4r12	1.85	570	355	t5r4	1.96	450	203	t6r2	1.82	807	457
t4r14	1.85	570	346	t5r6	1.06	250	270	t6r3	1.14	506	789
t4r17	1.24	380	301	t5r7	1.20	280	279	t6r4	0.96	426	643
t4r20	1.10	340	372	t5r8	1.20	280	268	t6r6	0.96	426	634
t4r24	1.05	320	353	t5r9	0.85	200	275	t6r8	1.05	466	690

Calculations for every test show that the value of f* mobilised seems to decrease with increasing permanent displacement of the walls, according to the limiting equilibrium approach. Apart from tests 2 and 3, the values derived for f* at the time of failure (full development of the failure surface) are similar: T1R28/1.16, T4R17/1.24, T5R6/1.06, and T6R3/1.14 for run/calculated friction coefficient respectively. For tests 2 and 3 they are T2R13/0.68 and T3R12/0.71. This again demonstrates that these two tests are somehow different to the others.

The corresponding values of R calculated at the same time as f* generally reduce as the tests progress. This trend is contrary to the observed trend of R increasing with increasing displacement of the walls. Thus the calculations show that ϕ must reduce during the tests. f* was isolated in the calculations for Table 6.12 above, with the result that the trend in the calculated k_h was contrary to the observed k_h. Only ϕ can change during the tests. In Table 6.13, forces were derived that showed a trend different to that observed. Again, the only parameter that can change is ϕ. The next section investigates the apparent mobilised angle of internal friction of the soil.

6.5.3. Mobilised ϕ using observed forces, k_h and α.

Table 6.14 shows the results of mobilised ϕ calculations using the computer programs written to solve the limiting equilibrium equations. Observed forces and observed failure surface angle α were used as the primary input, and the calculated k_h matched to the observed yield acceleration by changing the value of ϕ.

From Table 6.14 it can be seen that the mobilised ϕ appears to be about 46° or more (48.1, 45.8, 48.7, 44.7, 45.3, 47.0° for tests 1 to 6 respectively) near the beginning of each test. At the time the failure surface becomes fully developed, it is about 36° (37.2, 34.4, 33.8, 37.8, 39.0, 33.2° for tests 1 to 6). From Fig. 5.33, a value of 36° for ϕ corresponds to a confining stress of 30-35kPa, or a depth of 1.9 to 2.2m. at a density of 1.6 tonne/m^3. Clearly this is not possible in a 1m tall model. Either dilation of the sand undergoing shear causes a significant rise in the confining stress

Table 6.14

Mobilised ø calculated using observed forces, k_h and α in the limiting equilibrium formulation. Run numbers in italics are those in which 'failure' occurred.

test/ run	calc. k_h (g)	obs. k_h (g)	implied ø (°)	test/ run	calc. k_h (g)	obs. k_h (g)	implied ø (°)	test/ run	calc. k^h (g)	obs. k^h (g)	implied ø (°)
t1r8		none		t2r1	.355	0.36	45.8	t3r1	.242	none	48.7
t1r20	.368	0.37	48.1	t2r9	.336	0.33	42.4	t3r10	.197	0.20	41.3
t1r28	.254	0.25	37.2	*t2r13*	.237	0.24	34.4	*t3r12*	.083	0.08	33.8
t1r32	.236	0.24	34.4	t2r16	.202	0.20	30.4	t3r16	.057	0.06	35.5
t1r37	.230	0.23	32.1								
t4r8	.301	0.30	44.7	t5r2	.281	0.28	45.3	t6r1	.337	0.34	47.0
t4r12	.365	0.36	48.7	t5r4	.322	0.32	48.7	t6r2	.381	0.38	49.3
t4r14	.358	0.36	48.7	*t5r6*	.208	0.20	39.0	*t6r3*	.254	0.24	33.2
t4r17	.234	0.23	37.8	t5r7	.221	0.22	39.5	t6r4	.216	0.20	35.0
t4r20	.198	0.20	38.4	t5r8	.223	0.22	40.1	t6r6	.211	0.20	35.0
t4r24	.188	0.19	38.4	t5r9	.172	0.17	36.7	t6r8	.218	0.22	33.8

in the model walls, or the test results shown in Fig. 5.33 are incorrect, which may be the case considering the findings of Fukushima and Tatsuoka (1984), who found that ø does not rise significantly at low stress levels.

This finding, that ø reduces in value with increasing permanent displacement, is perhaps to be expected. Early in the tests, the soil is in a relatively unstrained state, so ø will be increasing towards the peak value. As the failure surface forms, ø passes the peak value and starts to reduce. As the failure surface grows, more and more of the sand (ie. the failure surface zone) passes the peak ø value and reduces towards the residual strength. Hence the average value of the mobilised soil friction angle would be expected to reduce. If this is the case, we would also expect the apparent mobilised ø to remain fairly constant or reduce only a little (due to overall straining of the failure block) after failure. Table 6.14 shows that this is indeed what happens.

We have now used the limiting equilibrium formulation to show that the average soil angle of internal friction ø decreases during seismic excitation of RE walls. We have found that the average mobilised friction coefficient f* is similar to the peak friction coefficient measured in sliding shear tests. We have also seen that the limiting equilibrium approach can be used to derive a value for the yield acceleration k_h, and also for the failure

surface angle α, although α tends to vary somewhat from wall to wall. Next, we will investigate the mobilised friction coefficient in some detail - it is a critical parameter in design of RE walls. First, we will use the R formulation (Eq. 4.6) to obtain an average value for f* for several test runs, then we will derive f* for individual strips using Eq. 5.3, which was effectively summed over the failure surface to derive Eq. 4.6.

6.6. Mobilised f* from strip pullout force formulations.

The formulation for R in Chapter 4 (Eq. 4.6) is stated again below:

$$R = 2bn\rho g f^* \left(\left(L - \frac{h}{\tan\alpha} \right) \sum_{i=p}^{m} y_i + \frac{1}{\tan\alpha} \sum_{i=p}^{m} y_i^2 \right) \qquad \text{.....(4.6)}$$

R is the total force in the strips at the failure surface, b is the strip width, n is the number of strips per lineal metre of wall, ρ is the soil density, g is gravity, L is the resistant length of the strip, y_i is the depth to the ith strip, p is the layer number of the lowest strip and m of the highest strip intercepted by the failure surface. This equation is used to calculate the average mobilised friction coefficient f* (ie. on all strips that cross the failure surface, simultaneously) from the observed forces, which were shown in Table 6.6 to Table 6.11. Results of these calculations are shown in the next section (§6.6.1). f* can also be calculated from Eq. 5.3 for each strip, again using the forces from Table 6.6 to Table 6.11. Eq. 5.3 was

$$f^* = \frac{T}{2bL\gamma y} \qquad \text{.....(5.3)}$$

where T is the measured tension force. An average f* can be derived for forces measured anywhere in the strips, assuming that the length L is the length from the measurement point to the free end of the strip. These results are shown in §6.6.2.

6.6.1. Mobilised friction coefficient f* from forces at the failure surface, using the R formulation (Eq. 4.6).

Table 6.15 shows the results of calculations of f* using the R formulation of Eq. 4.6 on forces at the failure surface, taken from Table 6.6 to Table 6.11. For tests 4 and 5 Eq. 4.6 was modified to sum over the top and bottom steps of the structure separately. This is necessary because the n values (number of strips per metre length of wall) are different in the top and bottom steps.

Table 6.15
f* calculated using the R formulation of Eq. 4.6; for tests 4 and 5 it summed over the top and bottom steps of the structure separately.

test/ run	calc. f*	test/ run	calc. f*	test/ run	calc. f*
t1r8	0.65	t2r1	0.64	t3r1	0.75
t1r20	1.01	t2r9	0.84	t3r10	1.19
t1r28	1.46	*t2r13*	1.04	*t3r12*	1.28
t1r32	1.65	t2r16	1.20	t3r16	1.00
t1r37	1.85				
$t4r8_t$*	1.38	$t5r2_t$	0.93	t6r1	1.33
$t4r12_t$	1.44	$t5r4_t$	1.02	t6r2	1.34
$t4r14_t$	1.44	*$t5r6_t$*	0.95	*t6r3*	2.31
$t4r17_t$	1.61	$t5r7_t$	1.20	t6r4	1.89
$t4r20_t$	1.43	$t5r8_t$	1.02	t6r6	1.86
$t4r24_t$	1.23	$t5r9_t$	1.11	t6r8	2.02
$t4r8_b$	1.14	$t5r2_b$	1.07		
$t4r12_b$	1.08	$t5r4_b$	0.92		
$t4r14_b$	1.04	*$t5r6_b$*	1.32		
$t4r17_b$	1.40	$t5r7_b$	1.31		
$t4r20_b$	1.16	$t5r8_b$	1.28		
$t4r24_b$	1.16	$t5r9_b$	1.31		

* $_t$ and $_b$ refer to the top and bottom steps of the stepped block structure.

There is a general rise in mobilised f* during tests 1 and 2, shown in Table 6.15. Tests 3 and 6 show a rise up to failure then a reduction afterwards. The stepped block structures, tests 4 and 5, show only small increases, if any. These trends will be checked against the individual strip values of apparent mobilised f*.

6.6.2. Mobilised friction coefficient f*: strip by strip using Eq. 5.3.

Figs. 6.56 to 6.61 show the mobilised friction coefficient f* at the failure surface, calculated using Eq. 5.3 and the forces in Table 6.6 to Table 6.11. Tables C.1 to C.6 in Appendix C show the same information. Figs. 6.62 to 6.67 show the values of f* calculated using Eq. 5.3 for forces at the measuring points 20mm from the facing, as shown on Figs. 6.44 to 6.49. This data is tabulated in Tables C.7 to C.12. Finally, Figs. 6.68 to 6.73 show f* values determined using Eq. 5.3 and the maximum force measured in each strip, and the data is tabulated in Tables C.13 to C.18. There is some discussion of the first two sets of data before the maximum force f* data is presented.

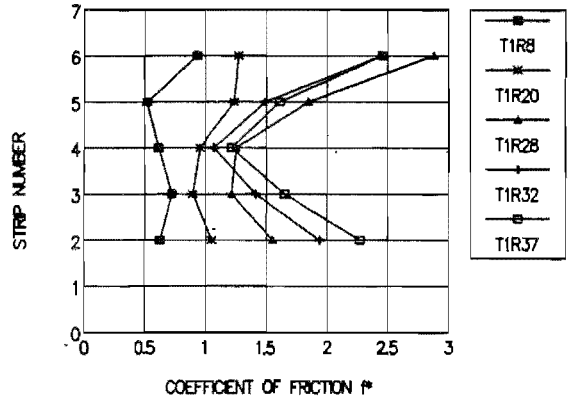

Fig. 6.56. Mobilised friction coefficient f* at the failure surface, test 1. Failure was at run 28.

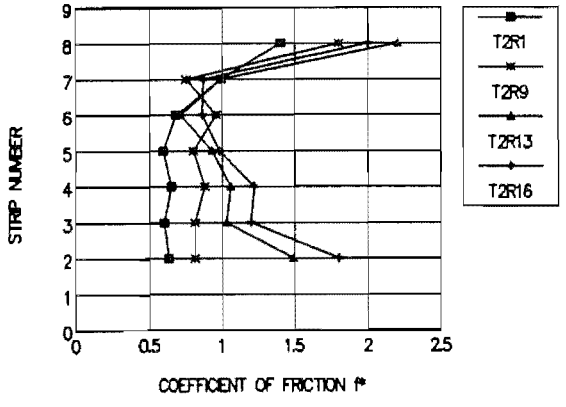

Fig. 6.57. Mobilised friction coefficient f* at the failure surface, test 2. Failure was at run 13.

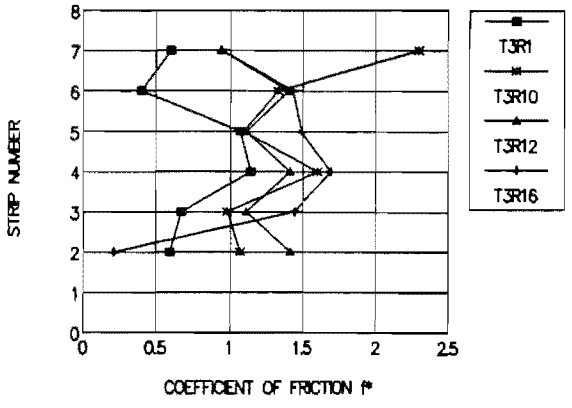

Fig. 6.58. Mobilised friction coefficient f* at the failure surface, test 3. Failure was in run 11.

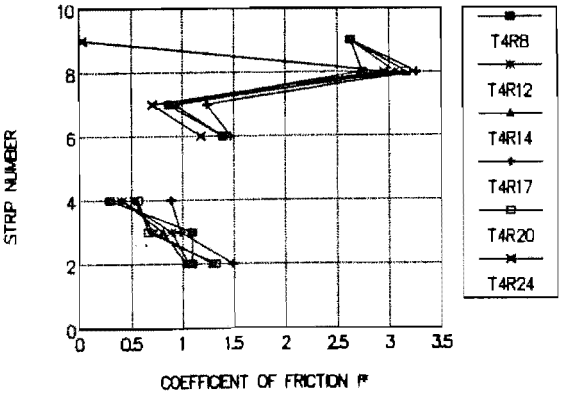

Fig. 6.59. Mobilised friction coefficient f* at the failure surface, test 4. Failure was in run 17.

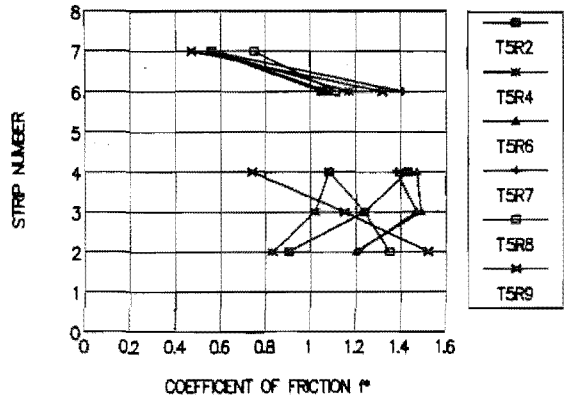

Fig. 6.60. Mobilised friction coefficient f* at the failure surface, test 5. Failure was in run 6.

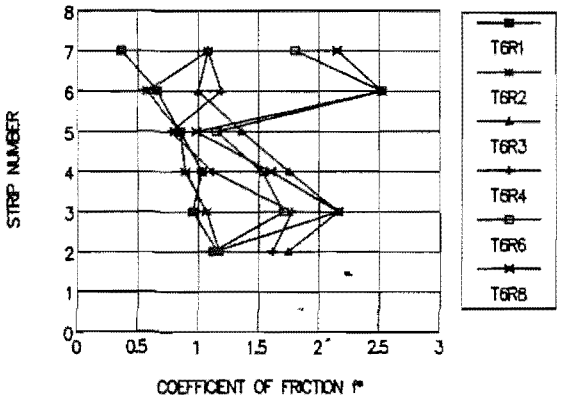

Fig. 6.61. Mobilised friction coefficient f* at the failure surface, test 6. Failure was in run 3.

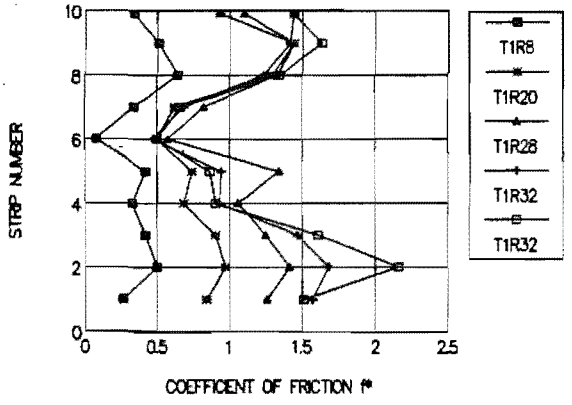

Fig. 6.62. Mobilised friction coefficient f* for maximum forces at the facing, test 1.

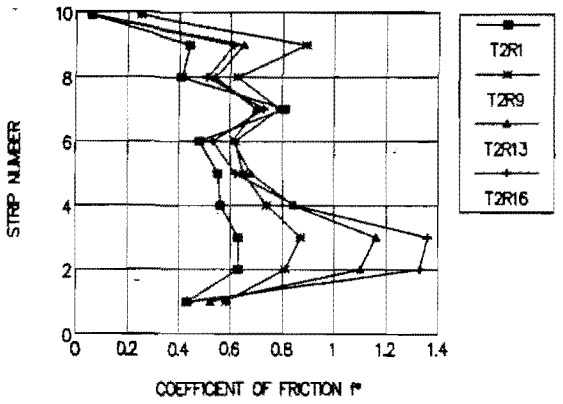

Fig. 6.63. Mobilised friction coefficient f* for maximum forces at the facing, test 2.

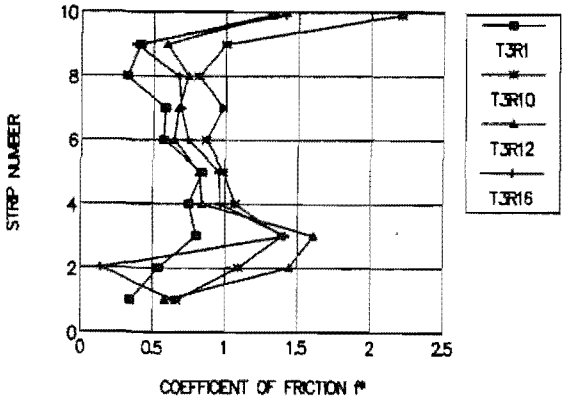

Fig. 6.64. Mobilised friction coefficient f* for maximum forces at the facing, test 3.

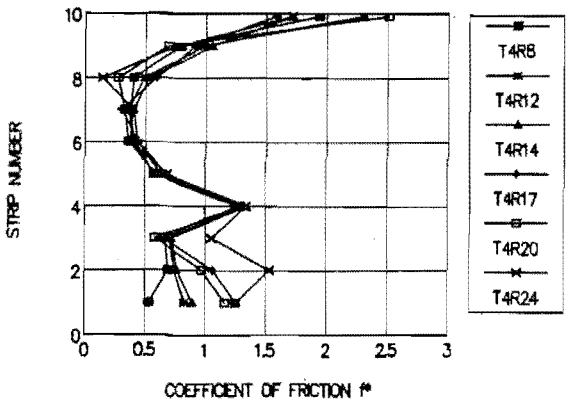

Fig. 6.65. Mobilised friction coefficient f* for maximum forces at the facing, test 4.

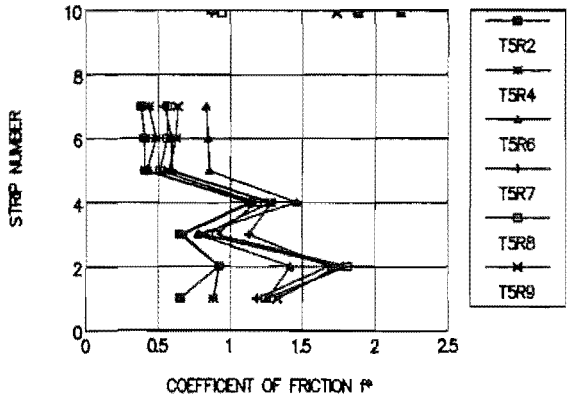

Fig. 6.66. Mobilised friction coefficient f* for maximum forces at the facing, test 5.

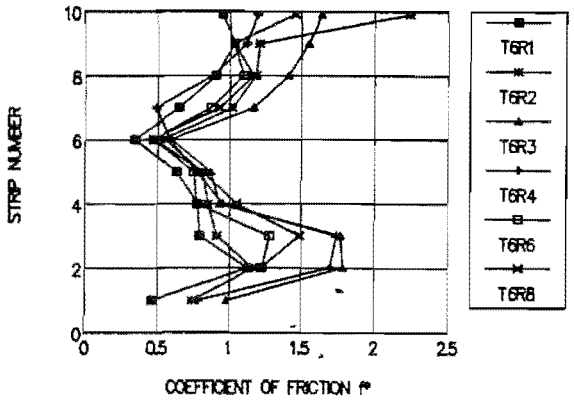

Fig. 6.67. Mobilised friction coefficient f* for maximum forces at the facing, test 6.

1. There is a marked increase in mobilised friction as the failure surface becomes fully formed (ie. the wall "fails"), both at the failure surface and at the facing. This is the case in every test in Figs. 6.56 to 6.67. The failure surface outcropped at the fill surface in t1r28, t2r13, t3r12, t4r17, t5r6, and t6r3.

2. After failure, in test 1, f* continued to increase in the lower half of the wall with continuing testing, and there was a small decrease in the topmost strip passing through the failure surface. The same thing happened in wall 2. Test 3 had a reduction in f* in the highest and lowest strips passing through the failure surface, but an increase in the mid-height strips (strips 2 to 6), after failure. The test 4 f* values at the failure surface reduced after failure. Test 5 strips 3 and 4 experienced a decrease in f* after failure, but in strips 2 and 6 f* increased. In wall 6, there was a reduction in f* in the lower part of the wall (strips 2 to 5) but a substantial increase in strips 6 and 7. The force distribution diagrams for test 6 strips 6 and 7 (Fig. 6.43) show that the forces measured near the facing decreased after failure, but towards the free end of the strips the post-failure forces were greater than at and before failure.

3. f* values at the facing behave slightly differently after failure. In test 5, f* increased after failure in the bottom part of the wall, but decreased over the remainder. Test 6 values generally decreased after

failure, as mentioned above. In wall 1, f* increased slightly near the top of the wall, decreased a little around midheight, and increased strongly in the lower part of the wall (strips 1, 2, and 3). f* increased consistently in the lower part of wall 2, was fairly constant in the middle part, and decreased in the upper part of the wall, after failure. Wall 3 f* values generally decreased slightly after failure, with strip 2 taking very little load in run 16: the facing panel was lying more or less horizontal by this stage and offering little resistance to outward movement of the wall. In wall 4 there was an increase in f* after failure in the bottom of the wall, and in the top strips it was variable, although in strip 8 f* reduced significantly after failure. In the middle part of this wall there was very little variation in f* at the wall face during the test.

4. With regard to the distribution of f* at the facing, there is a tendency for f* to be large near the surface of the fill. This is especially so in the stepped block structures (walls 4 and 5). In walls 1 and 2 there was a reduction in f* in the topmost strip. The force data for the top strips in both walls may not be reliable, as evidenced by the odd shapes of the force distributions (Figs. 6.38 and 6.39). Mobilised friction is usually smallest in the region of strip 6, and increases toward the base of the wall. There is also a reduction in f* mobilised at the facing in the lowest strip, no doubt because part of the load that would be taken by the reinforcing strips is taken by the burial soil in front of the wall. In walls 4 and 5 the reduction in f* around strip 6 extends to strips 5 and 8. In both these walls, there is a strange increase in f* at the facing in strip 4. It may be that the step in strip lengths from strip 5 (500mm) to strip 6 (900mm) throws some of the load that would be taken by strip 5, in a rectangular structure, onto strip 4, although why there is not a concomitant increase in friction mobilised in strip 6 is difficult to say.

5. The distribution of f* with wall height, at the failure surface, is much more variable than at the facing. In Fig. 6.62 it can be seen that there are fairly clearly defined patterns of f* vs. depth for each test, while in Fig. 6.56 the patterns are a little less obvious. Part of the reason for this is that f* values at the failure surface are much larger

for some strips than at the facing, and increases or decreases between runs are also much larger eg. strip 6 wall 1; strip 8 wall 2; strip 7 wall 3; strips 6, 7, 8, and 9 wall 4; strip 6 wall 5; and strips 6 and 7 wall 6. A closer look at the above list of strips reveals that they are all the upper-most (or nearly) strips intersected by the failure surface.

6. Around mid-height of the walls (strips 4, 5, 6 and 7), the apparent mobilised friction at the facing varied least during the testing. It was also generally at or near the minimum value in each wall at one of the strips situated in this area. At the failure surface this region of relative constancy of f* was reduced to usually one strip, and it was not always the same number strip.

7. The rectangular block structures show a greater range of f* values at any particular level, from run to run, than do the stepped block structures.

8. All tests show a reduction in mobilised f* in strip 1, the lowest strip, at the wall facing. This reflects the effect of the partial burial of the bottom facing panel according to the design requirement for burial to 8.5% of the overall height of the wall (MWD, 1980).

Below (Figs. 6.68 to 6.73) are the maximum-force values of f* occurring at the position, on the relevant strips, of the forces cited. The data is tabulated in Tables C.13 to C.18. Also given in the tables are the distances from the measuring point to the free end of the strip, L.

The maximum-force f* graphs (Figs. 6.68 to 6.73) show up the dubious nature of some of the force data. There are massive increases in f* for some strips: these generally reflect an odd peak in the force distribution graphs. Some strips have been left off these plots also, because of f* values thought to be excessive resulting from odd force distribution shapes. Similar points to those above for the f* values at the failure surface and the facing can be made.

1. f* increases, as mentioned above, as the failure surface becomes fully developed.

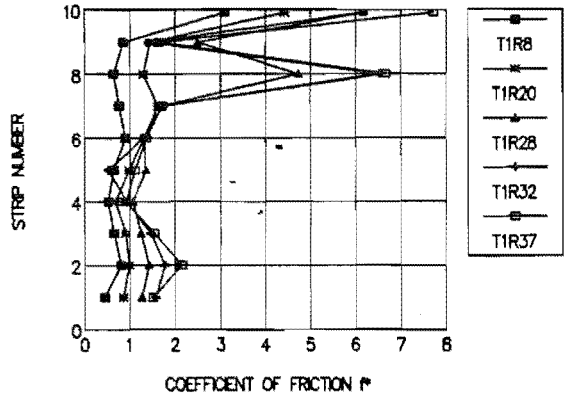

Fig. 6.68. Mobilised friction coefficient f* from maximum forces, test 1.

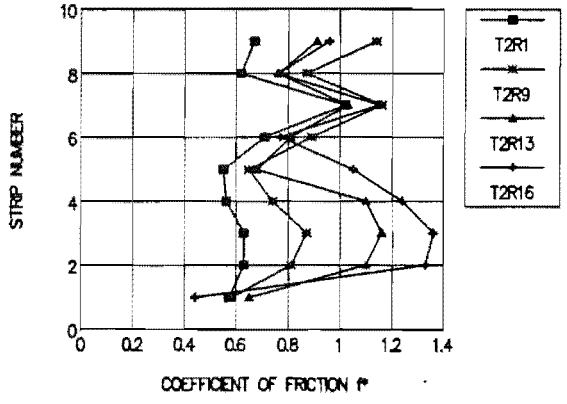

Fig. 6.69. Mobilised friction coefficient f* for maximum forces, test 2.

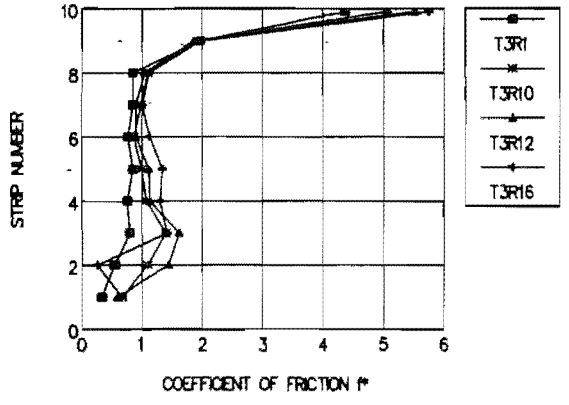

Fig. 6.70. Mobilised friction coefficient f* for maximum forces, test 3.

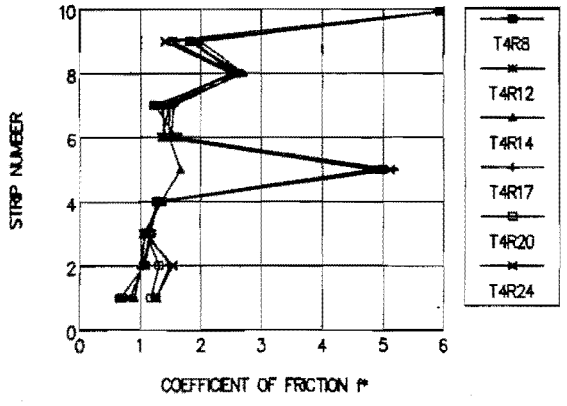

Fig. 6.71. Mobilised friction coefficient f* for maximum forces, test 4.

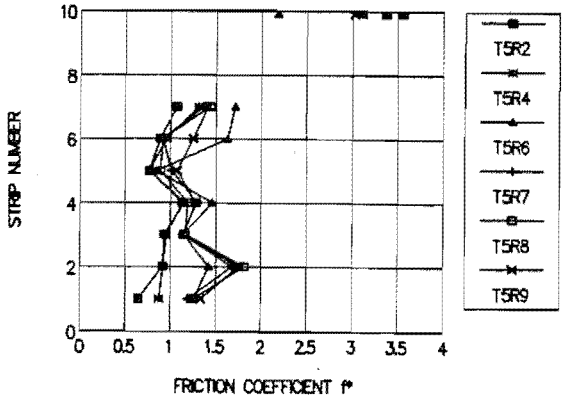

Fig. 6.72. Mobilised friction coefficient f* for maximum forces, test 5.

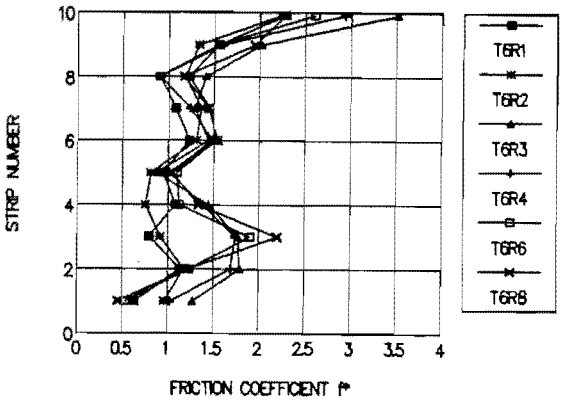

Fig. 6.73. Mobilised friction coefficient f* for maximum forces, test 6.

2. After failure, f* still generally increases in the lower part of the walls. In wall 1, f* increases after failure, whereas in the mid-height region it reduces. No real trend is evident in the top part of the wall: forces seem to be much larger than can be justified. Wall 2 behaved similarly, although there was also a decrease in f* in the upper part of the wall after failure. Test 3 f* values reduced in the upper part of the wall, increased in the middle part and decreased in the lower part. For test 4 f* decreased then increased again in the lower part of the wall, and was relatively stable over the upper 2/3 of the wall, after failure. In wall 5, the mobilised friction coefficient increased after the failure surface became fully developed, while in wall 6 it decreased in the lowest 2 strips and near the wall top, and increased in the middle portion of the wall.

3. As before, f* is generally a minimum around strip 5, near the mid-height of the walls. There is a sharp increase around strips 2 and 3, and a reduction in strip 1. It is difficult to be definitive about f* in the upper part of the walls from the maximum-force values, but it probably increases.

In the next section there is discussion of the design implications of the apparent mobilised friction coefficients shown above. First, though, there is some general reporting about what factors have been found to be important in friction in RE walls. The mobilised friction coefficient f* will be shown to be close to the maximum value measured in the sliding shear tests reported in §5.4.2.

6.7. Strip-soil friction in reinforced earth.

6.7.1. Introduction.

The following section gives an overview of previous research into strip-soil friction in reinforced earth. The tests used to investigate friction, and factors found to be important, are described. Then the current design rules are shown and discussed. Comparison is then made between friction

parameters measured and reported in Chapter 5, and the mobilised friction observed in the seismically excited test walls. It is found that peak sliding shear f* values are close to the maximum observed values seen in the previous section.

6.7.2. Previous research.

Soil-reinforcement friction was studied quite closely during the 1970's, but relatively little has been published on this topic since. In 1978 it was still felt to be little understood, not withstanding the many test reports in the literature (Lee, 1978, and McKittrick, 1978).

Several different types of test have been used to quantify the soil-strip friction, as follows (McKittrick, 1978):

i. direct shear (also called sliding shear) tests, at model and prototype scales;
ii. pullout tests, from RE walls at model, prototype and full scales;
iii. pullout tests from embankments;
iv. pullout tests with a rigid moving wall, model scale; and
v. pullout tests during vibration, model and prototype scale.

Of these tests, the direct shear is the easiest and most inexpensive to perform. Direct shear tests do not, however, allow investigation of the factors affecting the pullout resistance of reinforcing, but represent the two-dimensional case of an infinite sheet of reinforcing material (Schlosser and Long, 1974). In these tests the normal stress and shear stress are considered to be accurately known, so the results are expected to be quite accurate. With pullout tests, on the other hand, the normal stress is unknown because of the effects of dilatancy, so the derived friction coefficient is an "apparent" friction coefficient. Pullout tests are idealizations - the deformations of the strips, and the position of the maximum tensile force in the strips, may not represent the field situation. Guilloux, Schlosser and Long (1979) and Jewel (1979) also reported a group effect (interaction between strips) that may not be modelled by most pullout tests. Pullout tests give an average apparent friction coefficient over the length of strip-soil contact between points at which strip forces are measured. Where only the pullout force is measured the coefficient of friction derived

is an average over the entire length of strip-soil contact. Pullout tests can also show what factors influence f*.

Many of the pullout tests reported have been done with tubular sleeves at one or both ends of the strips being pulled (for example, Yourmann, 1978, at model scale). Sleeves at the facing are used in an attempt to negate any edge effects. Sleeves at both ends of the pulled strip are used to ensure a uniform length of strip in contact with the soil throughout the test, as well as to reduce any "far end" effect. Yourmann found that sleeves at the facing had little effect, causing a reduction of peak friction angle of about 1°.

Investigators have usually recommended that the peak apparent friction coefficient found in pullout tests be used in design (eg. McKittrick, 1978, and Schlosser and Elias, 1978).

McKittrick (1978) and Schlosser and Elias (1978), which are both summary papers given at conferences on earth reinforcing, state that the main factors affecting the pullout resistance of reinforcement in RE walls have been found to be the soil density, the geometry of the reinforcement, the normal stress on the reinforcement, the nature of the reinforcing strip surface, and the percentage of fines in the soil. Cormack et al (1980) point out that the moisture content of the soil is important. Hausmann and Ring (1980) state that for pullout tests the mechanical arrangement of the experiments affects the results, though they do not explain how. Soil dilatancy and relative strains (soil-reinforcement) are also important, so that the friction mobilised at each point in a RE wall is a function of the overall deformations of the reinforced mass. (Mitchell and Schlosser, 1979.) The main factors affecting pullout resistance are briefly discussed individually below.

Density. (Schlosser and Elias, 1978)

With low-density backfills, the peak pullout force is found at small displacement (a few millimetres), and is very accentuated with a rapid fall-off in pullout force with continued pulling after the peak. At higher density the peak force occurs at larger displacements (a few centimetres). In low density fills the strip acts as if rigid and friction is almost uniformly mobilised, whereas in high density fills the deformation of the strip domi-

nates and friction is mobilized in only portions of the reinforcing. The portions increase in size as the pullout force increases. At high density, the apparent coefficient of friction f* is much greater than tan ¥ (¥ is the friction angle between the soil and smooth reinforcement, found from sliding shear tests), while at low density f* is less than tan ¥.

The most important effect of density however, is its effect on the dilatancy of the soil. Dense sands are more dilatant than less dense ones, so shearing dense soils will cause a rise in the confining stress as the soil dilates, and hence an increase in f* (Mitchell and Schlosser, 1979). In low-density situations, pulling is thought to actually cause a local and limited collapse in the soil structure, which reduces the overburden stress and hence the pulling force required. (Schlosser and Elias, 1978). This partial collapse, together with soil arching, means that the strip is effectively pulled in a tunnel of low-density material. Usually, however, fills in RE walls are placed in a dense state. Hausmann and Ring (1980) confirmed experimentally that the rate of dilatancy (change in sample height divided by the shearing displacement) of a sand is a property of the sand material and its density, a conclusion that had previously been reached theoretically.

Width of the reinforcement.

Schlosser and Elias (1978) state that in model studies, f* decreases with increasing width of reinforcing strip, for heights of wall less than 18cm (very small models). The effect was not clear for walls greater than 18cm in height. Bacot et al (1978) reported tests of pullout from an embankment up to 2.8m. high. They found that f* reduced as the width of strip increased, and explained it by saying that wider strips are stiffer and thus "undulate more" (they mean less?) on placement in the soil, resulting in lower pullout strength. (They probably mean that the stiffer strips cannot undulate to match the fill surface when they are placed during construction, so they undulate more in relation to the soil surface than less stiff strips might.) No effect of width on f* has been reported in other full size pullout tests.

Two other factors Schlosser and Elias point out are that wider strips are less deformable, and that at some critical width dilatancy effects must start to decrease. We might expect that as the strip width increases, the

dilatancy is forced to reduce from a two-dimensional (lateral and vertical) to a one-dimensional (vertical only) expansion, resulting in a smaller rise in confining stress and a lower apparent f*. As regards the deformability of the strips, Jewel (1979) found that the less extensible the strips are, the more load they attract and the more effective they are as reinforcing in the soil. Yourmann (1978) reported that the ratio of residual to peak pullout strength increased (from about 0.25 to 1) with increasing width, at model scale.

Length of the reinforcement.

Full size pullout tests show that f* increases (at a decreasing rate) as the strip length increases, up to a length of about 8m. Thereafter elongation of the reinforcing becomes dominant and there is a slight falloff in the average apparent coefficient of friction (Schlosser and Elias, 1978; McKittrick, 1978). Yourmann (1978) found that the ratio of peak to residual pullout force was constant for all lengths he tested (model scale), and that the friction angle between mylar tape (one of his strip materials) and sand was constant for all lengths tested, contrary to Tso's (1988) report of his work. He also found that the deflection to peak strength was not proportional to the length or width of strip, for strips of both mylar and of glass fibre mesh. The ratio of peak to residual pullout force was constant for all lengths tested.

Yourmann also did what he called wall-moving tests, where he rotated outwards a rigid wall on a hinge at the base. Reinforcing strips were attached to the wall, and the pullout force measured at the facing. He found in these tests that the apparent coefficient of friction decreased with increasing strip length, contrary to the case in pullout tests. The difference was felt to be an indication of the difference between f* measured in a standard field pullout test and the friction developed in a yielding RE wall, the implication being that the pullout test did not represent the true situation inside a wall. It also implies that he is thinking of the small deformations in a wall not subject to earthquake excitation. Hausmann and Lee (1978) reported similar tests, although they did not compare mobilised friction with strip length. Their tests did show, however, that the mobilised soil-strip friction angle in rotating wall tests was much greater than in pullout tests using the same strip material and the same sand. RE walls

subject to seismic shaking do not fail by outward tilting though, so this type of test is not representative.

Overburden stress.

The value of the apparent friction coefficient has been found to decrease with increasing overburden pressure (Mitchell and Schlosser, 1979; Schlosser and Elias, 1978). Large overburden stresses are said to suppress dilation in the soil, causing f* to approach tan ϕ (ribbed strips) or tan Ψ (smooth strips). Mitchell and Schlosser also point out that most granular soils exhibit curved failure envelopes, with ϕ decreasing with increasing effective stress. Schlosser and Elias state that for low overburden stress (γh) f* is often very high (2 to 6), but decreases and becomes constant (at about tan ϕ) above $\gamma h \approx 100 kN/m^2$ (about 6m. depth for most soils). Yourmann found that the pullout deflection to peak strength was not proportional to the overburden stress.

Interwoven with the effects of overburden stress on the pullout strength in RE are the effects of soil dilatancy. Wernick (1978), pulling strips out of soil inside a metal cylinder, showed that the surrounding pressure around reinforcing during pullout is greater than the overburden pressure, maybe 8 times as high as the initial value, hence high values of f* are derived, as well as high apparent values of ϕ. Guilloux et al (1979), using constant volume direct shear tests, found up to 14 times increase in normal stress during shearing. McKittrick (1978) points out that constant volume derivations of Ψ were 10 to 15° higher than those from constant stress tests. Hence in conditions of low overburden stress, or shallow depth, f* values can be expected to be high: in these locations the dilatancy rate is high but there is some constraint against expansion of the soil, causing a rise in the mean normal stress above the value usually assumed to derive f* values.

Koivumäki (1983) attempted to find out why the apparent coefficient of friction for the upper part of a RE wall is greater than the lower part, and also sometimes greater than ϕ. Shear box tests and a simple energy equation were used to take into account the stress state, as well as the strain state (which is usually neglected). It was shown that the angle of shearing resistance has 2 components: "plastic state" friction, and dilatancy. The plastic state friction component was found to be almost constant, independent of the

initial density and also of pressure. The dilatancy component clearly depended on the confining pressure, and decreased with increasing normal stress. Schlosser, Jacobsen, and Juran (1983) comment that constant stress direct shear tests (used by Koivumäki) do not represent the restrained dilatancy that occurs around inclusions in real structures.

Hausmann and Ring (1980) carried out shear box tests on samples of sand and on samples of sand on metal plate coated with sand. They found that there was a clear difference in deformation patterns between loose and dense sand. The zone of deformation was twice as thick for sand-sand as for sand-plate. Sand-sand and sand-plate friction angles were approximately equal. The rate of dilatancy ((change in sample height) / (horizontal shear displacement)) was also approximately equal for sand-sand and sand-plate. Hence there was felt to be no relationship between the thickness of the shear zone and the rate of dilatancy. At low normal stress, there was complete slip of all soil at the sand-plate interface, whereas at high normal stress (> 70kPa) there was no slip of soil along the interface. Where there was no slip at the interface, the angle of friction (sand-plate) was equal to ϕ. Decreasing normal stress resulted in increasing slip and rate of dilatancy. For low normal stress they found that the angle of friction was greater than ϕ, for which they could offer no explanation and decided more work was necessary on this phenomenon. Their primary conclusion was that the magnitude of relative strains in zones of interaction were of prime importance to the behaviour of the reinforcing.

Jewel (1983) questioned the use of values of f^* greater than $\tan \phi$ in design of RE walls. He showed that the orientation of principal stress axes in the upper third of a (static) wall may be significantly different from the horizontal and vertical, contrary to what is tacitly assumed in the calculation of earth pressures during design of RE walls. (The major principal stress is assumed to be vertical, for example in the calculation of strip forces using an earth pressure.) Also, the high value of "apparent" earth pressure often observed in the upper part of RE walls may be in fact a high stress ratio existing in the soil rather than "at rest" conditions. (The earth pressure coefficient is taken as K_0 at the surface, reducing to K_a at 6m. depth, for design purposes.)

Nature of the reinforcing strip surface.

Schlosser and Elias (1978) summarized research on the effect of the surface characteristics of the reinforcing. In full size pullout tests, it was found that for ribbed strips, f* approaches tan ø at high normal stress, while for smooth strips, f* approaches tan W. The peak pullout force was measured at about 5mm displacement for smooth strips, and about 50mm for ribbed strips. The residual to peak strength ratio is about 0.5 for smooth and about 0.8 for ribbed strips. Yourmann (1978) had similar findings for model tests on mylar and fibreglass mesh strips. When smooth strips pull out, there is slip at the strip-soil interface, whereas with ribbed strips there is soil-soil shear a small distance away from the strip surface.

Percentage of fines in the soil.

Schlosser and Elias (1978) report that the relative volume of the fine grained portion of the soil has a strong effect on the ø of the soil, and hence on f*. They point out that as the percentage of fines in the soil increases, so ø decreases, because the fines destroy the intergranular contact within the soil skeleton. 15µm had been found to be the upper limit grain size of the fine portion. Hence in RE specifications there is a limit on the percentage of soil passing the 15µm sieve allowed in the backfill.

Other factors.

Murray et al (1979) describe pullout tests during vibration of the surface of the backfill using a rotating-mass vibrator. They found that the pullout force reduced during vibration. The reduction was put down to the reduction in normal stress during each cycle of vibration. They also showed that vibration could cause deformation even when the load on the strip was much less than the ultimate pullout force. Friction angles greater than ø were observed, as a result of which the authors stated that pullout test results should be "subject to interpretation" before use in design.

6.7.3. Values for use in design.

McKittrick (1978) states that since RE soils are granular, subject to low strain levels, usually stressed in plane strain, and compacted to a relatively high density, it is reasonable to use peak values of ø (and hence

f*), derived from plane strain compression tests, for static analysis of walls. He commented that the values should be adjusted as necessary for overburden conditions. Knowledge of the density, shear strength, void ratio, and strain state are important in selecting f* for design, as well as the nature of the strip surface. McKittrick gives the following rules for f* selection:

for $0 \leq y \leq 6m$, $f^* = f_0^* - (f_0^* - \tan \phi)(y/6)$,

where $f_0^* = 1.2 + \log CU$ (ribbed)

$= 0.4$ (smooth),

and for $y > 6m$, $f^* = \tan \phi'$ (peak, from plane compression tests, adjusted for dilatancy)

$= \tan \Psi$ (direct shear value, for non-dilatant soils, for both ribbed and smooth strips.)

CU is the coefficient of uniformity of the soil, D_{60}/D_{10}, and y is the depth from the top of the wall.

Yourmann felt that his wall-moving tests gave a better indication of the friction coefficient, even though the force distribution in the strips during "pulling" was different to that observed in full size walls. He found that there were several peaks in the force distribution in the strips, coinciding with Rankine failure surfaces observed through the glass side walls of his containing box. He conceded that wall-moving tests are impractical for full scale tests, so suggested that direct shear values of f* be used, with correction factors: for design of strips inside the active zone, use 80% of the direct shear peak friction; for the portion of strips outside the active zone, use 40% of the direct shear peak friction value. The use of a higher friction value inside the active zone is in keeping with what other researchers have found: that the strain state within the wall affects the mobilised friction (McKittrick, 1978).

Almost all of the work summarised above was applicable to statically designed RE walls. There is little data on values of the apparent friction coefficient to use in seismic design. Usually the static values are assumed to be applicable to seismic design. In the following section we will compare the values of f* found in the work reported here, and the current design specifications.

6.7.4. Comparison of observed f* and present current specifications.

6.7.4.1. Introduction.

First we must look at the values of f* and ø found in the testing reported in §5.4. Fig. 5.30 shows the relationship between f* and depth for the pullout tests done for this report. f* ranges from nearly 5 at small depths to about 2 at 700mm. Table 5.4 shows the values of f* determined in direct shear tests: peak was 1.3 to 1.5, residual about 0.8 or less. It is shown in Fig. 5.31 that f* reduced at a uniform rate during all pullout tests, irrespective of its initial value or the depth to the strip being pulled.

Fig. 5.33 showed the values determined for the angle of internal friction ø of Mount Somers sand, which was used in the testing. ø ranged between 57° (peak) at 10 kPa confining stress and 46° (residual) at 16kPa confining stress. In the 1m. tall sand fills used here we might expect normal stresses of up to about 16kPa. At 20kPa the residual ø was determined as about 40°, and at 100kPa ø was about 32°.

Finally, the coefficient of uniformity CU of the sand (D_{60}/D_{10}) is 2.36 (see the grading curve shown in Fig. 5.4). Using McKittrick's rule above, f_0* is 1.2 + log 2.36, or 1.57; this would be the value of the friction coefficient at the fill surface, reducing to tan ø at 6m. depth. This value is close to the direct shear value of f* mentioned above, but well below the pullout test values.

6.7.4.2. Comparison of observed f* values and f* test values.

Fig. 6.74 shows the values of f* at the failure surface, at the end of the run during which the failure surface first outcropped at the fill surface, taken from Figs. 6.50 to 6.55. Strip 5 in T4R17 appears to have an unrealistically large observed f* value. A look at the force diagrams (Fig. 6.41) shows that data for strip 5 in test 4 is not good, gauges 4 and 5

probably being bad. It is not possible to compare strip 5 in t4r17 with t5r6 because that strip did not intersect the failure surface in test 5 (tests 4 and 5 had the same stepped-block geometry). The general shape of the cluster of points on Fig. 6.74 is more or less indeterminate, so a straight line bound is suggested. Something over 2, say 2.2, would be a good upper bound for the apparent average friction coefficient for the portions of strip in the resistant zone, determined at the failure surface.

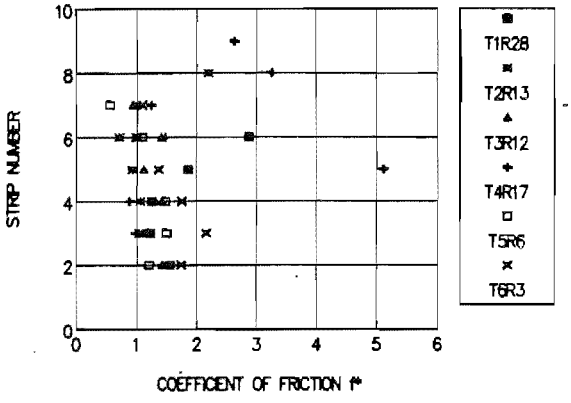

Fig. 6.74. Observed f* values at the failure surface, at 'failure'.

Fig. 6.75 shows values of f* determined at the gauge 20mm from the facing at failure. This f* is an apparent value, averaged over the length of strip from the gauge to the free end. The large value for f* for strip 5 in T4R17 is not evident in this figure. 1.8 would be a good upper bound for f*, although there is some "pinching" of the curves at strip 6. It is felt that a curved boundary would be of dubious value here because of the size of the model: current design rules have f* reducing linearly from the surface down to 6m. depth. More investigation is necessary before such a complicated boundary can be justified.

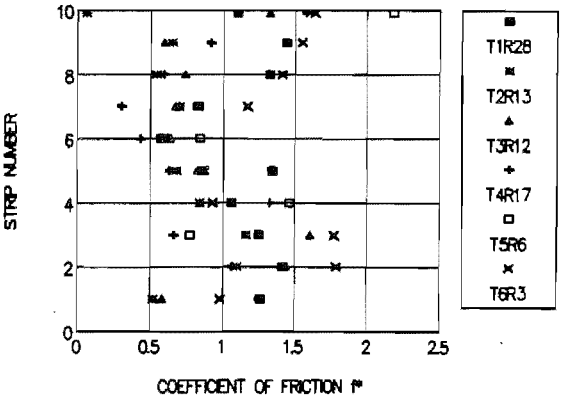

Fig. 6.75. Observed f* values at the facing, at 'failure'.

Comparing Fig. 6.74 and 6.75, it appears that the mobilised friction is larger in the resistant zone than in the active zone. This is to be expected, as the shear deformation adjacent to the strip is much greater in the resistant zone than the active zone.

Fig. 6.76 shows values of f* for the maximum forces at failure, taken at the position of the maximum force. Again, 1.8 would be an upper bound, except

in the uppermost strips, where f* increases to well above that value. Two data points have been left off the diagram, for T2R13 and T4R17, where f* at the maximum force was 17 and 20 respectively, unrealistically high values. Also, in Fig. 6.76, the problem mentioned above for strip 5 for T4R17 again causes a high apparent f*. Strip 8 of t1r28 also shows a large f* value; Fig. 6.38 shows that there is a peculiar rise in the measured forces in that strip after run 20. If the data is good, it is very difficult to explain such a rise. f* is again generally lower at the position of the maximum forces than at the failure surface.

This finding, that mobilised friction in the resistant zone is larger than in the active, is the opposite of the conclusion reached by research on the static stability of RE walls, and pointed out above. It is perhaps the case that in seismic failure, there is, overall, less deformation inside the active zone than occurs in static failure. In seismic failure there is a region of confused deformation in the area above the point where the failure surface exits the back of the reinforced block (for a not-contained failure surface). This is caused by a change in slope of the failure surface. Fig. 6.9 (§6.4.2.2) showed the result of this deformation at the end of test 3: a series of graben-like structures were developing around the rear of the reinforced block. If mobilised f* values are related to relative strains in the soil as pointed out above, we might expect there to be higher mobilised friction in the strips passing through this region. This can be seen in Fig. 6.76.

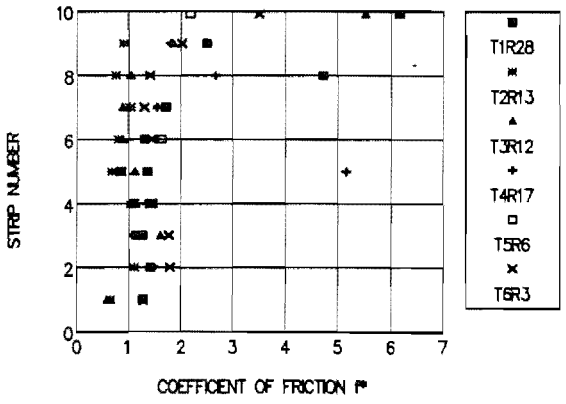

Fig. 6.76. Observed f* values at the maximum force position, at 'failure'.

In the area adjacent to the facing there is also a confusing displacement field, especially near the base of the wall. In a simplified view, we see that a rectangular slice behind the facing which is the full height of the wall before an earthquake is moved outward and reduced in height during the earthquake. The soil at the base of the failure wedge, which is also the bottom of this slice, undergoes large shear strains during wall movement.

f* values are slightly higher in this area (strips 2 and 3) than above and below. The lower value of friction mobilised in strip 1, the lowest strip in the wall, reflects smaller relative displacements. The failure surface probably meets the facing just above this strip, and the bottom panel is restrained by its burial to the required 8.5%-of-wall-height depth. Hence strip 1 takes little of the load induced by movement of the wall.

Fig. 6.77 shows the maximum values of f* observed at the failure surface during each test. The values are taken without regard to which run they were observed in. The figure is very similar to Fig. 6.74, except that there is

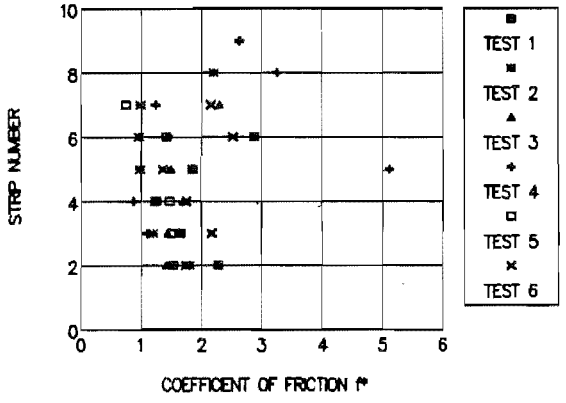

Fig. 6.77. Observed maximum f* values at the failure surface.

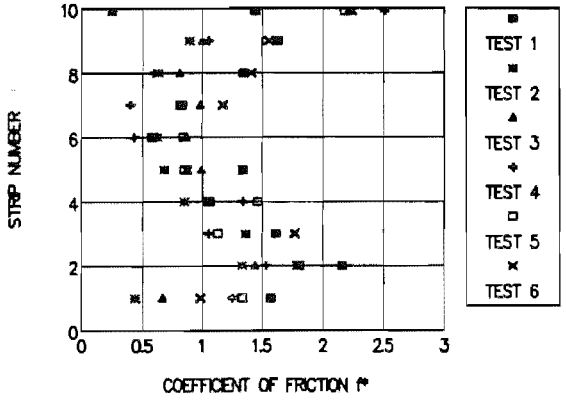

Fig. 6.78. Observed maximum f* values at the facing.

a slight increase in the upper boundary. Now about 2.5 might be a good upper bound, compared to 2.2 for Fig. 6.74. Similarly, Figs. 6.78 and 6.79 show the maximum values of f* observed at the facing and at the positions of maximum force. In Fig. 6.78, there is an increase at strips 2 and 10, and in Fig. 6.79 there is a small overall increase in f*. At the position of the maximum forces, the upper bound might shift to about 2 or 2.1, from 1.8 before, disregarding the large values at strip 5 (test 4) and strip 8 and 10 (test 1).

A major problem with design of RE walls for seismic resistance is the choice of level of protection to design for, whether to choose "failure" (first outcropping of the failure surface at the fill surface) or some other arbitrary point before or after failure. The comparison above of observed f* values at "failure" and the maximum observed f* values shows that there is relatively little difference. The only difficulty arises in deriving a way

to arrive at a suitable design value for f*.

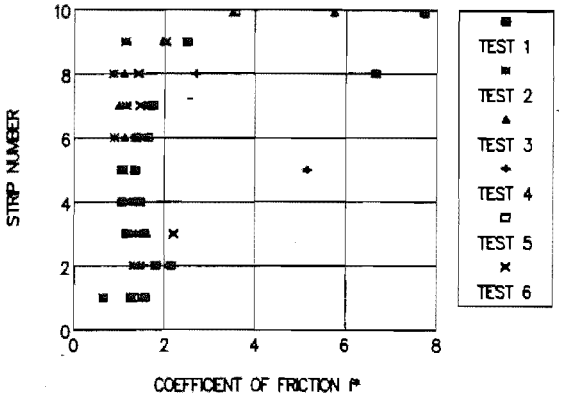

Fig. 6.79. Observed maximum f* values at the position of the maximum forces.

The peak values of f* measured in the sliding shear tests, 1.3 to 1.5, are approximately equal to tan ø for the peak ø measured in the vacuum triaxial tests (57°, at 10kPa confining stress). The observed maximum values of f* are 50% larger than this at about 2.2 to 2.5. The lowest pullout test values of f* were in this range at the maximum depth tested, 700mm. McKittrick's f_0* is in the range of the shear test results at 1.57. From this analysis, it would appear that peak sliding shear f* values are close to the observed values, though a little low.

We still have the problem that the observed apparent f* is greater than tan ø. There are several possible explanations for this. If there is an increase in overburden pressure, the apparent f* could be higher than tan ø. The sand will dilate during shear, and the overburden stress will increase if the expansion is restricted. Close to the fill surface we might expect most of the expansion to be relieved by raising of the surface, but a little deeper, the vertical expansion can be relieved a little but the lateral expansion is restrained, so causing an increase in the mean confining stress acting on the strip. So as we move deeper into the fill, the ability of the soil to expand is reduced, and we might expect the confining stresses to increase. But at the same time, the soil dilates less as the confining stresses increase. Increased stresses can also be relieved by grain crushing, which will occur at greater depths. A rotation of the principal stress axes, with a larger vertical component of stress resulting, could not account for any increase because we are already assuming that the major principal stress is vertical. If there is a change in the relationship between the major and minor principal stresses, while the mean normal stress remains the same, there could be an increase in the normal stress, but then we would expect the effects of dilation to be absorbed in the direction of the lowered principal stress, raising it again. Such a rearrangement of stress ratios seems unlikely.

Another possibility is that the shear surface around the strip is larger than we have assumed. In using Eq. 5.3 we have ignored the thickness dimension of the strip, and used just twice the strip width as the size of the shear surface. In fact, the strips measure 1.3 to 1.7mm thick, including the sand coating. If we take the mean thickness as 1.4mm, and assume that shearing takes place 1 average sand grain dimension away from the strip (glued sand) surface, the thickness is then 2mm, taking the average grain size as 0.3mm. (See the grading in Fig. 5.4.) So then instead of using 2b=20mm in Eq. 5.3, we should use 2x(10+0.3+0.3+2)=25.2mm, an increase of 25%. This will reduce the observed apparent f* values by a like amount, 25%. Figs. 6.80 - 6.82 show the results of this analysis when applied to the data shown in Figs. 6.77 - 6.79.

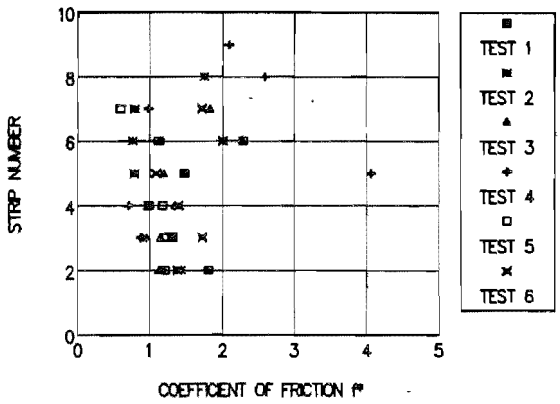

Fig. 6.80. Observed maximum f* values at the failure surface, adjusted for increased shear surface area.

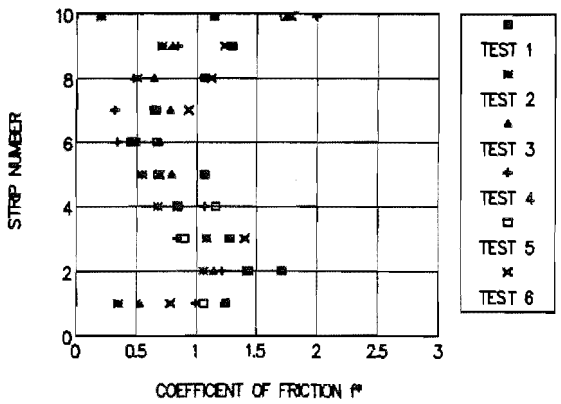

Fig. 6.81. Maximum observed f* values at the facing, adjusted for increased shear surface area.

An upper bound for the lines in Fig. 6.80 might be about 2, compared to 2.5 in Fig. 6.77. In Fig. 6.81 the upper bound would be about 1.5 or 1.6, compared to about 2 in Fig. 6.78, and in Fig. 6.82 it would be about 1.8, whereas in Fig. 6.79 it was about 2.2. These values for f* are closer to what we expect, but still a little larger than tan ϕ.

Jewel (1979) conducted model pullout tests using rough reinforcement bars in sand. Radiographic techniques were used to record displacements in the sand. In tests on a single bar he found that the zone of sand which undergoes large shear strains is of quite limited extent, perhaps 5 grains thickness next to the reinforcement. If we increased our shear surface to 2

grains thickness there would be a further reduction in apparent f* of about 10%. It is clear that in the testing reported here the assumed size of the shear surface has a profound effect on the magnitude of the observed apparent friction coefficient.

The same could be said about full size pullout tests. Reporters ignore the thickness dimension of the strips. For 60mm wide strips, 5mm thick, with 3mm ridges (the current standard Reinforced Earth Company design; McKittrick, 1978), the shear surfaces are at least 11mm apart. McKittrick reports work by others that showed that shearing when rough strips are pulled out occurs on a soil-soil interface, though where in relation to the strip surface is not stated. Although the edges of the strips are smooth, we might still expect a contribution to the pullout strength from this dimension as the soil trapped between the ridges on the strips must be sheared at the edges as well. If this is the case, the shear dimension rises from 2 x 60 = 120mm to 120 + 22 = 142mm, a rise of 18% which will cause a drop of 18% in the calculated f*. And if the shear surface is on average 2 mean grain diameters away from the top of the ridges, there is a further increase. We should also remember that Hausmann and Ring (1980) found that at high confining stresses there was no slip at their soil-plate boundary, so the lateral dimension may be larger than 60mm as well. This would be even more likely to be true after a wall has been in place for a while, as corrosion attacks and roughens the surface of the strips.

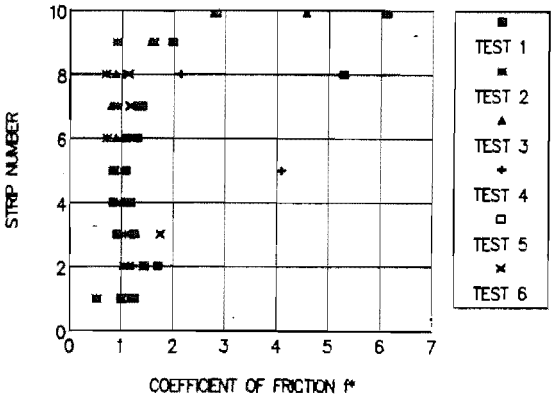

Fig. 6.82. Maximum observed f* values at the position of the maximum forces, adjusted for increased shear surface area.

It thus appears that the peak sliding shear values of f* are not so low after all, and are suitable for use in design. Obviously they must be derived at stresses applicable to the design wall and with the intended backfill soil, as they are related quite closely to the soil angle of internal friction ϕ.

Jewel also carried out many tests in a direct shear box, using reinforcing as a pin across the shear surface. This may be the predominant effect in RE walls in static situations, where a block of the wall tends to slump on a spiral-shaped slip surface, but from the observations in the testing in this report pullout is more important in seismic displacement than pinning or dowel action. In the lower third of the wall, the strip forces tend to be greatest at the facing, indicating that the reinforcing is acting more like an anchor for the facing than a pin across the failure surface.

One final point. The mobilised friction was generally seen to increase with increasing displacement of the walls. This implies that there is no distinctive peak in the friction coefficient, and perhaps it is asymptotic to an ultimate value. Above it was pointed out that strips pulled out of loose sands exhibited a pronounced peak in pullout force at small displacement, with rapid falloff as pulling continued. No such peak was observed in dense sands. It would appear then that the pullout force during earthquake loading is behaving as if the sand were extremely dense.

6.7.4.3. Conclusion.

It has been shown that the direct shear peak friction coefficient is close to the observed mobilised friction in seismically excited model RE walls. The mobilised friction is greater in the resistant zone than in the active zone, contrary to the situation reported for static walls. This perhaps indicates that there is less overall deformation inside the active zone in walls failing by seismic excitation than there is in walls in purely static loading. By considering the thickness dimension of the reinforcing, as well as the possibility that the shear surface around a strip during pullout is some small distance away from the strip, apparent mobilised friction values are more realistic in that they are reduced and are closer to tan ϕ.

6.8. Mobilised ø using the limiting equilibrium formulation and f* .

In section 6.5.3 the limiting equilibrium formulation was used to back-calculate the mobilised ø using observed forces and the observed failure angles, by calculating k_h to match the observed k_h. It was seen there (Table 6.14) that ø seemed to decrease during each test, from a starting value of about 46° to about 36° at the time the failure surface became fully developed. Here we do the same calculations again using, instead of the observed forces, an observed f* value from the previous section. By looking at Figs. 6.56 to 6.61, average values of f* are taken for each run, with some weighting towards the values near the bottom of the walls - the observed forces are highest there. The weighting is judgemental and basically arbitrary. Table 6.16 contains the results of the calculations.

Table 6.16
Mobilised ø calculated using observed f*, and observed k_h and α in the limiting equilibrium formulation. Run numbers in italics denote 'failure'.

test/ run	obs. f*	calc. k_h	obs. k_h	calc ø	test/ run	obs. f*	calc. k_h	obs. k_h	calc ø	test/ run	obs. f*	calc. k_h	obs. k_h	calc ø
t1r8	0.65		none		t2r1	0.62	.356	0.36	47.0	t3r1	0.78		none	
t1r20	1.0	.367	0.37	48.7	t2r9	0.83	.332	0.33	43.5	t3r10	1.18	.205	0.20	41.8
t1r28	1.4	.252	0.25	37.8	*t2r13*	1.05	.240	0.24	36.1	*t3r12*	1.28	.082	0.08	33.8
t1r32	1.4	.242	0.24	37.2	t2r16	1.26	.199	0.20	31.5	t3r16	1.3	.055	0.06	32.1
t1r37	1.7	.235	0.23	33.8										
t4r8	1.0	.302	0.30	47.0	t5r2	1.2	.277	0.28	43.5	t6r1	0.97	.337	0.34	47.6
t4r12	0.9	.362	0.36	51.6	t5r4	1.0	.316	0.32	47.6	t6r2	0.94	.383	0.38	50.4
t4r14	0.9	.362	0.36	51.6	*t5r6*	1.42	.196	0.20	37.2	*t6r3*	1.6	.237	0.24	34.4
t4r17	1.2	.234	0.23	40.7	t5r7	1.38	.218	0.22	38.4	t6r4	1.4	.204	0.20	34.4
t4r20	0.9	.200	0.20	42.3	t5r8	1.22	.224	0.22	40.1	t6r6	1.45	.195	0.20	33.8
t4r24	0.9	.190	0.19	41.8	t5r9	1.18	.172	0.17	37.2	t6r8	1.65	.217	0.22	32.7

We can now compare Table 6.16 and Table 6.14. Generally the same trends occur for each test, and in both tables the values of ø are quite similar. The apparent ø is large at the beginning of each test, and reduces as the test progresses. There is some difference between the stepped and rectangular block structures. In rectangular block structures (tests 1, 2 and 3), there is usually a continuing reduction in ø with succeeding runs. In the stepped block structures, however, there is an increase in the early runs, then a

reduction, then relative constancy at and after failure. Test 6, a rectangular block structure, behaves similarly to the stepped blocks. We might expect that the mobilised ϕ would be relatively constant after failure, as the zone of shearing (ie. the failure surface) is fully formed, and the sand in that zone is all at residual strength. Small reductions in ϕ probably reflect the continuing deformation of the sliding block, especially at the base and at the top rear.

One difference between the rectangular and stepped blocks is the apparent value of ϕ at the end of the tests: in tests 1, 2, 3 and 6 it is about 32°, while in tests 4 and 5 it is about 39°. A similar effect can be seen in Table 6.14, though the difference is not as pronounced as in Table 6.16. The reason for this dissimilarity is not clear: if there is less overall deformation, and the dilation it causes, in the stepped block structures, then perhaps ϕ will remain at slightly higher levels. Certainly the strip forces were found to be generally lower in these walls than in the rectangular block walls, and thus there would be smaller strains in the strips and in the adjacent soil, and also smaller shear strains between the strips and soil. The overall level of dilation would thus be less also, resulting in larger apparent ϕ values.

The large values of ϕ are generally in keeping with the values shown in Fig. 5.33 for a confining stress of about 15kPa. Ponce and Bell (1970) found a similar effect to that shown in Fig. 5.33, that ϕ rises steeply at low stresses. Fukushima and Tatsuoka (1984), however, found that ϕ does not rise appreciably at low confining stresses. They were very particular to consider the effect of the membrane stresses as well as the self-weight of the specimen in the analysis of their triaxial tests. If we consider Fukushima and Tatsuoka's results, it is quite difficult to see why the apparent ϕ should be so large early in the tests.

We have now seen what happens to the friction coefficient and ϕ during seismic displacement of model RE walls. The next section looks at what happens to the earth pressure coefficient, by looking at "dimensionless tension".

6.9. Dimensionless tension T*, a pseudo-earth pressure coefficient.

The earth pressure coefficient is used in design to calculate the force transferred to each level of strips from the facing. In static tests, and in instrumented full scale walls, the coefficient has been found to be K_a (or less) for depths greater than 6m. from the top of a RE wall, and increasing from K_a to K_o as depth decreases from 6m. (McKittrick, 1978). Calculations of dimensionless tension, which is like an earth pressure coefficient, mobilised in the tests reported here were done using forces observed at the facing, and also using the maximum forces. The data is tabulated in Tables C.19 to C.30, and was calculated using the relationship

$$T^* = \frac{T_i}{g y_i S_v S_h} \qquad \text{.....(6.2)}$$

where T_i is the tension in strip i, y_i is the depth of that strip, S_v and S_h are the vertical and horizontal separation of the strips respectively, and g is the unit weight of the soil. Figs. 6.83 to 6.94 show the data graphically.

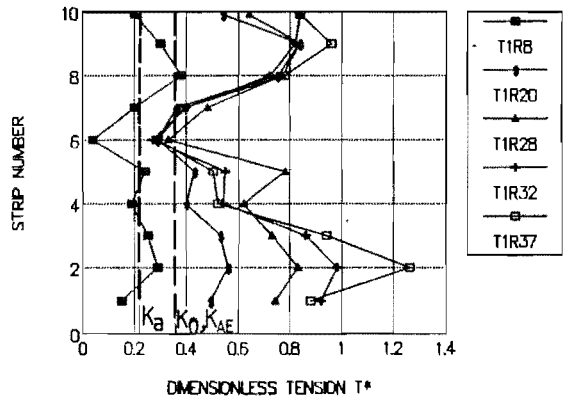

Fig. 6.83. Mobilised dimensionless tension T* for maximum forces at the facing, test 1.

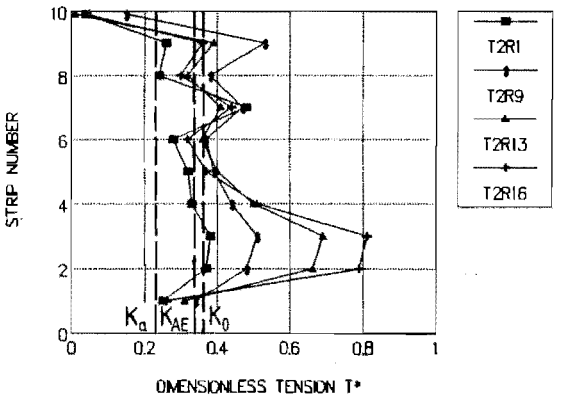

Fig. 6.84. Mobilised dimensionless tension T* for maximum forces at the facing, test 2.

Shown on the plots of dimensionless tension are the K_a, K_o, and K_{AE} earth pressure lines. K_a and K_o were calculated assuming $\phi = 40°$, and K_{AE} using the observed yield accelerations for each test in the M-O equation. Clearly, none of the lines bound the observed dimensionless tension.

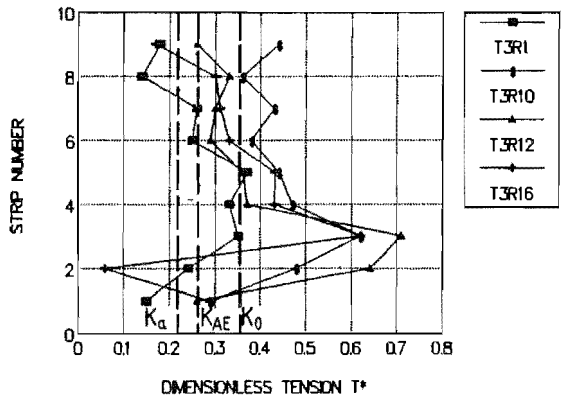

Fig. 6.85. Mobilised dimensionless tension T* for maximum forces at the facing, test 3.

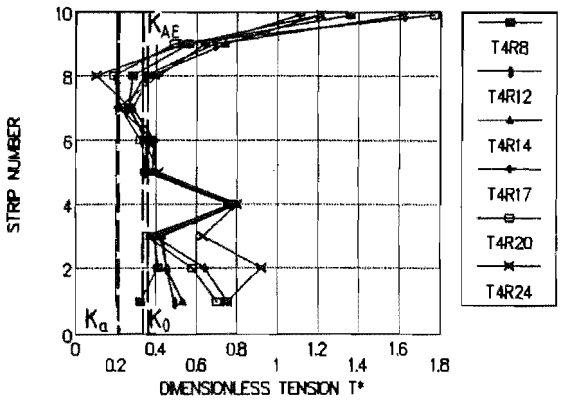

Fig. 6.86. Mobilised dimensionless tension T* for maximum forces at the facing, test 4.

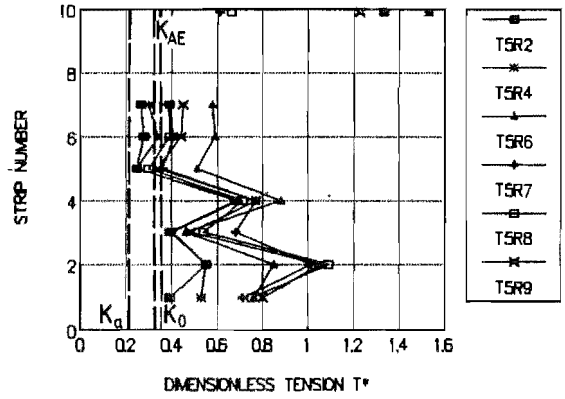

Fig. 6.87. Mobilised dimensionless tension T* for maximum forces at the facing, test 5.

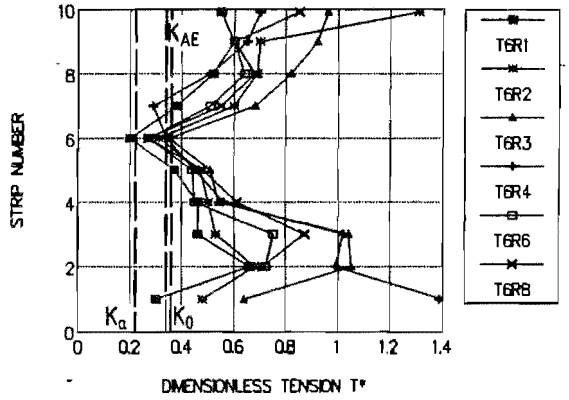

Fig. 6.88. Mobilised dimensionless tension T* for maximum forces at the facing, test 6.

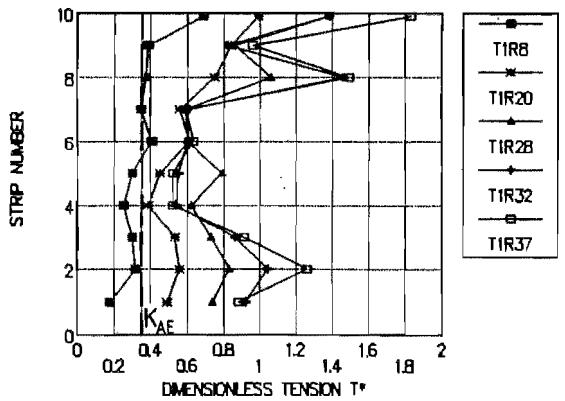

Fig. 6.89. Mobilised dimensionless tension T* for maximum forces, test 1.

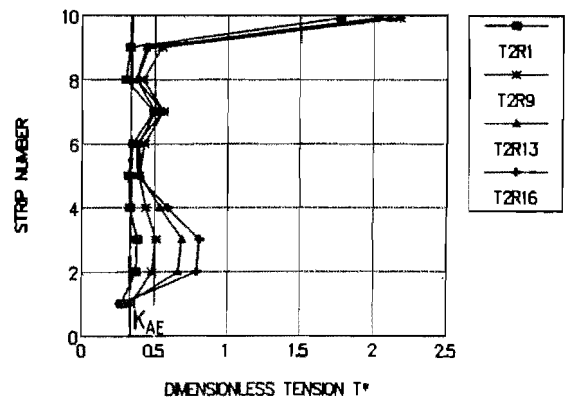

Fig. 6.90. Mobilised dimensionless tension T* for maximum forces, test 2.

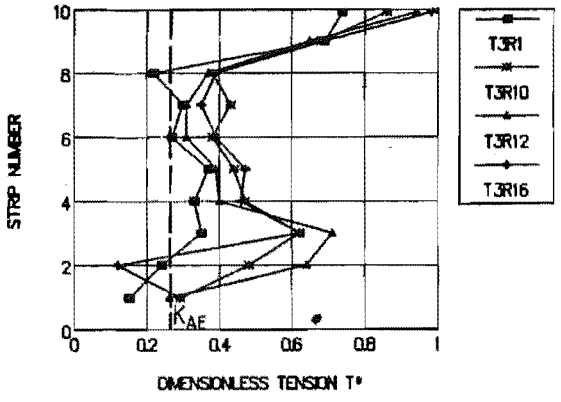

Fig. 6.91. Mobilised dimensionless tension T* for maximum forces, test 3.

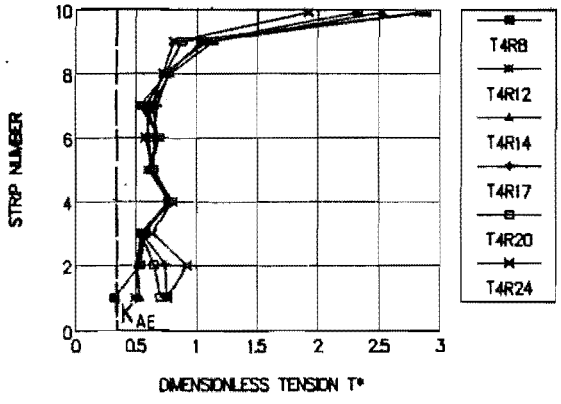

Fig. 6.92. Mobilised dimensionless tension T* for maximum forces, test 4.

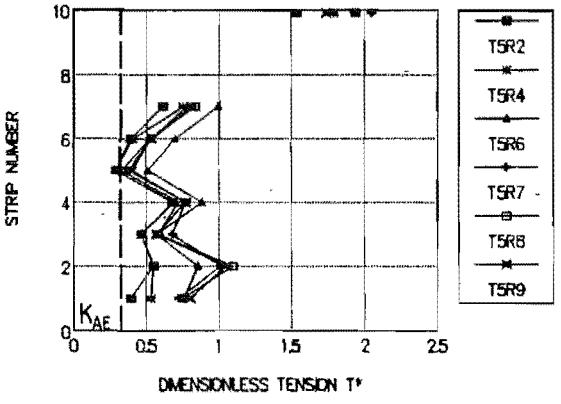

Fig. 6.93. Mobilised dimensionless tension T* for maximum forces, test 5.

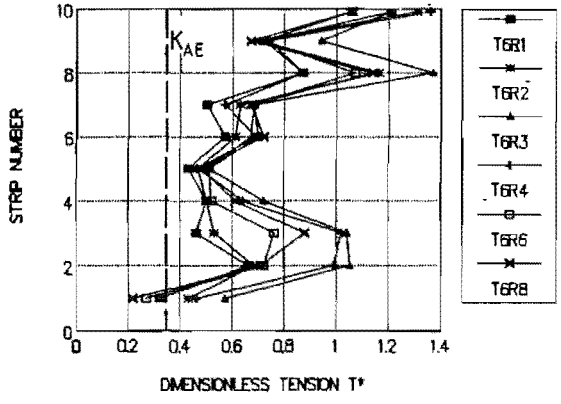

Fig. 6.94. Mobilised dimensionless tension T* for maximum forces, test 6.

Figs. 6.95 to 6.106 were derived using the same calculations, but the construction forces were subtracted from the observed forces first. Thus the dimensionless tension shown in those figures is purely the result of the dynamic excitation of the walls. K_{AE} is plotted on these figures, as well as a line that runs from $1.3K_{AE}$ to $2.6K_{AE}$. The last line is an attempt to bound the measured values of T*. Note that normally the M-O earthquake earth pressure K_{AE} applies to total forces, whereas here it is being compared to the dynamic forces only.

Before pursuing the bounding line idea, there are some general comments to be made about Figs. 6.95 to 6.106. In all the figures there is a minimum in the measured value of T* around strips 4 to 6, ie. near mid-height of the walls. The higher values near the base of the walls reflect the predominant effect the strips in that area have on the seismic performance of the wall.

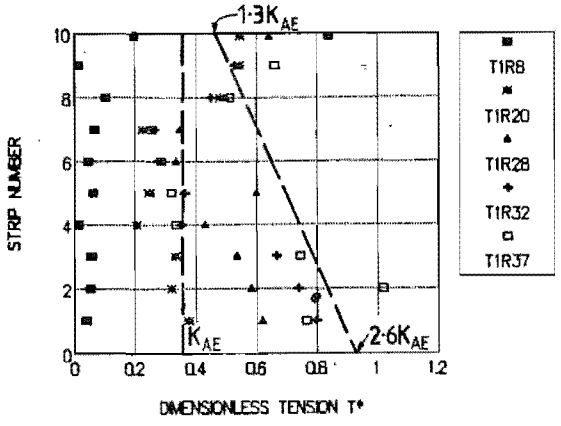

Fig. 6.95. Dimensionless tension at the facing for dynamic forces, test 1.

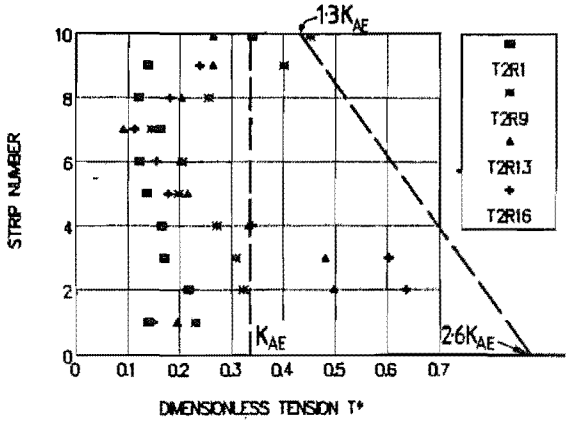

Fig. 6.96. Dimensionless tension at the facing for dynamic forces, test 2.

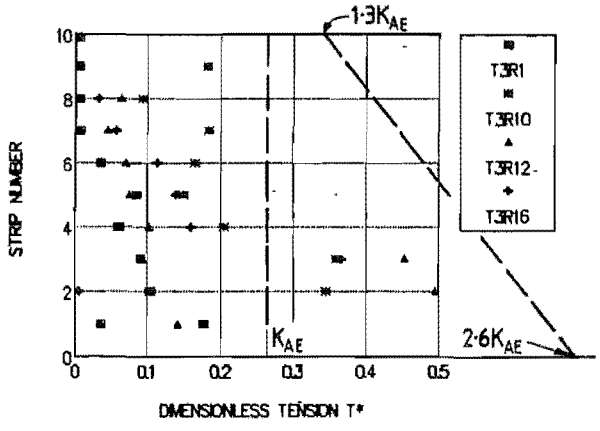

Fig. 6.97. Dimensionless tension at the facing for dynamic forces, test 3.

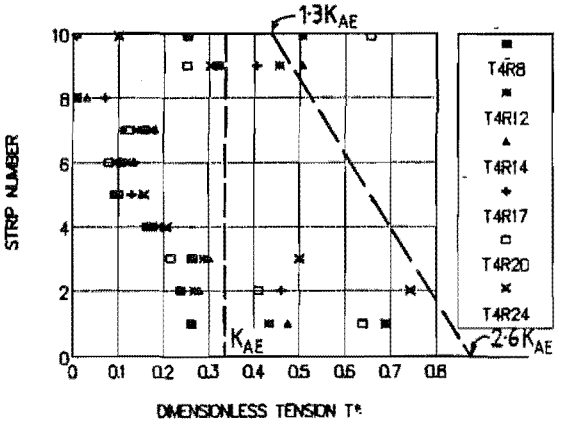

Fig. 6.98. Dimensionless tension at the facing for dynamic forces, test 4.

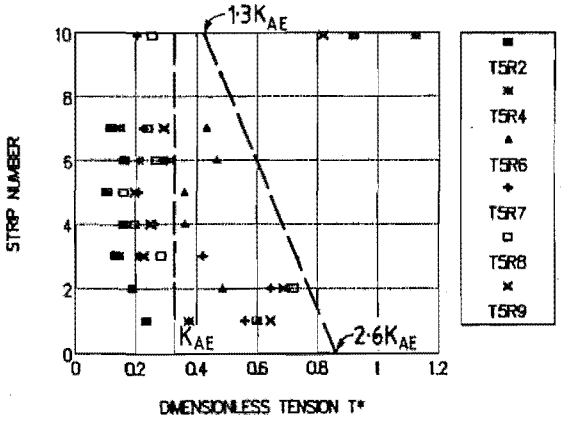

Fig. 6.99. Dimensionless tension at the facing for dynamic forces, test 5.

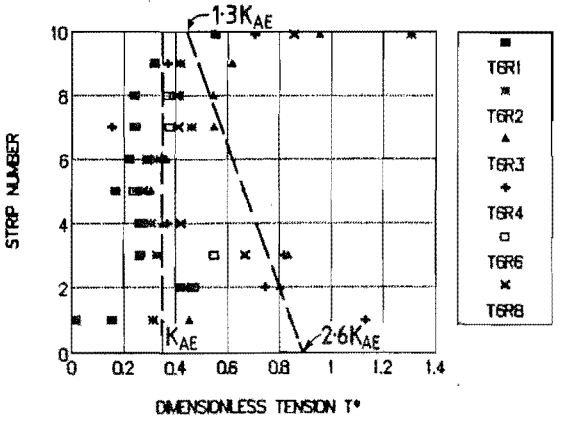

Fig. 6.100. Dimensionless tension at the facing for dynamic forces, test 6.

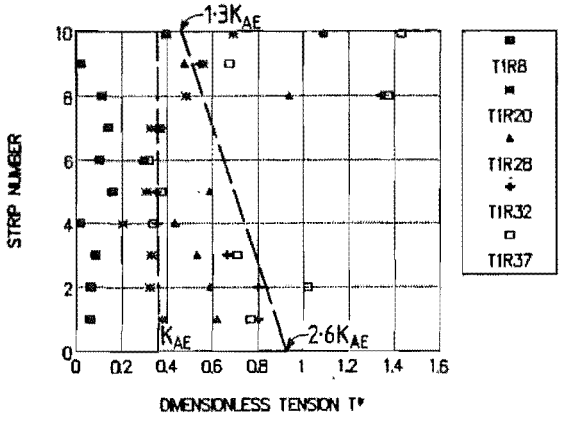

Fig. 6.101. Dimensionless tension at the maximum force for dynamic forces, test 1.

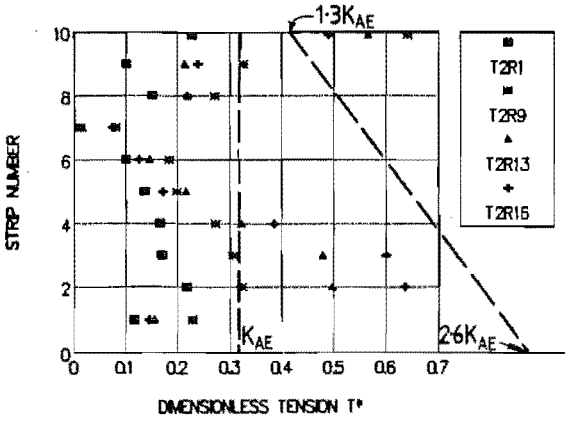

Fig. 6.102. Dimensionless tension at the maximum forces for dynamic forces, test 2.

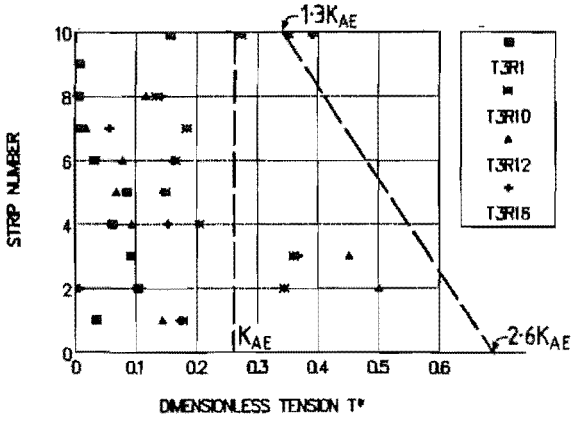

Fig. 6.103. Dimensionless tension at the maximum forces for dynamic forces, test 3.

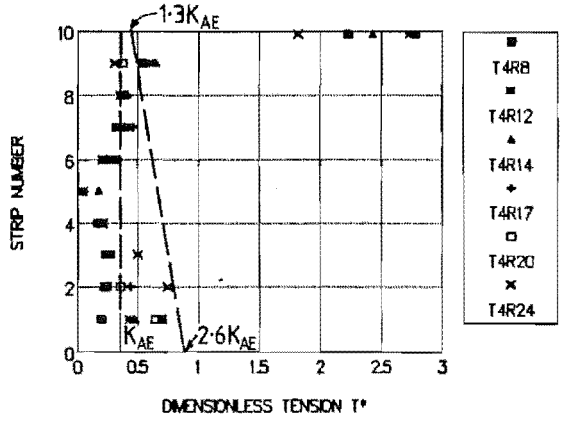

Fig. 6.104. Dimensionless tension at the maximum forces for dynamic forces, test 4.

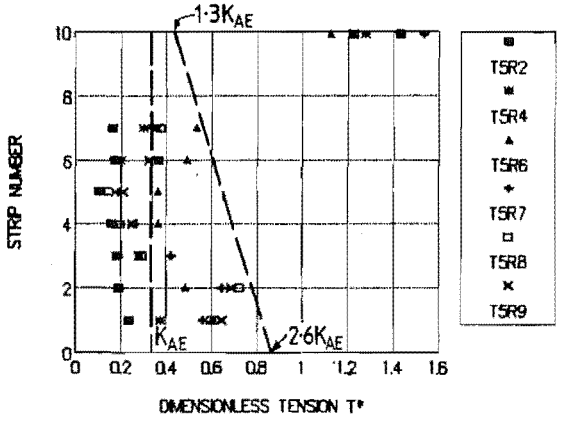

Fig. 6.105. Dimensionless tension at the maximum forces for dynamic forces, test 5.

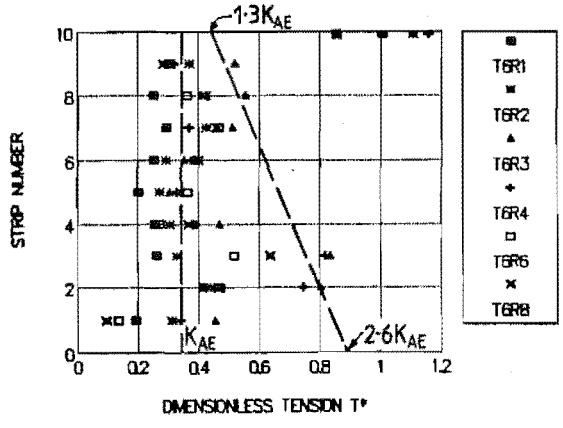

Fig. 6.106. Dimensionless tension at the maximum forces for dynamic forces, test 6.

The larger values near the surface reflect the small depth used in the calculation. Some of the apparently large values of T* found near the top of the walls are dubious though. For example, in wall 1 (Fig. 6.101), strips 8 and 10 showed a peculiar rise in the measured forces in the half of the strips furthest from the facing (Fig. 6.38). It is difficult to see how a rise like that could occur, unless one of the small scarps mentioned previously was forming and the strips were acting more like pins across this new failure surface. Such scarps were not seen at the surface of wall one, though, and these rises were not evident in the force distribution charts of any other wall, including wall 3 where the scarps were seen.

With respect to the number of points that plot outside the K_{AE} line, the stronger the wall, the more there are. It is clear that Richardson's (1978) design principle, that there is an increase in earth pressure with a decrease in wall stiffness, is not corroborated in the tests reported here. Walls 1 and 6 had observed yield accelerations of 0.24g and 0.22g respectively. They also tend to have more data points to the right of the K_{AE} line (ie. the observed T* is greater than K_{AE}) than do the other tests in Figs. 6.95 to 6.106. Walls 4 and 5 had slightly lower yield accelerations (0.21 and 0.20g) and also slightly fewer points to the right of the K_{AE} line. Wall 3, with a yield acceleration of 0.09g, has the least number of T* points to the right of the K_{AE} line. Wall 2, on the other hand, had an observed yield acceleration of 0.21, the same as wall 4, but its T* chart is quite similar to that of wall 3. Again, it seems to have behaved differently to the other walls tested.

To return now to the bounding line idea, the line from $1.3K_{AE}$ at the surface to $2.6K_{AE}$ at the base bounds most points, with the main exceptions being the values pertaining to the two top-most strips in most walls. It should be pointed out here that much of the force data for these top strips (eg. strips 8 and 10 in wall 1, 10 and perhaps 9 in wall 2, 9 and 10 in wall 3, 10 and perhaps 9 in wall 4, 8 and perhaps 9 in wall 6 - see Figs. 6.38 to 6.43) may be of doubtful reliability, with apparent bad zero readings and odd shapes to the graphs. Why this should be is not known; whether such variability is a property of the shallow strips in RE walls, or whether it is due perhaps to electrical or other problems in the data logger - certainly the same input channels were always used for these strips - is not clear.

If these points near the top of the wall can be safely discounted, and it is felt that they probably can, then the 1.3 to 2.6K_{AE} line bounds most points. If they cannot, then a line going from 2K_{AE} at the surface to 2.6K_{AE} at the base of the wall would be better. A parabola would perhaps best suit the shape of the plot, but the comments that were made about the friction coefficient bounding line apply here: there may be some scale effects involved, as both f* and the earth pressure coefficient (static, at full scale) reduce from a maximum at the surface to a uniform value at depths greater than 6m. Until more information is available, relating to larger or centrifuge models or full size walls, it is felt that a simple straight line is appropriate.

Using 2K_{AE}, or greater, for the dynamic earth pressure coefficient separately from the static earth pressure seems quite excessive at first sight, as K_{AE} was derived to include the static earth pressure as well. What does seem clear, though, is that the earth pressure coefficient used for design should be related to the strength of the wall, in terms of the yield acceleration, rather than to the earthquake. Richardson's revised (1978) design method actually did this, in a much more complicated way, by using a wall stiffness concept (see section 3.4). In this regard, K_{AE} seems ideal as one of the variables is $\tan^{-1} k_h$. The recommended 1.3K_{AE} to 2.6K_{AE} bounding line needs testing with many more earthquakes, of different characteristics, to check its reliability, as well as verification by centrifuge tests to check the effect at greater stress levels.

The MWD (1980) earthquake earth pressure coefficient was shown in Fig. 3.8. Some simple calculations can put it in terms of our dimensionless tension T*. At a depth of 50mm, the earth pressure derived from Fig. 3.8 would be h(1+1.5*0.95) = 2.425h kPa, and at 950mm, h(1+1.5*0.05) = 1.075h kPa. Then dimensionless tension at 50mm. depth for say 0.1x0.25m. strip spacing and h = 0.915m. would be (2425 * 0.915 * 0.1 * 0.25) / (0.05 * 16000 * 0.1 * 0.25) = 2.77, assuming that the earth pressure on the tributary area of a strip is all converted into force in the strip. In fact the strip spacing cancels out of the calculation. 16000N/m^3 is taken as an average unit weight of the soil. At 950mm depth, it would be (1075 * 0.915) / (0.95 * 16000) = 0.06. In terms of the test results shown in Figs. 6.95 to 6.106 this is very conservative near the top of the walls and quite unconservative near the base.

6.10. Displacements.

In this section displacements are discussed in four subsections. First the displacements and accelerations measured in the testing are given, and points arising from the data are examined. In the following three sections the measured displacements are compared to the three prediction systems outlined in Chapter 4: Sarma's, Lin and Whitman's, and using the Newmark / Franklin and Chang chart.

6.10.1. Measured displacements and accelerations.

As stated in Chapter 5, displacements were measured in two places on the walls: near mid-height (550mm from the top) and near the wall top (50mm down). Table 6.17 shows the permanent displacements measured for several runs in each

Table 6.17
Mean permanent displacements for several runs in each test. Italic run numbers are where the failure surface became fully formed. The potentiometers were removed after test 6 run 4.

test/ run	a_{max} (g)	perm. displt (mm)	total movemt (mm)	test/ run	a_{max} (g)	perm. displt (mm)	total movemt (mm)	test/ run	a_{max} (g)	perm. displt (mm)	total movemt (mm)
t1r4	0.20	1.9	2.2	t2r1	0.45	11.1	11.1	t3r1	0.20	5.1	5.1
t1r12	0.25	0.7	3.1	t2r3	0.46	2.5		t3r2	0.20	0.8	5.9
t1r14	0.32	1.1	5.3	t2r6	0.54	3.1		t3r3	0.32	4.9	10.8
t1r17	0.	0.9	10.3	t2r8	0.53	3.5	32.0	t3r5	0.36	4.1	15.9
t1r20	0.46	1.5		t2r9	0.54	3.3	35.3	t3r8	0.42	3.7	26.3
t1r23	0.45	1.9	17.6	t2r10	0.53	4.5	39.8	*t3r10*	0.45	6.4	44.0
t1r25	0.51	3.1	22.7	*t2r11*	0.54	5.5	45.0	t3r12	0.32	10.2	69.6
t1r28	0.51	5.6	37.6	t2r13	0.47	4.8	55.2	t3r14	0.25	13	94
t1r30	0.54	7.5	53.0	t2r16	0.41	5.0	75.4	t3r16	0.14	4	105
t1r32	0.44	4.7	63.4	t2r20	0.36	3	94				
t1r34	0.37	2.8	71.8								
t1r37	0.47	7	91								
t1r40	0.46	6	110								
				t5r2	0.41	5.4	6.0	t6r1	0.50	12.8	12.8
t4r8	0.36	1.4	5.1	t5r4	0.51	2.2	12.1	t6r2	0.61	11.2	24.0
t4r12	0.52	2.8	15.6	t5r5	0.64	6.1	18.3	*t6r3*	0.70	77	101
t4r14	0.52	3.8	21.0	*t5r6*	0.92	28.5	46.6	t6r4	0.58	51	152
t4r17	0.50	9.0	41.5	t5r7	0.68	21.4	68.0	t6r5	0.48	≈20	172
t4r20	0.36	3.5	55.8	t5r8	0.64	17.5	85.5	t6r6	0.51	≈20	192
t4r24	0.33	4.0	73.4	t5r9	0.64	24.5	110	t6r8	0.52	≈20	212

test, together with the total movement for the test up to the end of that run and the maximum acceleration observed in the run. The displacements given are the mean of mid-height and top of wall movement. In every case, the mid-height total displacement is slightly larger (10 to 20mm) than the wall top displacement. For tests 1 to 4 there was only 1 significant acceleration pulse causing an increase in permanent displacement, while in tests 5 and 6 (modified El Centro 1940 north-south excitation) there were several in each run. Figs. 6.107 to 6.119 show measured displacement for several runs, along with the accelerations observed during those runs.

In the tests where the first run is shown in Table 6.17 (2,3,5, and 6), it is seen that there was always a relatively large displacement in the first significant shake. In the other 2 tests (1 and 4) the first runs were of small acceleration, due to a very cautious approach to setting the controls of the shaking table at the beginning of each test sequence. (There was a 7 month separation in time between tests 3 and 4.) This large initial displacement must be due to the taking up of all slack in the strip-facing connections, and the displacement required to mobilise significant strip/soil friction. There is also an element of settlement of the backfill material causing some displacement. There was often about 10mm settlement of the fill surface behind the top facing panel, occurring early in the tests. Subsequent runs show reduced displacement, in 2 cases (tests 5 and 6) with increased acceleration.

The other major trend in the displacement data in Table 6.17 is the increase in displacements after failure (the failure surface becoming fully formed). The yield acceleration undergoes a significant decrease as this happens. Test 6 run 3 demonstrates this well: the failure surface became fully formed early in the "earthquake", and the yield acceleration reduced. This can be clearly seen in Fig. 6.118, where the displacements increase rapidly after about 0.9 seconds of the record. Most of the strong motion part of the excitation was through by this time.

Study of Fig. 6.107 - 6.119 reveals that permanent outward movement generally only occurs when the yield acceleration is exceeded by the base motion. In Fig. 6.113 (t5r2 data) for example, outward movement takes place at 0.1 sec., 0.22 sec., 0.42 sec., 0.55 sec, and 0.74 seconds in the record.

It appears that the first 2 peaks in the run were in fact missed by late starting of the data logger. Each negative acceleration peak (acceleration into the fill, causing outward movement of the wall) is followed by a positive peak, which causes movement of the wall back towards the fill. It is interesting to note that the outward displacement at 0.55 sec occurs at the time of a very small negative acceleration. It is probable that this movement is like an elastic rebound after the immediately preceding large inward movement. This particular inward movement is itself a little odd: the acceleration peak (positive) is relatively small, although the wall top amplifies it more than 2 times. The next positive peak is only a little smaller, but the inward movement at that time is very small.

If we look now at Fig. 6.114 (t5r6 data), we see a similar pattern, although the acceleration level is more than twice as great. The peak at 0.81 sec. is the same as that at 0.55 sec. in Fig. 6.113, although it is larger in Fig. 6.114. There is again the oscillatory motion with the large inward movement preceding a small outward movement.

The magnitude of the inward movements observed was somewhat unexpected. The Newmark (1965) sliding model assumes that the yield acceleration in the outward direction (causing inward movement) is infinite and that inward movement does not occur. Figs. 6.107 to 6.112, which show sinusoidal excitation data, show clearly that there is significant amplification of positive accelerations (three times or more) after negative accelerations that cause permanent outward displacement. These large amplifications occur at the wall top, and are about twice those at wall mid-height, indicating that the wall vibrates about the base like a single degree of freedom oscillator. Similarly, the displacement rebounds are about twice as large at the wall top as at mid-height. Note also that there is amplification of the next small negative acceleration eg. at 0.5sec in Fig. 6.109, and some outward displacement. This is likened to the damped decay of resonant vibrations. We should also note that there is small amplification of the first positive acceleration in each of Figs. 6.107 - 6.112, and some inward movement, especially of the wall top.

We might expect there to be some rebound after outward movement. Near the peak of the inward accelerations, which cause outward movement, we would

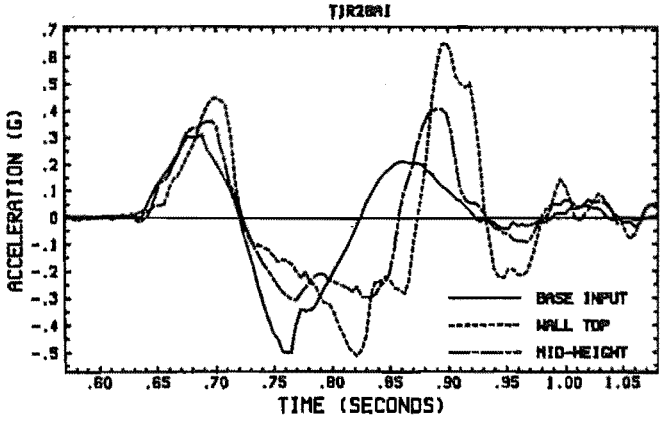

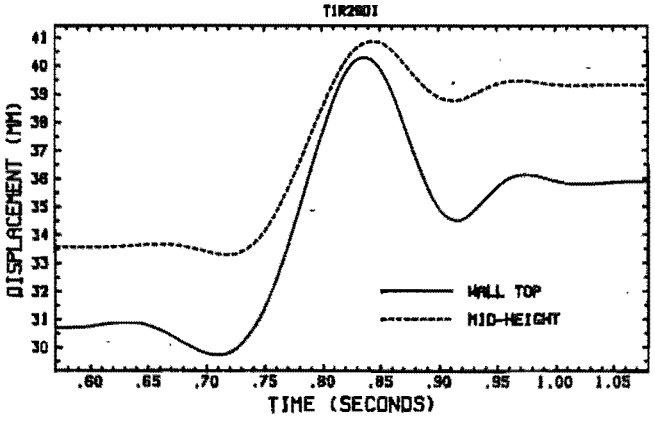

Fig. 6.107. Accelerations and displacements, test 1 run 28.

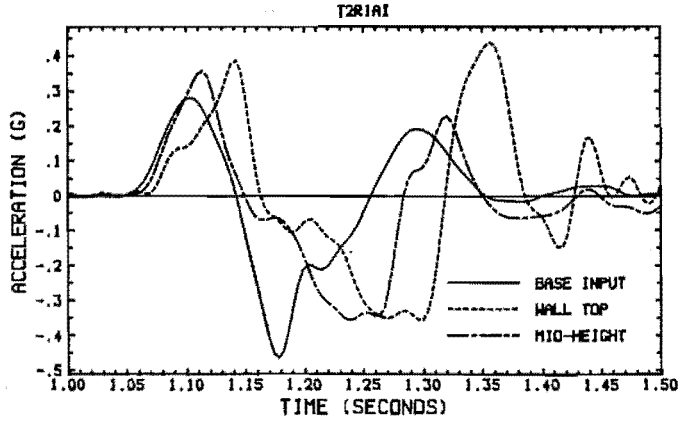

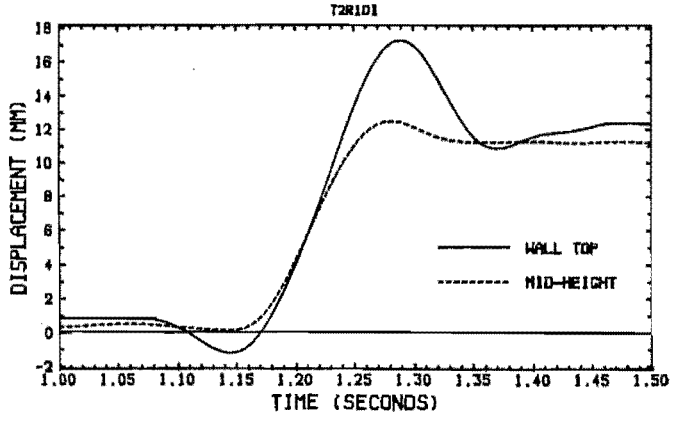

Fig. 6.108. Accelerations and displacements, test 2 run 1.

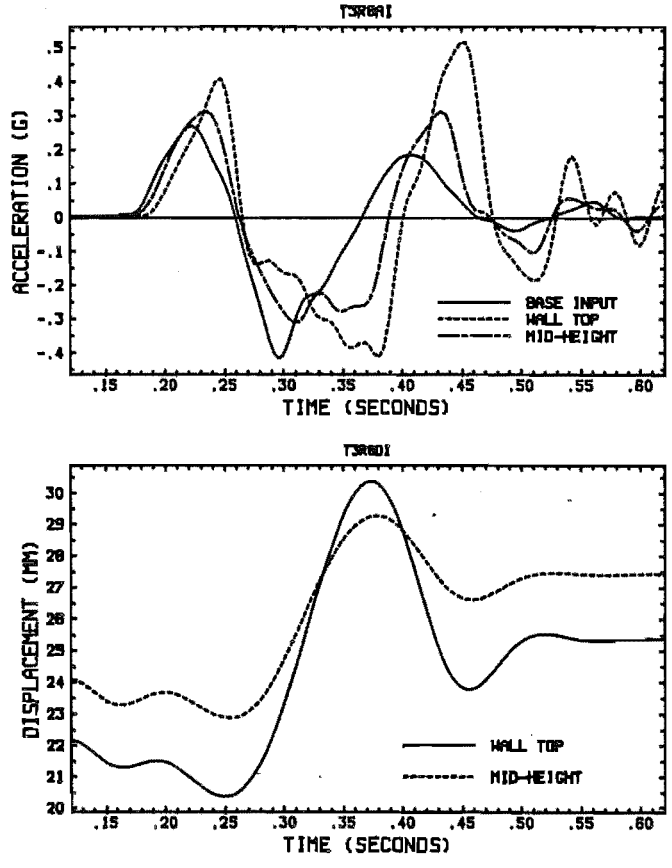

Fig. 6.109. Accelerations and displacements, test 3 run 8.

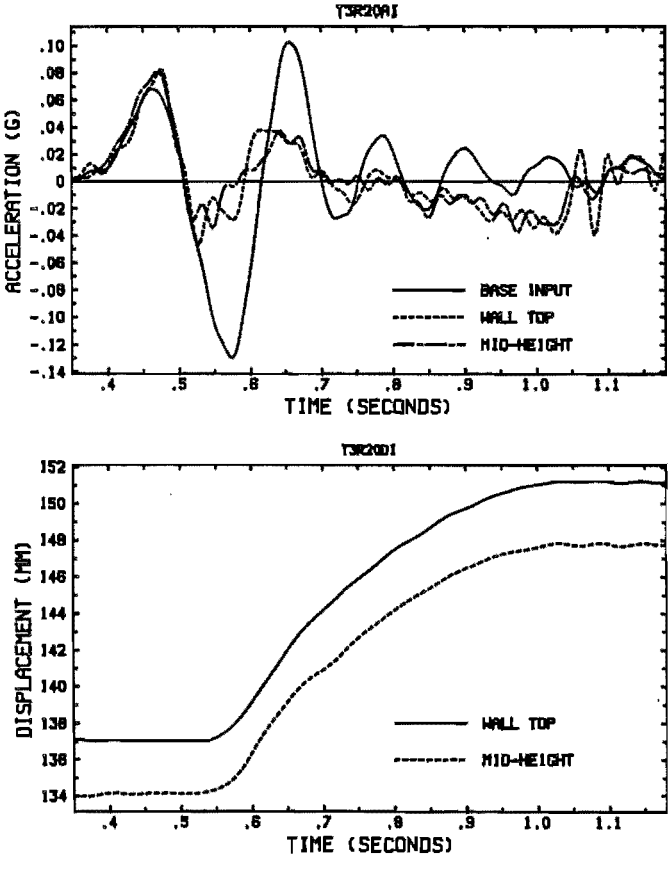

Fig. 6.110. Accelerations and displacements, test 3 run 20.

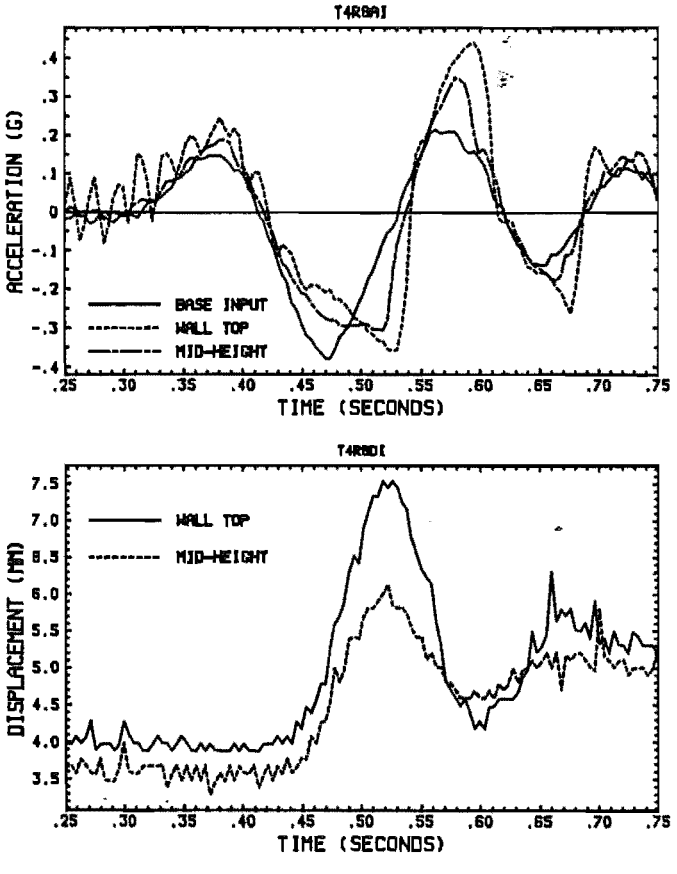

Fig. 6.111. Accelerations and displacements, test 4 run 8.

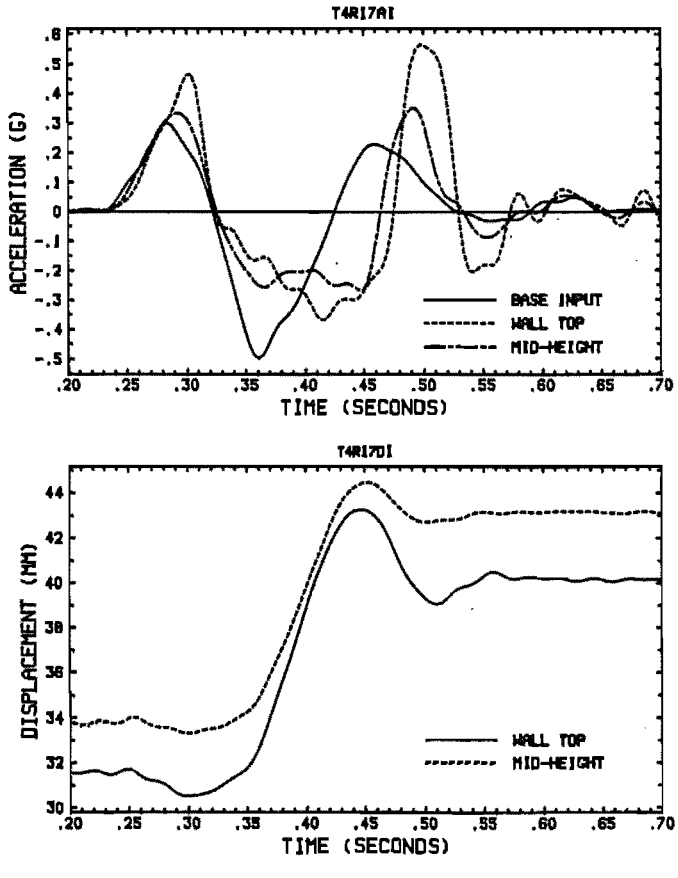

Fig. 6.112. Accelerations and displacements, test 4 run 17.

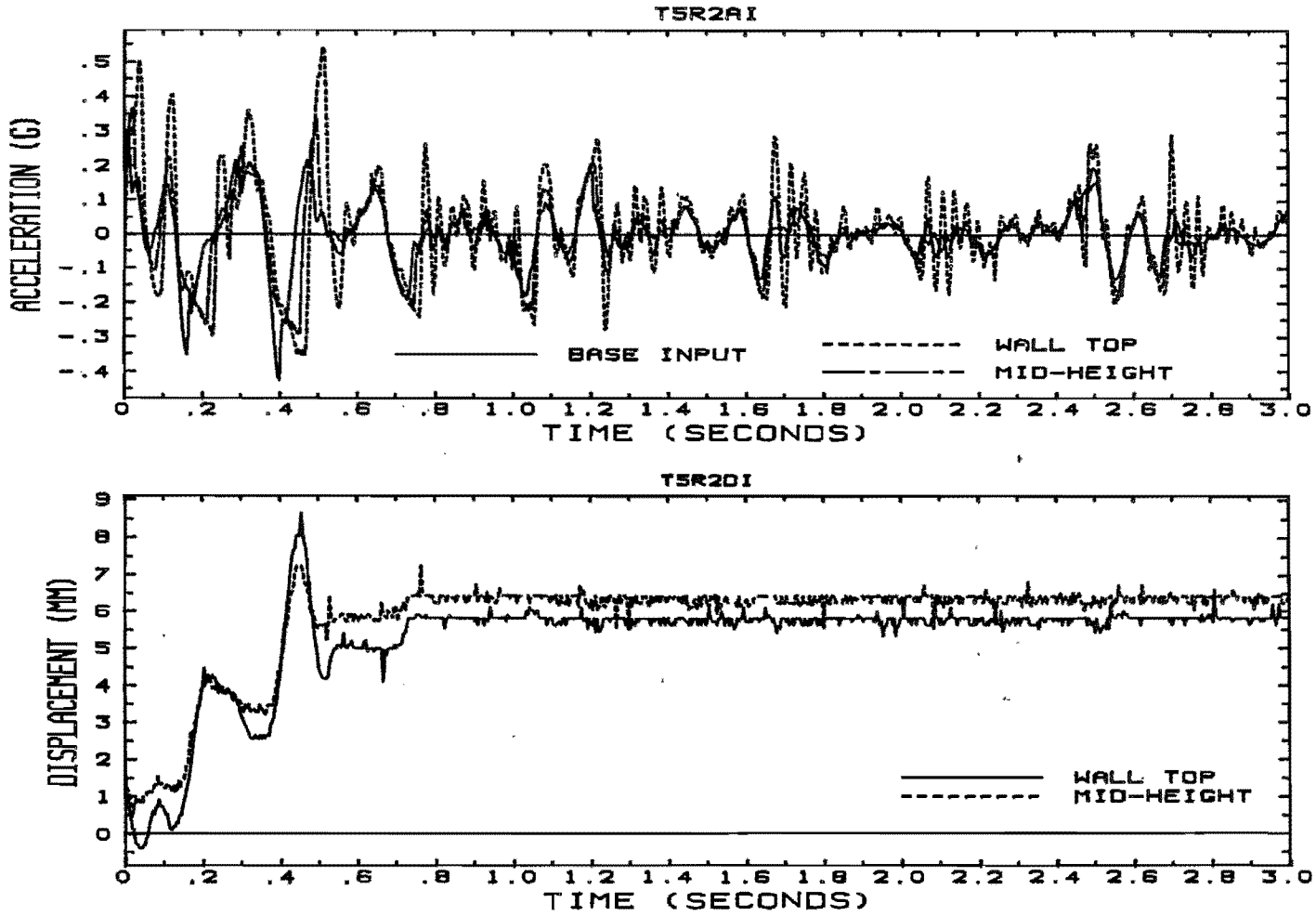

Fig. 6.113. Accelerations and displacements, test 5 run 2.

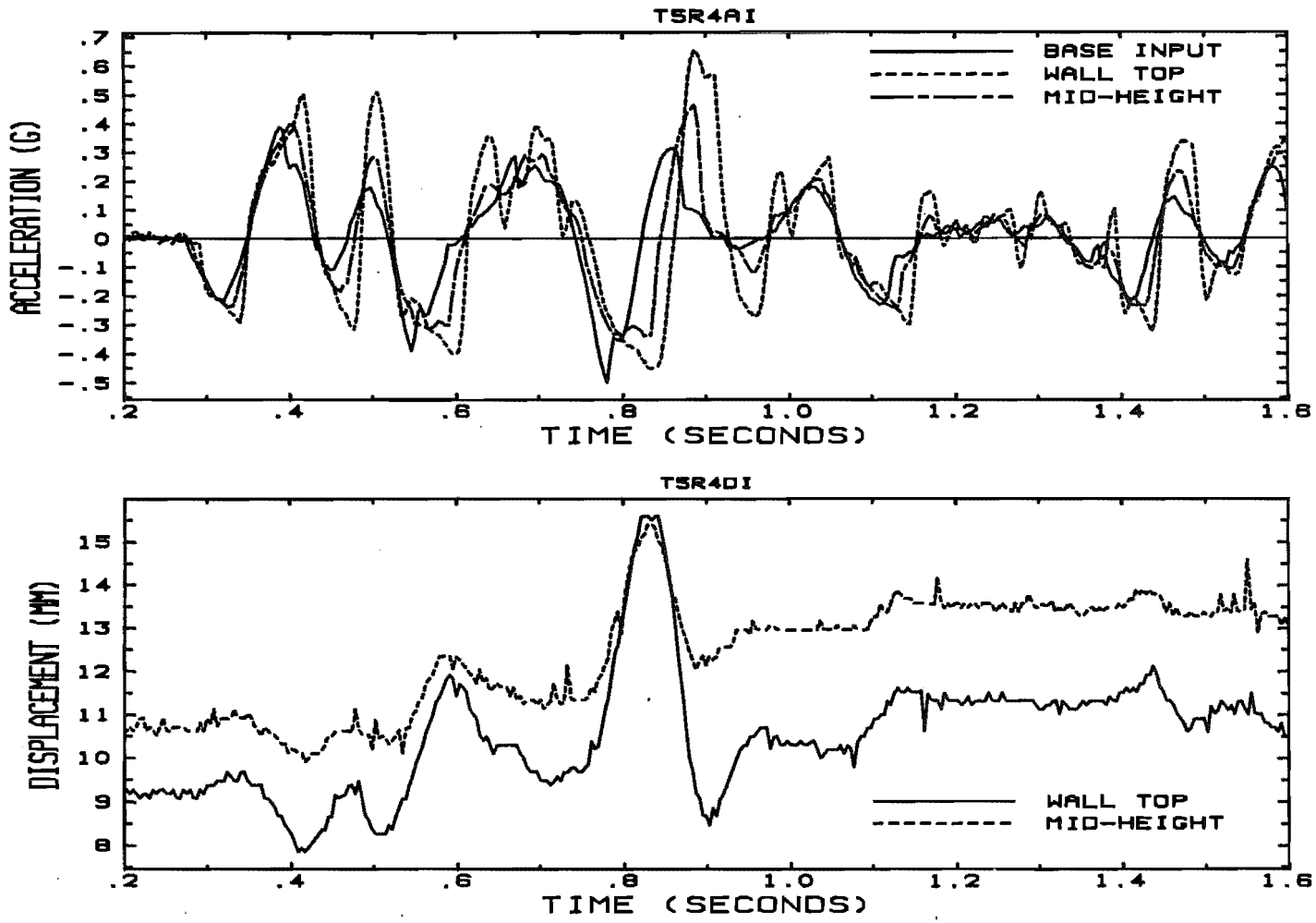

Fig. 6.114. Accelerations and displacements, test 5 run 4.

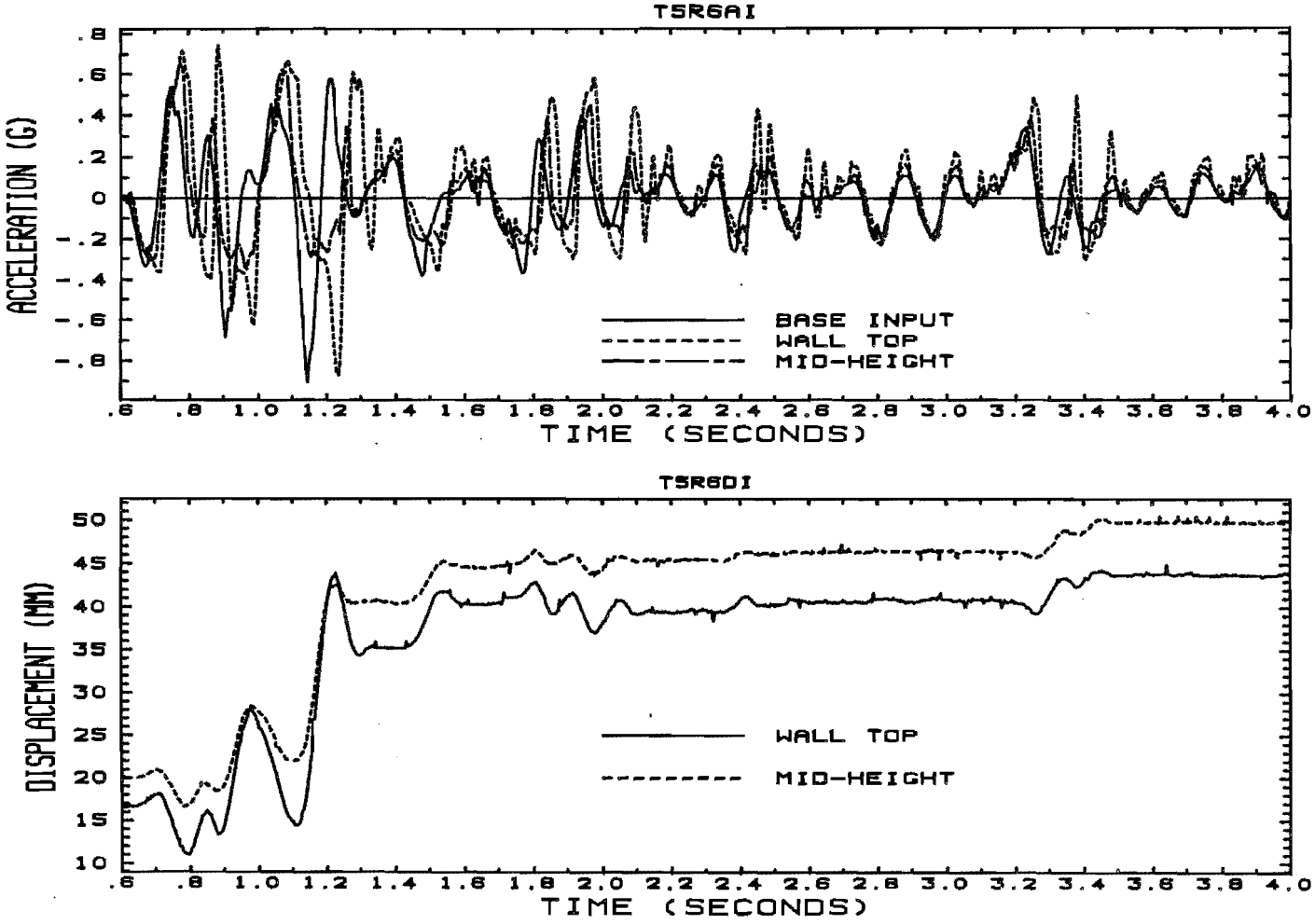

Fig. 6.115. Accelerations and displacements, test 5 run 6.

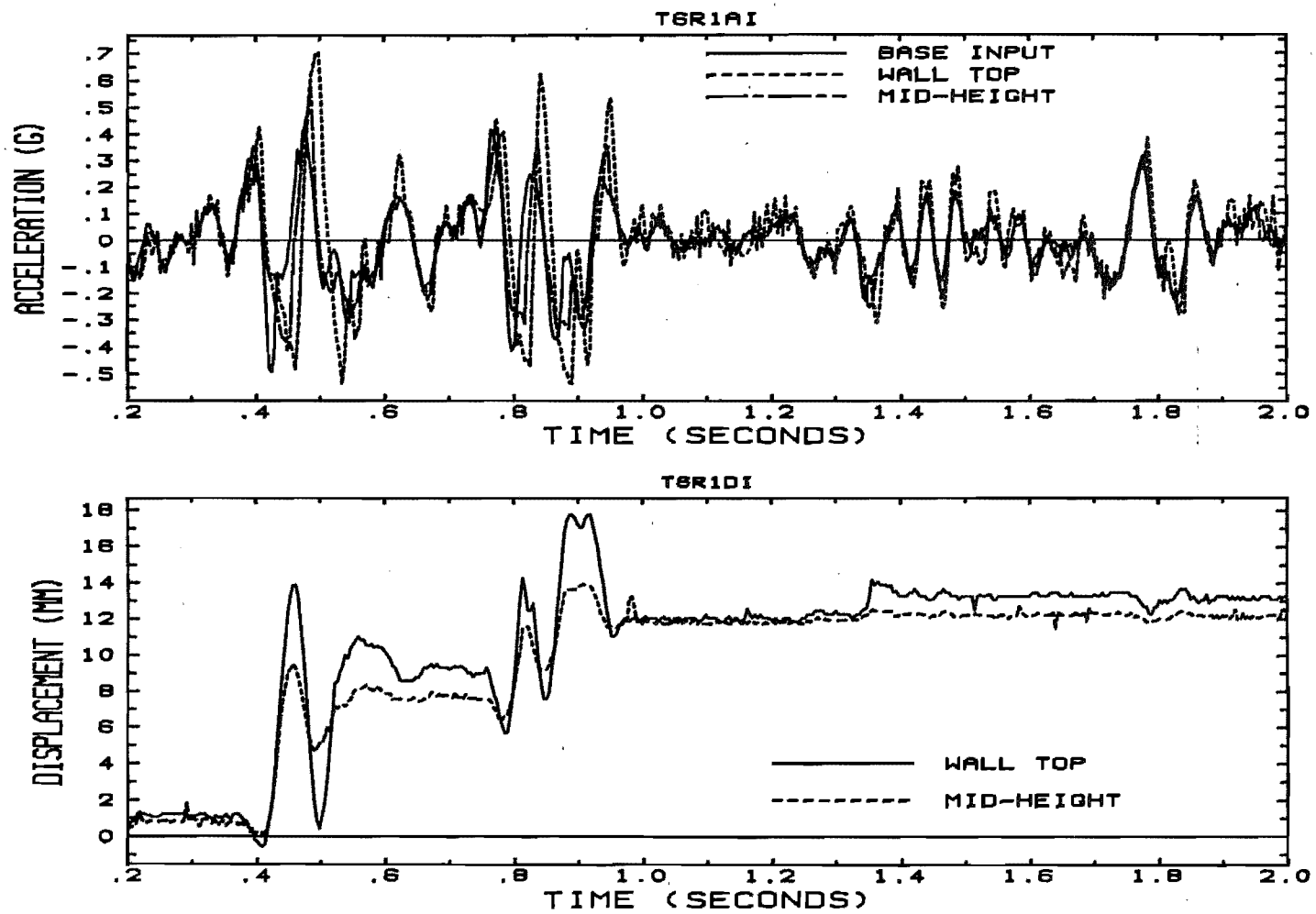

Fig. 6.116. Accelerations and displacements, test 6 run 1.

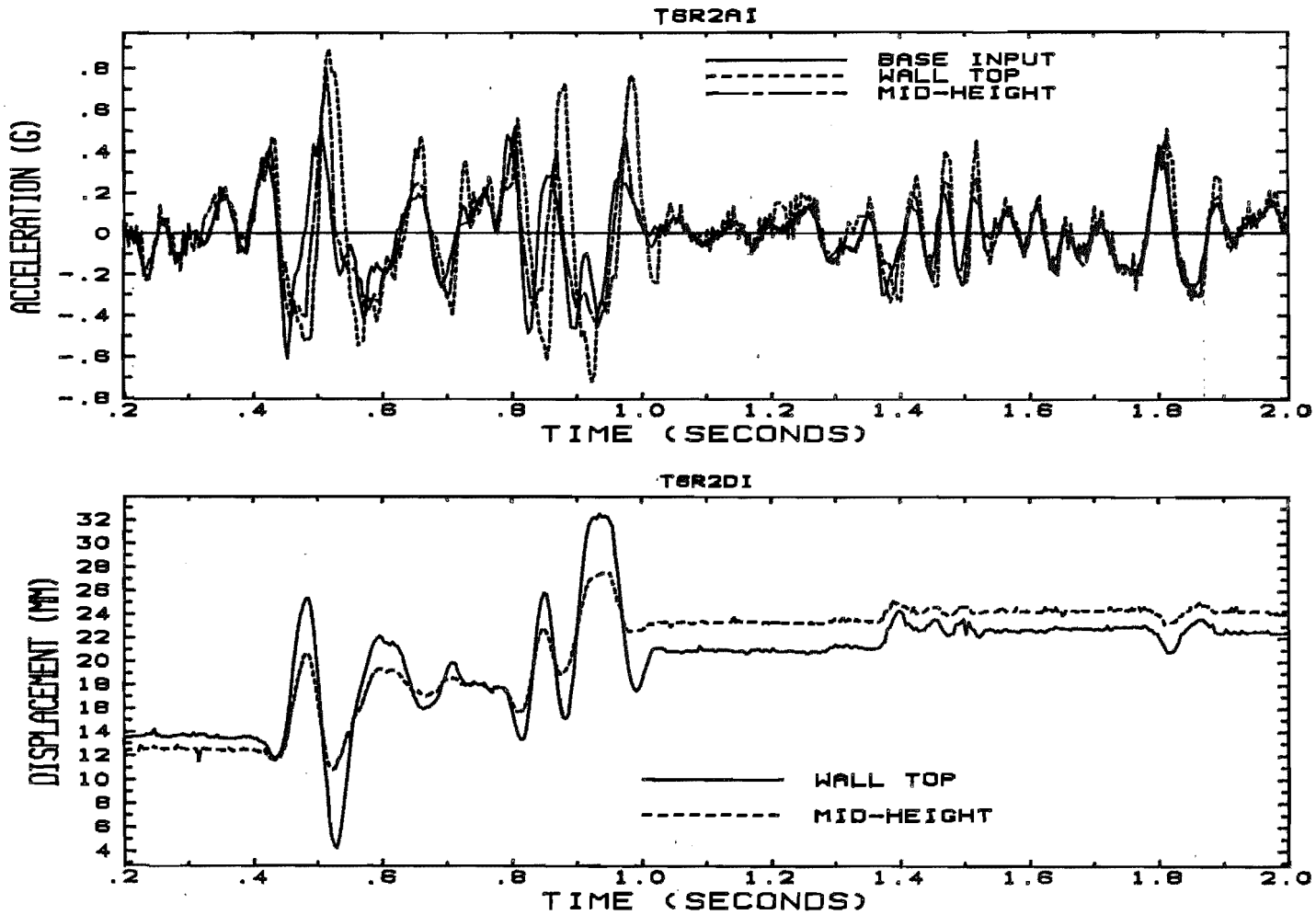

Fig. 6.117. Accelerations and displacements, test 6 run 2.

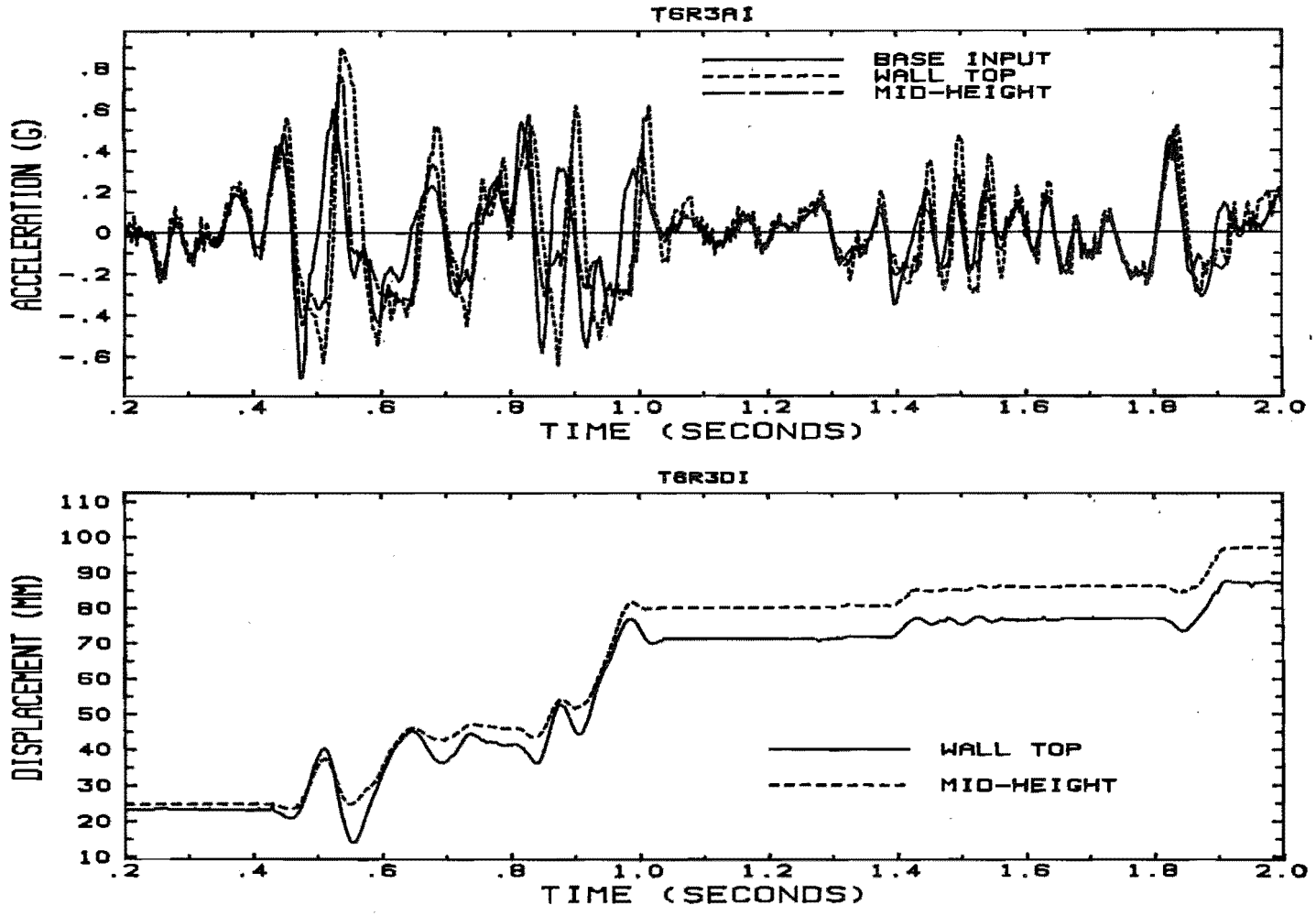

Fig. 6.118. Accelerations and displacements, test 6 run 3.

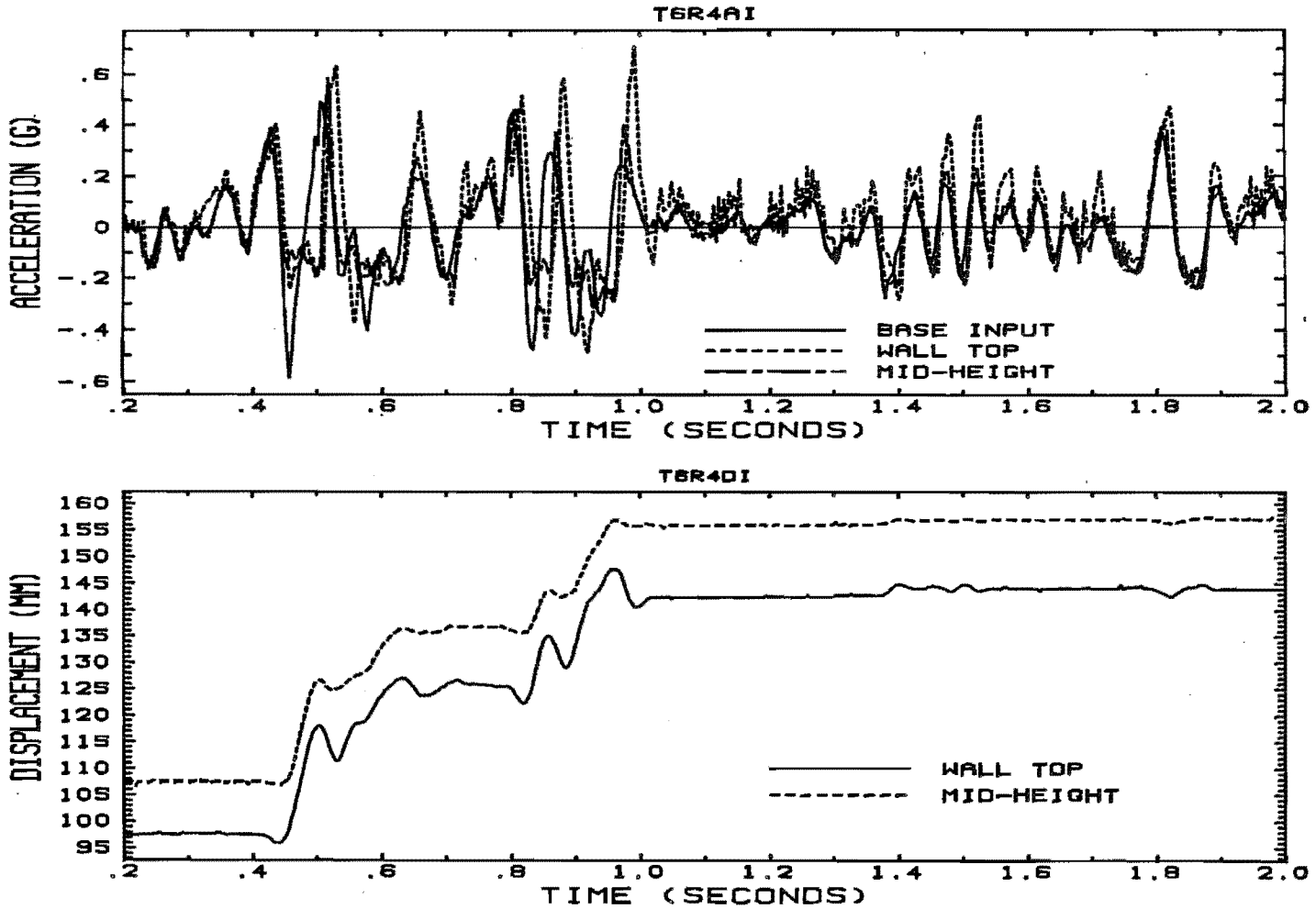

Fig. 6.119. Accelerations and displacements, test 6 run 4.

expect the fill to be momentarily rather loose, and the subsequent acceleration in the opposite direction to result in the fill returning to its former density, perhaps with a little overrun (compression) which is released on the next small negative pulse.

It is apparent in almost all Figs. 6.107 to 6.119 that there is relatively little amplification of the inward accelerations, while the outward accelerations are often greatly magnified. There is a limit to the amplification of accelerations possible. At acceleration levels above the yield acceleration the wall displaces, restricting the response acceleration to near the yield acceleration. If the structure amplified the base acceleration to a level above the yield acceleration it would in effect be self powered. With a structure such as this, it would be expected that at resonance amplification would lead to exceedence of the yield acceleration, hence movement, the structure softening and absorbing the inertial energy contained in the accelerations that are near and above the yield acceleration. So we might expect that amplification ratios to reduce as the base acceleration approaches the yield acceleration, and drop below 1 when the input acceleration is greater than the yield acceleration. This is what was observed by Rea and Wolf (1980), see Fig. 2.6. Yield accelerations in the outward direction (inward movement) are expected to be much higher (they were not actually observed) than in the opposite direction, hence the relatively large magnifications of the outward (positive) accelerations.

An important result of the amplified accelerations of the wall top is that any furniture or structure on top of the wall may experience severe shaking. Guard rails and walls, and bridge abutments founded on the fill surface, are examples of such objects. The posts of guard rails, for example, may lever on or even batter the wall facing near the top, causing damage to the facing and any sill or coping and possibly increased forces in the reinforcing strips in that area. Fierce oscillatory motions of the wall top would make it important to provide a sliding surface between a bridge deck and its abutment, if the abutment was founded on the wall. Such a joint would of course also be necessary to take up the permanent displacement of the wall. There is also the possibility of pounding of the bridge superstructure on the abutment.

The wall top consistently has higher response accelerations, however. If the wall is vibrating about the base, the wall top will experience larger oscillations than lower down, hence the larger accelerations. The yield acceleration phenomenon is obscure at the wall top with the larger accelerations, and also with oddly shaped peaks. For example, Fig. 6.112 of t4r17: there is a quite well-developed plateau in the mid-height acceleration, but the wall top trace continues to drift upwards. Figs. 6.111 (t4r8) and 6.109 (t3r8) are similar. In those figures, the wall top trace seems to have a "shoulder" at times 0.44 and 0.28 sec respectively, at a level that is half or less of the mid-height yield acceleration. Rea and Wolf (1980) said that at low levels of acceleration their walls vibrated like a continuous elastic body, but at high levels of acceleration they became like a rigid body on a horizontal surface vibrating horizontally (though asymmetrically). This perhaps explains the differences in the shape of the wall top response accelerations in Fig. 6.111 and 6.112. In test 4 the failure surface became fully formed in run 17. A similar change in shape of the wall top response acceleration trace can be seen in Fig. 6.118 and 6.119 for t6r3 and r4.

If we look at the displacements at which the failure surface became fully formed, it seems that there is some relationship between that displacement and the wall height. Table 6.18 shows the results of this analysis. The data for tests 5 and 6 in Table 6.18 are taken from the time immediately after the failure surface was fully developed, part way through the relevant runs. At the time of failure, it appears that the wall will have a displacement equal to about 4% of the wall height, although test 6 shows that the results cannot be relied upon. This result is probably related to the strength characteristics of the backfill material, specifically the amount of deformation necessary to reach the residual value of the soil angle of internal friction. Connected to this, especially for rough strips, is the deformation necessary to mobilise the soil/strip friction. In §6.7.2 it was pointed out that the deflection to peak pullout force was greatest for dense sand, some ten times that for loose sand. Thus the displacement to failure is probably related to the density of the backfill. In Nagel's (1985) wall 8, it seems that displacement was about

Table 6.18
Displacements D and dimensionless displacement ratios at wall failure.

test	D (mm)	D/H (%)
1	38	3.8
2	45	4.5
3	44	4.4
4	42	4.2
5	38	3.8
6	76	7.6

5.5% of wall height at failure. He does not state if/when the other walls failed. Richardson's et al (1976) tests of a full scale wall stopped at about 5.5% outward movement, although it would have been difficult for them to identify any failure surface outcrop due to blasting in the region where the outcrop would be. Only the Japanese have mentioned failure surface development in testing of RE walls, but the displacement at which it occurred has not been seen in the literature.

6.10.2. Sarma's equivalent pulse method of displacement calculation.

Fig. 6.120 shows some observed displacements plotted on Sarma's chart. The variable $C = \frac{\cos(\theta + \beta - \phi')}{\cos \phi}$ is calculated using $\phi = 45°$, $\theta = 0$ (ie. no vertical acceleration component), and $\beta = \alpha$, the observed failure surface angle to the horizontal. x_m is the observed displacement during the test run. K_m is the maximum inward input acceleration in the run, and T the predominant period, picked off a graph of the Fourier transform of the input motion. The observed yield acceleration k_h was used in the ratio k_h/K_m.

The plotted data shows some spread on the chart. A bounding line is difficult to fit without being excessively conservative, because of the T1R14, T2R1 and T6R4 points. T2R1 is unusual in that it had a large displacement compared to other runs. T1R12 is a pre-failure run (failure was in run 17), so why it plots so far over on the chart is not clear. T6R4 is a post failure run (fail-

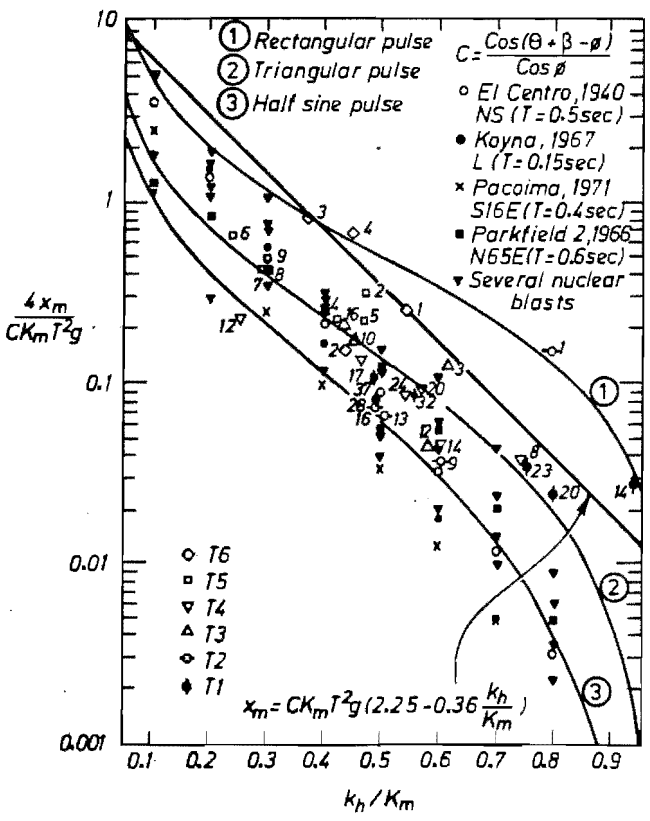

Fig. 6.120. Sarma's chart of dimensionless displacement vs k_h/k_m, with test data plotted.

ure was in run 3) and demonstrates the effect of a reasonably strong earthquake on a rectangular block structure after failure: a relatively large displacement.

The bounding line suggested has equation

$$x_m = CK_mT^2g\ (2.25 - 0.36\frac{k_h}{K_m}) \qquad \text{.....(6.3)}$$

A straight line is felt to be most appropriate with the limited data on the plot. To verify the bounding line, many more data points are needed on the plot.

Calculations of displacements using this line have the advantage that they can be done using the design earthquake spectrum, together with an estimate of the maximum acceleration expected. The limiting equilibrium formulation would be used to obtain the yield acceleration. There is, however, no provision for input of any other characteristics, such as the duration, of the design earthquake. Choice of a suitable bounding line to use in design would be mainly empirical, based on historical and calculated data plotted on the chart. In this way only could other important characteristics of the design earthquake or earthquake spectrum be accounted for. For this reason, in some situations the use of a bounding line may be conservative. It would probably be necessary to have three lines for New Zealand conditions, corresponding to seismic zones A, B and C in NZSS 4302:1984.

6.10.3. Lin and Whitman's method using random vibration theory.

A computer program was written to compute displacements using Lin and Whitman's (1986) method. It takes an acceleration time history and first computes the characteristics necessary to transform the data into a stationary Gaussian random process, then calculates the conditional expected displacement, using the theory described in §4.6.3. The power spectral density (PSD), required in the transformation of the motion, is estimated using the program "SPCTRM" (in Pascal) from Press et al (1985). For details of the PSD estimation procedure, and an attempt to verify the program, see Appendix D.

Only the earthquake records were used (tests 5 and 6) because of the problem pointed out by Lin and Whitman, and explained in Chapter 4: the record is transformed into a Gaussian process where it is expected that there will be more than one upward crossing of the yield acceleration. For the simple sinusoid excitations used in tests 1 to 4, there is only ever one such crossing, so the method cannot be expected to be useful.

Table 6.19 shows results for all the earthquake input acceleration records. Data sets of 1024 points with 512-point overlaps were used for all calculations (see Appendix D for an explanation of this). The portions of pre-earthquake shake-table ramping (ie. ramping to the starting displacement) that were logged are excluded from the calculations.

Table 6.19
Displacements observed and calculated using the Lin and Whitman (1986) method.

test/ run	data points used to calc. G(ω)	Properties of the record									Calc D (mm)	Obs. D (mm)
		T_o (s)	S_o (s)	n_r^+	R	δ	L_o (g)	α_o (g)	A_{max} (g)	k_h (g)		
t5r1, pts	1-1536	0.04	0.12	0	2.87	.82	.001	0.03	0.08	0.20	0	0
t5r2,	1-1536	0.05	0.94	8.54	2.66	.61	.024	0.16	0.43	0.20	1	5
t5r3,	1-1536	0.10	0.86	6.45	2.37	.67	.043	0.22	0.53	0.20	9	4
t5r4,	50-1586	0.11	1.00	5.76	2.41	.66	.043	0.21	0.50	0.20	9	2
t5r5,	150-1604	0.12	0.83	6.50	2.30	.60	.065	0.28	0.64	0.20	19	6
t5r6,	150-1604	0.13	0.76	6.99	2.23	.54	.126	0.41	0.91	0.20	48	28
t5r7,	130-1604	0.11	0.89	7.02	2.34	.62	.080	0.30	0.71	0.20	26	21
t5r8,	130-1604	0.11	0.94	6.73	2.37	.63	.070	0.27	0.64	0.20	21	18
t5r9,	80-1604	0.11	1.00	6.74	2.40	.64	.071	0.27	0.64	0.20	20	24
t6r1,	40-1576	0.13	3.42	3.51	2.82	.65	.105	0.18	0.49	0.22	12	13
t6r2,	40-1199	0.15	3.31	4.15	2.76	.61	.160	0.22	0.61	0.22	33	11
t6r3,	40-1199	0.15	3.28	4.52	2.74	.59	.220	0.26	0.70	0.22	57	77
t6r4,	50-1199	0.15	2.93	4.04	2.71	.59	.140	0.22	0.59	0.22	25	51
t6r5,	1-1199	0.14	3.43	3.12	2.80	.62	.100	0.17	0.47	0.22	10	≈20
t6r6,	1-1199	0.14	2.93	3.53	2.73	.60	.100	0.19	0.51	0.22	13	≈20
t6r7,	1-1199	0.14	2.47	3.89	2.67	.60	.100	0.20	0.54	0.22	17	≈20
t6r8,	1-1199	0.11	2.65	3.65	2.68	.59	.100	0.19	0.52	0.22	14	≈20

Comparing the observed and calculated displacements in Table 6.19 it can be seen that there are some quite large differences. The observed and calculated displacements are plotted against each other in Fig. 6.121. For a perfect fit of the theory with the observed displacements, we would expect the points to plot along a line at 45° to the X-axis. In fact they plot fair-

ly evenly on both sides of this line, indicating perhaps that there is little bias in the calculated displacements, which might have been caused by incorrect PSD estimation. The figure also shows that the scatter seen in the figures taken from Lin and Whitman (Fig. 4.12 and 4.13) is present here: in §4.6.3 it was shown that the predicted displacement was usually within a band of from half to twice the displacement calculated using time domain double integration of the acceleration time history.

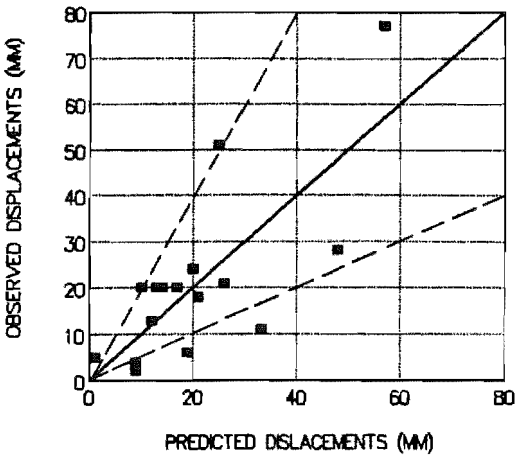

Fig. 6.121. Observed displacements vs. displacements predicted using the Lin and Whitman (1986) method.

Expected conditional displacements calculated by the Lin and Whitman method are in fact mean values. The scatter in Figs. 6.121, 4.12 and 4.13 indicates that the method as it stands is rather imprecise. This might be expected as k_h, σ_x, A_{max}, Ω, and δ are all random variables, and a non-stationary process is being modelled by a stationary one. The risk of exceedence of the predicted displacement must be included in the formulation. Lin and Whitman have done this by considering the probability distribution of the expected displacement and how it is affected by the distributions of the variables k_h, σ_x, A_{max}, Ω, and δ. The uncertainty in the central frequency Ω (or ω_g when using the K-T SDF) was found to be so large that it determines the shape of the final distribution. As a result of these considerations, they derive the conditional expected displacement $E[D|k_h, A_{max}]$ (ie. the expected displacement given k_h and A_{max}) and the conditional probability that the displacement D exceeds some arbitrary value D_o, $P(D>D_o|k_h, A_{max})$. The conditional expected displacement is normalized against A_{max} and plotted against k_h/A_{max}, producing the three lines shown in Fig. 6.122. Also shown in Fig. 6.122 are the calculated and observed displacements for the earthquake runs (tests 5 and 6), and the observed displacements for some of the sinusoidal runs in tests 1 to 4.

It is seen in Fig. 6.122 that the lines there are more or less upper bounds for the observed and predicted data from the testing that is the subject of this report. Test 3 run 16 and test 1 run 12 points plot outside

them however. By t3r16, the wall had a very low yield acceleration (0.09g), and the displacement trace (similar to Fig. 6.110) shows that it was probably close to having a static factor of safety of one. T1r12 is probably an aberration: A_{max} was just above the yield acceleration (0.25 vs. 0.24g), and the movement was quite small (0.7mm, from Table 6.46). The point is probably on the limit of accuracy of the chart. Lin and Whitman state that for most purposes the expected displacement lines shown are probably sufficient to estimate permanent displacement of a sliding block (they were considering earth dams), and with the limited data shown, Fig. 6.122 supports that contention. To be certain, however, data for tests with different earthquakes needs to plotted on the chart. Lin (1982) plotted predicted displacements, at two k_h/A_{max} levels, for all of the 140 earthquakes referenced by Vanmarcke and Lai (1980), showing that the lines on the chart are in fact means for the predicted displacement.

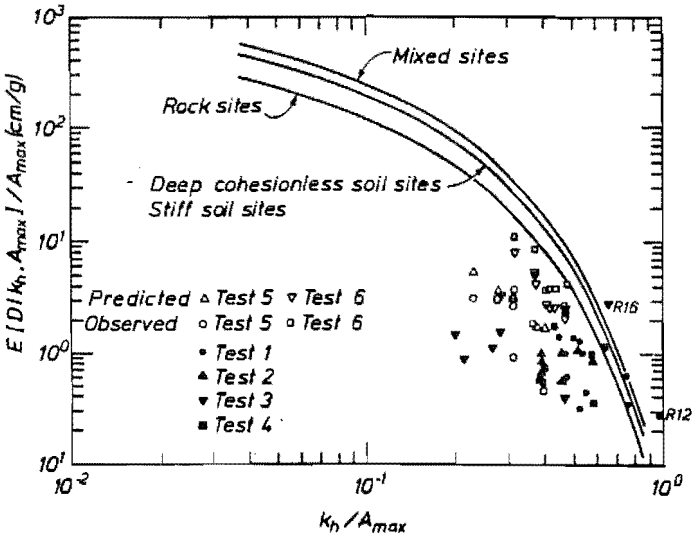

Fig. 6.122. Observed and calculated displacements plotted on Lin and Whitman's (1986) chart of normalized conditional expected displacement vs. normalized yield acceleration.

Fig. 6.123 is also taken from Lin and Whitman, and shows the conditional probability that the predicted displacement exceeds some value D_0, plotted against the ratio of D_0 to the conditional expected displacement. It is seen on the figure that there is up to about 30% chance that the predicted displacement is exceeded at some time. This probability can be reduced if we set a time duration over which to check

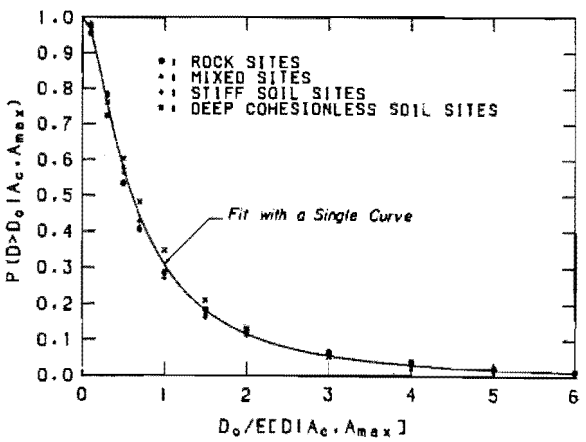

Fig. 6.123. Normalized conditional probability of exceedence of a permanent displacement for sliding blocks.

the chance of D being exceeded; this would be the normal procedure in design, the time duration being the design life of the structure. Lin and Whitman give an example of this calculation, using the equation

$$P(D>D_o \mid \text{time } t) = \sum_i \sum_j P(D>D_o \mid k_{h,i},\ A_{max,j}).P(A_{max,j} \mid \text{time } t).P(k_{h,i}) \qquad (6.4)$$

$P(A_{max} \mid \text{time } t)$, the probability of the maximum acceleration A_{max} occurring in time t, can be found from an earthquake hazard analysis. $P(k_h)$ can be found by considering the particular situation for which k_h is derived. Lin and Whitman use a simple relationship between k_h and the static factor of safety to derive the probability distribution of k_h.

The problem arises, however, that in New Zealand we usually design from the perspective of a response spectrum, rather than using a design earthquake for which we can compute a PSD. There is a way, however, to derive a PSD from a response spectrum, which assumes the earthquake to which the spectrum refers is a stationary process (which it never is). Vanmarcke (1976) gives the method, which is derived from random vibration theory. The relationship between the response spectrum and the PSD is not unique though: it depends on the chosen strong-motion duration S_o, on the exceedence probability *p* assigned, and on the damping level. Recall that the exceedence probability *p* is the probability that the acceleration exceeds the maximum value A_{max} chosen.

Vanmarcke's method, briefly, is as follows: divide the damped velocity response spectrum S_v by the peak factor $r_{s,p}$ at a set of target period values $\omega_n(i)$. (This is understood to mean that the periods correspond to the inverse of the frequencies $\omega_n(i)$.) The peak factor $r_{s,p} = A_{max}/\sigma_x$, where A_{max} is the maximum acceleration chosen for the "earthquake", σ_x is the rms acceleration chosen, and $S = S_o$ is the strong motion duration chosen, as in Chapter 4. This gives the "σ-spectrum" (ie. $\sigma_a(s)$ as a function of period, where σ_a^2 is called the pseudo-acceleration response variance), from which the PSD $G(\omega)$ can be obtained by iterating on the equation

$$\sigma_a^2(s) \approx G(\omega_n)\omega_n\left(\frac{\pi}{4\lambda} - 1\right) + \int_0^{\omega_n} G(\omega)\,d\omega \qquad \ldots\ldots\ldots\ldots\ldots\ldots\ldots\ldots (6.5)$$

The iteration proceeds by starting at the smallest value $\omega_n^{(1)}$, when the integration is negligible. At the arbitrary frequency $\omega_n^{(i)}$, $G(\omega_n^{(i+1)})$ is found by integrating $G(\omega)$ up to $\omega_n^{(i)}$ numerically, subtracting the total from $\sigma_a^2(s)$ and manipulating the rest of the equation. λ is the fraction of critical damping applying to S_v.

This procedure is said to be reversible: one can generate S_v from $G(\omega)$. Then the various damping values correspond to different specified probability levels. Vanmarcke also points out that there need not necessarily be a close relationship between the design response spectrum for a site and the spectral density function of strong earthquakes that may occur at the site. This is said to be because the design spectrum is probably derived to include both near and far field earthquakes, which will most likely have different frequency content and duration. This comment refers to the method of deriving simulated motions based on perhaps only one spectral density function: such a procedure is really only justified if the local geology precludes other types of earthquakes from occurring.

Instead of using a spectral density function derived from S_v, we could use the Kanai-Tajimi spectral density function (K-T SDF) to calculate displacements. Included in the computer program used here is the ability to do this. Fig. 6.124 shows some results using the K-T SDF in the Lin and Whitman method. The parameters λ_g and ω_g are nominally the ground damping and the ground natural frequency respectively. Their effect is to place the function peak on the frequency axis (ω_g) and to determine its width (λ_g). Once ω_g and λ_g have been chosen, the magnitude of the K-T SDF is scaled to a given root-mean-square acceleration σ_o after calculating the zeroth moment of the function. (σ_o is the square root of the zeroth moment, Eq. 4.41, and is equated to σ_x.) Once the PSD has been derived, the program is the same as for earthquake time history calculations, although this ignores the changes in ω_g and λ_g that occur as the wall deforms.

Lin (1982) uses an approach similar to the "simplified approach" of Newmark (1965), Seed and Martin (1966), Ambraseys and Sarma (1967), and Makdisi and Seed (1978), for calculating displacements for an earth dam. A RE wall is an earth structure with a sliding block in seismic failure so the approach should be equally as applicable. It is:

i. Select the design or study ground motions. Calculate ω_g, λ_g, and σ_x for each, and derive the distribution of ω_g and σ_x/A_{max}.

ii. Assume ω_g is a random variable, and calculate σ, δ, and Ω for the acceleration of the chosen failure block or wedge. Ω, the central frequency, is based on the small strain shear modulus. Thus for each ω_g, evaluate the shear strain, then calculate the SDF of the wedge acceleration and use it to calculate σ, δ, and Ω.

iii. Calculate the conditional expected displacement $E[D|k_h, A_{max}]$, and the probability of it exceeding some arbitrary value D_o $P[D>D_o|k_h, A_{max}]$: determine k_h, and for each ω_g and each σ_x calculate the duration S, $E[D|k_h, A_{max}, \omega_g]$, and $P[D>D_o|k_h, A_{max}, \omega_g]$. Then using total probability calculate $E[D|k_h, A_{max}]$ and $P[D>D_o|k_h, A_{max}]$.

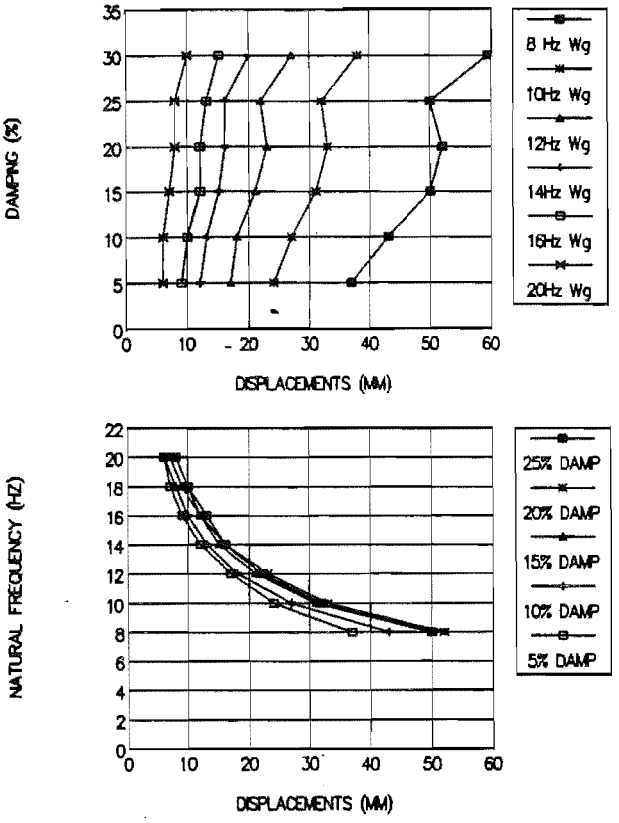

Fig. 6.124. Displacements calculated using the Kanai–Tajimi spectral density function in the Lin and Whitman (1986) method.

This is a fairly complicated method to use for everyday design. For most purposes, consulting Figs. 6.122 and 6.123 would be sufficient, with recourse to the complete calculation method only necessary for important, special or unusually difficult structures.

Lin (1982) in fact uses the K-T SDF to represent the PSD for a given earthquake time history. He uses the earthquake time history to estimate the K-T parameters G_o, ω_g, and λ_g, and then works with the K-T SDF. The Vanmarcke parameters S_o (strong motion duration), σ_x (rms acceleration), δ (bandwidth), and Ω (central frequency) are then derived for the K-T SDF. Of course, they are functions of the three derived K-T parameters. Lin mentions that there are two methods available to estimate G_o, ω_g, and λ_g from an earthquake time history: least squares fitting, and a spectral moment method.

The spectral moment method was said to be the better of the two, as shown by Binder (1978), so was used in his work. It is necessary to consult Binder to see how the calculations are done.

While Lin and Whitman's method seems the most rational and complete of the three approaches presented here, it is also the most complicated by far. In this regard, a full calculation of displacement would only be done for important, large or unusual RE walls. Use of Figs. 6.122 and 6.123 would be sufficient in most cases, although the total probability calculation (Eq. 6.4) would require the seismicity of the project site to be known in some detail.

6.10.4. Standardized displacements using the Newmark / Franklin and Chang chart.

§4.6.2 described the method used by Newmark (1965) and Franklin and Chang (1977) to standardize displacements for different earthquakes by scaling them to values expected from an earthquake of 0.5g peak acceleration and 30 in/sec (762mm/sec) maximum velocity. Standardized displacements were then plotted against N/A, the maximum resistance coefficient N (our k_h) divided by the peak acceleration A (scaled to 0.5g). Fig. 6.125 shows data from the tests described in this report plotted on Newmark's chart (originally shown as Fig. 4.9). Franklin and Chang's upper bound lines have been removed for clarity, except the bound for all San Fernando earthquake records because it is close to bounding all the upper bound lines.

Also drawn on Fig. 6.125 is a proposed upper bound line given by

$$d = 2 \frac{V^2}{Ag} \left(\frac{k_h}{A} \right)^{-3} \qquad \text{.....(6.5)}$$

where d is the standardized maximum displacement, V is the maximum velocity in the earthquake (30 in/sec in the chart), and A is the measured maximum acceleration coefficient (fraction of g) in the earthquake (0.5 in the chart). This line is straight and ignores the curvature shown in the Franklin and Chang upper bound lines. The curved part of their lines (very

large displacements) would apply to very soft, probably saturated, embankments, so is not really applicable to RE walls. Whitman and Liao (1984) proposed a curved boundary, but it plots well to the left of all the data points from this testing. There is insufficient data to fit a more complicated curved boundary line to the present chart.

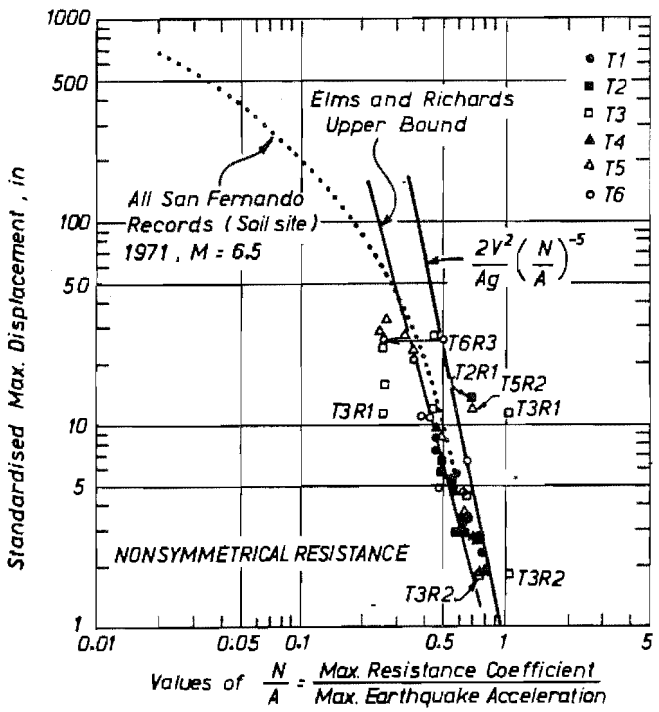

Fig. 6.125. Observed displacements plotted on the Newmark / Franklin and Chang chart.

The points for t2r1 and t5r2 are both outside the proposed upper bound line. It is felt that they are isolated points and a boundary including them would be overly conservative. If a line is dropped to the bounding line at the same N/A value, the standardized displacement at the intercept will be about half of the measured value. Considering the range of Lin and Whitman's calculated displacements (Figs. 4.12 and 4.13), this "inaccuracy" is not excessive. Two other points that are difficult to know what to do with are those for t3r1 and t3r2: there was no clearly defined yield acceleration observed. If the yield acceleration is set at the maximum acceleration observed in the mid-height accelerometer, both points plot at N/A = 1.05, which is well outside the proposed upper bound. If the first plateau in the wall top acceleration is taken as the yield acceleration for t3r1, that point plots well inside the upper bound. For t3r2, the response accelerations have a shoulder then a slower increase to the maximum. If a value of k_h is taken near the shoulder, the point plots beside the t4r8 point. The maximum acceleration values are probably greater than the yield acceleration for those runs, so the points are expected to be closer to the proposed upper bound line.

The Elms and Richards (1979) upper bound line is also shown on Fig. 6.125. Something over half of the data points plot outside this line, so it

would be unconservative to use it in design. The line was derived as a simple bounding line for use in the design of gravity walls.

6.10.5. Conclusions on displacement prediction.

It is felt that the Lin and Whitman theory is the most rational way to predict displacements of RE walls. A predicted displacement can be arrived at quite quickly, with somewhat more effort necessary to obtain the probability of exceedence of some arbitrary displacement, say during the design life of the structure. Without the use of the probability of exceedence, the predicted displacement may be from half to twice that calculated from time domain double integration of the acceleration time history. Similar variation was found when compared to the observed displacements from the testing. It is not readily apparent how to decide where a particular prediction is in this range. Accordingly, it must be used in conjunction with the probability analysis included in the paper. For design purposes, the factor of safety should be selected on the basis of the probability of exceedence of the predicted displacement. The necessity of using the probability analysis may make it still too complicated for many designers.

Lin (1982) points out that charts such as Sarma's and Newmark's do not properly account for some important ground motion characteristics, although they are reflected in A_{max} and V_{max}. It is difficult to see how those characteristics (such as predominant frequency, rms acceleration and duration) affect the displacement. Newmark's chart does not include the mechanism of build-up of the displacement either. Because the Newmark and Sarma charts are a blanket upper bound approach, they may produce conservative results in some situations.

In the light of the complications of using the Lin and Whitman method, the Newmark / Franklin and Chang or Sarma charts could be used. Sarma's chart is perhaps best because it can be used with a design spectrum, and an estimate of A_{max} (Sarma's K_m), quite expeditiously. It is a little more difficult to use the Newmark / Franklin and Chang chart because the maximum velocity V_{max} of the design earthquake or spectrum must be determined. An advantage of the

Newmark / Franklin and Chang chart is that it has been derived with a large data base (some 140 earthquake records), whereas Sarma's chart has a much smaller data base. To be more certain in the use of Sarma's chart, more earthquakes need to be analyzed and the results added to the chart. The suggested bounding line may need adjusting after that is done. For New Zealand conditions, it would probably be necessary to have three bounding lines, corresponding to the three seismic zones in the structural loading code (NZSS 4203:1984). Alternatively, reduction factors could be used to derive values for the other two zones from a line for one zone.

The main uses of predicted displacements would be to ensure that space is available for displacements of the order predicted, and also as an indicator of whether remedial work is necessary after an earthquake. If earthquake induced displacements are much less than the design predictions, perhaps reconsidered in the light of as-built conditions in the structure, then wall owners can be confident that the structure is safe and serviceable.

When structures, such as bridge abutments, are founded on the surface of RE walls, the predicted displacements will indicate how much room should be allowed between the superstructure and the substructure to take up earthquake dislocation. Consideration should also be given to differential settlement of the fill surface, especially at large displacements. Figs. 6.7 and 6.8, which show failure geometry with the fill surface shape at the end of tests 5 and 6, show that the rear of the reinforced block settles significantly relative to the top of the wall, at large displacements.

This now completes the discussion of the experimental results. In the following section there is a sensitivity analysis of the parameters in the limiting equilibrium formulation.

6.11. A sensitivity analysis of the limiting equilibrium formulation.

First there is a look at the sensitivity of the various parameters in the limiting equilibrium formulation as applied to the models tested for this project. In the subsequent section there is an analysis of sensitivity as it

affects a full scale wall. A 12m tall wall, with reinforcing strips 10m. long, is chosen.

6.11.1. Sensitivity of parameters as it affects model walls.

Fig. 6.126 shows the effect of ϕ on the yield acceleration predicted by the limiting equilibrium formulation. There is a linear rise in the yield acceleration with increasing ϕ, and the effect of f* decreases as f* increases (the f* lines become closer together). It appears that a high-friction backfill is important in providing a high yield acceleration.

Fig. 6.127 shows the effect of the friction coefficient on the predicted k_h. As f* increases, there is an increase in k_h, but the rate of increase decreases as f* increases. Thus to achieve a design yield acceleration, f* should be chosen first, followed by ϕ.

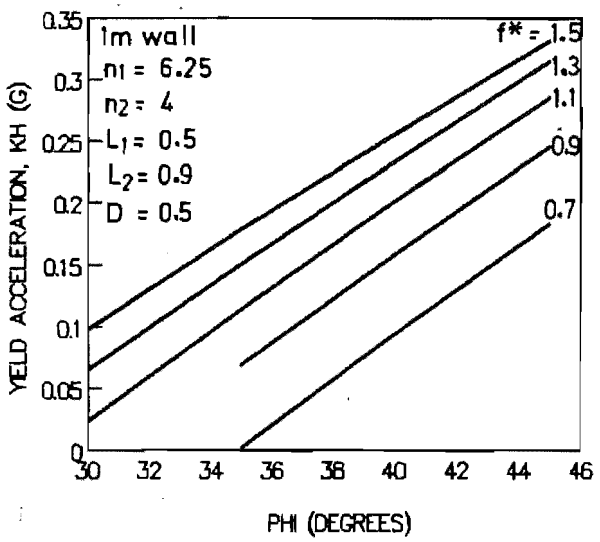

Fig. 6.126. Effect of ϕ on k_h and α.

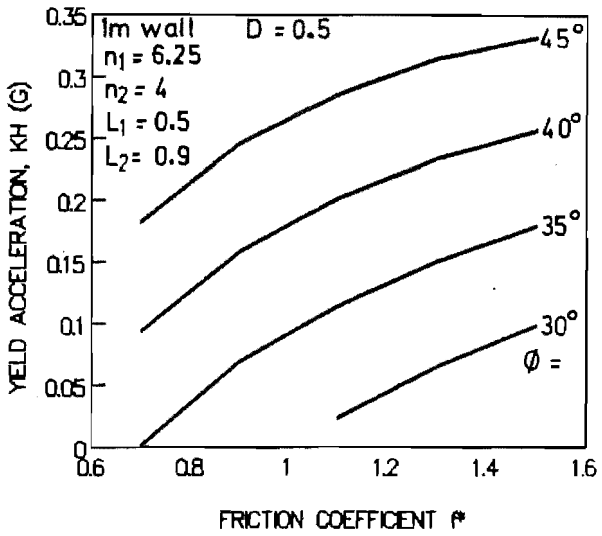

Fig. 6.127. Effect of f* on k_h and α.

Fig. 6.128 shows the effect of ϕ on the failure surface angle α. As ϕ decreases α becomes steeper. There appears to be a limiting value of ϕ (about 35°), though, after which α increases more slowly. Fig. 6.129 shows that α also increases at a fairly uniform rate as f* decreases, apart from a small region of slow decrease at large (reducing) values of f*.

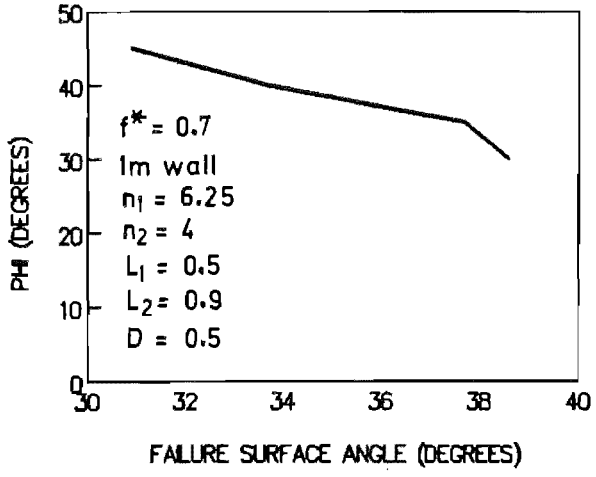

Fig. 6.128. Effect of ø on the failure surface angle α.

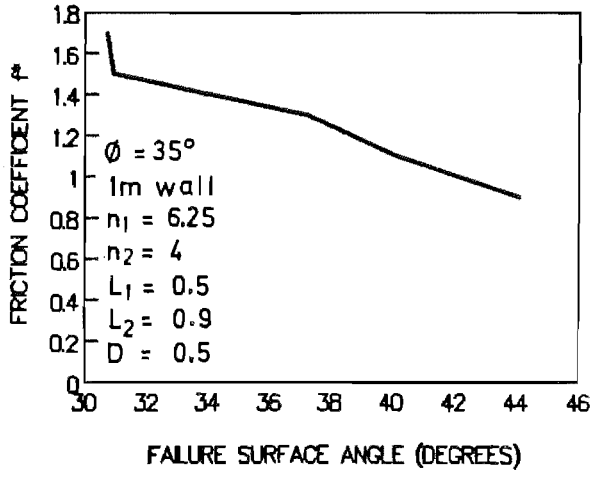

Fig. 6.129. Effect of the friction coefficient f* on α.

Fig. 6.130 shows the effect of the ratio of lengths in the top and bottom steps of a stepped block structure, together with where in the structure the step is. In this figure the steps have the same strip horizontal spacing. Fig. 6.131 shows the same effect, but with 1.56 times as many strips in the

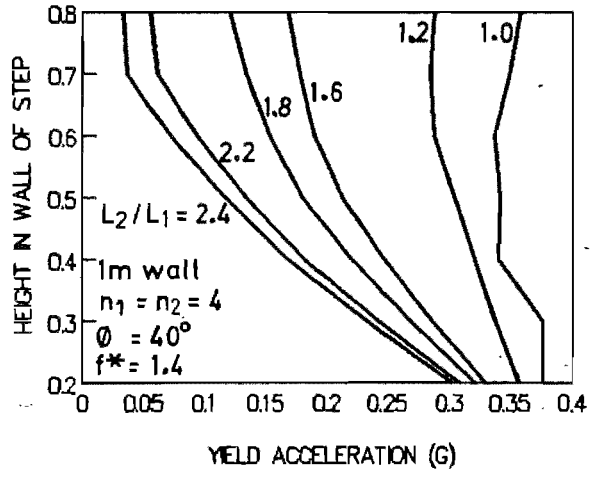

Fig. 6.130. Effect of ratio of strip lengths in two-step block.

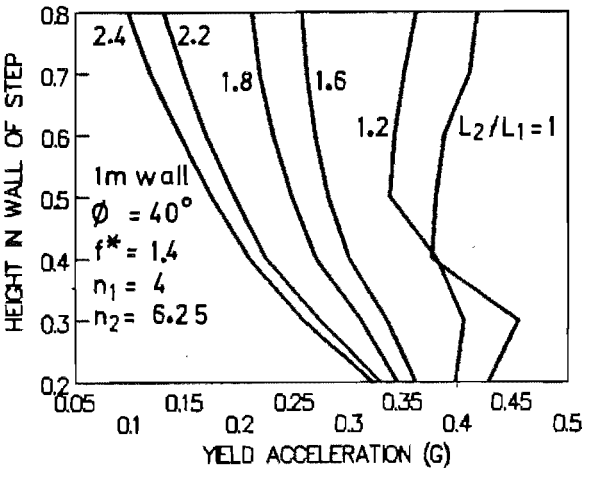

Fig. 6.131. Effect of ratio of strip lengths in two-step structure when shorter strips are closer together.

shorter bottom step as are in the top step. Both these figures show that the longer the bottom strips are (ie. the lower the L2/L1 ratio), the higher the yield acceleration. Thus it is better to provide more strips at a longer length than to shorten the bottom strips too much to prevent the strip forces from becoming excessive. The yield acceleration can also be seen to be slightly larger for the second figure, where there are more short strips per metre length of wall in the bottom step than there are long ones in the top step.

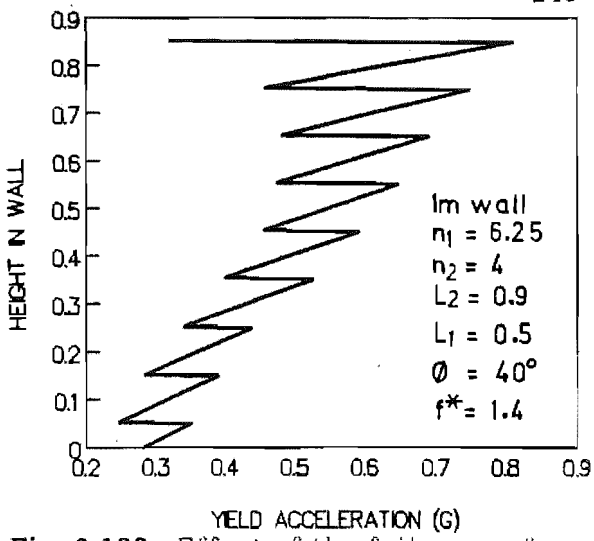

Fig. 6.132. Effect of the failure surface outcrop position at the facing.

Fig. 6.132 shows how the yield acceleration varies with the position of the outcrop of the failure surface at the facing. The saw-tooth shape arises because as the outcrop position rises past a strip, there is a rapid decrease in yield acceleration. We might intuitively expect this because there is, just above a strip, a height of soil up to the next level of strips with no reinforcing, which decreases as we move up towards that layer. The figure shows clearly that the minimum value of k_h occurs when the outcrop is just above the bottom strip. Thus we would expect the failure surface to form there: this is what was observed in 5 of the 6 tests. Test 2 was somehow different: the failure surface outcropped at about the level of the second strip up. It is not clear why wall 2 should behave differently to the other walls.

Bracegirdle (1979) also did an analysis of the effect of the position at which the failure surface met the facing. Instead of the yield acceleration being a little greater near the surface than at the base, as in Fig. 6.132, he in fact derived a lower yield acceleration near the top of the wall than at the base. He concluded that a failure near the top would occur first, resulting in a higher yield acceleration in that area. Failure of the wall overall would then occur from the base. Bracegirdle did not state how the failure near the top would occur: the implication is that the top portion of the wall would tilt outwards. Such failures were not seen in any of the walls tested here, nor in any of Nagel's (1985) testing. Indeed, it is difficult to see how this could occur, especially in the light of the observation that the structures seem to vibrate about the base, like a single degree of freedom oscillator. Fig. 6.132 terminates at just above the 150mm depth as the algorithm becomes unstable above that level. All calculations for this section were done using the computer program written to find the roots (k_h and the corresponding α) of Eq. 4.26 (and others for cases 1 to 3, Fig. 4.3, where necessary), the general equations for a two-step reinforced block structure.

6.11.2. Sensitivity of parameters as it affects a full scale wall.

In this section a full scale wall is checked. The wall is 12m. tall, with 10m. reinforcing strips. With the standard concrete facing panels, the vertical strip spacing is 750mm while the horizontal spacing is either 500 or 750mm (within a panel) and either 526 or 774mm between adjacent panels, giving an average n value (number of strips per lineal metre of wall) of either 1.96 or 1.32.

Fig. 6.133 shows the effect of the soil friction angle on the yield acceleration and the failure surface angle, for n=1.32. Recall that n is the number of strips per lineal metre of wall, in a layer of strips. It appears there that an increase in the value of ϕ results in an increase in the yield acceleration k_h, with a smaller change in the failure surface angle α. For example, for an increase in ϕ from 25° to 45° there is an increase in k_h from 0.16g to 0.56g, while α increases from 16.6° to 24.6° (taken from the minimum value of k_h on each curve. Also shown on Fig. 6.133 is a line for one value of ϕ at n=1.96. The effect of using the larger n is a small increase in k_h (from 0.36g to 0.41g), but a large decrease in α from 20.6° to 10.9°. The other point to note in Fig. 6.133 is that the failure surface angle is somewhat flatter than that seen in the model tests.

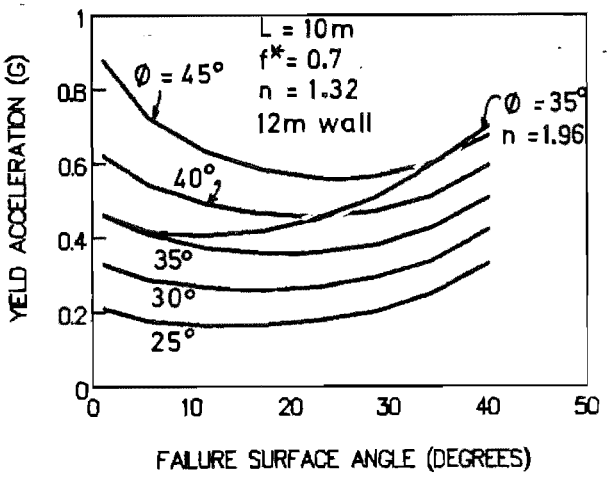

Fig. 6.133. The effect of the soil friction angle on the predicted yield acceleration and failure surface angle. A line for n=1.96 is also shown.

Fig. 6.134 shows the sensitivity of the formulation to the friction coefficient f*. If f* is 28% greater than expected (0.9 rather than 0.7), the yield acceleration will be only a little greater (0.39g vs. 0.36g) but the failure surface will be much flatter than predicted - 12.6° instead of 20.6°. f* being 28% less (0.5) than thought (0.7) causes a drop in k_h to 0.3g but an increase in α to 27.5°. To see more clearly what happens to the minimum-point in the curves as f* changes, Figs. 6.135 and 136 show k_h and α plotted

against f*. Clearly, the effect of f* on k_h reduces as f* increases, but there is only a slight falloff in effect of f* on α as f* rises.

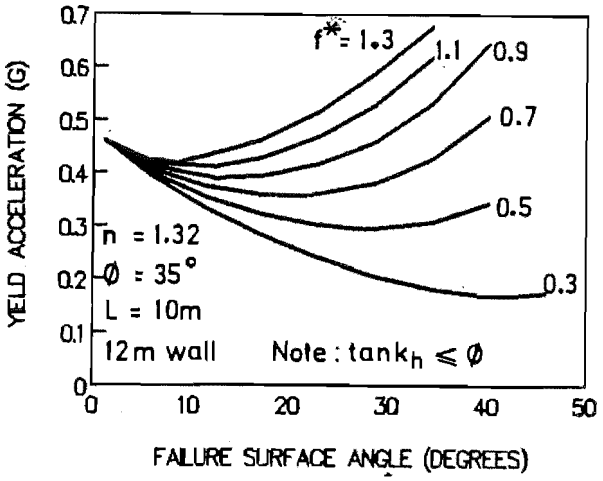

Fig. 6.134. Effect of soil-strip friction coefficient on the predicted yield acceleration and failure surface angle.

At this point we should compare the effects of ø and f* for model and full scale walls. In models, ø has very little effect on α, whereas at full scale there is somewhat more effect. ø in both cases has a marked effect on the yield acceleration predicted. Thus by carefully selecting the backfill, and compacting it well, the seismic resistance of a wall can be greatly enhanced. f* seems to have little effect on k_h in full size walls, as in model walls, although if f* is less than expected there is slightly more effect on k_h than when it is larger than expected.

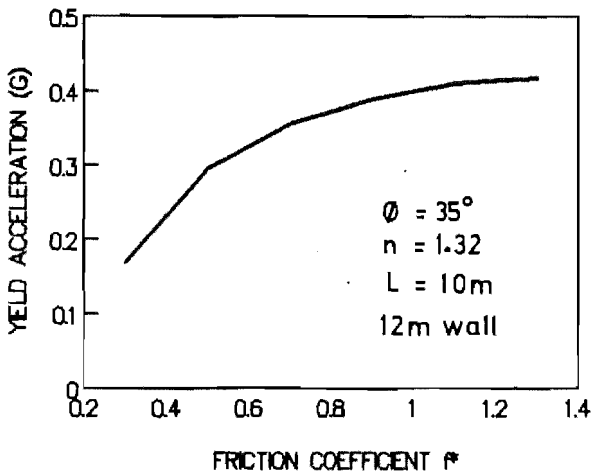

Fig. 6.135. Effect of soil-strip friction coefficient f* on yield acceleration k_h.

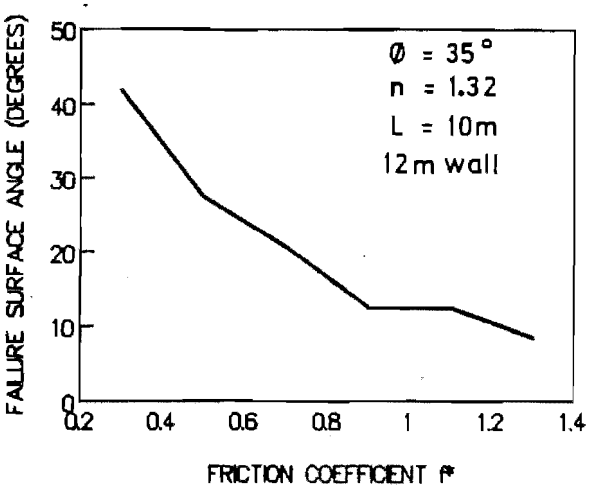

Fig. 6.136. Effect of friction coefficient f* on failure surface angle α.

The other aspect is that the failure surface is generally much flatter in full size walls, and as ø and f* increase it becomes even flatter. The result of this is that the strip forces may be relatively larger with less strips passing through the failure surface. Alternatively, as the failure surface becomes flatter, the wall is behaving more like a gravity wall sliding horizontally on its base, and a very simple analysis of the type proposed by

Elms and Richards (1979) (Richards and Elms (1979) is similar) may be done as a rough first approach, if required, in seismic design.

Fig. 6.137 shows the effect of strip length on the yield acceleration and failure surface angle. The same pattern as before is evident: stronger walls (with longer strips) have a higher yield acceleration with a flatter failure surface. The shortest length tested (8m.) is only 2/3 of wall height, and is becoming too short for adequate long term static stability: the Reinforced Earth Company (static) design rules state that the strips should be longer than 0.7 times the wall height (Boyd, 1985; see also Fig. 3.1).

Fig. 6.138 shows how the yield acceleration changes as the position at which the failure surface intersects the facing moves higher up the wall. Values plotted are those derived for when the failure surface outcrops just

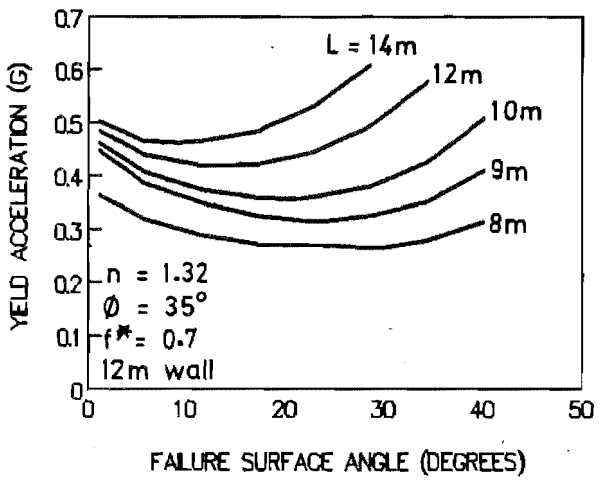

Fig. 6.137. Effect of strip length on k_h and α.

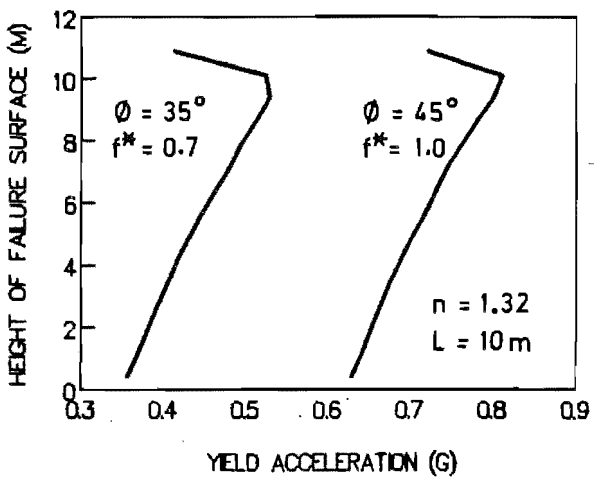

Fig. 6.138. Height at which the failure surface meets the facing vs. yield acceleration for two values of ϕ.

above a layer of strips, thus removing the sawtooth effect seen in Fig. 6.132 for the model-scale walls. Again, however, the yield acceleration predicted increases for surfaces outcropping higher in the facing. The minimum value of k_h derived is for when the failure surface outcrops just above the lowest strip layer, so we would expect the failure surface to form there. This is what was observed in the model tests, with the exception of wall two where the outcrop position was nearer the second level of strips. The apparently different behaviour of wall two is even more difficult to explain in the light of these calculations.

The odd point is, what causes the reduction in yield acceleration predicted for when the failure surface meets the facing near the top of the wall? Possibly the reason is that when the failure surface outcrops just above the second strip down (which is where the plot finishes), only one strip layer (the highest) is included in the model as contributing to the strength of the sliding block. In fact, the second strip layer is still holding the top of the second level and bottom of the top level of facing panels, which restrain the toe of the sliding block, and thus a significant portion of the resisting force holding the sliding block up is not accounted for in the model when it is applied at that level. As the outcrop position of the failure surface moves down the face, the proportion of the resisting force excluded from the calculation reduces, as more strip layers traverse the failure surface. The limit is reached when either the bottom of the wall is reached (contained failure surface, Fig. 4.1) or the failure surface first exits at the back of the reinforced block (the not contained case, Fig. 4.2).

Fig. 6.139 shows how the position of a step in length of the strips affects the yield acceleration. Generally, when the change in strip length is near the surface (height / wall height = 0.8), the yield acceleration is less than is predicted when the step is nearer the base (height / wall height = 0.2). Obviously, shorter strips have a lower resistance capacity with the shorter resistant length over which soil-strip friction can be mobilised. The main reason for using short strips near the base of a wall is to limit the strip forces and so ensure there is little chance of strip breakage leading to catastrophic collapse of the wall.

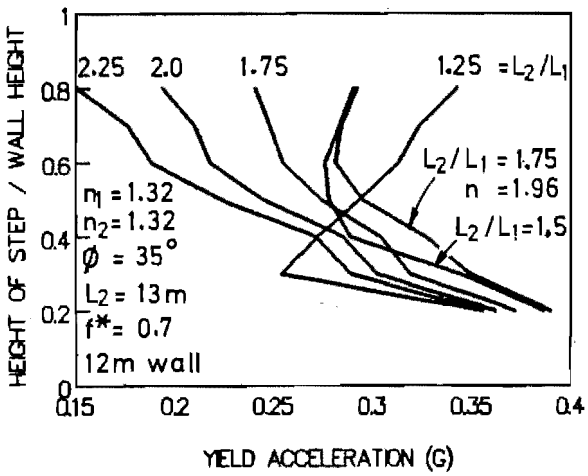

Fig. 6.139. Effect of the position of a step in strip length on the yield acceleration.

The second observation about Fig. 6.139 is that when the top step of the block is not significantly longer than the lower step, the yield acceleration may actually reduce as the position of the step moves down in the

structure. In this case, the small additional length of strip in the top part of the structure serves only to increase the inertial mass of the block without giving much increase in resistance to movement. For the blocks with the top strips much longer (1.75 times or more) than the lower strips, deepening the block of longer strips contributes immediately to increased strength of the structure.

Also shown on Fig. 6.139 is a line for when the number of strips per metre of wall is greater in the bottom (shorter) step. The effect of having more strips in the lower step is to effectively increase the importance of the lower strips in resisting the shaking, because when the step is moved down from near the surface the yield acceleration initially reduces, like it does when the top step is only a little longer than the bottom. Also, of course, having more strips in the critical bottom portion of the structure leads to an increase in yield acceleration.

6.11.3. Conclusions on sensitivity to parameters.

The parameter most important to the seismic strength of RE walls is the soil friction angle ϕ, followed by the related soil-strip friction coefficient f*. While ϕ affects the yield acceleration k_h more than the failure surface angle α, f* affects both, although the effect on k_h decreases as f* increases. The number of strips per metre length of wall, n, has a marked effect on α, causing a reduction in α as n increases, though much less effect on k_h - there is a small increase in k_h as n increases. Reinforcing strip length has some effect on k_h, and perhaps a little more effect on α: longer strips cause an increase in k_h and a reduction in α. In stepped block structures, when the longer strips (uppermost in the reinforced block) are significantly longer than the shorter strips (more than 1.5 times), lowering the height of the step in the wall causes a strong increase in k_h, due to the increased resistance to sliding available. When the longer strips are 1.5 times, or less, as long as the shorter strips, lowering the height of the step in fact causes a reduction in k_h: there appears to be little increase in resistance, but a more important increase in the inertial mass of the sliding block.

CHAPTER 7

CONCLUSIONS

7.1. Conclusions of the study.

Current design methods for reinforced earth walls in seismic situations are essentially working stress methods, and attempt to ensure there is no movement of the wall during an earthquake. An important characteristic of reinforced earth, however, is its flexibility, and a suitable design approach should make use of this flexibility to develop "ductility" during seismic events. "Ductility" in this context is intended to mean the ability of the structure to develop plastic deformations without collapse. Shaking tests on model walls, reported here, have shown that a reinforced earth wall will remain upright and move outward a calculable amount during seismic shaking. Movement occurs when the ground acceleration exceeds a yield acceleration. A limiting equilibrium formulation can be used to calculate the critical yield acceleration of a wall. Then the yield acceleration can be used in a method to calculate the expected displacement, and the wall detailed to allow for this movement. The reverse process could also be used: from a chosen maximum allowable displacement, a yield acceleration can be derived, and the limiting equilibrium formulation used to determine the number and length of reinforcing strips necessary to achieve the yield acceleration.

While maximum acceleration expected to be experienced by the wall in the inward direction (causing outward displacement) is near the yield acceleration, the ground accelerations in the opposite direction may be magnified 3 or more times at the wall top. The magnification decreases as the acceleration level increases. Thus accelerations at the wall top may be quite severe, and any structures or equipment founded on the fill surface near the wall must be detailed for this enhanced level of shaking.

As regards the internal design of the wall, some changes are recommended to the current practices. The peak coefficient of strip-soil friction derived from sliding shear tests can be used in design for seismic situations. An earth pressure coefficient based on the Mononobe-Okabe dynamic active earth pressure coefficient, K_{AE}, is recommended to calculate seismic strip forces, which are then added algebraically to static strip forces in seismic load cases. The present MWD earth pressure coefficient (MWD, 1980) was found to be very conservative near the top of the model walls and very unconservative near the base. Note that ultimate seismic reinforcing strip forces may be 6 or more times greater than static construction forces, with the greatest increases in the lowest third of the wall. Thus reduction in length of the lower strips (to lessen reinforcement forces and prevent strip breakage) has an adverse effect on the yield acceleration of RE walls, and a sensitivity analysis of the limiting equilibrium formulation showed that using more short strips has little beneficial effect on the yield acceleration.

The practice of ignoring the thickness dimension of the strips, and the distance of the shear surface away from the strips during strip pullout, may produce misleadingly high values (by some 25% or more) for the friction coefficient in back-calculations from measured forces. This explains, to some extent, the derivation of apparent friction coefficients that are greater than tan ϕ, ϕ being the angle of internal friction of the soil.

It is felt that the design of RE walls in seismic areas can be undertaken with more confidence as a result of the findings reported here. There is some certainty that the strip forces have an upper bound, and that a wall will not collapse if the strips do not break. It has also been demonstrated that the soil-strip friction coefficient is bounded during seismic shaking. The displacement findings show that deformations are calculable. Others have proposed earth pressure formulations, but it is felt that one related to the strength of the wall through the yield acceleration is more suited to the flexible nature of RE walls.

Specific conclusions, from which the above generalised comments were drawn, are itemised below.

i. Strip forces and the friction coefficient:

i.1. Seismic shaking and permanent displacement of RE walls cause quite dramatic increases in the forces in the reinforcing strips. This is especially so in the first shaking, when the fill settles, slack is taken up in the strip-facing connections, and the soil-strip and soil internal friction are mobilised. Strips in the lowest third of the wall have the largest increases and thus take most of the additional load imposed by displacement of the wall. The lowest strip ceased to increase before "failure" (failure is defined as when the failure surface first outcrops at the fill surface) because the burial soil in front of the lowest facing panel prevented that panel's outward movement.

i.2. Transient strip forces may be significantly larger than residual (end of shaking) forces. Thus they should govern in reinforcing strip design for RE walls.

i.3. Maximum post-failure strip forces may be 6 or more times greater than the construction forces, especially in the critical lower strips, and 4 or 5 times greater at failure.

i.4. With shaking, the maximum force position in the strips tends to move toward, and often meet, the wall facing in the lowest 40% of the wall. Above this level, the forces show a general increase, with little movement of the maximum along the strips. Strip forces being maximum at the facing means that the predominant action of the strips is that of anchoring the facing.

i.5. In stepped block structures, the forces are greatest in the lowest 2 strips. In rectangular block structures, the forces are greatest in the second and third strips from the bottom. In stepped blocks, the forces in the shorter strips in the lowest half of the walls were significantly lower than in the rectangular block walls, as expected.

i.6. Strip forces at the failure surface are fairly constant in stepped block structures, except for the run during which failure occurs,

when they are greater. In rectangular blocks, the forces generally increase with continuing shaking, sometimes with a reduction after failure followed by further increases from the reduced value with continuing shaking.

i.7. There is a marked increase in the apparent mobilised soil-strip friction coefficient, f^*, as the failure surface becomes fully formed, both at the facing and at the failure surface. f^* is usually smallest around mid-height of the wall. Rectangular block walls have greater variability of f^*, at any particular strip level, from run to run than stepped block walls. After failure f^* still generally increased in the lower part of the walls.

i.8. The apparent mobilised friction was greater in the resistant than in the active zone. This is the opposite of the static case, and implies that the strips pulling out of the resistant zone involve more displacement, and hence greater mobilised friction, than arises from the overall deformation within the active block.

i.9. Peak sliding shear f^* values were close to the observed f^*, though a little low. The size of the strip-soil shear surface assumed in the calculation greatly affects the value of f^* derived. By assuming that shear took place 2 average grain diameters away from the surface of the reinforcing, and including the thickness of the reinforcing in the shear surface, the f^* value derived was quite close to the peak sliding shear f^* value.

i.10. f^* values determined from pullout tests were somewhat higher than sliding shear values, and quite variable. The sliding shear test f^* values were much less variable than the pullout test results. Sliding shear f^* values were a little higher than tan ϕ, though the exact difference depends on the position assumed for the shear surface (see i.9 above). Previous researchers have found that f^* approaches tan ϕ at high confining stresses.

ii. Soil internal friction angle, ø.

ii.1. The average mobilised soil friction, ø, decreases during seismic excitation, although the rate of decrease is much less after failure. While the failure surface is forming, we might expect the soil friction mobilised at each point on the growing surface to reach peak strength, and then reduce towards the residual value after the failure surface has formed in that region. Thus as the failure surface grows, we would expect the average mobilised ø to decrease, until at failure the sand along the entire failure surface is close to its residual strength. Further small reductions in the average mobilised ø occur as the active block strains. Mobilised ø was slightly larger at the end of the tests of stepped block structures than for the rectangular block walls.

iii. The earth pressure coefficient, characterised by dimensionless tension, T*.

iii.1. Dimensionless tension, T*, a pseudo-earth pressure coefficient, is calculated assuming that the force in a strip is derived entirely from an earth pressure on the area of facing around the strip. T' behaved similarly to f*: it was smallest around mid-height of the walls, and greater at the bottom and top. Walls with the largest yield acceleration had the largest T* as well, which is the opposite of Richardson's (1978) observation that there was an increase in earth pressure with a decrease in wall stiffness.

iii.2. For calculation of design strip forces, a bounding line for seismic earth pressure is proposed, based on the Mononobe-Okabe dynamic earth pressure K_{AE}. The line runs from $1.3K_{AE}$ at the wall top to $2.6K_{AE}$ at the base. More information is needed, however, to see how T* behaves at higher (full size) stresses. This upper bound for the seismic earth pressure is applied to dynamic forces only; total forces must be calculated by adding seismic forces to static forces calculated using the present K_0 and K_a earth pressure rule. A relationship based on K_{AE} seems ideal for seismic earth pressure because one of the parameters in K_{AE} is an acceleration, for which the yield acceleration (see below) should be used.

iv. The yield acceleration k_h, and failure geometry.

iv.1. A RE wall will not collapse during an earthquake if the reinforcing strips do not break. The structure will actually deform in a "ductile" manner, a block consisting of part of the wall and reinforced block, and sometimes a retained wedge behind the block, moving outwards while the facing remains more or less vertical.

iv.2. During outward displacement of a RE wall, there is slight bulging around mid-height. However, wall mid-height displacements are not significantly greater than those of the wall top.

iv.3. There is severe deformation where the failure surface meets the wall facing ie. at the base of the sliding block. It is felt that parts of the current concrete facing panels will crush as one level of panels attempts to rotate outwards, hinging on the level below. Interlock between the cruciform panels may also restrain the rotation, perhaps causing cracking of the panels. Improved detailing of the joints between panels is necessary. Alternatively, it may be better to provide a platform near the wall base (perhaps on the fill surface in front of the wall) for the facing to slide on, in an attempt to prevent excessive damage to the panels.

iv.4. There is a yield acceleration, which is the level of excitation above which the wall will suffer permanent outward displacement. The yield acceleration is effectively the maximum acceleration that will be experienced in the inward direction, as the wall will move outward when subjected to higher ground accelerations.

iv.5. The failure surface upon which the active block moves outwards grows incrementally, from the bottom up, with continuing seismic shaking. As it does so, the yield acceleration decreases. The critical (minimum) yield acceleration is reached when the failure surface is fully formed and outcrops at the fill surface, ie. "failure" occurs. Thereafter, the yield acceleration is more or less constant.

iv.6. There is severe oscillatory motion at the wall top during seismic shaking. Outward accelerations are magnified 3 or more times, while

the maximum inward accelerations are more or less limited at the yield acceleration. Furniture and structures on the fill surface must be suitably detailed for this strong shaking. Amplification at the wall top is about twice that at mid-height, implying that the structure is oscillating (rotating) about the base.

iv.7. A limiting equilibrium formulation can be used to calculate the yield acceleration, the calculated level being the critical (minimum) yield acceleration. Also derived by the calculation is the angle the failure surface makes with the horizontal. Observed values of the yield acceleration and failure surface angle were predicted satisfactorily, within the limits of variation of the observations. Thus the assumption of a planar (or multi-planar) failure surface in the limiting equilibrium formulation is satisfactory. Observed failure surfaces were actually slightly curved, concave upward. The top part of the failure surface (when behind the reinforced block) is generally a little flatter then the Mononobe-Okabe theory predicts.

iv.8. The calculated yield acceleration is a minimum when the failure surface meets the facing just above the lowest layer of strips. Thus RE walls will usually fail with the failure surface meeting the face near the base. This was observed in 5 of the 6 walls tested. In the other wall, the failure surface met the facing at about the level of the second layer of strips up from the base. The reason for this difference is not known.

iv.9. The failure surface angle with the horizontal is fairly variable between walls with similar geometries, while the yield acceleration is only a little changeable. This may be a property of small models, but it is felt that this variability reflects the real situation, although in the case of the failure surface it is relatively unimportant.

iv.10. The failure surface should be much flatter in full size walls than in the models tested here. In some situations with a nearly horizontal failure surface, the Richards and Elms (1979) approach - Elms

and Richards (1979) is similar - for gravity walls may be useful for a preliminary seismic design.

v. Displacement and its calculation.

v.1. On the first shaking, there is a relatively large initial displacement of a RE wall. This is felt to be due to the taking up of slack in strip-facing connections, settlement of the fill to some critical density, and the displacement necessary to mobilise soil-strip and soil internal friction.

v.2. The outward displacement at failure is generally about 4% of the wall height, although in one test it was 7.6%. For Nagel's (1985) wall 8 it was 5.5%. This displacement is probably related to the density and ϕ of the backfill.

v.3. Any of the 3 displacement prediction methods tested (Sarma's chart, Lin and Whitman's charts, and Newmark's chart after Franklin and Chang) could be used in design. Sarma's chart has the advantage that it can be used with a design spectrum: the two independent earthquake characteristics required are the predominant period and the maximum acceleration. Newmark's chart requires the derivation of a maximum velocity, which is a little more difficult. The Lin and Whitman method, however, is the most rational method of the three, and considers the way the displacement is built up incrementally as well as other important earthquake factors such as the duration and frequency bandwidth. It also allows an estimate of the probability of exceedence of the predicted displacement, which neither of the other methods do. For this, though, the seismicity of the site needs to be known in some detail. For everyday design of RE walls, the Lin and Whitman method is probably too complicated, although use of the charts presented makes it much easier. The Lin and Whitman method is felt to be useful for important or special structures. Otherwise, Sarma's chart seems suitable to be used for design. Note that using both Sarma's and Newmark's charts may be conservative in some situations, as both are blanket upper-bound approaches.

v.4. The displacements experienced by a wall subject to an earthquake could be used as part of the investigation of whether the wall was still safe and serviceable, when compared to those calculated using, say, Sarma's chart. Displacements predicted in design must be allowed for, in clear space in front of the structure, and also in connections with any structures founded on the fill surface or attached to it. Also, there is some differential settlement of the fill surface, especially at large displacements, which must be considered.

vi. Sensitivity of the limiting equilibrium analysis to some important parameters used in it.

vi.1. The yield acceleration is directly proportional to ϕ, whereas the effect of f^* on k_h decreases as f^* increases. Thus the backfill and its compaction have an important effect on the strength of a wall.

vi.2. Longer bottom strips provide a greater k_h. Shortening the bottom strips to reduce the forces in them has the adverse effect that it also reduces the yield acceleration of the wall. Placing more strips at the same length in the lower part of a wall has only a small effect on k_h, but does cause a somewhat flatter failure surface.

7.2. Some closing remarks, and further work required.

The limiting equilibrium formulation is meant to be a simple and quick design analysis tool. It can rapidly become very complicated, however, in the details of applying it to multiple-step reinforced block structures. Examples of stepped structures include the Mt Messenger (Yong, 1983) and Naurangi interchange (Chalk, 1985) walls, both of which consist of reinforced blocks of up to four steps.

The complications arise when considering the various cases possible for the relationship between the failure surface and the rear of the reinforced

block, similar to those shown in Fig. 4.3. Instead of using the Meyerhof theory to derive forces in trapped wedges behind the reinforced block (such as the force p in Fig. 4.4), an approximate solution may be obtained by assuming that all or part of the rear of the reinforced block is in fact sloping. Assuming that the wall acts as a coherent gravity structure, the Mononobe-Okabe equation for K_{AE} (eq. 4.13) can be used, with the inclusion of the terms necessary for slope of the rear of the wall. Eq. 4.13 is a shortened version of the M-O equation, which in full is

$$K_{AE} = \frac{\cos^2(\phi-\theta-\beta)}{\cos\theta\,\cos^2\beta\,\cos(\delta+\beta+\theta)\,\left(1+\sqrt{\left(\frac{\sin(\delta+\phi)\,\sin(\phi-\theta-i)}{\cos(\delta+\beta+\theta)\,\cos(i-\beta)}\right)}\right)^2} \quad \ldots\ldots\ldots(7.1)$$

where i is the backfill slope and β is the slope of the rear of the wall, positive when the heel of the wall is further into the fill than the top rear. ϕ is the soil friction angle and θ is $\tan^{-1}k_h$, ignoring vertical accelerations, while δ is the friction angle between the soil and the rear of the wall and would be expected to be equal to or close to ϕ.

When using a sloping rear surface for the reinforced block, the correct strip lengths could still be used in the formulation for the resistant force R (derived from Eq. 4.5).

Another difficulty, and one that still needs investigation, is the effect of sloping fill surface and a surcharge (such as a bridge abutment) on the wall. It was seen in the testing that the top of the wall experiences quite large accelerations, especially in the outward direction. The yield acceleration is assumed in the limiting equilibrium formulation to be infinite in that direction, and while no doubt it is not, it is much larger than in the other direction. In the testing reported here, the accelerations that would cause passive movement of the wall may be 3 or more times as large as the maximum in the other direction, which is nominally the yield acceleration.

A fairly cautious approach has been taken here in the derivation of bounding lines for the apparent friction coefficient f^* and the earth pressure coefficient. In both cases a curved boundary is indicated, but because of the observation that both parameters reduce from a maximum value at the surface to a relatively constant value from 6m. depth in static situations, it was

felt that a curved upper bound was not prudent at this time. Additional seismic testing needs to be done at higher stress levels (for example, using a geotechnical centrifuge) to check the nature of the bounding lines for f* and the earth pressure coefficient in full size walls. Also, it not known whether the predominant frequency of the earthquake, related to the natural frequency of the wall, has any effect on f* or the earth pressure coefficient. Further study is necessary.

In displacement prediction, Sarma's chart (Fig. 6.120) seems the simplest to use. More data points should be plotted on it, however, to verify the bounding line chosen. All three of the methods outlined in this report have been derived with calculated data points only, and thus each still needs verifying with measured test data. Such data should include as many earthquakes as possible, to see how different earthquake characteristics affect the bounding lines.

It should now be possible to produce some design charts linking the maximum allowable displacement to some measure of wall strength. This measure should be in the form of a dimensionless ratio linking the strip length and spacing, strip-soil friction coefficient and soil internal friction angle. The displacement would also be as a dimensionless ratio, probably the outward displacement divided by the clear wall height (height above the burial soil in front of the wall toe).

With the force data from the testing reported here, "smoothing" could be done to remove the doubtful zero readings, and the dynamic forces added to the "smoothed" zero readings. Interpolation of new zero readings between other apparently good readings on the same strip would be a first step, and it may be that smoothing could also be done vertically, between strips. It is felt that at the very least, this would show that the values of f^ and T^ derived for many of the upper strips are excessive, and may give a clearer indication of the value of the proposed upper bounds.

The effect of the burial depth of soil in front of the toe of RE walls is not clear. In the model tests reported here, the burial depth was a little above the lowest layer of strips. When the failure block moved outward the top of the bottom panel was bent outwards along a horizontal axis, showing

that the failure surface met the facing at or just above the lowest reinforcing strips, but the bottom of the active block was restrained by the bottom panel and the burial soil. In tall full size walls, there may be several layers of strips below this burial depth, but where the failure surface will meet the facing then is not clear. By providing a weak point, such as a platform at or near the burial fill surface for the base of the active block to slide on, it may be possible to force the failure surface to start forming at that point and thus limit damage to the facing panels in that area when movement occurs.

In model testing the reinforcing strips are much closer together than they are in full size structures. Some researchers have reported a group effect, where each strip influences its neighbours (see §6.7.2). There may be a scale effect in the model testing, where this occurs to a much greater extent than in full size structures. Whether this is so needs investigating, and the effect, if any, on the yield acceleration needs to be determined.

The fill in RE walls is assumed to be well drained. Design rules have controls on the maximum fines content in the soil. But excess pore pressures may develop in some situations, and have an effect on the strength of the wall, in particular on the mobilised soil-strip friction. With the magnified acceleration levels noted at the wall top, this could be a significant problem if the fill is not in fact well drained. Investigation is necessary to check the likelihood and effect of excess pore pressure development. With the moves seen in the literature towards the use of clay in fills (for example, Dewel, 1979 has a chapter looking at the reinforcement of clay), this is particularly relevant.

REFERENCES.

1. Aggour, M.S. and C.B. Brown (1974). The prediction of earth pressure on retaining walls due to compaction. Géotechnique 24: No. 4, 489-502.

2. Al-Hussaini, M.M. and E.B. Berry (1978). Field Experiment of Reinforced Earth Wall. Proc. Symp. on Earth Reinforcement, Pittsburgh. ASCE, 127-156.

3. Ambraseys, N.N. and S.K. Sarma (1967). The response of earth dams to strong earthquakes. Géotechnique 17: No. 3, 181-213.

4. Ang, B.G. (1985). Seismic shear strength of circular bridge piers. Report 85-5, Dept of Civil Eng., Univ. of Canterbury, Christchurch, New Zealand.

5. Antia, A.E. and R.V. Whitman (1982). Predicting relative displacement for limited-slip seismic design of gravity retaining walls with non-liquefying backfills. Res. Report R82-34, Dept of Civil Eng, Massechusetts Inst. of Technology, Cambridge, Mass.

6. Arias, A. (1970). A measure of earthquake intensity, in Seismic Design of Nuclear Power Plants, R. Hansen (ed), M.I.T. Press, Cambridge, Mass.

7. Atkinson, J.H. and P.L. Bransby (1978). The Mechanics of Soils: an Introduction to Critical State Soil Mechanics. McGraw-Hill, Maidenhead, Berkshire, England.

8. Bacot, J., M. Iltis, P. Lareal, T. Paumier and G. Sanglerat (1978). Study of the Soil-Reinforcement Friction Coefficient. Proc. Symp. on Earth Reinforcement, Pittsburgh. ASCE, 157-185.

9. Bacot, J. (1974). Etude théorique et experimentale de soutenements realises en terre armée. PhD thesis, Univ. Claude Bernard, Lyon, France.

10. Baker, W.E., P.S. Westine, and F.T. Dodge (1973). Similarity Methods in Engineering Dynamics: Theory and Practice of Scale Modelling. Hayden Book Co, Rochelle Park, New Jersey.

11. Bendat, J.S. and A.G. Piersol (1971). Random data: analysis and measurement procedures. John Wiley and Sons, New York.

12. Binder, R. (1978). Strong Motion Duration and Spectral Density Functions for a Set of 39 Earthquake Ground Motions. Seismic Safety of Buildings Internal Study Report, No. 16, Dept of Civil Eng, Massachusettes Inst. of Technology, Cambridge, Mass.

13. Boyd, M.S. (1980). Reinforced earth applications in Australia and New Zealand. 3rd Austr.-NZ Conf. on Geomech., Wellington, NZ.

14. Boyd, M.S. (1985). Reinforced Earth Bridges. Seminar Notes, Reinforced Earth Ltd, NZ.

15. Bracegirdle, A. (1979). Reinforced earth walls: Static and dynamic considerations. M.Sc. report, Imperial College, Dept of Civil Engineering, London, England.

16. Bracegirdle, A. (1980). Seismic stability of reinforced earth retaining walls. Bull. NZ Natl Soc Earthq Eng, 13(4): 347-161.

17. Bransby, P.L. and A.A. Smith (1975). Side friction in model retaining-wall experiments. J. Geotech. Eng. Div, ASCE, 101: GT7, 615-632.

18. Brent, R.P.(1973). Algorithms for minimisation without derivatives. Prentice-Hall, Englewood Cliffs, New Jersey.

19. Brigham, E.O. (1974). The fast Fourier transform. Prentice Hall, Englewood Cliffs, New Jersey.

20. California Institute of Technology (1971). Strong-motion earthquake accelerograms. Digitized and plotted data. Earthquake Engineering

Research Laboratory, Report EERL 71-50: Vol II part A- Accelerograms IIA001 through IIA020.

21. California Institute of Technology (1972). Analyses of strong motion earthquake accelerograms. Earthquake Engineering Research Laboratory, Report EERL 72-100. Vol IV Fourier Amplitude Spectra, Part A- Accelerograms IIA001 through IIA020.

22. Cole, E.R.L. (1967). The behaviour of soils in the simple shear apparatus. PhD thesis, Univ. of Cambridge, Cambridge, England.

23. Cormack, L.G. et al (1980). Reinforced earth retaining walls with specific reference to earthquake resistant design. Beca Carter Hollings and Ferner, Consulting Engineers, Auckland, NZ. Vol. 2, papers 3 and 7.

24. Elms, D.G. and R.B. Nagel (1987). Dynamic model testing of reinforced earth walls. Proc. Pacific Conf. on Earthq. Eng, Wairakei, NZ.

25. Fendall, H.D.W. (1980). Laterally loaded pile groups. Report No. 251, Dept of Civil Eng, Univ. of Auckland, Auckland.

26. Franklin, A.G. and F.K. Chang (1977). Permanent Displacements of Earth Embankments by Newmark Sliding Block Analysis. Misc. Paper S-71-17, Soils and Pavements Lab, US Army Engineer Waterways Expt Stn, Vicksburg, Miss.

27. Fukushima, S. and F. Tatsuoka (1984). Strength and deformation characteristics of saturated sand at extremely low pressures. Soils and Foundations 24: No. 4, 38-48.

28. Goldsmith, P.R. (1979). Aspects of soil-pile interaction under static loads. Report No. 212, Dept of Civil Eng, Univ. of Auckland, Auckland.

29. Guilloux, A., F. Schlosser and N.T. Long (1979). Etude du frottement sable-armature en laboratoire. Proc. Int. Conf. on Soil Reinforcement: Reinforced Earth and other Composite Soil Techniques, Paris. Vol. 1: 35-40.

30. Harris, F.J. (1978). On the use of windows for harmonic analysis with the discrete Fourier transform. Proc. IEEE, 66: 51-83.

31. Hausmann, M.R. and G.J. Ring (1980). Measurement of soil/reinforcement interaction. Proc. 3rd Austr.-NZ Conf. on Geomech, Wellington, NZ.

32. Hornbeck, D.E. (1982). Laboratory Modelling of Reinforced Earth. PhD thesis, Georgia Inst. of Technology.

33. Idriss, I.M. and H.B. Seed (1968). Seismic Response of Horizontal Soil Layers. J. Soil Mech. Found. Div, ASCE 94: SM4, 1003-1031.

34. Ingold, T.S. (1979). The effects of compaction on retaining walls. Géotechnique 29: 265-283.

35. Ingold, T.S. (1982). Reinforced Earth. Thomas Telford, London.

36. James, R.G. (1965). Stress and strain fields in sand. PhD thesis, Univ. of Cambridge, Cambridge, England.

37. Jewel, R.A. (1979). Some effects of reinforcement on the mechanical behaviour of soils. PhD thesis, Univ. of Cambridge, Cambridge, England.

38. Jewel, R.A. (1983). Pressure and Friction in Reinforced Earth. Proc. 8th Euro. Conf. on Soil Mech. and Found. Eng, Helsinki. Vol. 3: 1187-1190.

39. Johnston, R.L. (1982). Numerical methods: a software approach. John Wiley and Sons, New York.

40. Jones, C.J.F.P. (1977). Practical Design Considerations. Proc. Symp. on Reinforced Earth and other composite soil techniques, Edinburgh. TRRL Suppl. Rep. 457.

41. Jones, C.J.F.P. (1978). The York Method of Reinforced Earth Construction. Proc. ASCE Symp. on Earth Reinforcement, Pittsburgh.

42. Jones, C.J.F.P. (1985). Earth Reinforcement and Soil Structures. Butterworths, London.

43. Kerisel, J. (1967). Scaling laws in soil dynamics. Proc. 3rd Pan-American Conf. on Soil Mech. and Found. Eng, Caracas, Venezuela. Vol. III, 69-92.

44. Koivumäki, O. (1983). Friction between sand and metal. Proc. 8th Euro. Conf. on Soil Mech. and Found. Eng, Helsinki. Vol. 1: 517-520.

45. Kolbuszewski, J.J. and R.H. Jones (1961). The preparation of sand samples for laboratory testing. Proc. Midland Soil and Found. Eng. Soc. 4: 107-123.

46. Kolbuszewski, J.J. (1948). An experimental study of the maximum and minimum porosity of sands. Proc. 2nd Int. Conf. on Soil Mech. and Found. Eng, Rotterdam, Vol. 1.

47. Langhaar, H.L. (1951). Dimensional analysis and theory of models. John Wiley and Sons, New York.

48. Lee, K.L. (1978). Mechanisms, Analysis and Design of Reinforced Earth. State-of-the-art Report, Proc. Symp. on Earth Reinforcement, Pittsburgh. ASCE, 62-76.

49. Lin, J-S. and R.V. Whitman (1983). Decoupling approximation to the evaluation of earthquake-induced plastic slip in earth dams. Earthq. Eng. and Str. Dyn. 11: 667-678.

50. Lin, J-S. and R.V. Whitman (1986). Earthquake-induced displacements of sliding blocks. J. Geotech. Eng. Div, ASCE 112: GT1, 44-59.

51. Lin, J-S. (1982). Probabilistic Evaluation of Seismically-induced Permanent Displacements in Earth Dams. Sc.D. thesis, Massachusetts Inst. of Technology, Cambridge, Mass.

52. Mahmood, A., J.K. Mitchell and U. Lindblom (1976). Effect of specimen preparation method on grain arrangement and compressibility in sand. Symp. on Soil Specimen Preparation for Lab. Testing, ASTM, Special Publication STP 599.

53. Makdisi, F.I. and H.B. Seed (1978). Simplified procedure for estimating dam and embankment earthquake-induced deformations. J. Geotech. Eng. Div, ASCE 104: GT7, 849-867.

54. McKittrick, D.P. (1978). Reinforced Earth: application of theory and research to practice. Proc. Symp. on Soil Reinforcing and Stabilizing Techniques in Eng. Practice, Sydney, Australia.

55. McKittrick, D.P. (1979). Reinforced earth: application of theory and research to practice. Ground Engineering, 12(1): 19-31.

56. Meyerhof, G.G. (1953). The Bearing Capacity of Foundations under Eccentric and Inclined Loads. Proc. 3rd Int. Conf. on Soil Mech. and Found. Eng, Switzerland.

57. Mitchell, J.K. and F. Schlosser (1979). Mechanisms and Behaviour - Design Methods: General Report. Int. Conf. on Soil Reinforcement: Reinforced Earth and other Composite Soil Techniques, Paris. Vol. 3: 25-62.

58. Mulilis, J.P., H.B. Seed, C.K. Chan, J.K. Mitchell and K. Arulanandan (1977). Effects of sample preparation on sand liquefaction. J. Geotech. Eng. Div, ASCE 103: GT2, 91-108.

59. Murray, R.T., D.R. Carder and J.V. Krawczyk (1979). Pull-out tests on reinforcements embedded in uniformly graded sand subject to vibration. Proc. 7th Euro. Conf. on Soil Mech. and Found. Eng, Brighton, England. Vol.3: 115-120.

60. Murray, R.T. and M.J. Irwin (1981). A Preliminary Study of TRRL Anchored Earth. TRRL Suppl. Rep. 674.

61. MWD (1973). Retaining Wall Design Notes. NZ Ministry of Works and Development, Civil Division Publication CDP 702/C, Wellington.

62. MWD (1980). Reinforced Earth: Notes on Design and Construction. Supplement to CDP 702/C, 1973: Retaining Wall Design Notes, NZ Ministry of Works and Development, Wellington.

63. Nadim, F. and R.V. Whitman (1983). Predicting Relative Displacement for Limited-Slip Seismic-Design of Gravity Retaining Walls with Non-Liquefying Backfills. Rep. R82-33, Dept of Civil Engineering, Massachusetts Inst. of Technology, Cambridge, Mass.

64. Nagel, R.B. (1985). Seismic behaviour of reinforced earth walls. Res. Rep. 85-4, Dept of Civil Eng, Univ. of Canterbury, Christchurch, NZ.

65. Newmark, N.M., J.A. Blume and K.K. Kapro (1973). Seismic Design Spectra for Nuclear Power Plants. J. Power Div, ASCE 99: PO2, 287-303.

66. Newmark, N.M. (1965). Effects of Earthquakes on Dams and Embankments. Géotechnique 15: No. 2, 139-160.

67. Newmark, N.M. (1975). Seismic Design Criteria for Above Ground Facilities other than Pipeline and Pumpstation Buildings, Trans-Alaskan Pipeline Systems. Report to Alyeska Pipeline Service Company.

68. NZSS 4203:1984. Code of Practice for General Structural Design and Design Loadings for Buildings. Standards Assoc. of NZ.

69. Otnes, R.K. and L. Enochson (1978). Applied time series analysis: Vol. 1. Basic techniques. John Wiley and Sons, New York.

70. Ponce, V.M. and J.M. Bell (1971). Shear Strength of Sand at Extremely Low Pressures. J. Soil Mech. and Found. Div, ASCE 97: SM4, 625-638.

71. Prendergast, B.B. and G. Ramsay (1980). Design of reinforced earth for NZ conditions. Proc. 3rd Austr.-NZ Conf. on Geomech, Wellington, NZ.

72. Press, W.H., S.A. Teukolsky, W.T. Vetterling and B.P. Flannery (1985). Numerical Recipes. Cambridge Univ. Press, Cambridge, England.

73. Rea, D. and W.E. Wolfe (1980). Earthquake-induced permanent displacements in model reinforced earth walls. Proc. 7th World Conf. on Earthq. Eng, Istanbul, Turkey. Vol. 7: 273-280.

74. Richards, R. Jr. and D.G. Elms (1979). Seismic Behaviour of Gravity Retaining Walls. J. Geotech. Eng. Div, ASCE 105: GT4, 449-464.

75. Richardson, G.N. and K.L. Lee (1975). Seismic design of reinforced earth walls. J. Geotech. Eng. Div, ASCE 101: GT2, 167-188.

76. Richardson, G.N., D. Feger, A. Fong and K.L. Lee (1977). Seismic testing of reinforced earth walls. J. Geotech. Eng. Div, ASCE 103: GT1, 1-17.

77. Richardson, G.N. (1978). Earthquake resistant reinforced earth walls. Proc. Symp. on Earth Reinforcement, Pittsburgh. ASCE, 664-684.

78. Rowe, P.W. (1971). Large scale laboratory model retaining wall apparatus. Proc. Roscoe Memorial Symposium, Univ. of Cambridge, Cambridge, England.

79. Sarma, S.K. and M.V. Bhave (1974). Critical acceleration vs. static factor of safety in stability of earth dams and embankments. Géotechnique 24: No. 4, 661-665.

80. Sarma, S.K. (1975). Seismic stability of earth dams and embankments. Géotechnique 25: No. 4, 743-761.

81. Sarma, S.K. (1976). Response and stability of earth dams during strong earthquakes. Report prepared for U.S. Army Procurement Agency (Europe).

82. Sarma, S.K. (1979). Response and stability of earth dams during strong earthquakes. Misc. paper GL-79-13, Imperial College, London, England.

83. Schlosser, F. and N.T. Long (1974). Recent Results in French Research on Reinforced Earth. J. Constrn Div. ASCE 100: CO3, 223-237.

84. Schlosser, F. and V. Elias (1978). Friction in reinforced earth. Proc. Symp. on Reinforced Earth, Pittsburgh. ASCE, 735-763.

85. Schlosser, F., H.M. Jacobsen and I. Juran (1983). Soil Reinforcement: General report. Proc. 8th Euro. Conf. on Soil Mech. and Found. Eng, Helsinki.

86. Schuring, D.J. (1977). Scale modelling in engineering. Pergamon Press, Oxford, England.

87. Seed, H.B. and I.M. Idriss (1970). Soil Moduli and Damping Factors for Dynamic Response Analyses. Rep. No. EERC 70-10, Univ. of California, Berkley, Calif.

88. Seed, H.B. and J.K. Mitchell (1980) unpublished report prepared for the Reinforced Earth Company, USA, and summarised in TAI (1985).

89. Seed, H.B. and R.V. Whitman (1970). The design of earth retaining structures for dynamic loads. ASCE specialty conference: Lateral stresses in the ground and design of Earth Retaining Structures. pp. 103-147.

90. Sharma N. (1989). Refined Sliding Block Model. Master of Engineering thesis (in preparation), Univ. of Canterbury, Christchurch, New Zealand.

91. Singh, A. (1969). Investigations of pile groups under lateral and vertical loads. PhD thesis, Univ. of Jodhpur, Jodhpur, India.

92. Sirwan, K.Z. (1965). Deformation of soil specimens. PhD thesis, Univ. of Cambridge, Cambridge, England.

93. Skempton, A.W. (1954). Pore Pressure Parameters A and B. Géotechnique 4: No. 4, 143-147.

94. Smith, A.K.C. and C.P. Wroth (1978). The failure of model reinforced earth walls. Proc. Symp. on Reinforced Earth and other Composite Soil Techniques. TRRL Sup. Rep. 457, Edinburgh. 109-131.

95. Sokolovski, V.V. (1960). Statics of soil media. Butterworth Scientific Publications, London, England.

96. Sokolovski, V.V. (1965). Statics of granular media. Pergamon Press, New York.

97. Sommers, S.A. and W.E. Wolfe (1984). Earthquake induced responses of model retaining walls. Proc. 8th World Conf. on Earthq. Eng, San Francisco. Vol. III: 517-524.

98. TAI (1985). Seismic Design of Reinforced Earth Walls. Terre Armée Internationale, Informative Report No. 14.

99. Terzaghi, K. (1932). Record earth pressure testing machine. Engineering News Record, Vol. 109, No. 13: 365-369.

100. Tso, Y.H. (1988). Investigation of Soil-Reinforcement Interaction in Reinforced Earth Structures. Res. Rep. 88-5, Dept of Civil Eng., Univ. of Canterbury, Christchurch, NZ.

101. Vanmarcke, E.H. and S-S.P. Lai (1980). Strong-motion duration and RMS amplitude of earthquake records. Bul. Seism. Soc. Am. 70: No. 4, 1293-1307.

102. Vanmarcke, E.H. (1976). Structural response to earthquakes. Chapter 8 in Lomnitz C. and Rosenblueth E. (ed), Seismic Risk and Engineering Decisions. Elsevier, Amsterdam.

103. Verge, G.C. and J.B. Reid (1976). Reinforced Earth Retaining Walls in Highways. Australian Road Research 6: No. 3, 56-63.

104. Vidal, H. (1966). La terre armée. Annales Inst. Tech. du Bâtim. Suppl. vol. 19, No. 223-224. Série Matériaux 30.

105. Vidal, H. (1969a). The principle of reinforced earth. Highw. Res. Rec. No. 282, 1-16.

106. Vidal, H. (1969b). La terre armée. Annales Inst. Tech. du Bâtim. Suppl. vol. 22, No. 259-260. Série Matériaux 38.

107. Vidal, H. (1970). Reinforced earth steel retaining wall. Civil Eng, ASCE (February), 72-73.

108. Vidal, H. (1978). The Development and Future of Reinforced Earth. Proc. ASCE Symp. on Earth Reinforcement, Pittsburgh.

109. Walker, B.P. and T. Whitaker (1967). An apparatus for forming uniform beds of sand for model foundations tests. Géotechnique 17: No. 2, 161-167.

110. Wernick, E. (1978). Stress and Strains on the Surface of Anchors. Revue Française de Géotechnique, No. 3.

111. Whitman, R.V. and S. Liao (1984). Seismic Design of Gravity Retaining Walls. Proc. 8th World Conf. on Earthq. Eng, San Francisco. Vol. III: 533-540.

112. Wolfe, W.E., K.L. Lee, D. Rea and A.M. Yourman (1978). The effect of vertical motion on the seismic stability of reinforced earth walls. Proc. Symp. on Earth Reinforcement, Pittsburgh. ASCE, 856-879.

113. Wolfe, W.E. (1979). Earthquake-induced Deformations in Reinforced Earth Walls. PhD thesis, Univ. of California, Los Angeles.

114. Wood, J.H. (1982). Unpublished test proposal for reinforced earth walls, Central Laboratories, NZ Ministry of Works and Development, Lower Hutt, NZ.

115. Yourmann, A.M. (1978). Determination of Soil-Tie Friction for Reinforced Earth Structures. M.S. thesis, Univ. of California, Los Angeles.

APPENDIX A

ADDITIONAL DETAILS ON EXPERIMENTAL WORK

A.1. Sidewall friction in the containing box.

Jewel (1980) reports Bacot (1974) as saying that for a medium sand, using glass side walls on the model-containing box, the effect of side-wall friction is insignificant when the RE wall failure height / wall (box) width ratio is less than one. Bacot did static model tests, in which he was interested in the maximum failure height of walls: the walls were built higher and higher until they failed. For failure height to width ratios greater than one, stability was said to be enhanced. For example, with a ratio of three, the wall could be built up to 50% higher than would otherwise be possible. This result is of little use in the present study because it is uncertain what the static failure height of the walls is.

Bransby and Smith (1975) presented an analysis of the effects of side wall friction on model retaining wall experiments. They point out that Terzaghi (1932) said that a wall should be twice as wide as it is high to avoid edge effects. Rowe (1971) is said to have found that width/height ratios of 1.5 to 3 were acceptable, although the exact value depended on whether there was a surcharge on the wall. Rowe and Bransby (1971) are reported as finding that the coefficient of passive earth pressure may be 33% higher for narrow than for wide walls. The purpose of Bransby and Smith's paper was to develop a theoretical method of predicting the magnitude of side friction effects for different configurations.

They assumed that the friction shear forces varied linearly from one end to the other of a model wall. This is said to be likely to overestimate the effects at the mid-plane and underestimate the effects at the side planes of a model. A simple formulation based on equilibrium is derived, and solved using Sokolovski's (1960, 1965) method, which is finite differences by the method of characteristics. It is based on two assumptions: equilibrium, and that the soil is everywhere yielding according to the Mohr-Coulomb failure criterion. This method was said to be good for earth pressures, although it does not consider deformation boundary conditions. In the method, the direction of the friction force at any point is related to the direction of the major principal stress.

Calculations were done for the sand/glass case, with a coefficient of friction μ of 0.1. Preliminary computations showed "predictions broadly in line with the limited experimental data that are available." Calculations were done for active and passive failure of rough and smooth walls, with ϕ of 50° and 35° (for dense and loose sand respectively). For rough walls, the wall/sand friction angle was δ=30° and 15° (dense/loose sand, passive case), and δ=49° and 30° (dense/loose sand, active case).

The results showed marked effects in the passive case and much less effect in the active case. Table A.1 shows the worst-case results for a wall twice as high as it is wide. The K factor is the ratio of vertical stress σ_z to the mean of the horizontal stresses σ_x and σ_y. There was also the ability

Table A.1
Effect of side friction for H/W=2.0, μ=0.1, K=0.37. (Bransby and Smith, 1975)

Passive or active	ϕ, in degrees	δ, in degrees	Side friction	Increase in earth pressure coefficients as a percentage
P	50	30	Partial	63
P	50	30	Full	139
P	50	0	Full	64
P	35	15	Partial	22
P	35	15	Full	34
P	35	0	Full	39
A	50	49	Full	-14
A	50	0	Full	-13
A	35	30	Full	-11
A	35	0	Full	-11

to use partial friction on the side walls, a condition which was said to be more realistic in the passive case, by setting μ to 0.05.

Bransby and Smith then examined deformations. They say that the deformations in a soil mass will be controlled by two parameters: the displacement boundary conditions and the shape of the zero extension lines. When the deformation boundary conditions are the same, the soil deformations depend only on the shape of the zero extension lines, which in turn depend on the angle of dilation (which they assume is the same whether there is side friction or not) and on the orientation of the principal stress in the soil mass (assuming coincidence of the axes of stress and strain increment). The orientation of the principal stress is determined everywhere as part of the Sokolovski calculation, and hence they were able to compare the orientations determined when there was no friction and when there was full friction. For the worst case (dense sand (ϕ=50°), narrow (H/W=2) and rough (δ=30°) wall) there was very little difference in the shape of the failure surface predicted.

In conclusion, Bransby and Smith recommend a wall 4 times as wide as it is high for the determination of passive earth pressure coefficients, though even then 6% error is expected. They recommend the same precautions for measurement of the active pressure coefficient, even though the effects of side friction are much less significant. It is pointed out that the effects of side friction are likely to be much more significant in footing tests. For our case, with an almost smooth wall and dense sand, and a rough side wall, the data presented in the paper indicate that a wall twice as wide as it is high should give no more than 10% error in Ka determinations, and probably much less.

A.2. Sand placement.

There are three main methods of placement in sand sample preparation:

i. with tamping in layers,
ii. with vibration, and
iii. by raining through air.

Mulilis et al (1977) found, using radiographs of samples, that tamping in layers did not produce uniform deposits. Each tamped layer was found to vary in density from loose at the bottom to dense at the top. Cole (1967) also reported that tamped samples were non-uniform.

Vibration can be done in several ways. Form vibrators can be used on the outside of the container, or the whole container can be put on a shaking table. Samples can be placed in layers and vibrated after each one, or placed slowly while vibration continues, or as one layer and vibrated after placement. Also, needle-type concrete vibrators have been used. Fendall (1980) reports Singh (1969) as saying that the concrete vibrator method produced quite non-uniform samples, as there were pockets of lower density at the places of insertion of the vibrator. Kolbuszewski (1948) found that vibration can produce quite substantial variations in density in a sample. Cole (1967) reports Sirwan (1965) who also found that vibrated samples were non-uniform. Mulilis et al (1977) found that high frequency vibration (120 Hz) in layers gave relatively uniform deposits, although there was a slightly more dense layer at the surface of each vibrated layer. They put this down to the influence of the surcharge weight they had in place while vibrating. (Radiographs of the prepared sand sample were used to check uniformity.) Fendall (1980) vibrated his container at 50 Hz on a shaking table while slowly adding sand. The variation in the average density (he weighed the entire volume of sand used) was less than 2% over the tests performed. This method gives no indication of the uniformity of the sample though. Fendall commented that the vibration caused rotation of the sand within the container, indicating that the vibration was quite severe. Fendall, Mulilis et al, and Goldsmith (1979) found that vibration could produce reasonably reliable dense samples, but was not good for producing uniform loose samples.

Kolbuszewski (1948) observed that the fall height and the intensity of the raining sand stream were the two main factors affecting the density of the resulting deposit. By intensity is meant the volume rate of raining sand. Density was found to increase with decreasing intensity (same fall height), and with increasing fall height (same intensity). He also pointed out that density striations in a rained sample are the result of the leading and trailing edges of the sand stream being less intense and producing a slightly more dense layer than the middle of the stream. Radiographs show these

alternating thin layers of loose and dense material (Mulilis et al, 1977). Cole (1967) tried the method of Walker and Whitaker (1967), whereby a curtain of raining sand is drawn back and forth across a container. Radiographs of the resultant deposit showed density variations similar to what Mulilis et al found. Cole concluded that to prevent these striations, one must rain continuously over the entire area of the container at once. He then found that several (2 or 3) screens across the sand stream were necessary to obtain a truly uniform deposit.

Another aspect of the striation effect is due to segregation of the sand as it falls: the larger particles fall at a lower velocity than the small due to drag in the air, and there tends to be a layer of small particles in front of and behind the main curtain of sand during raining. Slight but definite colour striations in the sand were observed through the glass walls of Nagel's test box (1985). It is not possible to tell if the visible layers are due to density or particle size variations. The smaller particles often appear to be a slightly different colour to the larger. This was certainly the case in the sand used in the testing described in this report.

Fendall tested the effect of varying the fall height. Over a range of 300 to 700 mm. he found that there was a very small effect, if any, on the mean density of the sample. Cole (1967) reported James (1965) as finding that for heights above 300mm. minor variations in the fall height have an insignificant effect on densities achieved.

Cole (1967) reports Kolbuszewski and Jones (1961) as showing that the fall velocity is controlled by the fall height and is independent of the depth of material stored in the raining hopper.

Walker and Whitaker (1967) observed that air currents generated by the sand raining were reflected off the container end walls, causing reduced intensity, thus local increases in density and loss of uniformity in the deposit. This same effect was observed in the testing reported here (see section 5.3.3). Walker and Whitaker used a series of baffles near the end of their container, with holes in the end of the receptacle itself, to prevent the air recirculating and to bleed it out of the holder.

Several researchers, for example Mahmood et al (1976), Mulilis et al (1977), and Goldsmith (1979), have found that the placement method of a sand deposit affects the strength characteristics of the deposit, although it is also dependent on the soil.

For the purposes of the work described here, vibration is not really an option. The effects of base motion and vibration are what is to be studied, and using it to also compact the soil would defeat the whole purpose of the exercise. Tamping (including the use of vibrating plate compactors) produces quite non-uniform deposits. So there was really no choice except to use some form of sand raining. To avoid problems with strength changes due to changes in placement method, the same method must be used throughout.

It was decided to use a V-shaped trough as the hopper and tow it along above the fill area. To avoid problems of catching on the box walls, the entire mechanism was kept above the box. Raining height was kept relatively constant, except for the initial 500mm, where it reduced from 1300mm to 800mm. In this range (800mm and above) there should be very little or no effect on the density from variations in the raining height. From the time the raining height reached about 800mm, the height was increased when the hopper was refilled. It was raised 50mm, which was the increase in fill height since the last fill. There was major turbulence near the box end wall as the hopper approached it, causing a hump to form about 400mm from the wall, and increased density (lower surface) between the hump and the wall. This was thought to be far enough away from the RE block (1.4m. minimum) to have no effect on its performance. Within the RE block, turbulence only affected the raining curtain of sand when someone came into the enclosing tent, which was rare because of the dusty conditions during raining. The density striations noted by Cole, Kolbuszewski and others would have to be accepted: it was not practicable to rain over an area of 2 x 3 m. at once, and raining would have to stop every 50mm anyway to fit a panel or a layer of strips. So while the density would not be absolutely uniform, it should have been quite good within the area of the reinforced block and reasonably repeatable from test to test.

A.3. Shaking table.

Details of the shaking table design and its capabilities have been discussed by Ang (1985).

A.4. Data Logging.

As stated in section 5.13, data was captured using an IBM PC-driven data logger, called CEDACS II. Di-An Micro Systems DMS 541 and DMS 542 interface cards were fitted in the PC, and plugged into the cards were DMS 230 successive approximation analog to digital converter (A/D) and DMS 233 multiplexer modules. The DMS 230 is a bipolar 12-bit (11-bit plus sign) software programmable gain (1,2,4,8) instrumentation amplifier, feeding a high speed (20 µsecond per conversion) A/D converter, with autozero circuitry and CMOS logic control. The DMS 230 obtains data on demand, and has a settling time of 20µsec, programmed after channel switching. In the present study a gain of 1 was set. The DMS 233 has a gain of 1, and may be operated with 16 single-ended or 8 differential input channels. They are set up in single-ended mode.

Signal conditioning input and power supply boards were developed for the Department of Civil Engineering. They use an Analog Devices AD624 Precision Instrumentation Amplifier in each channel to amplify the analog inputs, with switchable gains of 1, 200, 500, and 1000. Excitation voltage can be chosen in the range of 0 to 10 volts (supplied by a Topward Electronic Instrument Co. Dual Tracking DC power supply, model TRS-4000), and can be set accurately to ±0.01V. Limited adjustment of the zero reading is available, and for additional movement resistors can be placed in parallel with the transducer. Input can be in full, half, and quarter bridge configuration. 120 Ohm dummy resistors are provided internally (temperature-compensated for and fitted on steel).

The particular settings used in the testing were:
Channels 1 to 3: accelerometers - gain 1000, excitation 4.00V.
Channels 4 and 5: potentiometers - gain 1, single-ended or half bridge configuration, excitation 10.00V.

Channels 6 to 55: strain gauges - gain 1000, full bridge, external dummies (240 Ohm, temperature-compensated for aluminium), excitation 4.00V.

Scanning is controlled by software. It allows selection of any number of channels up to the maximum of 64, and manual (one scan of all channels per keystroke) or auto scan (one keystroke to start). Scanning frequency and duration can be chosen for auto-scanning. The maximum scan rate for 55 channels is 247 Hertz (per channel), so that was the speed used most of the time. The maximum rate for 64 channels is 213 Hertz. After the completion of scanning the data is saved on a 5¼ inch diskette. Hence the duration of scanning is limited in the first instance to the memory available, and in the second (controlling) instance by the space on a disk. At 247 Hertz for 55 channels, the maximum duration is thus about 13.3 seconds. Data is stored in binary integer format (2 bytes per integer), in the range -2047 to 2048. With 11 bit resolution, this means that a step of one in the integer value corresponds to a one bit change in the binary representation of the number. A 128 byte header is added to the beginning of the file by the software, giving time and date, scan rate, the number of channels scanned, the channel numbers scanned, and a 55 character comment.

There is also the capacity to have scanning started by a signal from the Apple IIe shake table driver computer, with a programmable delay between receiving and answering the signal from the Apple and starting scanning. This delay allows exclusion of the low-acceleration starting displacement ramp from the scanned data. (See section 5.12)

The captured data was troubled with noise (see section 6.1). In tests 1 to 3 the strips on which the dummy strain gauges where attached were hung on a rack near the input boards. Comments were made afterwards that they would have acted like radio aerials and picked up noise from ambient electro-magnetic signals. In tests 4 to 6 they were hung inside an earthed steel tube. Strain gauge wires in tests 1 to 3 were just pulled out parallel, and also probably picked up a lot of noise. In tests 4 to 6 each pair were twisted together. The wiring loom used between the strain gauge (etc) wiring and the input boards consisted of parallel twin core wires, not twisted, and is thought to have also contributed to the noise levels.

A.5. Reinforcing strip instrumentation.

A.5.1. Strain gauge attachment and wiring.

As stated in section 5.3.6, 5 pairs of electrical resistance strain gauges were attached to each instrumented strip. The gauges were Showa N11-FA-5-120-23 ie. polyester backed, 5mm long, 120 Ohm, temperature compensated for aluminium. They were attached using a cyanoacrylate glue, Loctite 496. Terminals were 5mm, attached using the same glue. Each pair was placed at the same distance from the RE wall end of the strip, one on top and the other on the underside of the strip. The gauges in a pair were bridged together by joining one terminal of each gauge with a wire loop. Thus each pair had only two wires to run to the data logger. In this configuration only the mean extension or shortening in that area of the strip could be logged. After attachment of wires, the gauges and terminals were coated with 4 to 6 coats of Shinkok SN/4 strain gauge coating cement for protection. Sand was applied once the cement had dried completely.

Quite small wires (0.1mm^2) were connected to the strain gauge terminals. Small wires were used to minimise their effect on the strength of the fill. This was in addition to the zigzagging technique used in laying them out in the fill (see section 5.3.6). Once the wires exited from the fill area, they were connected to larger diameter lines that were led to the data logger input boards.

Tables A.2 to A.6 show the strain gauge positions on the strips. It was intended for tests 1 to 3 that the strain gauges in the lowest 3 strips would be clustered near the likely position of the maximum forces. It was expected that the maximum forces would be near the failure surface, as is the case in static tests (McKittrick, 1978). Due to an oversight during construction of test wall 1, strips 1 and 3 were swapped (Table A.2). It turned out that the maximum forces were not in the areas expected (section 6.4.2.2) so the new strips made for tests 4 and 5 had the strain gauges evenly distributed along their length (Table A.5).

Table A.2
Gauge positions, test 1. Strips 750mm long.

Strip number	Distance of gauges from wall facing 1	2	3	4	5
10 to 4	20	170	320	470	620
3	20	120	220	380	550
2	20	250	350	450	550
1	20	250	400	550	650

Table A.3
Gauge positions, test 2. Strips 1000mm long.

Strip number	Distance of gauges from wall facing 1	2	3	4	5
10 to 4	20	200	400	600	800
3	20	300	500	700	850
2	20	250	420	580	780
1	20	120	220	400	700

Table A.4
Gauge positions, test 3. Strips 750mm long.

Strip number	Distance of gauges from wall facing 1	2	3	4	5
10 to 4	20	170	320	470	620
3	20	250	400	550	650
2	20	250	350	450	550
1	20	120	220	380	550

Table A.5
Gauge positions, tests 4 and 5. Strips 1 to 5, 500mm long, strips 6 to 10 900mm long.

Strip number	Distance of gauges from wall facing 1	2	3	4	5
10 to 6	20	200	400	600	800
5 to 1	20	100	200	300	400

Table A.6
Gauge positions, test 6. Strips 750mm long.

Strip number	Distance of gauges from wall facing 1	2	3	4	5
10 to 4	20	170	320	470	620
3	20	250	400	550	650
2	20	250	350	450	550
1	20	120	220	380	550

A.6. Calibration.

Two sets of short calibration strips were instrumented with one pair of gauges. They were for use in deriving the scale factor to convert the data logger integer readings into force values with units of Newtons. These strips were tested by clamping in a vertical orientation and hanging weights on the them. Data logger readings were taken. Fig. A.1 and A.2 show the readings against load, together with the fitted straight lines. Two sets of calibration strips were made because the strips used in the testing came from two separate sheets of aluminium. The two calibration factors derived were slightly different as well.

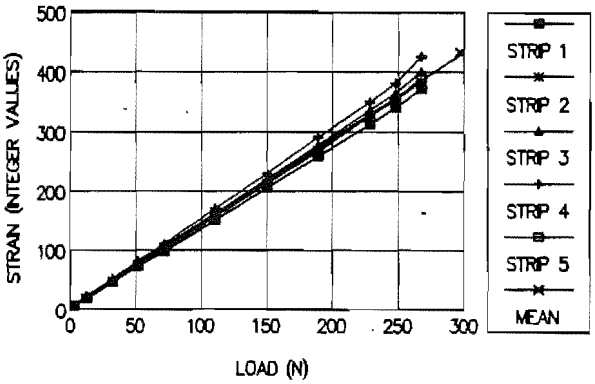

Fig. A.1 Strip calibrations, first set.

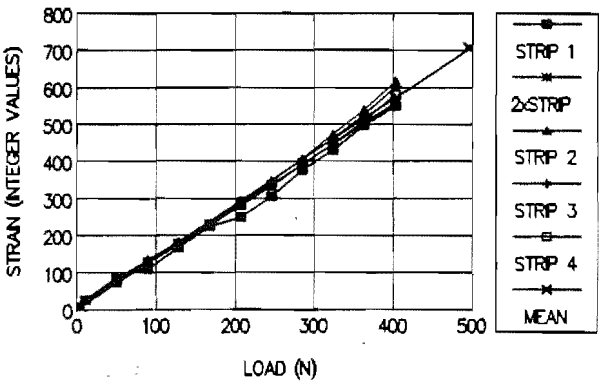

Fig. A.2 Strip calibrations, second set.

A.7. Test Excitations.

Table A.7 shows the excitations used for each run of each test. EQCV1D and FARLS2 are described in section 5.3.10.

Table A.7 (first part).
Test excitations. The failure surface outcropped at the fill surface in T1R28, T2R13.

Test and run No.	'Earthquake' excitation	Maximum acceleration (g)	Predominant frequency (Hz)
Test 1 Run 1	FARLS2	0.12 ?	2-10
Run 2	FARLS2	0.11 ?	2-10
Run 3	FARLS2	0.11 ?	2-10
Run 4	sine wave	0.2 ?	2
Run 5	sine wave	0.04	50*
Run 6	EQCV1D	0.07	2-10
Run 7	EQCV1D	0.11	2-10
Run 8	EQCV1D	0.086	2-10
Run 9	EQCV1D	0.14	2-10
Run 10	EQCV1D	0.19	"
Run 11	EQCV1D	0.23	"
Run 12	EQCV1D	0.25	"
Run 13	EQCV1D	0.31	"
Run 14	EQCV1D	0.32	"
Run 15	EQCV1D	0.34	"
Runs 16-19	EQCV1D	0.35	"
Run 20	FARLS2	0.45	"
Runs 21-24	FARLS2	0.47	"
Runs 25-29	FARLS2	0.52	"
Run 30	FARLS2	0.56	"
Run 31	FARLS2	0.47	"
Run 32	FARLS2	0.43	"
Runs 33-34	FARLS2	0.37	"
Runs 35-43	FARLS2	0.47	"
Test 2 Run 1	FARLS2	0.45	"
Run 2	FARLS2	0.4	"
Run 3	FARLS2	0.46	"
Runs 4-5	FARLS2	0.5	"
Runs 6-11	FARLS2	0.54	"
Run 12	FARLS2	0.51	"
Runs 13-15	FARLS2	0.47	"
Run 16	FARLS2	0.41	"
Runs 17-30	EQCV1D	0.36	"

*5Hz required. Shake table response not good at low acceleration levels.

Table A.7 (continued).

Test excitations. The failure surface outcropped at the fill surface in T3R12, T4R17, T5R6, and T6R3.

Test and run No.	'Earthquake' excitation	Maximum acceleration (g)	Predominant frequency (Hz)
Test 3 Runs 1-2	EQCV1D	0.19	2-10
Runs 3-4	EQCV1D	0.32	"
Run 5	EQCV1D	0.36	"
Runs 6-8	FARLS2	0.42	"
Runs 9-10	FARLS2	0.46	"
Run 11	FARLS2	0.40	"
Run 12	EQCV1D	0.33	"
Runs 13-14	EQCV1D	0.26	"
Run 15	EQCV1D	0.17	"
Runs 16-21	EQCV1D	0.14	"
Test 4 Run 1	EQCV1D	0.06	"
Run 2	EQCV1D	0.04	"
Runs 3-4	EQCV1D	0.006	"
Run 5	EQCV1D	0.18	"
Run 6	EQCV1D	0.27	"
Run 7	EQCV1D	0.29	"
Run 8	EQCV1D	0.38	"
Run 9	FARLS2	0.48	"
Run 10	FARLS2	0.50	"
Run 11	FARLS2	0.52	"
Runs 12-14	FARLS2	0.52	"
Runs 15-16	FARLS2	0.54	"
Run 17	FARLS2	0.50	"
Run 18	FARLS2	0.42	"
Run 19	EQCV1D	0.36	"
Runs 20-22	EQCV1D	0.35	"
Runs 23-26	EQCV1D	0.32	"
Test 5 Run 1	El Centro 40 NS	0.1	3-10
Run 2	El Centro 40 NS	0.42	3-10
Runs 3-4	El Centro 40 NS	0.49	3-10
Run 5	El Centro 40 NS	0.64	3-10
Run 6	El Centro 40 NS	0.90	3-10
Run 7	El Centro 40 NS	0.68	3-10
Runs 8-9	El Centro 40 NS	0.65	3-10
Test 6 Run 1	El Centro 40 NS	0.54	3-20
Run 2	El Centro 40 NS	0.62	3-20
Run 3	El Centro 40 NS	0.71	3-20
Run 4	El Centro 40 NS	0.58	3-20
Run 5	El Centro 40 NS	0.47	3-20
Runs 6-8	El Centro 40 NS	0.51	3-20

APPENDIX B

DESIGN OF TEST WALLS.

In this appendix the design of the project walls is outlined, using the Ministry of Works design method (MWD 1980).

Full wall height H = 1.00m. Embedment depth = H/12 = 0.085m. Depth y is measured from the wall top.

Vertical spacing of reinforcing strips = 0.10m. Try horizontal spacing of 0.25m.

Assume $\phi = 45°$; then $K_o = 0.293$ and $K_a = 0.172$.

Loading: - no surcharge or superimposed loads.

- assume $\rho_{sand} = 1600$ kg/m^3, then $\gamma = 15696$ N/m^3.
- assume seismic zone A:

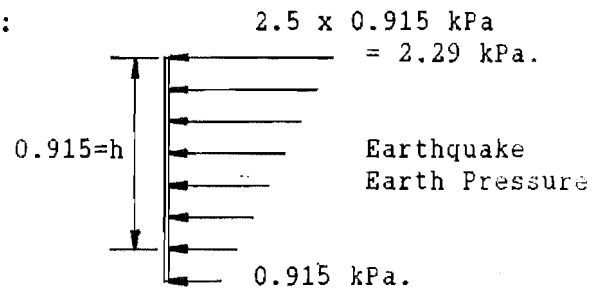

- load case to consider is Static earth pressure + Seismic earth pressure.
- depth is less than 6m. thus the static earth pressure coefficient is given by $K = K_o(1 - y/6) + K_a(y/6)$

Strip design:

Try strips 10mm wide by 0.45mm thick, made from aluminium. For aluminium, E = 7.2×10^4 MPa, and nominal yield is at 0.2% strain.

For surface treatment, glue sand onto the aluminium.

Soil/Strip friction:

The empirical relationship $f^* = 1.2 - (1.2 - \tan \phi)y/6$ is available in the absence of any pullout or other test data for the friction coefficient. Note there is a depth relationship. For y = 0.05 (top strips), this gives f' = 1.2, and for y = 0.95, $f^* = 1.17$. Tests described in section 5.4 gave a value for f^* of 0.85, but as the design was done before the tests, in this design $f^* = 1.18$ will be used.

Strip length:

The pullout force F at depth y is given by $F = \sigma_h A_t$ where $\sigma_h = K\gamma y + \Delta\sigma_h$ and A_t is the tributary area of a strip (horizontal spacing x vertical spacing). $\Delta\sigma_h$ is the lateral pressure due to superimposed or seismic loading. Then the effective length L_E of the strip is given by $L_E = F/(2by\gamma f^*)$, b being the strip width. The total strip length L is then $L = L_E + L'$, where L' is that part of the total strip length in the active zone. Active zones for static and seismic load cases were shown in Fig. 3.9. Table B.1 shows these calculations, with the static case alone, and the seismic load case including the static contributions, with L' in that case found using the seismic active zone.

Table B.1

Calculations of strip length. The seismic calculations are for load case static + seismic.

Strip No.	y (m)	Static σ_h (kPa)	Static F (N)	Seismic σ_h (kPa)	Seismic F (N)	Static L_E (m)	Static L' (m)	Static L (m)	Seismic L_E (m)	Seismic L' (m)	Seismic L (m)
10	0.05	0.228	5.7	2.449	61.2	.308	.300	0.608	3.304	.570	3.874
9	0.15	0.673	16.8	2.757	68.9	.302	.300	0.602	1.240	.510	1.750
8	0.25	1.103	27.6	3.049	76.2	.298	.300	0.598	0.823	.450	1.273
7	0.35	1.518	38.0	3.327	83.2	.293	.300	0.593	0.642	.390	1.032
6	0.45	1.919	48.0	3.590	89.8	.288	.300	0.588	0.539	.330	0.869
5	0.55	2.304	57.6	3.838	96.0	.283	.243	0.526	0.471	.270	0.741
4	0.65	2.675	66.9	4.071	101.8	.278	.189	0.467	0.423	.210	0.633
3	0.75	3.030	75.8	4.289	107.2	.273	.135	0.408	0.386	.150	0.536
2	0.85	3.371	84.3	4.492	112.3	.268	.081	0.349	0.357	.090	0.447
1	0.95	3.697	92.4	4.681	117.0	.263	.027	0.290	0.333	.030	0.363

Strip maximum forces:

The maximum tensile force in the strips can be found using $T_{max} = \sigma_h A_t$. The lateral earth pressure σ_h is given by $\sigma_h = K\sigma_v + \Delta\sigma_h$. In general the highest

forces are in either the top or bottom strips, so T_{max} only needs to be checked there.

For the top strips, $\sigma_v = \gamma y + \Delta\sigma_v$, where $\Delta\sigma_v$ is the earth pressure due to superimposed vertical loads, in this case zero. For the bottom strips, $\Delta\sigma_v = P_b$, the foundation bearing pressure, which is found using Meyerhof theory. This theory considers the block equilibrium as follows:

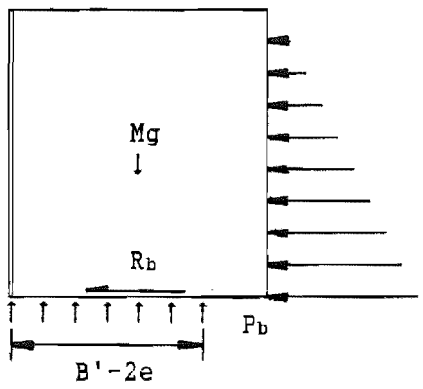

For the seismic + static load case, Mononobe-Okabe earthquake earth pressures are used. Moment equilibrium is considered for moments taken about the toe of the wall. $(B'-2e)P_b$ is equal to Mg by vertical equilibrium. Then T_{max} is checked against the factored maximum allowable load in the strips, including an allowance for corrosion. In this case there is no problem with corrosion.

For $k_h = 0.25g$, $K_{AE} = 0.30$ when wall friction δ is set to zero (the aluminium rear surface of the wall is assessed as smooth for design purposes). $B'-2e = 0.349$ for a rectangular reinforced block with 750mm long strips.

Then $P_b = 33.73$ kPa. Thus $T_{max} = 253$ N. For a 0.45x10mm strip, this corresponds to a stress of 56 MPa, or a strain of 0.00078, or 0.078%. This is 39% of nominal yield of the aluminium. Thus strips at the maximum expected force are within the "linear elastic" range of the aluminium. In fact, maximum observed forces (in test 1) were nearly twice this design maximum value, but at no time was any distress observed in the strips upon dismantling the models.

APPENDIX C.

TABULATED DATA FROM CHAPTER 6.

Tabulated in this appendix are the data from which the diagrams of mobilised friction coefficient f^* in §6.6.2 and of observed dimensionless tension T^* in §6.9 are drawn.

Table C.1
Observed forces T and mobilised friction coefficient f^* at the failure surface, test 1. Forces are in Newtons.

Strip	run 8		run 20		run 28		run 32		run 37	
	T	f^*	T	f^*	T	f^*	T	f^*	T	f^*
6	11	0.93	15	1.27	34	2.88	29	2.46	29	2.46
5	20	0.52	47	1.23	71	1.85	57	1.49	62	1.61
4	45	0.61	70	0.95	92	1.25	79	1.07	89	1.21
3	85	0.72	105	0.89	142	1.21	166	1.41	194	1.65
2	105	0.62	178	1.05	263	1.55	330	1.94	386	2.27

Table C.2
Observed forces T and mobilised friction coefficient f^* at the failure surface, test 2. Forces are in Newtons.

Strip	run 1		run 9		run 13		run 16	
	T	f^*	T	f^*	T	f^*	T	f^*
8	7	1.40	9	1.80	11	2.20	10	2.00
7	24	0.99	18	0.75	24	0.99	21	0.87
6	36	0.68	51	0.96	38	0.71	46	0.86
5	54	0.59	74	0.80	86	0.93	90	0.98
4	92	0.65	124	0.88	149	1.06	172	1.22
3	119	0.60	161	0.81	206	1.03	239	1.20
2	169	0.63	216	0.81	296	1.49	358	1.80

Table C.3
Observed forces T and mobilised friction coefficient f* at the failure surface, test 3. Forces are in Newtons.

Strip	run 1		run 10		run 12		run 16	
	T	f*	T	f*	T	f*	T	f*
7	7	0.60	27	2.30	11	0.94	-11	0.94
6	12	0.40	40	1.33	42	1.40	43	1.43
5	59	1.07	60	1.09	61	1.11	82	1.49
4	99	1.14	139	1.60	122	1.41	147	1.69
3	84	0.67	123	0.98	139	1.11	180	1.44
2	100	0.59	183	1.07	240	1.41	36	0.21

Table C.4
Observed forces T and mobilised friction coefficient f* at failure surface, test 4.

Strip	run 8		run 12		run 14		run 17		run 20		run 24	
	T	f*	T	f*	T	f*	T	f*	T	f*	T	f*
9	1	2.63	1	2.63	1	2.63	1	2.63	1	2.63	0	0
8	26	2.74	29	3.05	29	3.05	31	3.26	30	3.16	28	2.95
7	22	0.86	24	0.93	24	0.93	32	1.24	22	0.86	18	0.70
6	68	1.39	68	1.39	68	1.39	72	1.47	68	1.39	58	1.18
5	49	5.11	49	5.11	49	5.11	49	5.11	49	5.11	49	5.11
4	10	0.29	14	0.41	14	0.41	30	0.88	19	0.56	18	0.53
3	72	1.09	59	0.89	53	0.80	65	0.98	44	0.66	47	0.71
2	114	1.09	111	1.06	108	1.03	157	1.49	139	1.32	135	1.29

Table C.5
Observed forces T and mobilised friction coefficient f* at failure surface, test 5. Forces are in Newtons.

Strip	run 2		run 4		run 6		run 7		run 8		run 9	
	T	f*	T	f*	T	f*	T	f*	T	f*	T	f*
7	6	0.56	6	0.56	6	0.56	6	0.56	8	0.75	5	0.47
6	34	1.05	38	1.17	35	1.08	46	1.41	36	1.11	43	1.32
5	-		-		-		-		-		-	
4	29	1.43	22	1.08	30	1.47	28	1.38	22	1.08	15	0.74
3	68	1.24	56	1.02	82	1.49	81	1.47	68	1.24	63	1.15
2	88	0.90	81	0.83	117	1.20	118	1.21	132	1.35	49	1.52

Table C.6.
Observed forces T and mobilised friction coefficient f^ at failure surface, test 6.

Strip	run 1		run 2		run 3		run 4		run 6		run 8	
	T	f^	T	f^	T	f^	T	f^	T	f^	T	f^
7	1	0.36	3	1.08	3	1.08	3	1.08	5	1.80	6	2.15
6	14	0.66	12	0.57	21	1.00	25	1.19	53	2.52	53	2.52
5	40	0.85	40	0.85	64	1.36	36	0.77	54	1.15	46	0.98
4	83	1.03	72	0.89	141	1.75	90	1.12	123	1.53	129	1.60
3	116	0.95	130	1.07	263	2.16	215	1.77	207	1.70	263	2.16
2	198	1.16	200	1.17	297	1.74	274	1.61	192	1.12	193	1.13

Table C.7
Observed forces T and mobilised friction coefficient f^ at the facing, test 1. Forces are in Newtons.

Strip	run 8		run 20		run 28		run 32		run 37	
	T	f^	T	f^	T	f^	T	f^	T	f^
10	4	0.34	11	0.93	13	1.10	17	1.44	17	1.44
9	18	0.51	51	1.44	51	1.44	50	1.41	58	1.63
8	38	0.64	76	1.29	78	1.32	73	1.23	79	1.34
7	28	0.34	51	0.62	68	0.82	56	0.68	55	0.66
6	8	0.08	52	0.50	61	0.57	50	0.47	52	0.50
5	54	0.42	96	0.74	174	1.34	122	0.94	112	0.86
4	51	0.33	104	0.68	163	1.06	143	0.93	138	0.90
3	75	0.42	160	0.90	221	1.25	261	1.47	285	1.61
2	101	0.50	194	0.97	284	1.41	338	1.68	434	2.16
1	59	0.26	189	0.84	283	1.26	352	1.57	339	1.51

Table C.8
Observed forces T (N) and mobilised friction coefficient f^ at the facing, test 2.

Strip	run 1		run 9		run 13		run 16	
	T	f^	T	f^	T	f^	T	f^
10	1	0.06	4	0.25	-1	0.06	1	0.06
9	21	0.44	42	0.89	31	0.65	29	0.61
8	32	0.41	50	0.63	43	0.54	40	0.51
7	90	0.81	87	0.79	77	0.70	81	0.73
6	68	0.48	88	0.62	87	0.61	76	0.53
5	95	0.55	113	0.65	118	0.68	107	0.62
4	115	0.56	152	0.74	173	0.84	175	0.85
3	150	0.63	205	0.87	274	1.16	322	1.36
2	169	0.63	217	0.81	296	1.10	358	1.33
1	128	0.43	173	0.58	156	0.52	131	0.44

Table C.9
Observed forces T and mobilised friction coefficient f* at the facing, test 3. Forces are in Newtons.

Strip	run 1		run 10		run 12		run 16	
	T	f*	T	f*	T	f*	T	f*
10	-15	1.32	-25	2.21	-15	1.32	-16	1.41
9	14	0.41	34	1.00	20	0.59	13	0.38
8	18	0.32	46	0.81	42	0.74	38	0.67
7	46	0.58	78	0.98	53	0.67	55	0.69
6	58	0.57	88	0.86	66	0.64	76	0.74
5	105	0.84	123	0.99	102	0.82	120	0.96
4	110	0.75	158	1.07	124	0.84	143	0.97
3	134	0.80	237	1.39	273	1.61	240	1.41
2	105	0.54	210	1.09	277	1.44	27	0.14
1	73	0.34	142	0.66	125	0.58	141	0.65

Table C.10
Observed forces T and mobilised friction coefficient f* at the facing, test 4. Forces are in Newtons.

Strip	run 8		run 12		run 14		run 17		run 20		run 24	
	T	f*	T	f*	T	f*	T	f*	T	f*	T	f*
10	27	1.94	32	2.30	24	1.72	22	1.58	35	2.51	24	1.72
9	33	0.79	41	0.98	44	1.05	38	0.91	29	0.69	32	0.76
8	28	0.40	34	0.49	37	0.53	41	0.59	19	0.27	10	0.14
7	36	0.37	34	0.35	39	0.40	29	0.30	31	0.32	38	0.39
6	49	0.39	51	0.41	54	0.43	54	0.43	44	0.35	47	0.37
5	48	0.57	48	0.57	56	0.67	53	0.63	49	0.59	57	0.68
4	125	1.26	127	1.28	131	1.33	130	1.32	127	1.28	132	1.34
3	75	0.66	80	0.70	82	0.72	75	0.66	66	0.58	120	1.05
2	89	0.69	96	0.74	98	0.76	137	1.06	126	0.97	198	1.53
1	77	0.53	118	0.82	128	0.89	180	1.25	168	1.16	180	1.25

Table C.11
Observed forces T and mobilised friction coefficient f* at the facing, test 5. Forces are in Newtons.

Strip	run 2		run 4		run 6		run 7		run 8		run 9	
	T	f*	T	f*	T	f*	T	f*	T	f*	T	f*
10	26	1.89	30	2.18	30	2.18	12	0.87	13	0.94	24	1.74
9	?		?		?		?		?		?	
8	?		?		?		?		?		?	
7	37	0.38	41	0.43	80	0.83	52	0.54	54	0.56	61	0.63
6	50	0.40	59	0.48	104	0.84	73	0.59	69	0.56	77	0.62
5	34	0.41	35	0.42	70	0.85	49	0.59	42	0.51	47	0.57
4	110	1.13	112	1.15	143	1.46	126	1.29	116	1.19	125	1.28
3	73	0.65	75	0.67	87	0.77	127	1.13	101	0.90	91	0.81
2	118	0.92	118	0.92	181	1.42	215	1.68	231	1.81	224	1.75
1	93	0.65	126	0.88	180	1.26	170	1.19	179	1.25	190	1.33

Table C.12

Observed forces T and mobilised friction coefficient f* at the facing, test 6. Forces are in Newtons.

Strip	run 1		run 2		run 3		run 4		run 5		run 6	
	T	f*	T	f*	T	f*	T	f*	T	f*	T	f*
10	11	0.95	26	2.24	19	1.64	14	1.20	11	0.95	17	1.46
9	36	1.03	42	1.21	54	1.55	39	1.12	36	1.03	36	1.03
8	52	0.90	69	1.19	82	1.41	51	0.88	64	1.10	68	1.17
7	53	0.65	83	1.02	95	1.17	40	0.49	71	0.87	76	0.93
6	36	0.34	56	0.54	62	0.59	61	0.58	49	0.47	49	0.47
5	81	0.63	103	0.81	111	0.87	99	0.77	96	0.75	104	0.81
4	118	0.78	128	0.85	140	0.93	144	0.95	116	0.77	158	1.05
3	138	0.79	158	0.91	309	1.77	304	1.74	223	1.28	259	1.49
2	223	1.13	231	1.17	354	1.79	335	1.70	242	1.23	240	1.22
1	102	0.46	163	0.74	216	0.98	173	0.78	gauge damaged			

Table C.13.

Maximum observed forces T and mobilised friction coefficient f*, test 1. L is the length in cm. to the free end of the strip from the position of the maximum force.

Strip	run 8			run 20			run 28			run 32			run 37		
	T	L	f*	T	L	f*	T	L	f*	T	L	f*	T	L	f*
10	14	28	3.09	20	28	4.41	28	28	6.17	28	28	6.17	35	28	7.72
9	24	58	0.85	51	73	1.44	52	43	2.49	50	73	1.41	58	73	1.64
8	38	73	0.64	76	73	1.29	107	28	4.72	148	28	6.53	151	28	6.66
7	49	58	0.75	79	43	1.62	84	43	1.72	85	43	1.74	84	43	1.72
6	75	58	0.89	112	58	1.32	110	58	1.30	110	58	1.30	115	58	1.36
5	66	58	0.64	100	58	0.97	175	73	1.35	122	73	0.53	115	58	1.11
4	65	58	0.53	103	73	0.67	163	73	1.06	143	73	0.93	138	73	0.90
3	92	58	0.65	160	73	0.90	221	73	1.25	261	73	1.47	275	73	1.55
2	110	50	0.80	194	73	0.97	285	73	1.42	358	73	1.78	433	73	2.15
1	68	50	0.44	190	73	0.85	283	73	1.26	352	73	1.57	340	73	1.51

Table C.14

Maximum observed forces T (in N) and mobilised friction coefficient f*, test 2. L is the length in cm. to the free end of the strip, from the position of the maximum force.

Strip	run 1			run 9			run 13			run 16		
	T	L	f*	T	L	f*	T	L	f*	T	L	f*
10	47	20	14.6	58	20	18.0	56	20	17.4	54	20	17.8
9	26	80	0.67	44	80	1.14	35	80	0.91	37	80	0.96
8	40	80	0.62	56	80	0.87	49	80	0.76	49	80	0.76
7	92	80	1.02	105	80	1.16	93	80	1.03	104	80	1.15
6	83	80	0.71	103	80	0.89	94	80	0.81	89	80	0.77
5	95	98	0.55	113	98	0.65	118	98	0.68	112	60	1.05
4	115	98	0.56	152	98	0.74	185	80	1.10	207	80	1.24
3	150	98	0.63	205	98	0.87	274	98	1.16	322	98	1.36
2	169	98	0.63	217	98	0.81	296	98	1.10	358	98	1.33
1	136	78	0.57	173	98	0.58	155	78	0.65	131	98	0.44

Table C.15

Maximum observed forces T (in N) and mobilised friction coefficient f*, test 3. L is the length in cm. to the free end of the strip, from the position of the maximum force.

Strip	run 1			run 10			run 2			run 16		
	T	L	f*	T	L	f*	T	L	f*	T	L	f*
10	19	28	4.37	22	28	5.06	24	28	5.52	25	28	5.75
9	53	53	1.96	52	53	1.92	50	53	1.85	53	53	1.96
8	28	43	0.84	49	53	1.09	47	53	1.04	50	53	1.11
7	53	58	0.84	78	73	0.98	56	58	0.89	63	58	1.00
6	62	58	0.76	88	73	0.86	72	58	0.89	91	58	1.12
5	105	73	0.84	123	73	0.99	110	58	1.11	132	58	1.33
4	110	73	0.75	158	73	1.07	132	58	1.13	152	58	1.30
3	134	73	0.79	237	73	1.39	273	73	1.61	240	73	1.41
2	105	73	0.54	210	73	1.09	278	73	1.44	51	50	0.26
1	72	73	0.33	142	73	0.66	125	73	0.58	141	73	0.65

Table C.16

Maximum observed forces T (in N) and mobilised friction coefficient f*, test 4. L is the length in cm. to the strip free end, from the position of the maximum force.

Strip	run 8			run 12			run 14			run 17			run 20			run 24		
	T	L	f*	T	L	f*	T	L	f*	T	L	f*	T	L	f*	T	L	f*
10	46	18	16.1	56	18	19.6	50	18	17.5	57	18	20.0	57	18	20.0	38	18	13.3
9	62	72	1.81	65	72	1.90	68	72	1.99	62	72	1.81	52	72	1.52	48	72	1.40
8	74	36	2.59	71	36	2.49	77	36	2.70	76	36	2.66	73	36	2.56	71	36	2.49
7	73	54	1.22	82	54	1.37	88	54	1.47	93	54	1.55	80	54	1.34	88	54	1.47
6	123	54	1.60	120	54	1.37	122	54	1.47	116	54	1.51	108	54	1.40	104	54	1.35
5	87	10	4.99	84	10	4.82	87	30	1.66	90	10	5.16	86	10	4.93	89	10	5.10
4	125	48	1.26	127	48	1.28	131	48	1.33	130	48	1.32	127	48	1.28	132	48	1.34
3	110	40	1.16	108	40	1.14	102	40	1.07	105	40	1.10	103	40	1.08	120	48	1.05
2	115	40	1.07	112	40	1.04	109	40	1.01	159	40	1.48	140	40	1.30	198	48	1.53
1	78	40	0.65	118	48	0.82	128	48	0.89	180	48	1.25	168	48	1.16	180	48	1.25

Table C.17

Maximum observed forces T (in N) and mobilised friction coefficient f*, test 5. L is the length in cm. to the strip free end, from the position of the maximum force.

Strip	run 2			run 4			run 6			run 7			run 8			run 9		
	T	L	f*	T	L	f*	T	L	f*	T	L	f*	T	L	f*	T	L	f*
10	38	72	3.37	35	72	3.11	30	88	2.18	40	72	3.55	30	54	3.55	34	72	3.02
9	?			?			?			?			?			?		
8	?			?			?			?			?			?		
7	84	72	1.07	103	72	1.31	135	72	1.71	107	72	1.36	113	72	1.43	111	72	1.41
6	68	54	0.89	73	54	0.96	124	54	1.63	93	72	0.92	93	72	0.92	95	54	1.25
5	40	30	0.77	40	30	0.77	70	48	0.85	52	30	1.01	46	30	0.89	55	30	1.07
4	110	48	1.13	112	48	1.15	143	48	1.46	126	48	1.29	116	48	1.19	125	48	1.28
3	89	40	0.95	88	40	0.93	107	40	1.14	127	48	1.13	109	40	1.16	107	40	1.14
2	118	48	0.92	118	48	0.92	181	48	1.42	215	48	1.68	231	48	1.81	224	48	1.75
1	93	48	0.65	126	48	0.88	180	48	1.26	170	48	1.19	179	48	1.25	190	48	1.33

Table C.18

Maximum observed forces T (N) and mobilised friction coefficient f*, test 6. L is the length in cm. to the strip free end, from the position of the maximum force.

Strip	run 1			run 2			run 3			run 4			run 6			run 8		
	T	L	f*	T	L	f*	T	L	f*	T	L	f*	T	L	f*	T	L	f*
10	21	58	2.28	26	73	2.24	24	43	3.51	27	58	2.93	24	58	2.60	21	58	2.28
9	43	58	1.55	42	66	1.33	56	58	2.02	44	58	1.59	43	58	1.55	40	43	1.95
8	52	73	0.90	69	73	1.18	82	73	1.41	52	73	0.90	64	66	1.22	68	73	1.17
7	70	58	1.08	88	58	1.36	95	66	1.29	80	58	1.24	94	58	1.46	93	58	1.44
6	102	58	1.23	109	58	1.31	120	58	1.44	124	58	1.49	126	58	1.52	128	58	1.54
5	95	58	0.94	103	73	0.81	111	73	0.87	103	58	1.01	111	58	1.09	106	58	1.04
4	130	58	1.08	128	73	0.75	185	58	1.44	165	58	1.38	134	58	1.12	159	58	1.33
3	138	73	0.79	158	73	0.91	309	73	1.77	304	73	1.74	227	50	1.90	263	50	2.20
2	223	73	1.13	231	73	1.17	354	73	1.79	335	73	1.69	242	73	1.23	240	73	1.22
1	120	63	0.63	163	73	0.96	216	73	1.27	173	73	1.02	101	63	0.53	85	63	0.45

Table C.19

Observed forces T (in N) and mobilised dimensionless tension T* at the facing, test 1. g = 16196 N/m³, S_h = 0.25.

Strip	run 8		run 20		run 28		run 32		run 37	
	T	T*	T	T*	T	T*	T	T*	T	T*
10	4	0.20	11	0.54	13	0.64	17	0.84	17	0.84
9	18	0.30	51	0.84	51	0.84	50	0.82	58	0.96
8	38	0.38	76	0.75	78	0.77	73	0.72	79	0.78
7	28	0.20	51	0.36	68	0.48	56	0.40	55	0.39
6	8	0.04	52	0.29	61	0.33	50	0.27	52	0.29
5	54	0.24	96	0.43	174	0.78	122	0.55	112	0.50
4	51	0.19	104	0.40	163	0.62	143	0.54	138	0.52
3	75	0.25	160	0.53	221	0.73	261	0.86	285	0.94
2	101	0.29	194	0.56	284	0.83	338	0.98	434	1.26
1	59	0.15	189	0.49	283	0.74	352	0.92	339	0.88

Table C.20

Observed forces T (in N) and mobilised dimensionless tension T* at the facing, test 2. g = 16108 N/m³, S_h = 0.33.

Strip	run 1		run 9		run 13		run 16	
	T	T*	T	T*	T	T*	T	T*
10	1	0.04	4	0.15	-1	?	1	0.04
9	21	0.26	42	0.53	31	0.39	29	0.36
8	32	0.24	50	0.38	43	0.32	40	0.30
7	90	0.48	87	0.47	77	0.41	81	0.44
6	68	0.28	88	0.37	87	0.36	76	0.32
5	95	0.32	113	0.39	118	0.40	107	0.37
4	115	0.33	152	0.44	173	0.50	175	0.51
3	150	0.38	205	0.51	274	0.69	322	0.81
2	169	0.37	217	0.48	296	0.66	358	0.79
1	128	0.25	173	0.34	156	0.31	131	0.26

Table C.21

Observed forces T (in N) and mobilised dimensionless tension T* at the facing, test 3, $g = 15529\ N/m^3$, $S_h = 0.33$.

Strip	run 1		run 10		run 12		run 16	
	T	T*	T	T*	T	T*	T	T*
10	-15	?	-25	?	-15	?	-16	?
9	14	0.18	34	0.44	20	0.26	13	0.17
8	18	0.14	46	0.36	42	0.33	38	0.30
7	46	0.26	78	0.43	53	0.30	55	0.31
6	58	0.25	88	0.38	66	0.29	76	0.33
5	105	0.37	123	0.44	102	0.36	120	0.43
4	110	0.33	158	0.47	124	0.37	143	0.43
3	134	0.35	237	0.62	273	0.71	240	0.62
2	105	0.24	210	0.48	277	0.64	27	0.06
1	73	0.15	142	0.29	125	0.26	141	0.29

Table C.22

Observed forces T (in N) and mobilised dimensionless tension T* at the facing, test 4, $g = 15843\ N/m^3$, $S_h = 0.16$ (strips 1 to 5), and 0.25 (strips 6 to 10).

Strip	run 8		run 12		run 14		run 17		run 20		run 24	
	T	T*	T	T*	T	T*	T	T*	T	T*	T	T*
10	27	1.36	32	1.62	24	1.21	22	1.11	35	1.77	24	1.21
9	33	0.56	41	0.69	44	0.74	38	0.64	29	0.49	32	0.54
8	28	0.28	34	0.34	37	0.37	41	0.41	19	0.19	10	0.10
7	36	0.26	34	0.25	39	0.28	29	0.21	31	0.22	38	0.27
6	49	0.35	51	0.37	54	0.39	54	0.39	44	0.32	47	0.34
5	48	0.34	48	0.34	56	0.40	53	0.38	49	0.35	57	0.41
4	125	0.76	127	0.77	131	0.80	130	0.79	127	0.77	132	0.80
3	75	0.39	80	0.42	82	0.43	75	0.39	66	0.35	120	0.63
2	89	0.41	96	0.45	98	0.45	137	0.64	126	0.58	198	0.92
1	77	0.32	118	0.49	128	0.53	180	0.75	168	0.70	180	0.75

Table C.23

Observed forces T and mobilised dimensionless tension T* at the facing, test 6, $g = 15647\ N/m^3$, $S_h = 0.16$ (strips 1 to 5), and 0.25 (strips 6 to 10).

Strip	run 2		run 4		run 6		run 7		run 8		run 9	
	T	T*	T	T*	T	T*	T	T*	T	T*	T	T*
10	26	1.33	30	1.53	30	1.53	12	0.61	13	0.66	24	1.23
9	?		?		?		?		?		?	
8	?		?		?		?		?		?	
7	37	0.27	41	0.30	80	0.58	52	0.38	54	0.39	61	0.45
6	50	0.28	59	0.34	104	0.59	73	0.41	69	0.39	77	0.44
5	34	0.25	35	0.25	70	0.51	49	0.36	42	0.30	47	0.34
4	110	0.68	112	0.69	143	0.88	126	0.77	116	0.71	125	0.77
3	73	0.39	75	0.40	87	0.46	127	0.68	101	0.54	91	0.48
2	118	0.55	118	0.55	181	0.85	215	1.01	231	1.09	224	1.05
1	93	0.39	126	0.53	180	0.76	170	0.71	179	0.75	190	0.80

Table C.24

Observed forces T (in N) and mobilised dimensionless tension T* at the facing, test 6. $g = 15912\ N/m^3$, $S_h = 0.25$.

Strip	run 1		run 2		run 3		run 4		run 6		run 8	
	T	T*	T	T*	T	T*	T	T*	T	T*	T	T*
10	11	0.55	26	1.31	19	0.96	14	0.70	11	0.55	17	0.85
9	36	0.60	42	0.70	54	0.92	39	0.65	36	0.60	36	0.60
8	52	0.52	69	0.69	82	0.82	51	0.51	64	0.64	68	0.68
7	53	0.38	83	0.60	95	0.68	40	0.29	71	0.51	76	0.55
6	36	0.20	56	0.31	62	0.35	61	0.34	49	0.27	49	0.27
5	81	0.37	103	0.47	111	0.51	99	0.45	96	0.44	104	0.48
4	118	0.46	128	0.50	140	0.54	144	0.56	116	0.45	158	0.61
3	138	0.46	158	0.53	309	1.04	304	1.02	223	0.75	259	0.87
2	223	0.66	231	0.68	354	1.05	335	0.99	242	0.72	240	0.71
1	102	0.30	163	0.48	216	0.64	473	1.40	gauge damaged			

Table C.25

Observed maximum forces T (in N) and mobilised dimensionless tension T* at location of the max. forces, test 1. $g = 16196\ N/m^3$, $S_h = 0.25$.

Strip	run 8		run 20		run 28		run 32		run 37	
	T	T*	T	T*	T	T*	T	T*	T	T*
10	14	0.69	20	0.99	28	1.38	28	1.38	35	1.83
9	24	0.39	51	0.84	52	0.86	50	0.82	58	0.96
8	38	0.38	76	0.75	107	1.06	148	1.46	151	1.49
7	49	0.35	79	0.56	84	0.59	85	0.60	84	0.59
6	75	0.41	112	0.61	110	0.60	110	0.60	115	0.63
5	66	0.30	100	0.45	175	0.79	122	0.55	115	0.52
4	65	0.25	103	0.39	163	0.62	143	0.54	138	0.52
3	92	0.30	160	0.53	221	0.73	261	0.86	275	0.91
2	110	0.32	194	0.56	285	0.83	358	1.04	433	1.26
1	68	0.18	190	0.49	283	0.74	352	0.92	349	0.89

Table C.26

Observed maximum forces T (in N) and mobilised dimensionless tension T* at the location of the maximum forces, test 2. $g = 16108\ N/m^3$, $S_h = 0.33$.

Strip	run 1		run 9		run 13		run 16	
	T	T*	T	T*	T	T*	T	T*
10	47	1.77	58	2.18	56	2.11	54	2.03
9	26	0.33	44	0.55	35	0.44	37	0.46
8	40	0.30	56	0.42	49	0.37	49	0.37
7	92	0.49	105	0.56	93	0.50	104	0.56
6	83	0.35	103	0.43	94	0.39	89	0.37
5	95	0.32	113	0.39	118	0.40	112	0.38
4	115	0.33	152	0.44	185	0.54	207	0.59
3	150	0.38	205	0.51	274	0.69	322	0.81
2	169	0.37	217	0.48	296	0.66	358	0.79
1	136	0.27	173	0.34	155	0.31	131	0.26

Table C.27

Observed maximum forces T (in N) and mobilised dimensionless tension T^* at the location of the maximum, test 3. g = 15529 N/m³, S_h = 0.33.

Strip	run 1		run 10		run 12		run 16	
	T	T^*	T	T^*	T	T^*	T	T^*
10	19	0.74	22	0.86	24	0.94	25	0.98
9	53	0.69	52	0.68	50	0.65	53	0.69
8	28	0.22	49	0.38	47	0.37	50	0.39
7	53	0.30	78	0.43	56	0.31	63	0.35
6	62	0.27	88	0.38	72	0.31	91	0.39
5	105	0.37	123	0.44	110	0.39	132	0.47
4	110	0.33	158	0.47	132	0.40	152	0.46
3	134	0.35	237	0.62	273	0.71	240	0.62
2	105	0.24	210	0.48	278	0.64	51	0.12
1	72	0.15	142	0.29	125	0.26	141	0.29

Table C.28

Observed maximum forces T and mobilised dimensionless tension T^* at the maximum force, test 4. g = 15843 N/m³. S_h = 0.16 (strips 1 to 5), and 0.25 (6 to 10).

Strip	run 8		run 12		run 14		run 17		run 20		run 24	
	T	T^*	T	T^*	T	T^*	T	T^*	T	T^*	T	T^*
10	46	2.32	56	2.83	50	2.52	57	2.88	57	2.88	38	1.92
9	62	1.04	65	1.09	68	1.14	62	1.04	52	0.88	48	0.81
8	74	0.75	71	0.72	77	0.78	76	0.77	73	0.74	71	0.72
7	73	0.53	82	0.59	88	0.63	93	0.67	80	0.58	88	0.63
6	123	0.69	120	0.67	122	0.68	116	0.65	108	0.61	104	0.58
5	87	0.62	84	0.60	87	0.62	90	0.65	86	0.62	89	0.64
4	125	0.76	127	0.77	131	0.80	130	0.79	127	0.77	132	0.80
3	110	0.58	108	0.57	102	0.54	105	0.55	103	0.54	120	0.63
2	115	0.53	112	0.52	109	0.51	159	0.74	140	0.65	198	0.92
1	78	0.32	118	0.49	128	0.53	180	0.75	168	0.70	180	0.75

Table C.29

Observed maximum forces T and mobilised dimensionless tension T^* at the maximum forces, test 5. g = 15647 N/m³, S_h = 0.16 (strips 1 to 5), and 0.25 (6 to 10).

Strip	run 1		run 4		run 6		run 7		run 8		run 9	
	T	T^*	T	T^*	T	T^*	T	T^*	T	T^*	T	T^*
10	38	1.94	35	1.79	30	1.53	40	2.05	30	1.53	34	1.74
9	?		?		?		?		?		?	
8	?		?		?		?		?		?	
7	84	0.61	103	0.75	135	0.99	107	0.78	113	0.83	111	0.81
6	68	0.39	73	0.41	124	0.70	93	0.53	93	0.53	95	0.54
5	40	0.29	40	0.29	70	0.51	52	0.38	46	0.33	55	0.40
4	110	0.68	112	0.69	143	0.88	126	0.77	116	0.72	125	0.77
3	89	0.47	88	0.47	107	0.57	127	0.68	109	0.58	107	0.57
2	118	0.55	118	0.55	181	0.85	215	1.01	231	1.09	224	1.05
1	93	0.39	126	0.53	180	0.76	170	0.72	179	0.75	190	0.80

Table C.30

Observed maximum forces T (in N) and mobilised dimensionless tension T* at the location of the maximum forces, test 6. $g = 15912$ N/m³, $S_h = 0.25$.

Strip	run 1		run 2		run 3		run 4		run 6		run 8	
	T	T*	T	T*	T	T*	T	T*	T	T*	T	T*
10	21	1.06	26	1.31	24	1.21	27	1.36	24	1.21	21	1.06
9	43	0.72	42	0.70	56	0.94	44	0.74	43	0.72	40	0.67
8	52	0.87	69	1.16	82	1.37	52	0.87	64	1.07	68	1.14
7	70	0.50	88	0.63	95	0.68	80	0.57	94	0.68	93	0.67
6	102	0.57	109	0.61	120	0.67	124	0.69	126	0.70	128	0.72
5	95	0.43	103	0.47	111	0.51	103	0.47	111	0.51	106	0.48
4	130	0.50	128	0.50	185	0.72	165	0.64	134	0.52	159	0.61
3	138	0.46	158	0.53	309	1.04	304	1.02	227	0.76	263	0.88
2	223	0.66	231	0.68	354	1.05	335	0.99	242	0.72	240	0.71
1	120	0.32	163	0.43	216	0.57	173	0.46	101	0.27	85	0.22

APPENDIX D.

ON CALCULATING SPECTRAL DENSITY FUNCTIONS

D.1. Introduction.

In this appendix there is some consideration of the calculation of the spectral density function (SDF, also called power spectral density, PSD). It relates to the Lin and Whitman (1986) method of calculating the expected displacement of a sliding block. In the next section there are some comments on methods to calculated PSDs, and then there is a section about the problems caused by the necessity of dealing with finite length time histories ie. they are in effect truncated infinitely long records. Finally there is an attempt to verify the program used in this work by calculating some characteristic properties for two earthquake records and comparing the results to those published by Vanmarcke and Lai (1980).

D.2. Computation procedures.

Otnes and Enochson (1978) state that there are three usual ways to estimate power spectra:

i) frequency band averaging, which is the averaging together of neighbouring "raw" spectral estimates;

ii) ensemble averaging, which means averaging together complete power spectral functions, each computed from different segments of a time history or pair of time histories;

iii) a combination of the above two methods.

The "raw" spectral estimates can be calculated as the square of the Fourier spectral amplitudes. Press et al (1986) call such a power spectrum estimate a *periodogram* estimate, and point out that the standard deviation is always

100% of the value, independent of N, the number of points transformed. They point out that using method *i)* above (frequency band averaging), the standard deviation of the result can be reduced by a factor $1/\sqrt{K}$ where K is the number of consecutive discrete frequency values averaged. Using method *ii)* (ensemble averaging), the standard deviation of the PSD estimates can be reduced by a factor $1/\sqrt{K}$, where K this time is the number of segments into which the sampled data is partitioned. Each segment is of 2M consecutive sampled points, and the PSD is estimated at M+1 discrete frequencies with resolution 1/2MT. T is the time domain sampling interval. The second technique is, according to Press et al, computationally more efficient than the first because it is faster to do several shorter Fast Fourier transforms than to take one longer one. Otnes and Enochson state that identical results are never obtained from these two methods, but that the results should generally be equivalent if the resolution and the number of degrees of freedom (described below) are the same.

Otnes and Enochson state that PSD estimates often approximate an n-degree-of-freedom chi-square distribution, where $n = 2B_eP$. B_e is the resolution bandwidth, which for the fast Fourier transform with no averaging = 1/NT (N is the number of points transformed and T is the time domain sampling interval), and P is the record length. The effect of increasing the degrees of freedom of a PSD, for a given duration P, is to make it appear smoother because there are fewer frequency points at which the spectrum is sampled.

The subroutine SPCTRM, from Press et al, was used to estimate the PSDs required here. SPCTRM uses method *ii)* above, ensemble averaging. The data is partitioned into K segments of 2M points, each of which is FFT'd separately to produce a periodogram estimate of the PSD. The K periodogram estimates are then averaged at each frequency.

Press et al state that there is a further refinement available to reduce the variance of the PSD estimates. By overlapping the segments by one half of their length, the spectral variance can be reduced by a factor 9K/11. The reduction is not a full factor of K because the segments are not now statistically independent. With this method, the first and second sets of 2M points (overlapping by M) are said to be segment number 1; the second and

third sets of 2M points are segment number 2; and so on. This implies that there is an M-point overlap within a segment and a 2M overlap between segments. There is further discussion about this in the section on verification of the program.

The following section outlines the problems caused by truncation of the time function that is sampled.

D.3. Leakage.

Another problem that arises in Fourier transform computations is that of leakage (Brigham, 1974; Otnes and Enochson, 1978; Press et al, 1986). Brigham gives a simple graphically based description of the phenomenon, which is paraphrased below.

The Fourier transform of an infinite sampled function could be as shown in Fig. D.1(a). Next, the time function is truncated - we can only deal with finite length data arrays. The truncation is the same as multiplying by a box function as shown in Fig. D.1(b), which has the transform shown on the right hand side of Fig. D.1(b). Multiplying in the time domain is the same as convolving in the frequency domain, so truncation results in the frequency function shown in Fig. D.1(c). Next we must sample the frequency function (Fig. D.1(d)), with the resulting transform pair shown in Fig. D.1(e). It can be seen that the resultant sampled frequency spectrum of the truncated time function (e) is the same, within a scaling factor, as that of the sampled infinite continuous function (a). The inverse transform is also the same (within a scale factor)

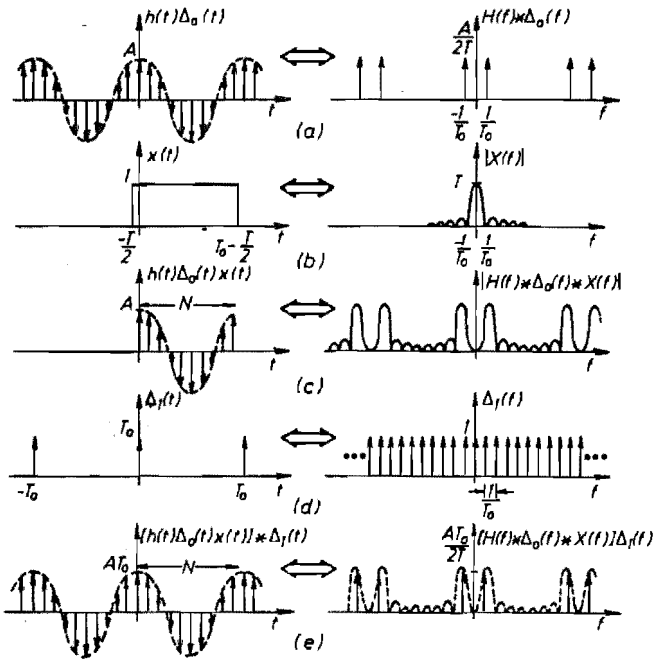

Fig. D.1 Operations in the computation of the discrete Fourier transform of a bandlimited function, truncated at an integral multiple of the period.

as the original time function. This will only occur for one class of functions, those where the truncation interval is equal to the period of the function. One further restriction should also be applied, that the time function sampled is bandlimited, with the maximum frequency component being no greater than half the sampling frequency. This removes the effects of aliasing from the transform.

We can do the same process again, with a different truncation interval. The result is shown in Fig. D.2. The sampled spectrum in (e) is now quite different: this phenomenon is called leakage, because the power that would be in the correctly sampled frequency bins has "leaked" into the adjacent bins. (A "bin" is a point at which the frequency spectrum is sampled. It is so called because it contains the power in the frequency bandwidth between points half way to the previous bin and half way to the next one.) Thus the spectrum is distorted. The inverse transform of the sampled spectrum is now different to the original time function as well, with sharp discontinuities at the truncation interval. In the spectrum, there is a component at zero frequency: this is called the dc value, and is the average value of the truncated waveform. As the truncated waveform is not an even number of cycles, we cannot expect its average value to be zero. This is the more general class of functions than when the truncation interval is equal to the period. Note that in general, time history data contains many frequency components, and it is impossible to truncate at a point that is an integer multiple of all their periods at once. Again we should state that the sampled time function is bandlimited.

D.3 shows an expanded view of the central portions of the spectra shown in D.1(e) and D.2(e). The difference between the two examples arises because the zeros of the transformed truncation function (the $\sin x/x$ function) in the second example are not coincident with each frequency sample value, as they were in the first example.

To reduce leakage, we must reduce the size of the side lobes in the transform of the time domain truncation function. It is usual to multiply, in the time domain, by a different function to the box function, one with tapering ends, although its transform can be convolved with the spectrum in the frequency domain as well. This process is called "data windowing" and the

truncation function is called a window. There are a multitude of windows in the literature, with different characteristics in the frequency domain. Harris (1978) gives a comprehensive summary of the characteristics of many windows.

In the program used here to calculate the PSD, a Parzen window was used. It is recommended for general purpose PSD calculations by Press et al. The Parzen window is triangular in shape, being zero at the ends and of height one at the midpoint. When using a window, we must scale the spectrum derived to ensure that the power contained in the time domain data is also present in the frequency domain. The scale factor used is the relationship between the squares of the area of the window used and of the box function. The assumption in doing this is that the power is evenly distributed along the time domain record, which is not the case for the El Centro 1940 North-South component used to excite the test model walls. The early stages of that earthquake are of stronger intensity than the later parts. To ensure that the power in this strong motion part of the earthquake was not lost by windowing, the last third of the record was moved to

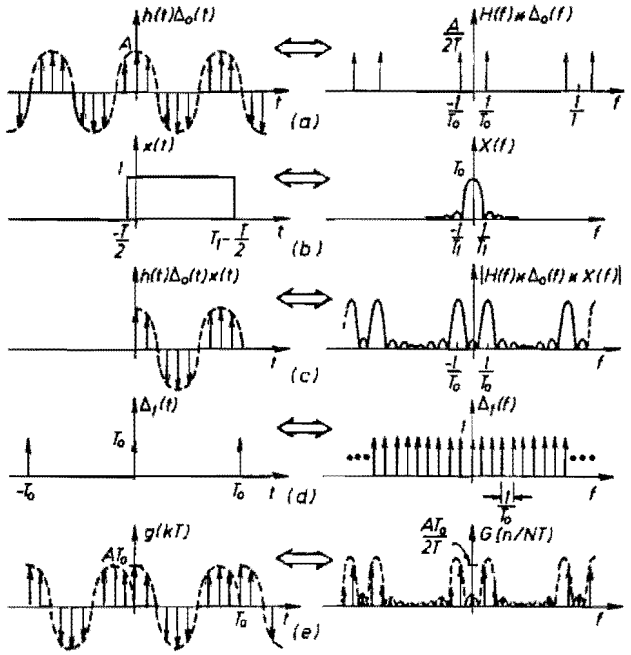

Fig. D.2 Operations in the computation of the discrete Fourier transform of a bandlimited function, *not* truncated at an integral multiple of the period.

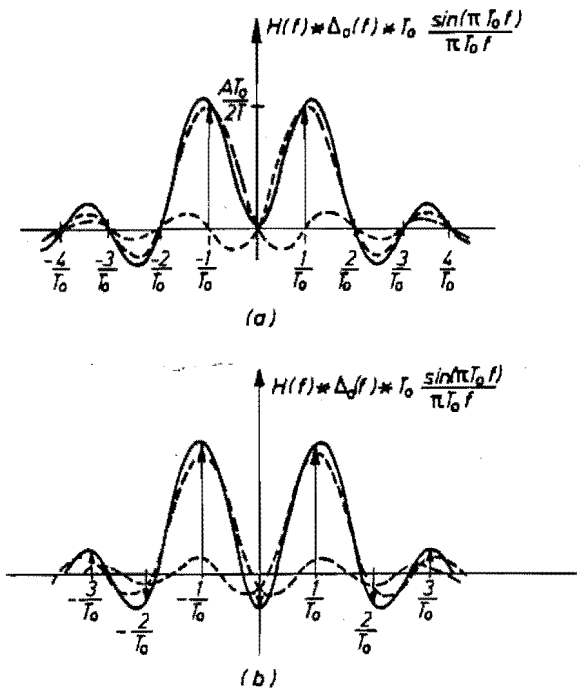

Fig. D.3 Expanded central portions of spectra of a) truncation at integer multiple of period and b) truncation interval not a multiple of period.

was moved to the beginning. This was not done in the Borrego Mountain computations (described below).

The next section describes the calculations done in an attempt to verify the program used to calculate the PSD, and to derive some of the parameters used in the Lin and Whitman (1986) method of predicting displacement of sliding blocks subject to seismic excitation.

D.4. Verification of the program.

Vanmarcke and Lai (1980), Lin (1982) and Lin and Whitman (1986) do not say anything about how they calculated the PSD, including whether they windowed the data, the number of points at which the PSD was estimated, and whether they used an averaging algorithm or not. As pointed out in Chapter 4, they also use a definition of the power that has a scale factor of π in the relationship between the time domain and the frequency domain power estimates. This will affect the value of r derived (shown in Table D.1) and hence the value derived for the root mean square acceleration σ_x. If there is unsuppressed leakage, the values of the first and second moments (Eq. 4.38) will be affected, but not the rms acceleration: the total power will still be present but distributed differently on the frequency axis. Thus the central frequency Ω and the bandwidth δ will both be affected by unsuppressed leakage, but not by the scale factor π as it will cancel out of the equations (Eq. 4.39 and 4.40).

In order to verify the PSD calculation algorithm, and to check that the program worked correctly, an attempt was made to calculate the properties of two earthquakes for which Vanmarcke and Lai (1980) had published results of their calculations. Two horizontal components of the Borrego Mountain earthquake of April 8, 1968 (California Institute of Technology number A019) were used. Results of these calculations are shown in Table D.1. In these trials, two K values were used, 2 and 4, and for K=4 Vanmarcke and Lai's approximate (see Eq. 4.47) and exact (see Eq. 4.45) formulations for calculating the strong motion duration S_0 were used. For the exact solution for S_0, a zero-finding algorithm from Brent (1973) was used to iterate with Eq. 4.45 (made homogeneous by subtracting S_0 from both sides) to the answer. Brent's algorithm is essentially a modified bisection method, where the new

Table D.1.
Earthquake properties calculated by Vanmarcke and Lai (1980) and using a PSD estimation program from Press et al (1986).

Component.	Properties					Calculation by:
	A_{max} (g)	T_o (sec)	r (*)	I_o/A_{max}^2 (sec)	S_o (sec)	
S00W	0.130	0.34	2.73	0.925	7.07	Vanmarcke and Lai
	0.130	0.54	2.55	0.925	6.00	2 segments, approx. S_o
	0.130	0.50	2.58	0.925	6.15	4 segments, approx. S_o
	0.130	0.50	2.51	0.925	5.82	4 segments, exact S_o
N90E	0.057	0.34	3.23	3.030	31.55	Vanmarcke and Lai
	0.057	0.53	2.98	3.030	26.95	2 segments, approx. S_o
	0.057	0.43	3.05	3.030	28.23	4 segments, approx. S_o
	0.057	0.43	3.14	3.030	29.87	4 segments, exact S_o

* $r = A_{max}/\sigma_x$

estimate of the root is found by interpolation rather than simple bisection. Convergence to a solution is guaranteed (a feature of the bisection method) and few iterations are usually required (the result of the interpolation modifications).

Vanmarcke and Lai did not state which version ("corrected" or uncorrected) of the CIT accelerograms they had used in their calculations. "Corrected" accelerograms were used for the calculations reported here, taken from CIT (1971). There are 4371 points in the digitized record.

For the K = 2 calculation, the segments were:

points 1 to 2048 and 1024 to 3072;

points 2048 to 4096 and 3072 to 5120.

These segments were derived after a study of the program given by Press et al. The overlaps are different to those expected from the way they describe the overlap method, given above. In fact, the sets of 2M points always overlap by M, whether inside a segment or between segments. As it is explained above, and they explain it, we expect an M-point overlap inside a segment and the succeeding segment to overlap the previous one by 2M.

The transforms were done in an efficient way by sending the first series of points (eg. 1-2048) in the real part, and the second series of points (eg.1024-3072) in the imaginary part of the complex input to the Fourier

transform subroutine (also from Press et al, 1985). The input data was padded with zeros from point 4372 to 5120. Since there were 2048 points in the transform input data (complex) array there were 1024 points in the array returned from the transform subroutine, giving a frequency resolution bandwidth of 50/2048 = 0.0244 Hertz. (50 Hertz is the digitization frequency of the input data.)

For the k = 4 calculations, the point segments were:

points 1 to 1024 and 512 to 1536;
points 1024 to 2048 and 1536 to 2560;
points 2048 to 3072 and 2560 to 3584;
points 3072 to 4096 and 3584 to 4608.

As before, the data was padded with zeros to make up 4608 points. The transform is now 512 points, with a frequency resolution bandwidth of 50/1024 = 0.0488 Hertz.

Notwithstanding the lack of agreement shown in Table D.1 it was decided to continue with the calculations of displacements using the records of the shaking table accelerations as input. If σ_x is biased up or down it should show up as all the calculated displacements would be biased in the opposite direction. (As σ_x increases up to and above the yield acceleration k_h the calculated displacements are reduced.)